Moving Contact Lines, Wetting Transitions and Interfacial Instabilities in Confined Environments

by

Amir Alizadeh Pahlavan

B.S., University of Tehran (2008)
M.S., University of Illinois at Urbana-Champaign (2010)

Submitted to the Department of Mechanical Engineering
in partial fulfillment of the requirements for the degree of

Doctor of Philosophy in Mechanical Engineering

at the

MASSACHUSETTS INSTITUTE OF TECHNOLOGY

September 2018

Signature redacted

Author . . . .

Department of Mechanical Engineering

Aug 17, 2018

Certified by . . . . **Signature redacted** . . . . .

Ruben Juanes
Professor, Civil and Environmental Engineering
Thesis Supervisor

Certified by . . . . **Signature redacted** . . . . .

Gareth H. McKinley
Professor, Mechanical Engineering
Thesis Supervisor

Signature redacted

Accepted by . . . .
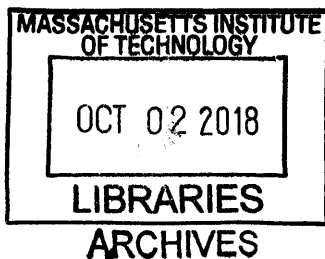
Rohan Abeyaratne
Professor, Mechanical Engineering
Chairman, Graduate Program Committee

Moving Contact Lines, Wetting Transitions and Interfacial Instabilities in Confined Environments

by

Amir Alizadeh Pahlavan

Submitted to the Department of Mechanical Engineering
on Aug 17, 2018, in partial fulfillment of the
requirements for the degree of
Doctor of Philosophy in Mechanical Engineering

Abstract

Immiscible fluid flows are ubiquitous in nature and industry, from multiphase-flow phenomena on geologic scales such as CO2 sequestration and methane venting from seafloor sediments to bubble/drop/emulsion generation in microfluidic techniques. All these flows are inherently multi-scale, from the intermolecular interactions on the nanometer scale in the vicinity of contact lines, where fluid phases meet the surrounding solid surface, to the micrometer scale of the confinement in a pore or microfluidic device, and finally to kilometer scale of the natural geologic phenomena. The multi-scale nature of immiscible fluid flows combined with the inherent disorder present in many natural or industrial systems renders description of these flows a formidable task.

Here, using a combination of experimental observations and theoretical modeling we show that the interplay between confinement and contact line motion leads to novel and non-trivial consequences on the dynamics and instability of immiscible fluid fronts.

We first present a theoretical model for thin-film flows on solid surfaces in the partial wetting regime and show that a self-consistent description of free energy of this system at equilibrium leads to a Cahn–Hilliard form with an effective height-dependent surface tension due to the intermolecular forces in the vicinity of the contact line. Within the framework of non-equilibrium thermodynamics, we then study the consequences of this new form of free energy on the spreading of drops and dewetting of thin films in the partial wetting regime. We show that on macroscopic scales, our model recovers the classic hydrodynamic Cox–Voinov description of moving contact lines and is consistent with experimental observations. We further show that on the microscopic scale our model is consistent with the molecular kinetic theory, therefore bridging the gap between the two descriptions across the scales. We finally show that our model captures the dynamics of nanometric dewetting thin films in spinodal and nucleation regimes as well as their long-time coarsening behavior and brings the theoretical predictions closer to the previous experimental observations.

We then revisit the classic Taylor–Bretherton problem in the partial wetting

regime, where air displaces a highly viscous liquid in a capillary tube. In contrast with the classic results for complete wetting, we show that the presence of a moving contact line induces a wetting transition at a critical capillary number that is contact angle dependent. Beyond wetting transition, a film of the defending liquid coats the tube walls. The entrained liquid film immediately starts receding along the tube wall, forming a growing dewetting rim behind the contact line, which finally leads to the breakup of the bubble. The bubble pinch-off is an example of singularity formation, where separation of length scales close to the point of singularity are expected to lead to self-similar and universal dynamics. We show that the breakup of a bubble confined in a capillary tube undergoes a sequence of two distinct self-similar regimes even though the balance remains between viscous and surface-tension forces. While the breakup of a bubble in an unbounded reservoir is known to be non-universal, we demonstrate that the presence of the early-time self-similar regime in a confined system effectively erases the system's memory and restores universality to bubble breakup.

We then revisit the classic Saffman–Taylor instability in the imbibition regime, where a more wetting and less viscous liquid displaces a less wetting and more viscous liquid in a radial Hele-Shaw cell (two plates separated by a small gap). We show that the wetting liquid invades the cell in the form of a thin-film front, which becomes unstable and leads to a viscous fingering pattern. To gain an understanding of the front dynamics, we develop a thin-film model, which predicts the base state of the invading thin films to be an undercompressive shock, which has previously been shown to lead to stable fronts. Using linear stability analysis and nonlinear simulations, we show that consistent with our experimental observations the thin film front in a Hele-Shaw cell is unstable. The instability here is due to the pressure coupling between the two fluid flows in a confined domain. We further show that the scaling of the wavelength of instability in thin-film front is different from the Saffman-Taylor instability, suggesting that it belongs to a new pattern formation class.

In the final part of this thesis, we explore how the interplay between wetting and disorder influences the pattern formation. We introduce disorder into the Hele-Shaw system by making one of the surfaces randomly rough. In particular, we show that in the imbibition regime aside from the primary thin films that we observed in smooth cells, secondary thin films of the scale of roughness appear. These secondary films wick into the crevices of the rough surface with a diffusive dynamics and change the effective wettability of the medium. We therefore show that disorder on the micro-scale affects the macroscopic morphology of unstable fluid fronts.

Thesis Supervisor: Ruben Juanes
Title: Professor, Civil and Environmental Engineering

Thesis Supervisor: Gareth H. McKinley
Title: Professor, Mechanical Engineering

Acknowledgments

First, I would like to sincerely thank my advisors Ruben Juanes, and Gareth McKinley. Thank you for your support, wisdom, and giving me the freedom to explore. It has been a privilege to interact with you and learn from you over the past few years.

Thank you to my committee members, Luis Cueto-Felgueroso, Peko Hosoi, and Mehran Kardar. Luis, I have been lucky to have you as my mentor; your insight and kindness has always been an inspiration for me. Peko, thank you for your constant stream of encouragement, positive energy and great ideas to explore. Mehran, thank you for your insightful questions and suggestions. I am truly grateful to all of you.

During my PhD, I have had the pleasure of interacting with many wonderful scientists; these interactions have always inspired me to learn more and have helped me to improve myself as a researcher. Thank you Jens Eggers, Jacco Snoeijer, Howard Stone, Tom Witelski, Detlef Lohse, Andrea Bertozzi, John Bush, Irmgard Bischofberger, Kostya Turitsyn. I would like to thank Denis Bartolo in particular for his kindness and sharing his insight.

To my friends at MIT, thank you for the discussions over many long lunch/coffee/tea hours and and lots of great memories.

To my parents, I cannot thank you enough for your selfless devotion, support, encouragement, and doing everything in your power to make sure we had the best opportunities. I am forever grateful for everything you have done for me.

And to Setareh, for being my everything; I have been blessed to have you by my side over all these years; thank you for your patience, love, and support. This thesis is dedicated to you and Soren.

Contents

Introduction

Patterns are ubiquitous in nature, from snowflakes (Libbrecht, 2017) to valley networks (Perron et al., 2009) (Fig. 0-1). How these complex macroscopic patterns arise from simple microscopic rules has always fascinated and attracted scientists. From an engineering viewpoint, understanding these processes is a first step in designing self-organized or self-assembled structures from few basic rules (Manoharan, 2015; Zeravcic et al., 2017). Considerable progress has been made in understanding, and describing pattern formation using different classes of models (Gollub and Langer, 1999; van Saarloos, 2003). However, given the complexity and seemingly infinite variety of patterns that can be observed in nature, one wonders if there is a universality in these phenomena.

While in critical phenomena, the microscopic details are screened and macroscopic quantities follow universal laws (Kadanoff, 2000; Kardar, 2007), phenomena associated with pattern formation are often very sensitive to the microscopic details. For instance, in the dendritic growth and side-branching observed in solidification processes, noise at the atomic scale is thought to be responsible for many of the observations on macroscopic scales (Gollub and Langer, 1999; Libbrecht, 2017). In the dynamical systems language, this is due to the fact that in many of the pattern forming phenomena, unstable fixed points can be sampled if the system is perturbed, and this often is the case due to the presence of thermal noise or other experimental perturbations. Therefore, a good understanding of the microscopic physics is needed to be able to describe and control macroscopic patterns (Kessler et al., 1988).

One of the archetypes of pattern formation is the Saffman–Taylor instability (?), which occurs when a less viscous fluid displaces a more viscous fluid in a Hele-Shaw cell
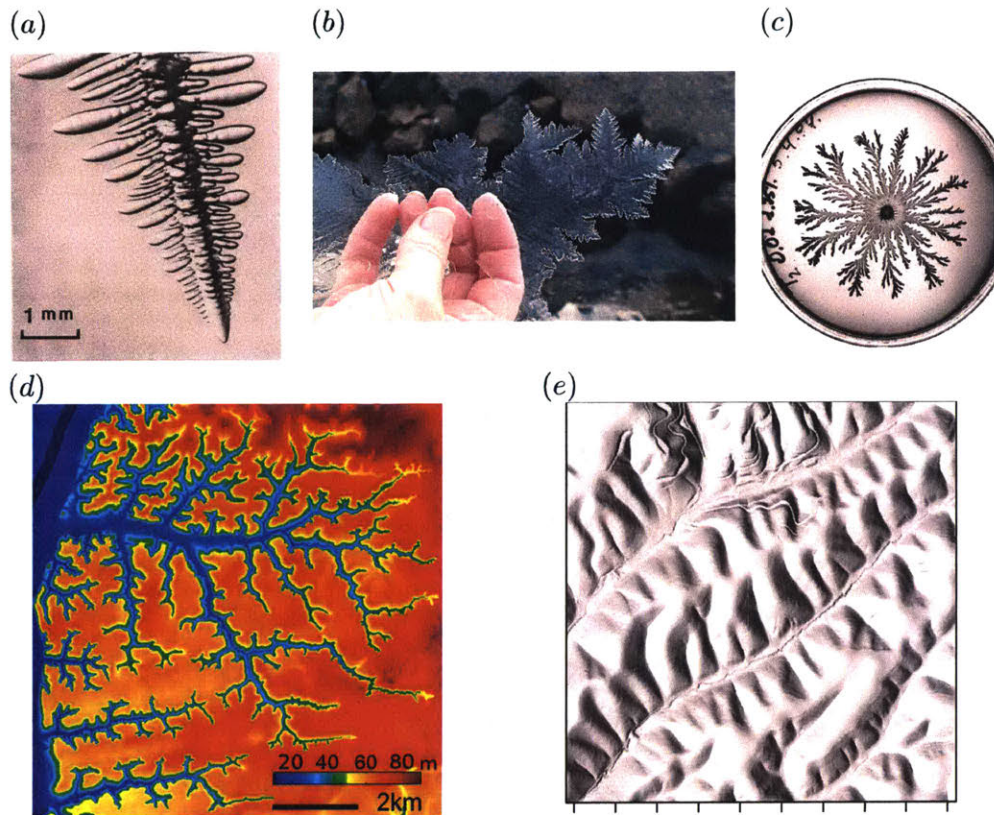
Figure 0-1: Pattern formation in natural phenomena across the scales: (a) dendritic patterns observed in the growth of succinonitrile in its undercooled melt (Langer, 1989); (b) an ice crystal sheet naturally grown on the surface of a lake (Libbrecht, 2017); (c) growth of Paenibacillus dendritiformis dendron on the surface of agar gel (Ben-Jacob et al., 2000); (d) groundwater flow has shaped the networks of valleys, Florida, USA (Devauchelle et al., 2012); (e) uniformly-spaced valleys in Gabilan Mesa, California (Perron et al., 2009); the spacing between ticks is 200m.

consisting of two parallel plates separated by a tiny gap, leading to the formation of "viscous fingers" (Fig. 0-2). The question of pattern selection in the Saffman–Taylor instability attracted much attention over the past few decades (Pitts, 1980; Park and Homsy, 1984, 1985; Saffman, 1986; Tabeling et al., 1987; Casademunt, 2004; Nagel and Gallaire, 2013). The original work by Saffman and Taylor neglected surface tension and obtained an infinite family of solutions, from which only one was observed in the experiments. Later, it became clear that this problem is singular, where neglecting surface tension leads to the non-uniqueness of the solution (Bensimon et al., 1986; Homsy, 1987). More recent works have shown that three-dimensional effects close
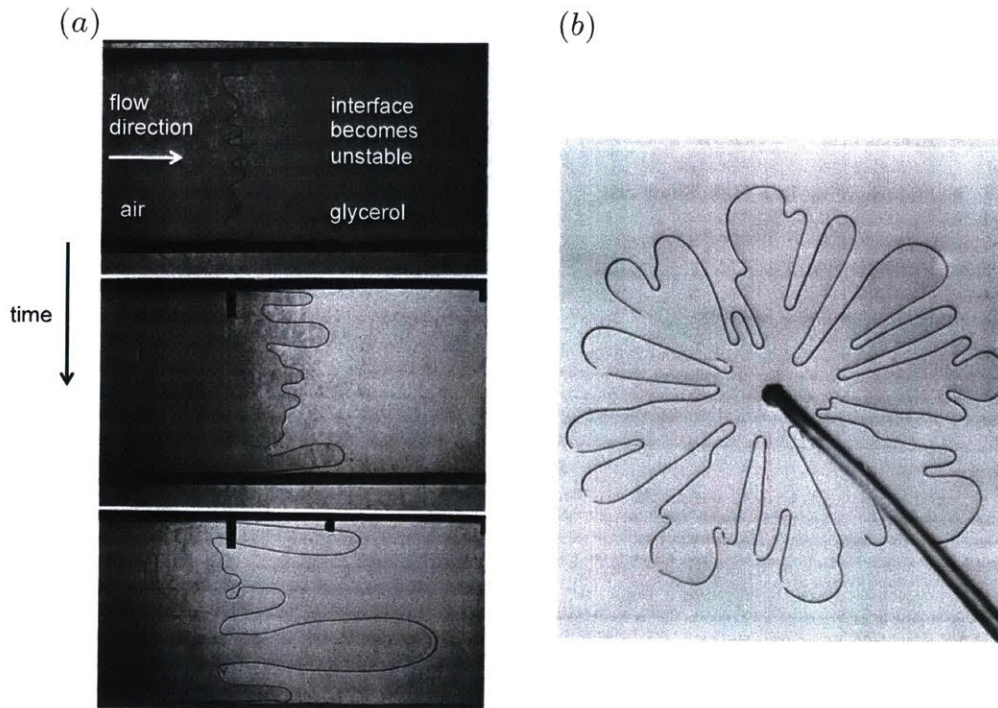
Figure 0-2: The Saffman–Taylor instability, in which a less viscous fluid displaces a more viscous liquid: (a) the original experiment by Saffman and Taylor, where air displaces glycerol in a Hele-Shaw cell, leading to the formation of viscous finger (?); (b) air displacing glycerol in a radial Hele-Shaw cell, where injection is done at the center of the cell (Paterson, 1981).

to the fluid-fluid interface may render the gap-averaged equations invalid (Ledesma-Aguilar et al., 2007a,b). The question of pattern selection in the Saffman–Taylor instability, its control and variations to this instability is an active and rich research area (Nagel, 2017; Juel et al., 2018).

Dendritic patterns can also be observed in the Saffman–Taylor instability if the system is perturbed. Figure 0-3 illustrates several examples, where perturbations in the form of etched grooves, bubbles, or a wire are introduced and it is observed that the patterns can be quite different in their morphology from that in the ideal case (Couder et al., 1986b,a). While we have achieved considerable progress in describing these patterns and their sensitivity to the ever-present perturbations (Langer, 1989; Ben-Jacob and Garik, 1990; McCloud and Maher, 1995), the questions are far from being completely addressed and are subject to ongoing investigation (Franco-Gómez

(i)

(ii)
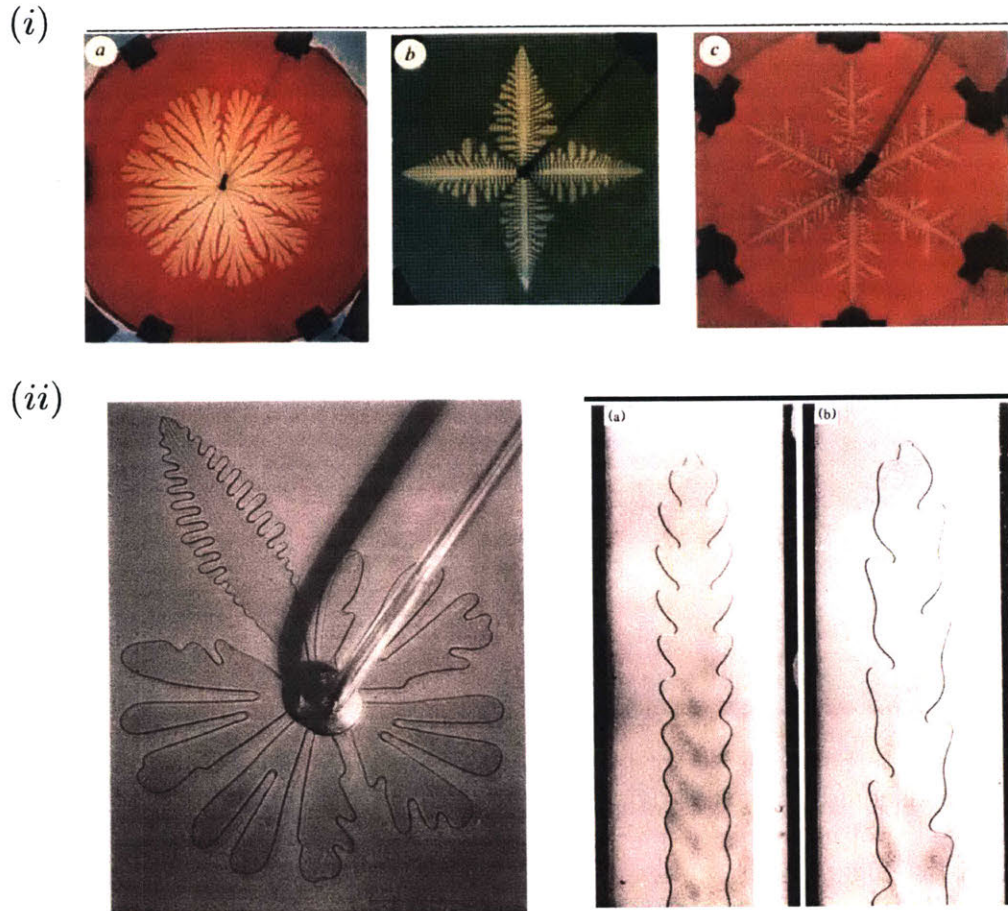
Figure 0-3: Experimental perturbations to the Saffman–Taylor instability: (i) etching grooves on one of the surfaces of the cell leads to the dendritic growth of the patterns, i.e. introduce anisotropy in the effective surface tension (Ben-Jacob and Garik, 1990). (ii) introducing bubbles or a wire into the cell leads to the growth of dendritic patterns, where the perturbed finger travels faster than the unperturbed ones (Couder et al., 1986b,a).

et al., 2016).

Hele-Shaw flows are commonly used as analogue systems to study porous media flows. The reason for this analogy is that Darcy's law governs single-phase flow through both a porous medium and a Hele-Shaw cell. While Darcy's law for single-phase flow in porous media can be rigorously derived from microscopic physics using a thermodynamically consistent upscaling procedure (Hassanizadeh and Gray, 1979a,b, 1980; Hassanizadeh, 1986a,b), generalized Darcy equations that are commonly used to describe immiscible flows in porous media (Bear, 1972) cannot be derived from

14

first principles (Hassanizadeh and Gray, 1990, 1993a,b), and do not account for the dynamic effects (Hassanizadeh et al., 2002). In fact, averaging from micro scale to the Darcy scale introduces new parameters that need closure (Gray and Miller, 2005; Miller and Gray, 2005; Jackson et al., 2009). The generalized Darcy's law involves capillary pressure and relative permeability functions that are saturation-dependent and more importantly history-dependent (Cueto-Felgueroso and Juanes, 2016)—the drainage and imbibition procedures lead to different flow curves and empirical models have commonly been used to describe these curves (Blunt, 2017). This hysteresis has been associated with the fact that the generalized Darcy's model is mainly empirical and misses the important physical ingredients of two-phase flow in porous media. A school of thought in developing a new generalized multiphase flow model in porous media has been to introduce more information (interfacial area, connectivity, etc) into the generalized Darcy's law to allow the capillary pressure and relative permeability curves be uniquely defined based on the combination of saturation, interfacial area, connectivity, etc (Reeves and Celia, 1996; Joekar-Niasar et al., 2008; Niessner et al., 2011); while this approach has led to some level of success in removing hysteresis from the description, deriving evolution equations for the extra parameters introduced in this procedure remains and open question and subject to ongoing debate (Gray et al., 2013, 2015).

The need for a new class of models for immiscible fluid flows in porous media becomes more clear knowing that the current models often fail to reproduce the unstable fronts, which are common in applications such as infiltration of water into soil or CO_2 sequestration, as illustrated in Fig. 0-4 (Cueto-Felgueroso and Juanes, 2008a; Cinar and Riaz, 2014). To address the need for new models for immiscible flows in porous media, we have to resort to simpler analogue systems such as Hele-Shaw cells or micromodels, which allows isolating the underlying physics of the system.

Based on micromodel experiments and pore network simulations, Lenormand et al. (1988) proposed a phase diagram for immiscible displacements in the drainage regime (less wetting liquid displacing a more wetting one) as a function of the viscosity ratio between the liquids and injection rate, classifying the observed patterns into

(i)   (ii)
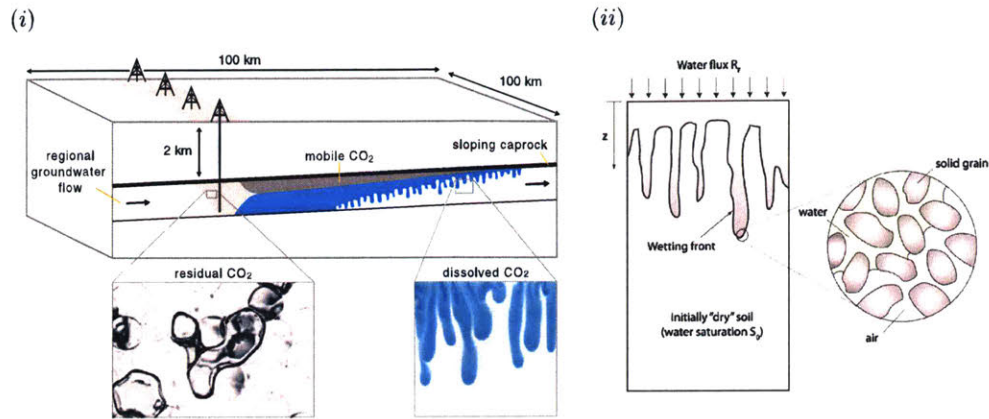
Figure 0-4: Immiscible fluid flows in porous media typically lead to unstable fronts: (i) shows a schematic of the CO_2 sequestration process in a saline aquifer (Szulczewski et al., 2012). Supercritical CO_2 is less than the surrounding brine and rises due to buoyancy. On short time scales, the rise of the plume leads to capillary trapping of CO_2 on the back of the plume where brine displaces the CO_2 in an imbibition process (Juanes et al., 2006; Hesse et al., 2008), whereas on longer time scales the mixing of the CO_2 front with brine leads to gravitational fingering (Ennis-King and Paterson, 2005; Riaz et al., 2006), (ii) shows a schematic of the gravity infiltration of water into unsaturated soil (Cueto-Felgueroso and Juanes, 2008a). The classical Richards equation for infiltration (Richards, 1931) predicts the front to be stable, which is in clear contradiction with the experimental observations (DiCarlo, 2013; Wei et al., 2014).

three groups: capillary fingering corresponding to invasion percolation (Wilkinson and Willemsen, 1983), viscous fingering corresponding to diffusion limited aggregation (Witten and Sander, 1981; Paterson, 1984; Måløy et al., 1985), and stable displacement (Fig. 0-5).

Changing the wetting properties of the medium, however, has a profound influence on the displacement patterns; for instance Stokes et al. (1986) performed experiments in a Hele-Shaw cell filled with glass beads, and showed that in the drainage regime, the width of the fingers is in the order of the pore size whereas in the imbibition regime finger width becomes macroscopic (multiple pore size) and depends on the injection rate in the form of the capillary number with a macroscopic surface tension (Fig. 0-6). Trojer et al. (2015) revisited this classic experiment in a radial Hele-Shaw cell filled with glass beads; by systematically changing the wetting properties of the medium, they showed that the patterns observed by Lenormand can all be reproduced, i.e.
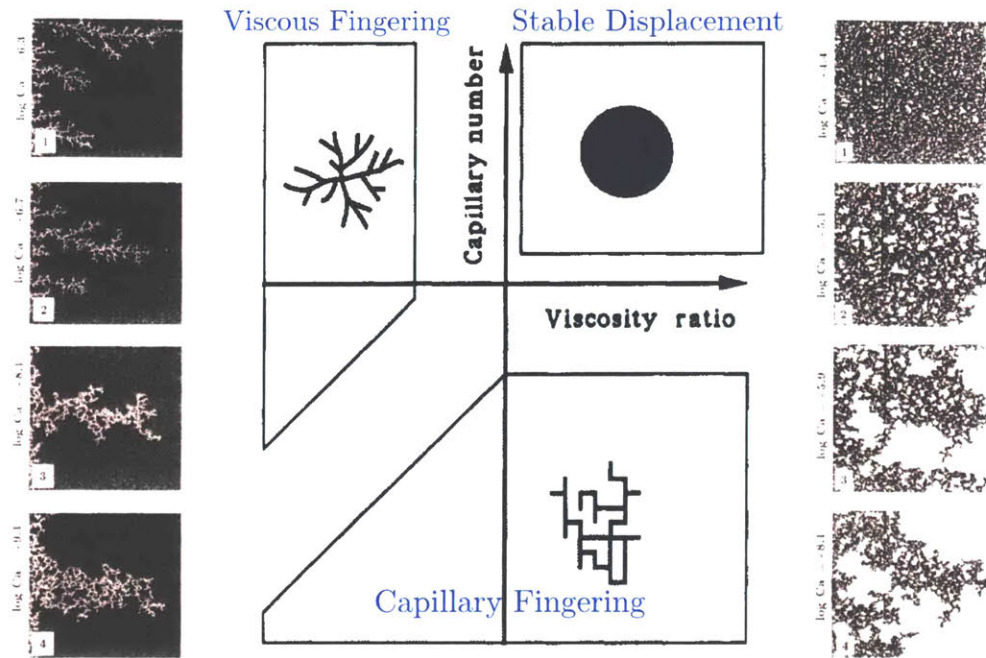
Figure 0-5: Phase diagram proposed by Lenormand et al. (1988) based on micromodel experiments and pore network simulations categorizing the observed flow regimes in drainage into three distinct groups, depending on the viscosity ratio of the two fluids, and the injection velocity as defined by the capillary number, representing the ratio of viscous to capillary forces. The left column shows air displacing oil, leading to viscous fingering at high injection rates and capillary fingering at low rates. The right column shows mercury (a non-wetting liquid) displacing air, leading to stable displacement at high injection rates when viscous forces are dominant. At low injection rates, however, the interface becomes unstable due to the dominance of capillary forces and the disorder in the pore size distribution of the micromodel, leading to the emergence of the capillary fingering regime.

capillary fingering, viscous fingering, and compact displacement; displacing a more viscous liquid by a less viscous one, we expect to observe a fingering instability; they however, showed that the cooperative pore filling mechanism in the imbibition regime can lead to a stable displacement (Fig. 0-7).

The experimental observations by Trojer et al. (2015) at low injection rates verified the quasi-static theoretical modeling of Cieplak and Robbins (1988, 1990); Martys et al. (1991), who observed a transition from invasion-percolation type behavior to a cooperative pore-filling mechanism (Fig. 0-8). While the invasion-percolation regime leads to a fractal structure of the front, the cooperative pore filling regime leads to a

drainage   imbibition
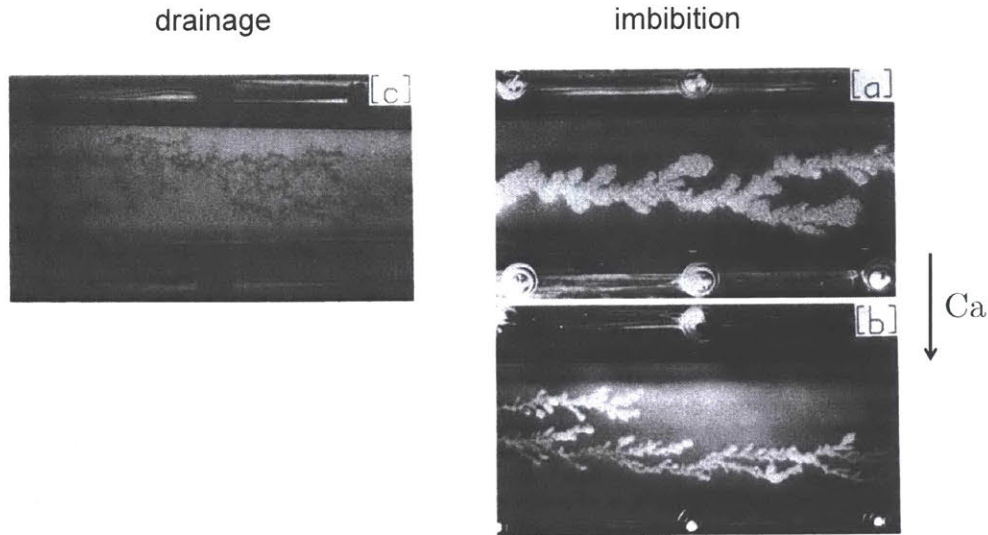
Figure 0-6: The immiscible fluid flow experiments in glass bead-filled Hele-Shaw cells Stokes et al. (1986), in which a less viscous fluid displaces a more viscous liquid. In the drainage regime, the pore size determines the finger width. In the imbibition regime, however, finger width is macroscopic (multiple finger width) and depends on the flow rate as well as permeability of the medium; here, the normalized finger width scales as $Ca^{-1/2}$, where $Ca = \mu U/\gamma$, with μ as the viscosity of the defending fluid, U as the characteristic velocity, and γ as the surface tension.

compact front. The transition between these two regimes therefore marks the onset of a self-organized criticality, where the correlation length diverges. Martys et al. (1991) argue that this transition can be categorized as a depinning transition, where the quenched disorder in porous media pins the contact line while the external pressure or force together with elasticity of the interface tend to depin the interface. This observation implies that the onset of flow in the cooperative pore-filling regime is analogous to the self-organized criticality (Bak et al., 1987) in other systems such as charge-density-wave conductors (Fisher, 1983), advancing crack fronts (Kardar, 1998; Alava et al., 2006), or earthquake faults (Carlson and Langer, 1989).

While the displacement of a more viscous liquid by a less viscous fluid is hydrodynamically unstable (?), the cooperative pore filling in imbibition regime stabilizes the interface leading to a compact front. In engineering applications, such as oil and gas recovery, there is a strong evidence for the importance of wettabiity (Jadhunandan and Morrow, 1995; Buckley et al., 1998; Manrique et al., 2007; Spiteri et al., 2008),
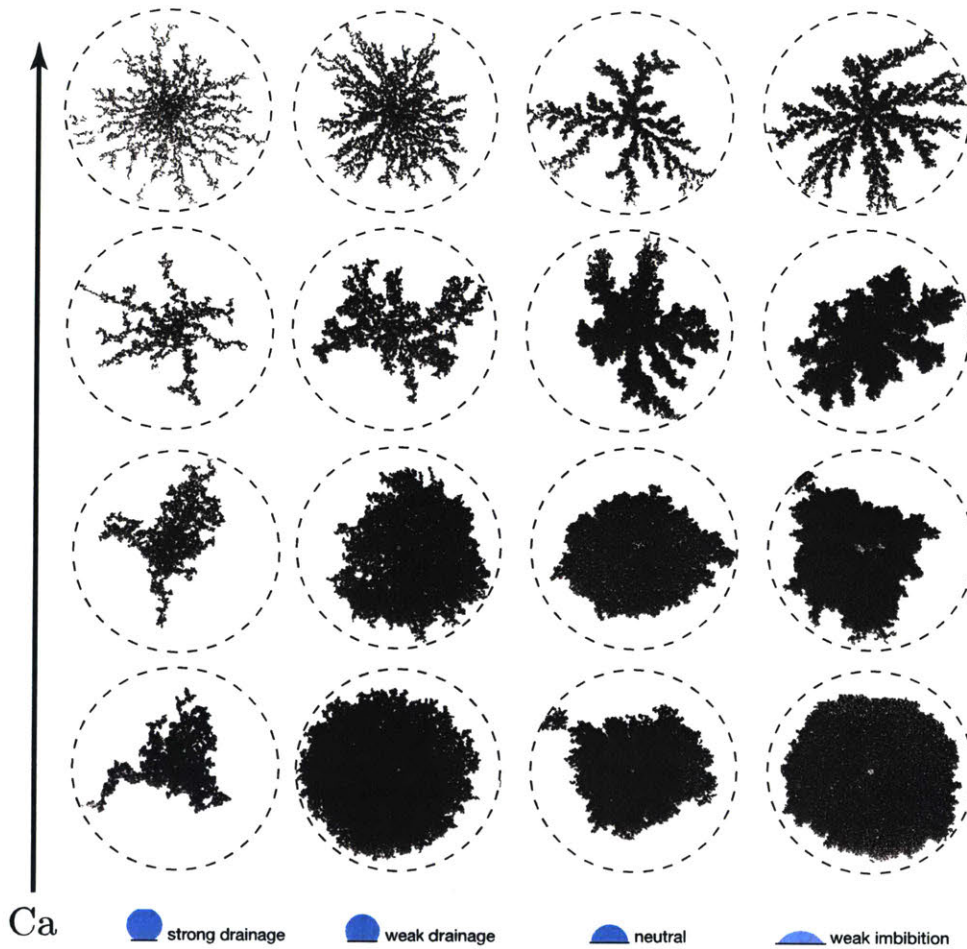
Figure 0-7: The immiscible fluid flow phase diagram based on experiments in glass bead-filled Hele-Shaw cells (Trojer et al., 2015): changing the wetting properties of the medium profoundly changes the displacement patterns. The cooperative pore filling mechanism in the imbibition regime leads to a complete suppression of fingering instability at low enough flow rates, resulting in a stable displacement pattern.

and different methods such as low-salinity water flooding (Morrow and Buckley, 2011) or surfactant flooding (Standnes and Austad, 2003; Chen and Mohanty, 2013) are typically used to alter the wettability of the medium. To maximize the recovery of oil, we may then conclude that the best practice is to make the displacing fluid as wetting to the medium as possible and inject at the lowest possible rate to achieve a stable compact displacement and maximize the extraction efficiency. Recent experiments, however, indicate that this conclusion is not correct.

Zhao et al. (2016) studied immiscible displacement of a viscous oil by a less viscous
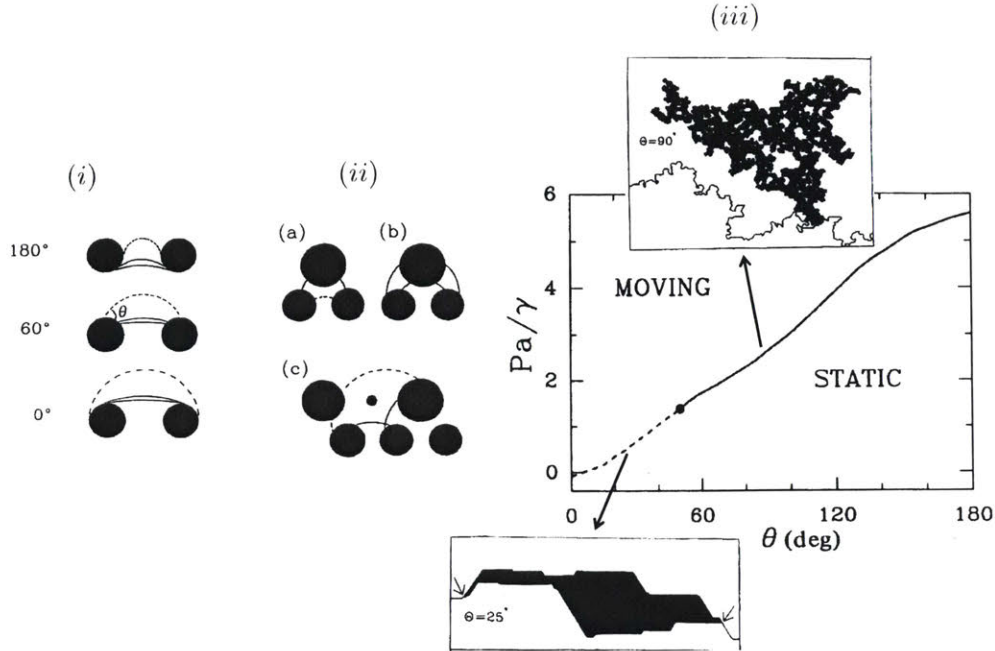
Figure 0-8: Quasi-static modeling of immiscible displacement in a micromodel (Cieplak and Robbins, 1990; Martys et al., 1991): (i) as the pressure of the invading fluid is increased, the front location shown here between two identical cylinder adjusts until at a critical pressure the interface becomes unstable, i.e. no static equilibrium solutions can be obtained. The last stable arc is shown by the dashed line, (ii) an unstable interface can advance by (a) burst-like behavior, (b) touching the next cylinder, or (c) overlapping the arc in a neighboring pore space, (iii) pressure–contact angle phase-diagram of quasi-static invasion, where the solid line indicates the onset of invasion percolation transition, whereas the dashed line represents the onset of depinning transition.

water phase in a micromodel system. They tuned the wettability of the system from the strong drainage regime, where a non-wetting fluid displaces a wetting fluid, all the way to the strong imbibition regime, where the invading fluid is almost completely wetting to the medium. Their observations indicated that while changing the wettability from drainage to weak imbibition leads to a more stable front at low injection rates, in the strong imbibition regime the interface becomes unstable leading to a ramified front (Fig. 0-9). The underlying reason for this instability is the emergence of thin films of the invading liquid in the strong imbibition regime.

The emergence of thin films of the invading fluid in the strong imbibition regime were first reported in the experiments by Levaché and Bartolo (2014) on Hele-Shaw
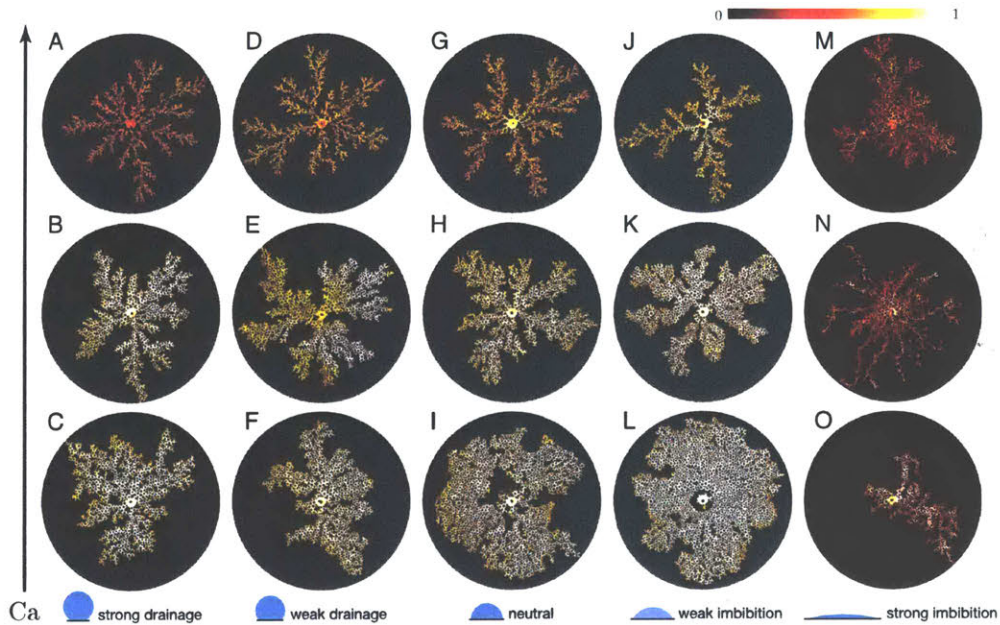
Figure 0-9: Immiscible fluid flow phase diagram based on experiments in micromodels (Zhao et al., 2016): here a less viscous liquid, water, displaces a more viscous liquid, silicone oil. The wettability of the medium is changed all the way from oil-wet (strong drainage) to water-wet (strong imbibition). In the drainage regime, capillary fingering is observed at low injection rates, whereas viscous fingering persists at high injection rates. In the weak imbibition regime, at low injection rates, the interface becomes stabilized due to the cooperative pore filling mechanism, consistent with earlier theoretical and experimental observations (Cieplak and Robbins, 1988; Trojer et al., 2015). In the strong imbibition regime, however, thin films of the invading liquid become entrained on the surfaces and make the front unstable.

cells and have since been observed in micromodel systems (Zhao et al., 2016; Odier et al., 2017). The micromodel observations in particular point to the importance of this regime since it drastically influences the displacement efficiency. The work by Levaché and Bartolo (2014) proposed a theoretical framework for the onset of wetting transition leading to the entrainment of the thin films. The dynamics and subsequent observed instability of these films, however, have remained open questions.

While Hele-Shaw flows are commonly used as analogue systems to study porous media flows, the intrinsic disorder of porous media is absent in a Hele-Shaw system. Disorder, however, can be introduced in a Hele-Shaw cell in the form of defects or surface roughness. This setting has been widely used in studying the stable imbibi-
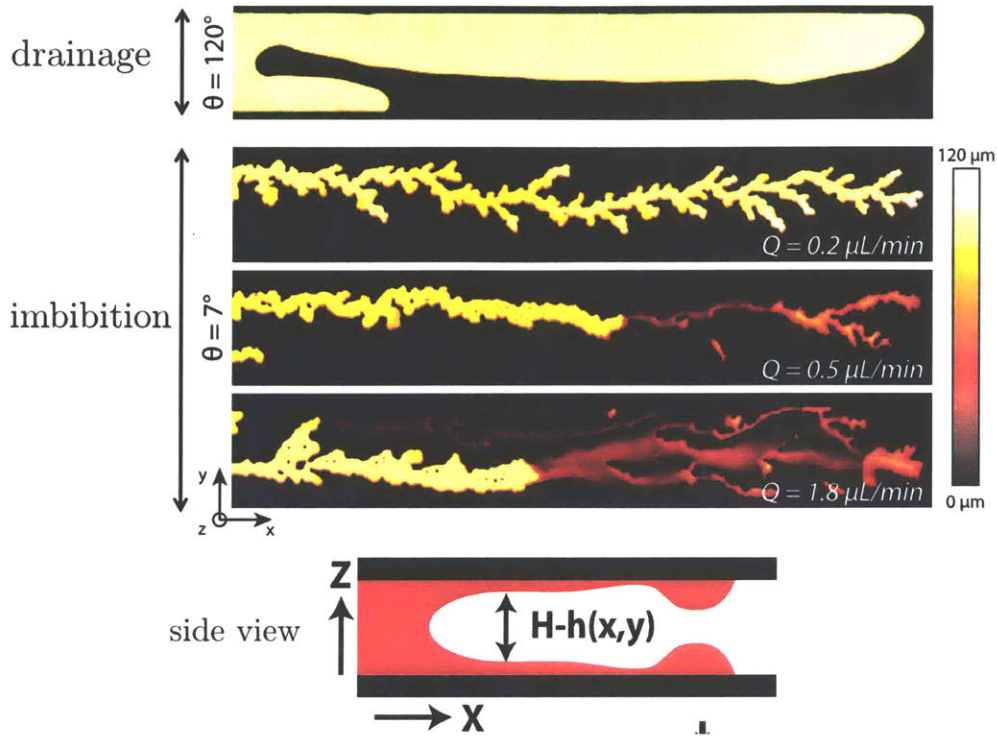
Figure 0-10: Entrainment of thin films of the invading liquid in the unstable imbibition regime (Levaché and Bartolo, 2014): while in the drainage regime in a Hele-Shaw cell, one recovers the classic Saffman–Taylor instability, changing the medium wettability to strong imbibition leads to the emergence of a ramified structure. Beyond a critical displacement rate in the imbibition regime, thin films of the invading liquid become entrained on the channel walls and travel ahead of the main meniscus. While the onset of this wetting transition has been explained (Levaché and Bartolo, 2014), the dynamics and instability of the thin film front remain open questions.

tion regime, where a viscous wetting liquid displaces a non-wetting gas or less viscous liquid; the presence of disorder leads to many interesting phenomena like kinetic roughening and avalanche behavior of advancing fronts (Fig. 0-11). The question of universality class of disordered fronts in stable imbibition and its connection to surface growth phenomena has been an active area of research in the past decades and is still of interest and relevance (Alava et al., 2004; Planet et al., 2009; Clotet et al., 2014). The influence of disorder on other flow regimes, and in particular on the unstable imbibition, however, has received much less attention. This is surprising given that the unstable imbibition regime may be relevant to many applications; for instance, carbonate reservoirs are typically water-wet, which indicates that the un-
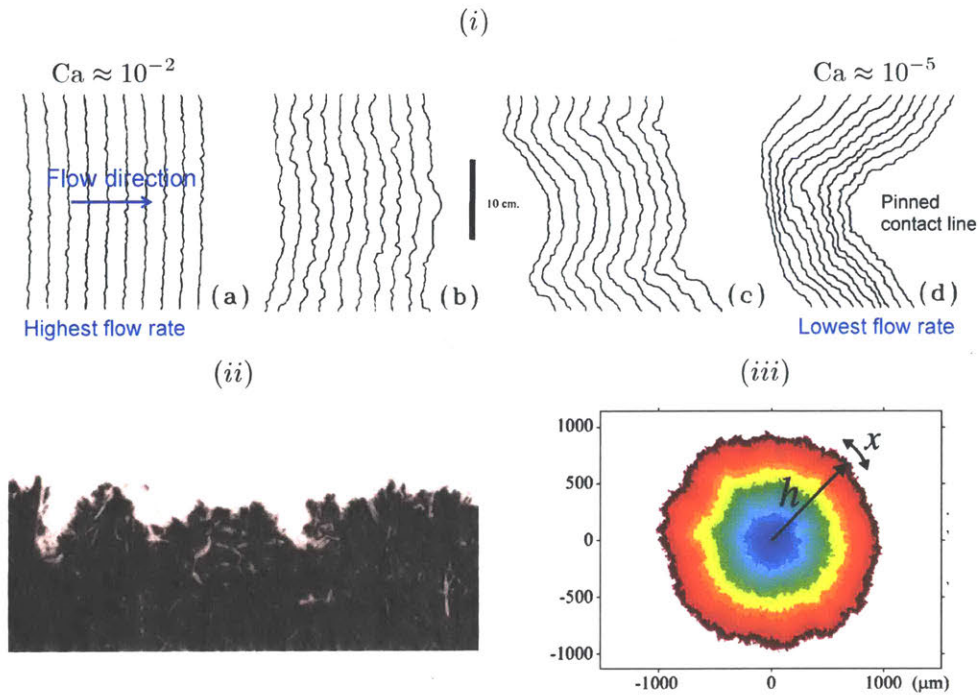
Figure 0-11: Kinetic roughening of the front in stable imbibition: (i) water flowing into a Hele-Shaw cell filled with glass beads (He et al., 1992); as the displacement rate decreases from left to right, the interface become more sensitive to the disorder and gets pinned. (ii) dyed water imbibing spontaneously into a disordered fiber network (i.e. a paper towel); the front roughness reflects the inherent complexity and disorder of the medium (Alava et al., 2004), (iii) the evolution of an interface between two different turbulent states in a convective nematic liquid crystal, where disorder is caused by the topological defects in the defending phase, leading to a local surface growth process (Takeuchi et al., 2011).

stable imbibition regime and film flows can play key role in the displacement process.

In this thesis, we focus on the role of contact line motion on immiscible fluid flows in confined environments. We begin by developing a theoretical model for moving contact lines in the context of thin-film flows in the partial-wetting regime. Moving contact lines are inherently multiscale and multiphysics (Fig. 0-12). We derive the free energy of the system at equilibrium and show that to achieve an equilibrium droplet in the partial-wetting regime, one needs to take the intermolecular interactions close to the contact line into account. We show that these molecular interactions lead to a height-dependent surface tension in the vicinity of contact line. This new feature leads to multiple new observations, including compact support for the drop at equilibrium

23
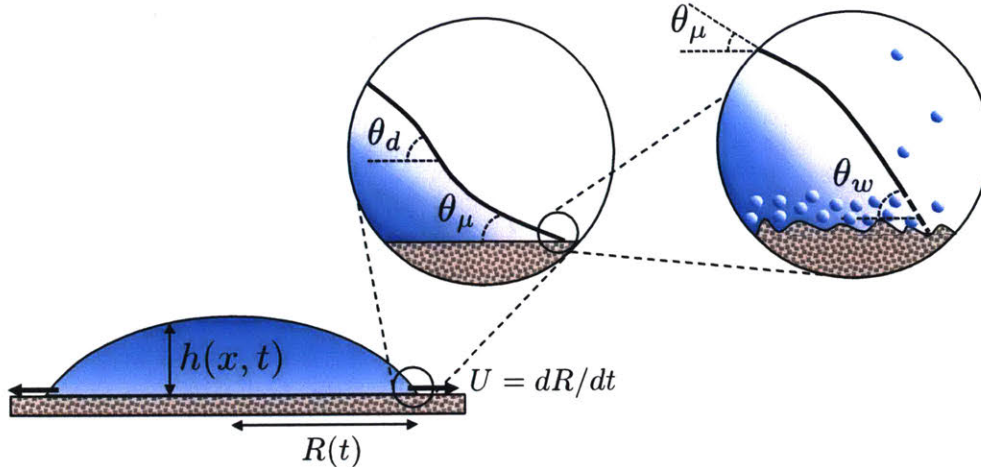
Figure 0-12: A schematic of the multiscale nature of the moving contact lines in a spreading drop with radius R and contact line velocity U: in the hydrodynamic description of moving contact lines, the dynamic contact angle θ_d is velocity-dependent and follows the Cox–Voinov law, while the microscopic contact angle is considered to be constant and equal to the equilibrium contact angle (Bonn et al., 2009; Snoeijer and Andreotti, 2013). In the molecular kinetic theory, however, the contact line meets the surface with an angle that is also velocity-dependent, but follows a scaling different from that of the hydrodynamic theory (Blake, 2006). Our model bridges the gap between these two descriptions.

(no precursor film), a localized slip mechanism, convexity of the contact line profile at the nano-scale, and faster dewetting of nanometric thin films (Pahlavan et al., 2015; Alizadeh Pahlavan et al., 2018a,c). These results collectively bring theoretical predictions closer to the experimental observations and propose a new framework for a self-consistent approach to describe moving contact lines.

Immiscible fluid flows generally take place in confined geometries, such as a microfluidic cell or the pore space of porous media. Confinement exacerbates the role of nonhydrodynamic intermolecular forces due to the larger surface-to-volume ratio, and also introduces a nonlocal coupling between the flowing fluid phases. To understand the role of confinement, we then describe fluid-fluid displacement in the simple geometry of a capillary tube. The simplicity of this geometry allows us to understand the role of contact line motion on the meniscus dynamics as well as the stability of thin films coating the tube surface. These insights will prove essential in the understanding of interfacial dynamics during phase entrapment and phase change in porous media.

24
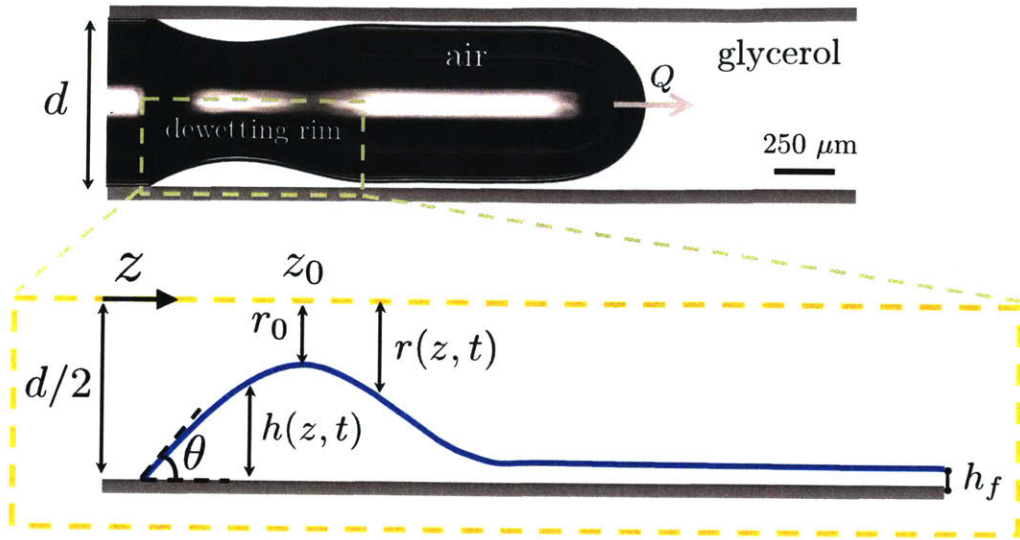
Figure 0-13: Dewetting rim next to the receding contact line: beyond the wetting transition, a growing dewetting rim appears, which ultimately leads to the pinch-off. The dynamics of this film is decoupled from the dynamics of the bubble front and can be described within a long-wave approximation framework (Zhao et al., 2018).

We analyze the onset of wetting transition, in which a film of the defending liquid becomes entrained on the walls, as well as the dynamics of the growing dewetting rim beyond transition (Fig. 0-13). As the contact line keeps receding, the rim grows and finally leads to the pinch-off of the bubble. This phenomenon is an example of singularity formation, which is characterized by self-similarity and universality. We show that the pinch-off dynamics undergoes a sequence of two distinct self-similar regimes and restores universality to the bubble breakup, which is lost in the bubble formation in unbounded domains.

We then extend the description of immiscible displacements from a capillary tube (1D geometry) to the gap between two parallel plates, or Hele-Shaw cell (2D geometry). In particular, we focus on the regime of unstable imbibition, where a wetting liquid displaces a less wetting and more viscous liquid. We observe in this regime thin films of the invading liquid get entrained on the cell surface and the thin-film front becomes unstable, leading to the formation of viscous fingers. Using a thin-film model, we analyze the stability of the front and show that the base state is an undercompressive shock— a mathematical structure encountered in thin-film flows in
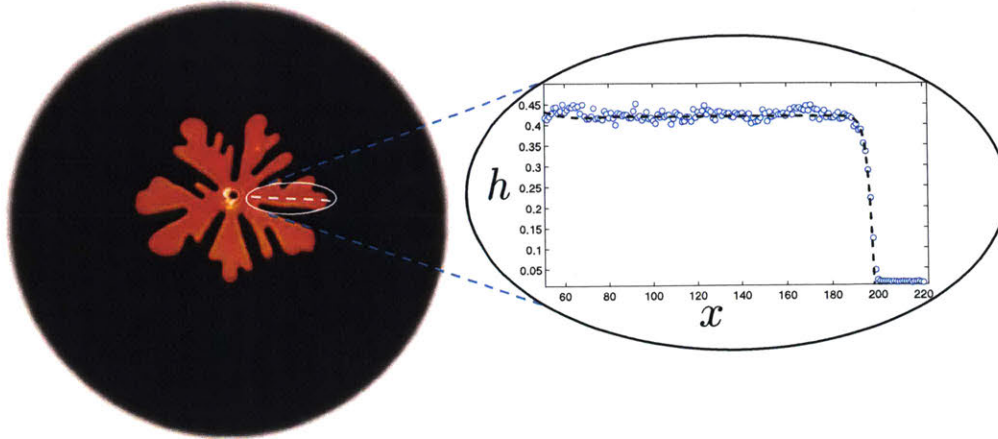
Figure 0-14: Thin-film fornt instability in unstable imbibition regime in a radial Hele-Shaw cell: the 1D cut of the profile shows a side viiew of the thin-film finger, which seems like an undercompressive shock structure; symbols represent experimental data and the dashed line shows the result of the theoretical model.

unbounded domains, which was found to lead to stable fronts (Bertozzi et al., 1998, 1999). However, consistent with our experimental observations, we find the base state to be unstable due to the non-local coupling of the pressure fields between the two fluids in the confined geometry. We further show that the scaling of the wavelength of instability in the thin-film front in unstable imbibition is different from that of the Saffman-Taylor instability. These observations further emphasize on the significant role of the interplay between contact line motion and confinement in emergence of novel flow regimes that were previously unnoticed.

In the last part of this thesis, we focus on the impact of disorder on the pattern formation in a Hele-Shaw cell. While disorder is known to fundamentally alter the patterns in the classic Saffman-Taylor instability (drainage regime), and in stable imbibition regime, much less is known about its influence in other wetting conditions and in particular on the unstable imbibition regime. We show that the presence of disorder in the form of micro-scale roughness on one of the Hele-Shaw cell surface leads to macroscopic changes in the pattern formation and morphology of the front. In particular, we show that roughness leads to the "hemi-wicking" of the invading liquid into the grooves of the surface with a diffusive dynamics and changes the effective wettability of the medium. These observations are of significance for instance in

26
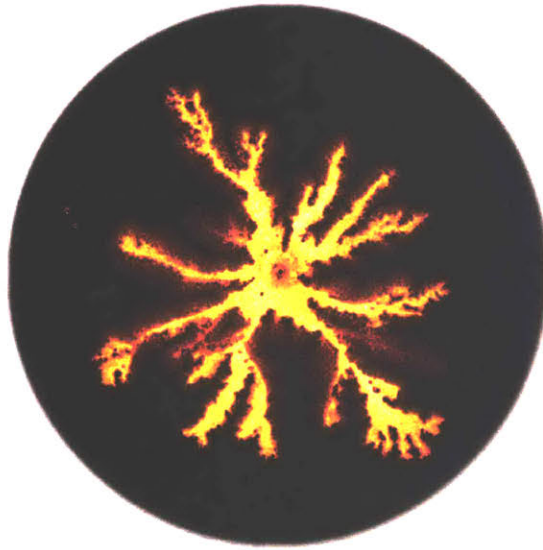
Figure 0-15: The interplay between contact line motion and disorder in a radial Hele-Shaw cell: the bright yellow regions show thin films of the invading liquid, which show a more ramified front compared with the smooth case, and the red halos surrounding them show the secondary films that wick into the crevices of the rough surface.

water-wet carbonate reservoirs, where film flows can have a dominant influence on the displacement processes on kilometer scale.

Part I

Thin films in partial wetting

Chapter 1

Stability, dewetting and coarsening

Understanding the underlying physics of how fluids coat solid substrates has been a long-standing quest in fluid dynamics (Blake and Ruschak, 1979; Ruschak, 1985; Quéré, 1999; Weinstein and Ruschak, 2004; Snoeijer and Andreotti, 2013). With the advent of micro and nano scale lithography techniques enabling manipulation at increasingly small scales (Xia and Whitesides, 1998; Gates et al., 2005; Qin et al., 2010), and with applications ranging from micro/nano-fluidics to additive manufacturing (Stone et al., 2004; Schoch et al., 2008; Wijshoff, 2010; Kumar, 2015), questions arise regarding the relevant description of fluid physics at the nano-scale and the validity of continuum modeling at such small scales (Squires and Quake, 2005; Bocquet and Charlaix, 2010; Colin et al., 2012; Bocquet and Tabeling, 2014; Lohse and Zhang, 2015). As the thickness of a liquid film on a solid substrate becomes smaller than approximately 100 nm, the atoms at the liquid–solid and liquid–gas interfaces start interacting with each other, giving rise to additional intermolecular forces that need to be considered in continuum modeling (Israelachvili, 2011; Rauscher and Dietrich, 2008; Bonn et al., 2009).

A uniform nanometric thin liquid film on a solid substrate can become unstable due to these intermolecular forces. The instability leads to dewetting of the film and formation of drops. Both liquid and solid-state dewetting at the nano-scale are relevant in many phenomena (Blossey, 2012; Gentili et al., 2012; Thompson, 2012; Mukherjee and Sharma, 2015; Pierre-Louis, 2016) such as pumping liquids using

nanowires (Huang et al., 2013), patterning via self-assembly (Gau et al., 1999; Higgins and Jones, 2000; Lopes and Jaeger, 2001; Huang et al., 2005; Segalman, 2005; van Hameren et al., 2006; Pokroy et al., 2009; Fowlkes et al., 2011; Han and Lin, 2012; Thiele, 2014; Wu et al., 2015; Kong et al., 2015, 2016), synthesis of core-shell nanoparticle arrays (McKeown et al., 2015), droplet generation (Yamamoto et al., 2015; Keiser et al., 2017), needle growth (Yu et al., 2013), understanding slip and rheology of nanometric films (Herminghaus et al., 2002; Fetzer et al., 2005, 2007a; Bäumchen and Jacobs, 2010; Bäumchen et al., 2012; Bäumchen et al., 2014; McGraw et al., 2014), tear film dynamics (Braun, 2012), film flow in heat pipes (Kundan et al., 2017), Rayleigh–Plateau instability of nano-wires or liquids in nano-channels (Molares et al., 2004; Chen et al., 2007), or stability of bubbles/drops in micro/nano-channels (Huerre et al., 2015; Hammoud et al., 2017).

Reiter (1992, 1993) was the first to experimentally characterize the dewetting of a nanometric polymer film on a solid substrate. He observed that, initially, some holes form with a seemingly characteristic wavelength between them; these holes then expand with a ridge formed at the receding front; these ridges ultimately meet and form a network of polygonal patterns. The ridges later collapse due to the Rayleigh–Plateau instability, forming small droplets of approximately uniform size. On a much longer time-scale still, these droplets can coarsen to ultimately form a single drop; the time-scale associated with this last stage, however, is very long and not readily accessible within typical experiments.

The theory for instability of thin liquid films under the influence of intermolecular forces far predates the experimental observations, dating back to Vrij (1966); Sheludko (1967); Ruckenstein and Jain (1974); Williams and Davis (1982); Wyart and Daillant (1990); Brochard-Wyart et al. (1993); Sharma and Reiter (1996); Sharma and Khanna (1998); Oron (2000). The Navier–Stokes equations describing the fluid motion can be greatly simplified using the long-wave/lubrication approximation when the characteristic lateral length of the flow is much larger than its characteristic height, an approach that has its origins in the work of Reynolds to describe the pressure distribution for slider bearings (Reynolds, 1886). For ultra-thin liquid films, an additional

disjoining pressure term arises due to the intermolecular interactions between the solid–liquid and liquid–gas interfaces.

Assuming a particular form for the intermolecular forces, one can use linear stability analysis of the thin film equation to arrive at a prediction for the scaling of the wavelength of the instability and its growth rate as a function of the initial uniform film thickness (Oron et al., 1997; Craster and Matar, 2009); this regime predicted by the linear theory is known as the spinodal regime. In apolar systems, typically van der Waals (vdW) forces are the main long-range attractive interactions, scaling with the film thickness as $\sim 1/h^2$, leading to a scaling of $\sim h^2$ and $\sim 1/h^5$ for the most unstable wavelength and fastest growth rate, respectively. These scalings therefore serve as a qualitative benchmark for the experiments to determine if they are within the spinodal regime. Making quantitative predictions, however, requires prescribing the exact form of the interface potential.

The observations by Reiter (1992, 1993) led to a wave of experimental studies focusing on dewetting of thin liquid films. Jacobs et al. (1998) showed that the holes observed in the experiments of Reiter (1992, 1993) have a Poisson distribution, a signature of the nucleation regime, and that the scaling of the film-rupture time as a function of film thickness did not match the theoretical predictions of the spinodal regime; films in the nucleation regime are linearly stable, yet instabilities can still grow due to the presence of defects on the substrate or in the film itself (Jacobs et al., 1998). The first observations of the spinodal regime were reported by Bischof et al. (1996) and Herminghaus et al. (1998) using thin gold films on quartz substrates, where the correlations between the holes was rigorously shown using Minkowski functionals (Mecke, 1998; Mantz et al., 2008).

The presence of residual stresses in thin polymer films can further complicate the dewetting process; Reiter et al. (2005) observed dewetting through nucleation for large film thicknesses, where the film is expected to be linearly stable. They realized that the number of holes is a strong function of the ageing time of the polymer before the temperature is raised above the glass transition temperature to perform the experiments; they further speculated that the reason behind this observation

could be that during the spin-coating process, the solvent evaporates quickly, leaving the polymer chains in non-equilibrium configurations leading to a residual stress in the film, which can be responsible for the unexpected instability of the films. The observations by Reiter et al. (2005) therefore point to the need for extreme caution in conducting and interpreting experiments on thin films in spinodal and nucleation regimes (Stange et al., 1997; Thiele et al., 1998; Xie et al., 1998; Segalman and Green, 1999; Meredith et al., 2000; Bollinne et al., 2003; Sharma, 2003; Nguyen et al., 2014).

Seemann et al. (2001a) conducted a series of well-controlled experiments using polystyrene films spin-cast on silicon (Si) wafers. They demonstrated that by tuning the thickness of the silicone oxide coating of the Si wafer, they could alter the interface potential and classify three categories of instabilities: 1) spinodal dewetting for linearly unstable regions, 2) thermal nucleation at the edge of the linearly unstable region, where thermal fluctuations can overcome the energy barrier leading to dewetting, and 3) heterogeneous nucleation within the linearly stable region, where defects on the substrate or in the film give rise to the appearance of holes and instabilities. The spinodal regime is easily distinguishable as it gives rise to a well-defined characteristic wavelength of instability, from which the interface potential can be reconstructed. The key feature distinguishing regimes 2 and 3 is that holes continuously appear throughout the experiment in the thermal nucleation regime, whereas they all form within a limited time window in the heterogenous nucleation regime.

Becker et al. (2003) observed good agreement between experimental observations and theoretical predictions, with the caveat that experiments showed a faster rupture time. To explain the time-scale mismatch between theory and experiments, Mecke and Rauscher (2005); Grün et al. (2006); Fetzer et al. (2007b) suggested that accounting for thermal fluctuations is necessary. They showed that thermal noise at the typical temperatures used in the experiments can speed up the initial rupture process, thereby bringing the theoretical predictions closer to the experimental observations.

Here, we revisit the theory of thin liquid films in partial wetting and show that the intermolecular forces in thin films give rise to a height-dependent surface tension.

We show that the free energy of the system can be cast in the following form:

$$\Gamma = \int \left(f(h) + \frac{1}{2}\kappa(h)(h_x)^2 \right) dx\,, \tag{1.1}$$

which resembles the Cahn–Hilliard framework for phase separation in binary alloys (Cahn and Hilliard, 1958; Langer, 1971), an idea that dates back to van der Waals (Rowlinson, 1979; Rowlinson and Widom, 1982). Here, $f(h)$ is the bulk free energy and $\kappa(h)$ is a height-dependent surface tension term; this feature has important consequences for stability of liquid films, leading to a slightly smaller wavelength of instability and a faster rupture rate than the classical theory (by up to 6 times), bringing the theory closer to the experimental observations, and suggesting that the height-dependence of surface tension could play a role along with the presence of thermal noise.

Within the framework of nonequilibrium thermodynamics (Hohenberg and Halperin, 1977; Bray, 1994; Cross and Hohenberg, 1993), our model in non-dimensional form can be written succinctly as follows (Pahlavan et al., 2015):

$$\frac{\partial h}{\partial t} = \frac{\partial}{\partial x}\left(\mathcal{M}\frac{\partial}{\partial x}\left(\frac{\delta\Gamma}{\delta h} \right) \right)\,, \tag{1.2}$$

with the mobility $\mathcal{M}$, and the pressure defined as the variational derivative of the free energy as $\tilde{P} = \delta\Gamma/\delta h = df/dh - \sqrt{\kappa}\partial/\partial x\,(\sqrt{\kappa}\partial h/\partial x)$; here, h represents the height of the liquid film, κ is the height-dependent surface tension, and f is the bulk free energy.

Our model leads to a generalized form of the disjoining pressure defined as:

$$\Phi(h, h_x, h_{xx}) = \frac{d\phi_{\mu,1}}{dh} + \sqrt{\phi_{\mu,2}}\frac{\partial}{\partial x}\left(\sqrt{\phi_{\mu,2}}\frac{\partial h}{\partial x} \right)\,, \tag{1.3}$$

with $\phi_{\mu,1}(h)$ and $\phi_{\mu,2}(h)$ as components of the vdW force. As indicated in Eq.(1.3), this generalized disjoining pressure depends not only on the film height, but also on its slope and curvature. This model allows describing the spreading and dewetting of drops and thin films in the true partial-wetting regime (Brochard-Wyart et al., 1991;

de Gennes et al., 2004) without the need to invoke a precursor film (Pahlavan et al., 2015).

Using the new thin-film model, we revisit the instability and dewetting of a partially wetting thin liquid film on a solid substrate. We first analyze the equilibrium film and droplet solutions predicted by this model and contrast it with the classical model, showing that in our model the equilibrium droplets exhibit compact support and show a nonzero equilibrium angle at the contact line, whereas the classical thin film model cannot admit solutions with compact support and the equilibrium droplet only asymptotically meets the substrate through a precursor film (Brenner and Bertozzi, 1993). Analyzing the stability of uniform film solutions, we show that the new model predicts a faster growth rate and smaller wavelength of instability in the spinodal regime than the classical model. Upon dewetting, the newly-formed liquid droplets arrive at a metastable state; they are connected by ultrathin fluid films of nonzero thickness and slowly coarsen to lower the energy of the system; this coarsening process, however, occurs on very long time scales as the dynamics is now mainly driven by drainage through the ultrathin films and the mobility scales as $\sim h^3$, leading to very small rates of mass transfer between the droplets. We show that the coarsening process arrives at a self-similar intermediate-asymptotic behavior (Barenblatt, 1996), which is independent of the details of the contact line models and even in the presence of thermal fluctuations matches the existing predictions for the classical thin film model (Glasner and Witelski, 2003; Gratton and Witelski, 2008, 2009). We, however, observe a skewed drop-size distribution for larger drops in the new model; while the long-tailed distribution follows a Smoluchowski equation, it is not associated with a coalescence-dominated coarsening process, calling into question the association made between coalescence and skewed drop-size distribution in some earlier experiments.

1.1 Free energy at equilibrium: emergence of Cahn–Hilliard framework with height-dependent surface tension

Consider a nanometric thin liquid film sitting on a solid substrate as shown in Fig. 1-1. When the film is perturbed, it can become unstable if the solid prefers to be in contact with the gas phase; in this configuration the uniform film has the lowest interfacial area, so dewetting lowers the bulk energy of the system at the expense of increasing its interfacial energy. We can write the energy of a half drop in 1D as:

$$\Gamma = \int_0^{x_0} \phi(h, h_x) dx, \tag{1.4}$$

where ϕ is the free energy density, $x = 0$ marks the center of the drop and $x = x_0$ is where the liquid, solid, and gas meet, i.e., the contact line. At equilibrium, the variation of the free energy is zero, i.e., $\delta\Gamma = 0$:

$$\delta \left(\int_0^{x_0} (\phi(h, h_x) - Ph) \, dx \right) = 0, \tag{1.5}$$

where the operator δ indicates variation of the functional and the Lagrange multiplier P is introduced to enforce mass conservation. Expanding the above equation leads to

$$\int_0^{x_0} (\frac{\partial \phi}{\partial h} - P)\delta h dx + \int_0^{x_0} \frac{\partial \phi}{\partial h_x}\delta h_x dx + \phi \Big|_{x_0} \delta x_0 = 0. \tag{1.6}$$

Using integration by parts, we can rewrite the second integral in Eq. (1.6) leading to:

$$\delta \int_0^{x_0} (\phi(h, h_x) - Ph) \, dx = \int_0^{x_0} \left[\frac{\partial \phi}{\partial h} - \frac{d}{dx} \left(\frac{\partial \phi}{\partial h_x} \right) - P \right] \delta h dx$$
$$+ \left(\frac{\partial \phi}{\partial h_x} \right) \delta h \Big|_0^{x_0} + \phi \Big|_{x_0} \delta x_0 = 0. \tag{1.7}$$

We can further use the Taylor expansion for the boundary terms and write $\delta h|_{x_0} = -\delta x_0 \frac{\partial h}{\partial x}\big|_{x_0}$.
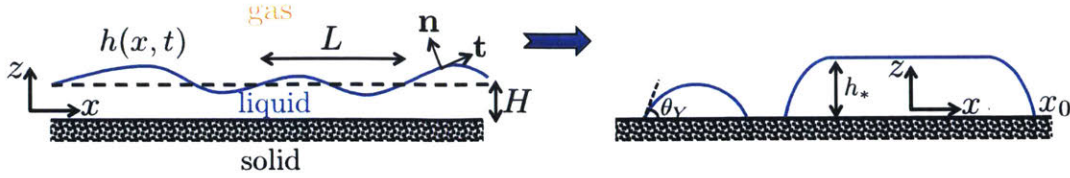
Figure 1-1: Schematic of a liquid film on a solid substrate; films with a height less than ≈ 100 nm can become unstable to infinitesimal perturbations if the liquid does not completely wet the substrate; in such situations, the instabilities grow and the film dewets from the substrate forming small droplets that can then coarsen to form larger drops; the shape of the small drops is governed mainly by surface tension leading to a spherical cap shape with a macroscopic Young contact angle θ_Y; deviations from the spherical cap shape can occur due to the intermolecular forces very close to the contact line. If the height of the drop becomes comparable to the capillary length $l_\gamma = \sqrt{\gamma/(\rho g)}$, gravitational force becomes important leveling the drop and forming a puddle shape; gravity sets the upper limit $h_* = 2l_\gamma \sin(\theta_Y/2)$ for the puddle height.

At equilibrium, the integrand as well as the boundary terms need to be independently zero. The integrand represents the Euler–Lagrange equation (Yeh et al., 1999; Starov et al., 2007; Arfken et al., 2013)

$$\left[\frac{\partial \phi}{\partial h} - \frac{d}{dx}\left(\frac{\partial \phi}{\partial h_x} \right) \right] = P. \tag{1.8}$$

The boundary condition at $x = x_0$ then becomes

$$-h_x \left(\frac{\partial \phi}{\partial h_x} \right) \bigg|_{x_0} + \phi \bigg|_{x_0} = 0. \tag{1.9}$$

This equation is known as the transversality condition or the Augmented Young equation. Note that the boundary terms at $x = 0$ automatically cancel out due to the symmetry conditions.

We therefore have two constraints on the free energy as we approach the contact line: 1) it should satisfy the Augmented Young equation (1.9), and 2) it should recover the solid–gas free energy at the contact line to allow for a continuous variation of the energy. Our objective therefore is to find the functional form of the free energy, whose minimizer at equilibrium satisfies these two conditions. Considering the macroscopic contributions to the free energy, i.e., gravity and interfacial energies, we can write the

36

free energy as:

$$\Gamma_M = \int_0^{x_0} \left(\frac{1}{2}\rho g h^2 + (\gamma_{sl} - \gamma_{sg}) + \gamma\sqrt{1 + h_x^2} \right) dx, \qquad (1.10)$$

where $\rho g h^2/2$ represents the gravitational potential energy, γ_{sl}, γ_{sg} represent the solid–liquid, and solid–gas interfacial energies, and the term $\gamma\sqrt{1 + h_x^2}$ represents the liquid–gas interfacial energy contribution. Neglecting gravity, the Euler–Lagrange Eq. (1.8) will simplify to the usual Laplace equation for the pressure jump across an interface. We can now proceed to check whether the macroscopic free energy density satisfies the two constraints given above for equilibrium.

As the film height goes to zero, ϕ must be equal to the solid–gas interfacial energy; in the above representation of the free energy, we have subtracted this contribution, so we require $\phi(h = 0) = 0$. Therefore as we move close to the contact line, we have $(\gamma_{sl} - \gamma_{sg}) + \gamma\sqrt{1 + h_x^2}\big|_{x_0} = 0$. Here we consider the true partial wetting regime, where a droplet is surrounded by a dry solid substrate. The same arguments can be applied for the case of pseudo partial wetting, where the droplet is surrounded by a precursor film of height h_f; in this case, the height at the contact line goes to h_f instead of zero.

The Augmented Young equation further requires the following

$$-h_x \left(\gamma\frac{h_x}{\sqrt{1 + h_x^2}} \right)\Bigg|_{x_0} + \gamma\sqrt{1 + h_x^2}\Bigg|_{x_0} + (\gamma_{sl} - \gamma_{sg}) = 0. \qquad (1.11)$$

Note that this equation can be simplified to give us the Young equation, i.e., $(\gamma_{sl} - \gamma_{sg}) + \left(\gamma/\sqrt{1 + h_x^2} \right)|_{x_0} = 0$, which in turn simplifies to $\gamma\cos\theta_Y = (\gamma_{sg} - \gamma_{sl})$, where θ_Y is the macroscopic Young contact angle (Young, 1805).

Putting the Augmented Young equation and the continuity constraint together leads to the following conclusion:

$$\left(\gamma\frac{h_x^2}{\sqrt{1 + h_x^2}} \right)\Bigg|_{x_0} = 0. \qquad (1.12)$$

The only way for this equation to be satisfied is if $h_x(x_0) = 0$; if we substitute $h_x(x_0) = 0$ back in the Augmented Young equation, we arrive at $(\gamma_{sl} - \gamma_{sg}) + \gamma = 0$; using the Young equation, this leads to $\gamma(1 - \cos\theta_Y) = 0$, indicating that $\theta_Y = 0$. In other words, the liquid needs to completely wet the surface for the constraints on the free energy to be satisfied. An alternative way of arriving at this conclusion is to consider a uniform flat film; the energy of this film is then written as $\int \left(\frac{1}{2}\rho g h^2 + (\gamma_{sl} - \gamma_{sg}) + \gamma\right) dx$; as we thin down the film and its height goes to zero, we need to recover the solid–gas interfacial energy, therefore we require $(\gamma_{sl} - \gamma_{sg}) + \gamma = 0$, which leads to the same result.

The macroscopic contributions to the free energy are therefore insufficient to model the partial wetting regime; we need to incorporate the physics at the nanoscale close to the contact line. As the height of the liquid film becomes small, the liquid–solid and liquid–gas interfaces start to interact with each other, leading to an additional contribution in the free energy, commonly known as the disjoining pressure (de Gennes, 1985). We can therefore write the free energy in the following form:

$$\Gamma = \Gamma_M + \Gamma_\mu = \int_0^{x_0} \left(\frac{1}{2}\rho g h^2 + (\gamma_{sl} - \gamma_{sg}) + \gamma\sqrt{1 + h_x^2} + \phi_\mu(h)\right) dx, \qquad (1.13)$$

where $\phi_\mu(h)$ represents the intermolecular interactions close to the contact line. We now can check whether this form of the free energy satisfies the continuity constraint and the Augmented Young equation. The continuity of the free energy dictates:

$$(\gamma_{sl} - \gamma_{sg}) + \gamma\sqrt{1 + h_x^2}\Big|_{x_0} + \phi_\mu(h = 0) = 0. \qquad (1.14)$$

The Augmented Young equation leads to the following:

$$-h_x\left(\gamma\frac{h_x}{\sqrt{1 + h_x^2}}\right)\Big|_{x_0} + \gamma\sqrt{1 + h_x^2}\Big|_{x_0} + (\gamma_{sl} - \gamma_{sg}) + \phi_\mu(h = 0) = 0. \qquad (1.15)$$

This equation represents the so-called Derjaguin–Frumkin equation (Starov et al., 2007), relating the Young angle to the microscopic forces close to the contact line: $\gamma\cos\theta_Y = \gamma\cos\theta_\mu + \phi_\mu(h = 0)$, where θ_μ represents the microscopic angle at the

contact line and we have used $h_x|_{x_0} = \tan\theta_\mu$ and Young equation $\gamma_{sg} - \gamma_{sl} = \gamma\cos\theta_Y$ (Yeh et al., 1999; Starov et al., 2007; Starov, 2010). The above two constraints on continuity of the energy and the augmented Young equation lead to $h_x(x_0) = 0$, or $\theta_\mu = 0$. Putting $h_x(x_0) = 0$ back into either of the above equations leads to $\phi_\mu(h = 0) = \mathcal{S}$, where $\mathcal{S} \equiv \gamma_{sg} - \gamma_{sl} - \gamma$ is known as the spreading parameter. Therefore, we arrive at the conclusion that while the macroscopic Young angle (θ_Y) can be non-zero, the microscopic angle at the contact line (θ_μ) needs to be zero to satisfy the energetic constraints; this regime is commonly known as pseudo-partial wetting, where a macroscopic liquid drop is surrounded by a microscopic precursor film (Heslot et al., 1990; Brochard-Wyart et al., 1991; Sharma, 1993a). To describe the true partial wetting regime, in which a liquid droplet sits on a dry surface without a precursor film (de Gennes et al., 2004), additional physics are needed.

Surface tension at a liquid–gas interface arises due to the collective interactions between the liquid and gas molecules (Marchand et al., 2011; Israelachvili, 2011). In the case of a uniform thin liquid film of nanometric thickness on a solid substrate, where liquid–gas and liquid–solid interfaces come very close to each other, the collective interactions also give rise to an excess free energy in addition to the interfacial tensions. For a nearly uniform thin film, this excess energy simply depends on the height of the film as represented by $\phi_\mu(h)$ (Israelachvili, 2011). Close to the contact line, however, the interfaces are not parallel, and therefore the collective intermolecular interactions between solid, liquid, and gas molecules lead to a slope-dependent excess free energy, i.e., $\phi_\mu(h, h_x)$ for a liquid wedge sitting on a solid substrate (Hocking, 1993; Wu and Wong, 2004; Dai et al., 2008). Using density functional theory, this excess free energy can be represented as a non-local integral of all the interactions (Keller and Merchant, 1991; Merchant and Keller, 1992; Getta and Dietrich, 1998; Snoeijer and Andreotti, 2008); however, here we use a simplified local approximation of the excess free energy, which has been shown to agree well with the non-local formulations (Bauer and Dietrich, 1999; Bonn et al., 2009). We can therefore write the

free energy as:

$$\Gamma = \int_0^{x_0} \left(\frac{1}{2} \rho g h^2 + (\gamma_{sl} - \gamma_{sg}) + \gamma \sqrt{1 + h_x^2} + \phi_\mu(h, h_x) \right) dx.$$ (1.16)

Continuity of the free energy leads to the following constraint at the contact line:

$$(\gamma_{sl} - \gamma_{sg}) + \gamma \sqrt{1 + h_x^2} \bigg|_{x_0} + \phi_\mu(h, h_x) \bigg|_{x_0} = 0.$$ (1.17)

The augmented Young equation further becomes:

$$-h_x \left(\gamma \frac{h_x}{\sqrt{1 + h_x^2}} + \frac{\partial \phi_\mu}{\partial h_x} \right) \bigg|_{x_0} + \gamma \sqrt{1 + h_x^2} \bigg|_{x_0} + (\gamma_{sl} - \gamma_{sg}) + \phi_\mu(h, h_x) \bigg|_{x_0} = 0.$$ (1.18)

Based on the derivations of Dai et al. (2008), we propose to decompose the vdW interactions, $\phi_\mu(h, h_x)$, into two parts: a height-dependent part, and a slope-dependent part: $\phi_\mu = (\phi_{\mu,1}(h) + \phi_{\mu,2}(h)) - \phi_{\mu,2}(h) \sqrt{1 + (h_x)^2}$; using the long-wave approximation, this form further simplifies to $\phi_\mu = \phi_{\mu,1}(h) - \frac{1}{2} \phi_{\mu,2}(h)(h_x)^2$; note that for parallel interfaces, $h_x = 0$, we recover the original height-dependent potential. An alternative way to arrive at the proposed form for the vdW forces is based on simple symmetry arguments: ϕ_μ cannot be linearly dependent on h_x as it should have the same sign everywhere around the droplet; therefore it must be a function of even powers of h_x leading, in the simplest case, to the proposed gradient-squared form above.

The augmented Young equation can thus be written as:

$$-h_x \left((\gamma - \phi_{\mu,2}) \frac{h_x}{\sqrt{1 + h_x^2}} \right) \bigg|_{x_0} + \gamma \sqrt{1 + h_x^2} \bigg|_{x_0} + (\gamma_{sl} - \gamma_{sg}) + \phi_\mu(h, h_x) \bigg|_{x_0} = 0.$$ (1.19)

Simplifying this equation leads to the following relation: $\gamma \cos \theta_Y = [\gamma - \phi_{\mu,2}(h = 0)] \cos \theta_\mu + [\phi_{\mu,1}(h = 0) + \phi_{\mu,2}(h = 0)]$. Combining the augmented Young equation (1.19) and the continuity constraint (1.17) leads to the following condition at the contact line:

$$\left((\gamma - \phi_{\mu,2}) \frac{h_x^2}{\sqrt{1 + h_x^2}} \right) \bigg|_{x_0} = 0.$$ (1.20)

40

To satisfy this condition at the contact line, we either need to have $h_x(x_0) = 0$ leading to a zero microscopic angle as before, or $\phi_{\mu,2}(h = 0) = \gamma$, which does not constrain the value of the microscopic contact angle; this allows the microscopic angle to naturally arise as part of the solution; this outcome is consistent with the predictions of nonlocal density functional theory (Snoeijer and Andreotti, 2008). The augmented Young equation (1.19) simplifies to $\gamma \cos \theta_Y = \phi_{\mu,1}(h = 0) + \gamma$; having $\phi_{\mu,1}(h = 0) = S$ therefore leads to the Young equation $\gamma \cos \theta_Y = \gamma_{sg} - \gamma_{sl}$.

Allowing for slope-dependence of the vdW forces therefore leads to a form of the free energy that satisfies all the constraints of the partial-wetting regime. Using the long-wave approximation, i.e., $\sqrt{1 + (h_x)^2} \approx 1 + \frac{1}{2}(h_x)^2$, the total Helmholtz free energy can be written as

$$\Gamma = \int_0^{x_0} \left(f(h) + \frac{1}{2}\kappa(h)(h_x)^2 \right) dx \,, \tag{1.21}$$

which, interestingly, resembles the Cahn–Hilliard formulation (Cahn and Hilliard, 1958). The free energy here is divided into a bulk contribution, $f(h) = \frac{1}{2}\rho g h^2 - S + \phi_{\mu,1}(h)$, and an interfacial contribution with a height-dependent interfacial tension, $\kappa(h) = \gamma - \phi_{\mu,2}(h)$. The above constraints on $\phi_{\mu,1}$ and $\phi_{\mu,2}$, therefore, lead to $f(h = 0) = 0$ and $\kappa(h = 0) = 0$, which allow for compactly-supported droplets sitting on a dry solid substrate (Benzi et al., 2011; Cueto-Felgueroso and Juanes, 2012; Pahlavan et al., 2015). Note that the height-dependent interfacial term leads to a new nonlinear term of the Kadar–Parisi–Zhang (KPZ) type (Kardar et al., 1986); similar forms have also been recently proposed in the context of active suspensions (Stenhammar et al., 2013; Wittkowski et al., 2014). The idea of an order parameter-dependent interfacial tension has been proposed in the context of binary alloys (Cahn, 1961) and polymer blends (de Gennes, 1980), and the dependence of surface tension on height has also been recently proposed in the context of capillary waves on thin liquid films (MacDowell et al., 2013, 2014). In the context of moving contact lines, Shikhmurzaev (1997, 2007) has proposed that the idea of a dynamic surface tension close to the contact line can resolve the moving contact line singularity and lead to

41

a natural emergence of the dynamic contact angle (Sibley et al., 2014); both these features are also reproduced in our model (Pahlavan et al., 2015).

1.2 A generalized disjoining pressure

Having defined the free energy, we can write the evolution equation for the height of the liquid film in the form of a mass-conservative gradient flow as (Hohenberg and Halperin, 1977; Bray, 1994; Cross and Hohenberg, 1993):

$$\frac{\partial h}{\partial t} = \frac{\partial}{\partial x}\left(\mathcal{M}\frac{\partial}{\partial x}\left(\frac{\delta \Gamma}{\delta h}\right)\right),$$

(1.22)

where $\mathcal{M}$ represents the mobility, and the variational derivative of the free energy is defined as $\delta\Gamma/\delta h = \partial\Gamma/\partial h - \partial/\partial x\,[\partial\Gamma/\partial(h_x)]$ (Anderson et al., 1998).

An alternative way to arrive at the same thin-film model is to start from the Navier–Stokes equations of motion and simplify them using the lubrication approximation:

$$\rho\left(\frac{\partial \mathbf{u}}{\partial t} + \mathbf{u}\cdot\nabla\mathbf{u}\right) = -\nabla P + \nabla\cdot\mathbf{T} - \rho g\mathbf{e}_z,$$

(1.23)

in which ρ is the liquid density, $\mathbf{u} = (u, w)$ is the velocity field, P is the isotropic liquid pressure, $\mathbf{T}$ is the stress tensor, and the last term in the equation represent the gravitational force. The stress tensor can be further decomposed into two parts, $\mathbf{T} = \boldsymbol{\tau} + \mathbf{M}$, where $\boldsymbol{\tau}$ is the deviatoric stress and $\mathbf{M}$ represents the stress due to external body forces, taken to be zero in this work.

We non-dimensionalize the equations in the following way: $\tilde{x} = x/L$, $\tilde{z} = z/H$, $\tilde{h} = h/H$, $\tilde{u} = u/U$, $\tilde{w} = w/(\epsilon U)$, $\tilde{t} = t/\left(\mu L^4/\gamma H^3\right)$, $\tilde{P} = P/\left(\gamma H/L^2\right)$, and $\tilde{\tau} = \tau/\left(\gamma H^2/L^3\right)$, where $\epsilon = H/L$ and H, and L represent a characteristic height and length, respectively. This leads to three dimensionless groups, $\mathrm{Re} = \rho U H/\mu$, $\tilde{\mathrm{Ca}} = \mathrm{Ca}/\epsilon^3$ with $\mathrm{Ca} = \mu U/\gamma$, and $\mathrm{Bo} = (L/l_\gamma)^2$ with $l_\gamma = \sqrt{\gamma/\rho g}$ as the capillary length.

The above equations of motion then need to be supplemented by boundary conditions at the wall and at the liquid–gas interface. At the wall, we impose a Navier slip boundary condition: $\tilde{u}|_{\tilde{z}=0} = \beta\partial\tilde{u}/\partial\tilde{z}|_{\tilde{z}=0}$, where $\beta = b/H$ is the non-dimensional slip or extrapolation length (Granick et al., 2003; Neto et al., 2005; Lauga et al., 2007); we also assume no penetration at the wall: $\tilde{w}|_{\tilde{z}=0} = 0$. At the liquid–gas interface, one must satisfy the kinematic boundary condition $\tilde{w}_s = (1/\tilde{\mathrm{Ca}})\partial\tilde{h}/\partial\tilde{t} + \tilde{u}_s\partial\tilde{h}/\partial\tilde{x}$,

43

where $\tilde{u}_s$ and $\tilde{w}_s$ are the velocity components at the interface. The stress boundary condition at the interface can be written as:

$$([P]\mathbf{I} - [\mathbf{T}]) \cdot \mathbf{n} = (\gamma \mathcal{K} + \Phi)\,\mathbf{n}, \qquad (1.24)$$

where $[-]$ represents the jump across the interface, $\mathbf{n} = (-h_x, 1)/\sqrt{1 + h_x^2}$ is the unit vector normal to the interface, $\mathbf{t} = (1, h_x)/\sqrt{1 + h_x^2}$ is the unit vector tangent to the interface, $\mathcal{K} = -\nabla_s \cdot \mathbf{n} = h_{xx}/(1 + h_x^2)^{3/2}$ represents the curvature with $\nabla_s = (\mathbf{I} - \mathbf{nn}) \cdot \nabla$. The jump in the liquid pressure and stress across the interface is represented by the terms on the right-hand side of the equation: the first term gives the Laplace pressure jump due to the interface curvature, Φ arises due to the intermolecular interactions between the solid–liquid and liquid–gas interfaces and only becomes relevant when these two interfaces are closer than a few nanometers (Israelachvili, 2011; Bonn et al., 2009).

Using the above non-dimensionalization and long-wave approximation, $\epsilon \ll 1$, and negligible inertia, $\epsilon \text{Re} \ll 1$, and surface tension-dominated flow, $\check{C}a = O(1)$, the x-momentum equation reduces to $0 = -\partial \tilde{P}/\partial \tilde{x} + \partial \tilde{\tau}_{zx}/\partial \tilde{z}$. Further, assuming $\epsilon^3 \text{Re} \ll 1$, the z-momentum equation further simplifies to $0 = -\text{Bo} - \partial \tilde{P}/\partial \tilde{z}$. The slip and kinematic boundary conditions remain unchanged under the lubrication approximation. The stress boundary condition however, simplifies further; the tangential component becomes $[\tilde{\tau}_{zx}] = 0$ and the normal component reduces to $[\tilde{P}] = -\tilde{h}_{\tilde{x}\tilde{x}} + \tilde{\Phi}$. The deviatoric stress is a function of the strain rate $\boldsymbol{\epsilon} = (\nabla \mathbf{u} + \nabla \mathbf{u}^T)/2$, and for a Newtonian liquid can be simply written as $\tau_{ij} = \mu(\partial u_i/\partial x_j + \partial u_j/\partial x_i)$. Using this definition and integrating the z-momentum equation and applying the normal stress boundary condition, we can write the liquid pressure as follows $\tilde{P} = \text{Bo}(\tilde{h} - \tilde{z}) - \tilde{h}_{\tilde{x}\tilde{x}} + \tilde{\Phi}$.

Integrating the continuity equation and using the kinematic boundary condition, we arrive at $(1/\check{C}a)\partial \tilde{h}/\partial \tilde{t} + \partial/\partial \tilde{x} \int_0^{\tilde{h}} \tilde{u}\,d\tilde{z} = 0$. Replacing the x-velocity component in the above equation we therefore arrive at the evolution equation for the height of the film:

$$\frac{\partial \tilde{h}}{\partial \tilde{t}} = \frac{\partial}{\partial \tilde{x}} \left\{ \left[\frac{\tilde{h}^3}{3} + \beta \tilde{h}^2\right] \frac{\partial \tilde{P}}{\partial \tilde{x}} \right\}. \qquad (1.25)$$

44

Comparing Eq. (1.25) above and Eq. (2.19) in the main manuscript, it is evident that they are equivalent if $\tilde{P} = \delta\tilde{\Gamma}/\delta\tilde{h} = d\tilde{f}/d\tilde{h} - \sqrt{\tilde{\kappa}}\frac{\partial}{\partial\tilde{x}}\left(\sqrt{\tilde{\kappa}}\tilde{h}_{\tilde{x}}\right)$, where $\tilde{\Gamma} = \Gamma/\left(\gamma H^2/L^2\right)$, $\tilde{f} = f/\left(\gamma H^2/L^2\right)$, and $\tilde{\kappa} = \kappa/\gamma$; we therefore find the disjoining pressure to be:

$$\tilde{\Phi}(\tilde{h}, \tilde{h}_{\tilde{x}}, \tilde{h}_{\tilde{x}\tilde{x}}) = \frac{d\tilde{\phi}_{\mu,1}}{d\tilde{h}} + \sqrt{\tilde{\phi}_{\mu,2}}\frac{\partial}{\partial\tilde{x}}\left(\sqrt{\tilde{\phi}_{\mu,2}}\tilde{h}_{\tilde{x}}\right), \tag{1.26}$$

where $\tilde{\phi}_{\mu,1} = \phi_{\mu,1}/\left(\gamma H^2/L^2\right)$ and $\tilde{\phi}_{\mu,2} = \phi_{\mu,2}/\gamma$, and $\tilde{\Phi}$ is a generalized disjoining pressure that depends not only on the film height, but also on its slope and curvature. Similar ideas for a generalized disjoining pressure have been proposed in the past: by integrating the intermolecular interactions in a liquid wedge, Miller and Ruckenstein (1974); Hocking (1993) derived a slope-dependent disjoining pressure, which was later generalized by Wu and Wong (2004), who incorporated the interactions with the molecules of the gas phase and showed that it leads to the appearance of a higher order curvature term in the disjoining pressure. Snoeijer and Andreotti (2008) compared these results with the predictions of Keller and Merchant (1991) and Merchant and Keller (1992) and showed that the disjoining pressures do not recover the correct macroscopic Young contact angle. Dai et al. (2008) later showed that the form derived by Wu and Wong (2004) does not recover the classical Lifshitz formulation (Dzyaloshinskii et al., 1961) in the limit of parallel interfaces, and derived a new consistent form for the disjoining pressure. The functional form of disjoining pressure we have proposed here in Eq. (1.26) resembles that of Dai et al. (2008), and simplifies to a height-dependent form for parallel interfaces, recovering the classical height-dependent Lifshitz theory for parallel interfaces.

Information about the detailed form of the disjoining pressure becomes essential in studying many phenomena such as moving contact lines (Gogotsi et al., 2001; Sibley et al., 2012, 2014), the final stages of coalescence of drops (Yiantsios and Davis, 1991; Leal, 2004; Zeng et al., 2007; Li, 2016) or in applications such as solidification (Tao et al., 2016). Here, we further show the consequences of the form of the disjoining pressure on the instability and dewetting of thin liquid films in the partial wetting

regime.

1.3 Equilibrium Solutions

Here, we review the analysis of Bertozzi et al. (2001a); Glasner and Witelski (2003) and Gratton and Witelski (2008) for equilibrium solutions of the thin-film equation. We use the following form of the disjoining pressure for parallel interfaces, consisting of the "non-retarded" attractive van der Waals interactions and a short-ranged repulsive term: $\Pi(h) = d\phi_{\mu,1}/dh = \mathcal{A}/(h+d_0)^3(1 - (h_f + d_0)/(h+d_0))$, with $d_0 = \sqrt{\mathcal{A}/6\pi\gamma} \approx$ 0.2nm representing the Born repulsion length (Sharma, 1993a,c; de Gennes et al., 2004; Dai et al., 2008; Israelachvili, 2011; Pahlavan et al., 2015); this form of disjoining pressure is regularized to allow for the film heights to go to zero. Here, $\mathcal{A}$ represents the Hamaker constant, and h_f represents the equilibrium or precursor film thickness. In our model, the height-dependence of surface tension does allow the droplets to have a compact support without a precursor film, i.e. $h_f = 0$ (Pahlavan et al., 2015) (see Fig. 1-3 (b)). However, for the purpose of the present study, we focus on thin films with a surrounding precursor film of non-zero height ($h_f > 0$) since we are interested in modeling dewetting and coarsening phenomena, and our objective is to compare the results of the new model with the existing results on the classical model with a constant surface tension; this regime is commonly known as pseudo-partial wetting (Brochard-Wyart et al., 1991). We can simplify the form of the disjoining pressure by shifting the heights by d_0, i.e. $\bar{h} = h + d_0$, which leads to $\Pi(h) = \mathcal{A}/h^3(1 - h_f/h)$, where we have dropped the overbars for convenience of notation. Since both components of the disjoining pressure arise from the same source (intermolecular interactions between the interfaces), we believe it is reasonable to assume they would follow the same scalings; we therefore define $\phi_{\mu,2}(h) = \gamma\phi_{\mu,1}(h)/\phi_{\mu,1}(h_f)$, leading to $\kappa(h) = \gamma(1 - \phi_{\mu,1}(h)/\phi_{\mu,1}(h_f))$, thereby $\kappa(h_f) = 0$. We take $\mathcal{A} = -6h_f^2\mathcal{S}$, which leads to $\phi_{\mu,1}(h_f) = \mathcal{S}$.

With the above definition of the disjoining pressure, we can now write the bulk free energy as follows:

$$\tilde{f}(\tilde{h}) = \frac{1}{2}\text{Bo}\,\tilde{h}^2 - \frac{\delta^2}{\tilde{h}^2}\left(\frac{1}{2} - \frac{\delta}{3\tilde{h}}\right) + \frac{1}{6}, \tag{1.27}$$

47
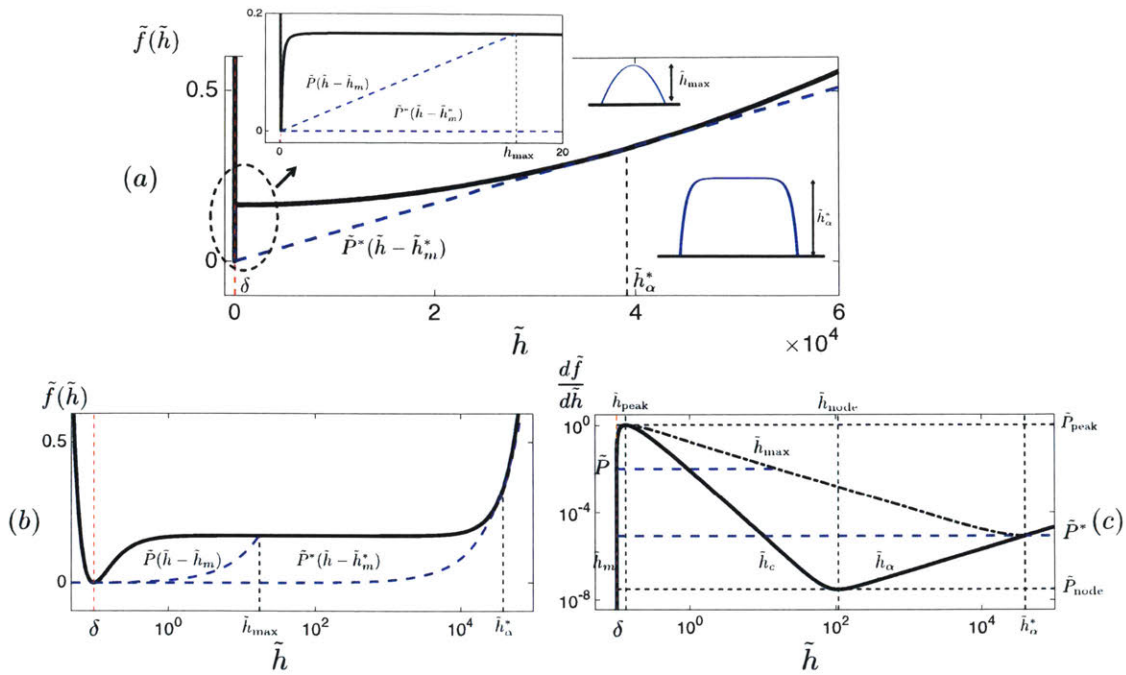
Figure 1-2: (a) The bulk free energy $\tilde{f}(\tilde{h})$ given by Eq. (1.27) with $\mathrm{Bo} = 2.2 \times 10^{-10}$ and $\delta = 0.1$ (solid line). The blue dashed line shows the Maxwell double-tangent construction, which is tangent to the bulk free energy at $\tilde{h}_m^*$, the precursor film thickness, and at $\tilde{h}_\alpha^*$, the puddle height. **The inset** shows a zoomed-in view of the bulk free energy for small heights. Here, an arbitrary line with slope $\tilde{P}^* < \tilde{P} < \tilde{P}_{\text{peak}}$ is tangent to the free energy at $\tilde{h}_m$ and intersects it at $\tilde{h}_{\text{max}}$ (blue dashed line). (b) The bulk free energy redrawn on a semilog scale. While vdW forces act at nano-scale, gravity only becomes relevant on the mm-scale; this 6 orders of magnitude separation of scales is shown here. Note that the tangent lines become curved in this semilog representation. (c) The bulk pressure defined as $d\tilde{f}/d\tilde{h}$. Droplet solutions exist for $\tilde{P}^* < \tilde{P} < \tilde{P}_{\text{peak}}$, where a typical constant pressure line ($\tilde{P} = $ constant) intersects the curve at three fixed points corresponding to the three branches $\tilde{h}_m$, $\tilde{h}_c$, and $\tilde{h}_\alpha$ as indicated. Uniform films on the $\tilde{h}_c$ branch are linearly unstable since their corresponding $d^2\tilde{f}/d\tilde{h}^2 < 0$. The $\tilde{h}_{\text{max}}$ branch shows the maximum height of the droplet solutions surrounded by a corresponding film of thickness $\tilde{h}_m$; these are solutions homoclinic to $\tilde{h}_m$, where a line with slope $\tilde{P}$ is tangent to the bulk free energy at $\tilde{h}_m$ and intersects it at $\tilde{h}_{\text{max}}$ (the blue dashed tangent line). In the limit of very large drops (i.e., puddles) $\tilde{h}_m$ and $\tilde{h}_{\text{max}}$ approach $\tilde{h}_m^*$ and $\tilde{h}_\alpha^*$ respectively and we recover the common tangent line with slope $\tilde{P}^*$ (the blue dashed tangent line) (see also Brochard-Wyart et al. (1991); Gratton and Witelski (2008); de Gennes et al. (2004)).

where $\delta = h_f/H$ is the non-dimensional precursor film height, and we have chosen $L^2/H^2 = \gamma h_f^2/\mathcal{A} = 1/(6(1 - \cos\theta_Y))$.

At equilibrium, the thin film Eq. (1.22) simplifies to:

$$\tilde{P} = \frac{\delta\tilde{\Gamma}}{\delta\tilde{h}} = \frac{d\tilde{f}}{d\tilde{h}} - \sqrt{\tilde{\kappa}}\frac{d}{d\tilde{x}}\left(\sqrt{\tilde{\kappa}}\frac{d\tilde{h}}{d\tilde{x}}\right),\tag{1.28}$$

where $\tilde{P}$ is a constant pressure; the fixed points of the above equation are the solutions of $\tilde{P} = d\tilde{f}/d\tilde{h}$. The typical form of the dimensionless free energy $\tilde{f}(\tilde{h})$ is shown in Fig. 1-2. Within the range $\tilde{P}_{\text{node}} < \tilde{P} < \tilde{P}_{\text{peak}}$, we can find three fixed points. Using a singular perturbation analysis in the limit $\delta \to 0$, we find these points to be:

$$\tilde{h}_m = \delta + \delta^2 P + \delta^3\left(4P^2 - \text{Bo}\right) + O(\delta^4),\tag{1.29a}$$

$$\tilde{h}_c = P^{-1/3}\delta^{2/3} - \frac{1}{3}\delta + \frac{1}{3}\left(\text{Bo}P^{-5/3} - \frac{2}{3}P^{1/3}\right)\delta^{4/3} + O(\delta^{5/3}),\tag{1.29b}$$

$$\tilde{h}_\alpha = \frac{P}{\text{Bo}} - \frac{\text{Bo}^2}{P^3}\delta^2 + \frac{\text{Bo}^3}{P^4}\delta^3 + O(\delta^4),\tag{1.29c}$$

where, to leading order, only the equilibrium film thickness is independent of the pressure. The fixed points obtained here are not affected by the height-dependence of the surface tension $\tilde{\kappa}(\tilde{h})$ as they only depend on the bulk free energy (Gratton and Witelski, 2008). The pressure in the liquid phase, however, can be affected by the non-constant surface tension, as we will show later; this pressure change will then affect the fixed points.

The heights $\tilde{h}_m$ and $\tilde{h}_\alpha$ are saddle points, whereas $\tilde{h}_c$ is a center (Gratton and Witelski, 2008). In the range of $\tilde{P}_{\text{node}} < \tilde{P} < \tilde{P}_{\text{peak}}$, we can find three types of solutions that are bounded in height (Thiele et al., 2001a; Gratton, 2008): localized hole/dimple solutions that are homoclinic to $\tilde{h}_\alpha$ in the range $\tilde{P}_{\text{node}} < \tilde{P} < \tilde{P}^*$, droplet solutions that are homoclinic to $\tilde{h}_m$ in the range $\tilde{P}^* < \tilde{P} < \tilde{P}_{\text{peak}}$, and heteroclinic orbits from $\tilde{h}_m$ to $\tilde{h}_\alpha$ at $\tilde{P} = \tilde{P}^*$. To obtain the maximum height of these droplets,

we integrate Eq. (1.28) as follows:

$$\mathcal{R}(\tilde{h}) \equiv \frac{1}{2}\left(\tilde{\kappa}(\tilde{h})\left(\frac{d\tilde{h}}{d\tilde{x}}\right)^2\right) = \tilde{f}(\tilde{h}) - \tilde{f}(\tilde{h}_m) - \tilde{P}(\tilde{h} - \tilde{h}_m), \qquad (1.30)$$

where at the maximum height of the drop we have $d\tilde{h}/d\tilde{x} = 0$, i.e., $\mathcal{R}(\tilde{h}_{\max}) = 0$; in the limit $\delta \to 0$, we can then obtain

$$\tilde{h}_{\max} = \frac{1}{\text{Bo}}\left(\tilde{P} - \sqrt{\tilde{P}^2 - \frac{\text{Bo}}{3}}\right) + \frac{\tilde{P}}{\sqrt{\tilde{P}^2 - \frac{\text{Bo}}{3}}}\delta + O(\delta^2), \qquad (1.31)$$

which is the branch shown in Fig. 1-2 (c). As the pressure decreases towards $\tilde{P}^*$, a saddle–saddle heterogeneous orbit appears between $\tilde{h}_m$ and $\tilde{h}_\alpha$, and the $\tilde{h}_{\max}$ branch intersects with the $\tilde{h}_\alpha$ branch. At this point, we then obtain $\tilde{P}^* = \sqrt{\text{Bo}/3} + (\text{Bo}/2)\,\delta + O(\delta^2)$; this critical value of pressure is the slope of the Maxwell common tangent line (Rowlinson and Widom, 1982) shown in Fig. 1-2 and satisfies the following equations:

$$\tilde{P}^* = \frac{\tilde{f}(\tilde{h}_\alpha^*) - \tilde{f}(\tilde{h}_m^*)}{\tilde{h}_\alpha^* - \tilde{h}_m^*}, \qquad (1.32a)$$

$$\tilde{P}^* = \left.\frac{d\tilde{f}}{d\tilde{h}}\right|_{\tilde{h}_m^*} = \left.\frac{d\tilde{f}}{d\tilde{h}}\right|_{\tilde{h}_\alpha^*}, \qquad (1.32b)$$

where $\tilde{h}_m^*$ and $\tilde{h}_\alpha^*$ are the values of $\tilde{h}_m$ and $\tilde{h}_\alpha$ as calculated at pressure $\tilde{P} = \tilde{P}^*$. At $\tilde{P}_{\text{node}}$ and $\tilde{P}_{\text{peak}}$, the $\tilde{h}_c$ branch merges with the other two branches and we have $d^2\tilde{f}/d\tilde{h}^2 = 0$. Following the procedure above, in the limit of $\delta \to 0$ and using a singular perturbation analysis, we find the corresponding film heights:

$$\tilde{h}_{\text{peak}} = \frac{4}{3}\delta + \left(\frac{4}{3}\right)^5 \frac{\text{Bo}}{3}\delta^3 + O(\delta^7), \qquad (1.33a)$$

$$\tilde{h}_{\text{node}} = \left(\frac{3}{\text{Bo}}\right)^{1/4}\delta^{1/2} - \frac{1}{3}\delta + O(\delta^2), \qquad (1.33b)$$

which lead to the following pressures:

$$\tilde{P}_{\text{peak}} = \frac{27}{256\delta} + \frac{4\text{Bo}}{3}\delta + O(\delta^3), \tag{1.34a}$$

$$\tilde{P}_{\text{node}} = 4\left(\frac{\text{Bo}}{3}\right)^{3/4}\delta^{1/2} - \frac{\text{Bo}}{3}\delta - \frac{2}{3}\left(\frac{\text{Bo}}{3}\right)^{5/4}\delta^{3/2} + O(\delta^2), \tag{1.34b}$$

which mark the upper and lower boundaries of the pressure range for which equilibrium droplet solutions exist. Note that the results we have obtained so far are only indirectly affected by the height-dependence of surface tension through the change of liquid pressure at equilibrium, as we show later.

The droplet solutions of Eq. (1.28) can be divided into three regions: (i) core, (ii) contact line, and (iii) equilibrium film. Here, we focus on the limit of small drops, where gravity can be neglected (Bo $\to$ 0). In the core (region (i)), away from the contact line and in the absence of intermolecular forces, surface tension is the dominant force, and Eq. (1.28) simplifies to $\tilde{P} = -\tilde{h}_{\tilde{x}\tilde{x}}$, leading to a parabolic profile, $\tilde{h}_{\text{core}} = \frac{1}{2}\tilde{P}\left(\tilde{w}^2 - \tilde{x}^2\right)$, where $\tilde{w}$ is the effective width of the droplet. The maximum height of the core region at its center $\tilde{x} = 0$ is therefore $\tilde{h}_{\text{max}} = \tilde{P}\tilde{w}^2/2$. Before, we derived the maximum height of the droplet in the presence of gravity and intermolecular forces. In the limit of zero Bond number, we can then show $\tilde{h}_{\text{max}} = 1/(6\tilde{P}) + \delta + O(\delta^2)$; equating this to the maximum height of the parabolic core, we find the effective width of the drop to leading order: $\tilde{w} = 1/(\sqrt{3}\tilde{P})$. In the second region (region (ii)), i.e., the region near the contact line, the drop profile asymptotically matches the droplet core to the equilibrium film outside. In this region, we use the following transformation $\tilde{h}(\tilde{x}) = \delta\tilde{H}(\tilde{x})$ with $\tilde{x} = -\tilde{w} + \delta\tilde{z}$, and defining $\tilde{f}(\tilde{h}) \equiv \tilde{F}(\tilde{H})$ we re-scale Eq. (1.28) to leading order as follows:

$$\frac{d\tilde{F}}{d\tilde{H}} - \left(1 - \frac{\tilde{F}(\tilde{H})}{\tilde{F}(1)}\right)\tilde{H}_{\tilde{z}\tilde{z}} + \frac{1}{2\tilde{F}(1)}\frac{d\tilde{F}}{d\tilde{H}}\tilde{H}_{\tilde{z}}^2 = 0, \tag{1.35}$$

where we have used the definition $\tilde{\kappa} = 1 - \tilde{F}(\tilde{H})/\tilde{F}(1)$, which appears in the second term. This equation can be integrated to obtain $\tilde{H}_{\tilde{z}}^2/2 = -\tilde{F}(1)$, relating the slope of the profile in the contact line region to the intermolecular forces. Consistent with the

51
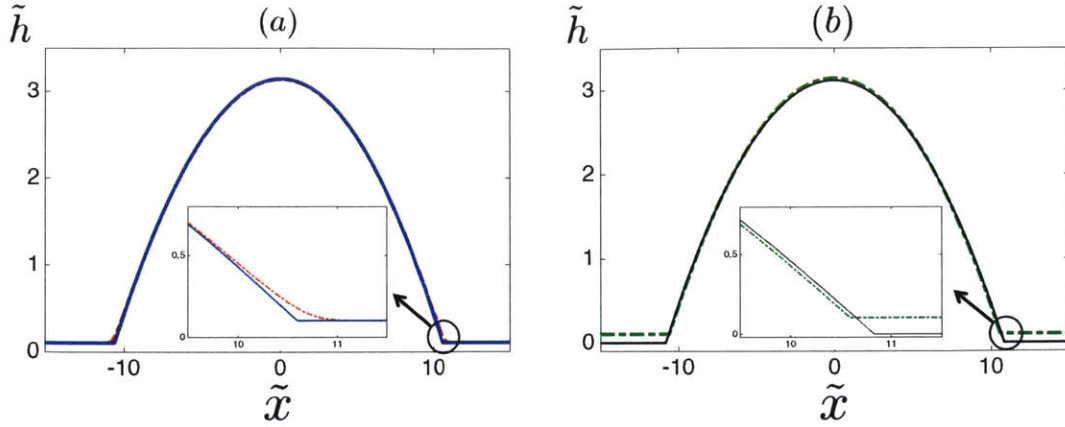
Figure 1-3: Equilibrium droplet profiles for a) constant (red dash-dotted line) and height-dependent (solid blue line) surface tension models with a surrounding precursor film, and b) the height-dependent surface tension model with (green dash-dotted line) and without (solid black line) a surrounding precursor film.

experimental observations (Pompe and Herminghaus, 2000) and density functional calculations (Snoeijer and Andreotti, 2008), the height-dependence of surface tension leads to a non-zero contact angle at the contact line. In this model the droplet width is a finite value that can be unambiguously defined, where the droplet meets the surrounding wet or dry surface at a non-zero angle (Fig. 1-3 (b)). This is in clear contrast with the classical model with a constant surface tension, $\tilde{\kappa} = 1$, for which we obtain $\tilde{H}_{\tilde{z}}^2/2 = \tilde{F}(\tilde{H}) - \tilde{F}(1)$, leading to a zero contact angle as the droplet asymptotically meets the precursor film, i.e., $\tilde{H} \to 1$ (Fig. 1-3 (a)). In the classical model, only the macroscopic contact angle far away from the contact line can be non-zero; we therefore need to take the limit of $\tilde{H} \to \infty$, where $\tilde{F}(\tilde{H}) \to 0$, recovering the result $\tilde{H}_{\tilde{z}}^2/2 = -\tilde{F}(1)$. Using the dimensional version of this result leads to $h_x^2/2 = \mathcal{A}/(6\gamma h_f^2)$, which simplifies to $h_x^2/2 = (1 - \cos\theta_Y)$ using the definition $\mathcal{A} = -6h_f^2\mathcal{S}$; in the limit of small contact angles ($\theta_Y \ll 1$), we can therefore relate the droplet slope to the Young contact angle: $h_x \approx \theta_Y$.

We can more generally define the width of the droplets as follows:

$$\tilde{w}(\tilde{P}) = \int_{\tilde{h}_m}^{\tilde{h}_{\max}} \sqrt{\frac{\tilde{\kappa}(\tilde{h})}{2\mathcal{R}(\tilde{h})}} \, d\tilde{h}, \tag{1.36}$$

52
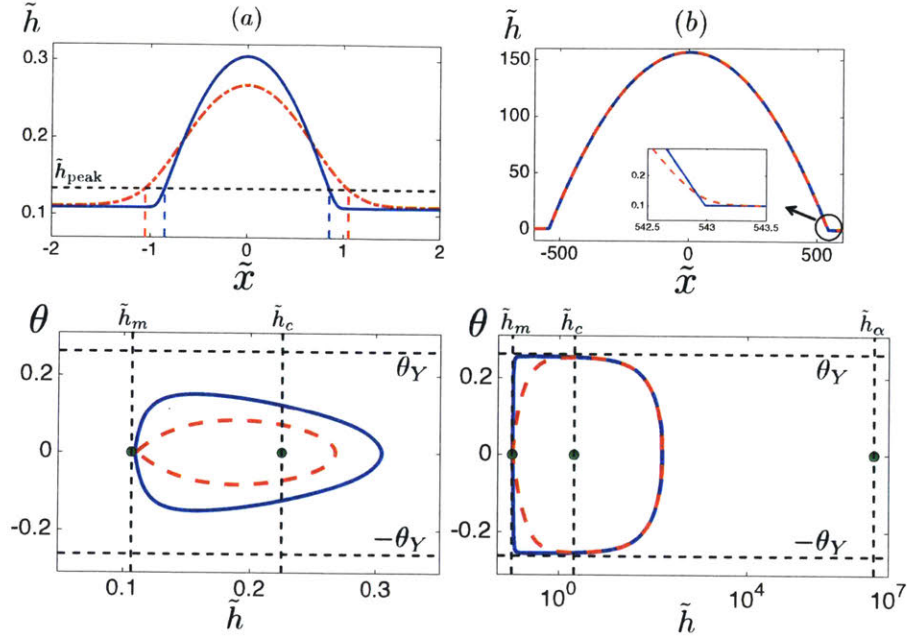
Figure 1-4: Droplet solutions for two different volumes with pressures in the range of $\tilde{P}^* < \tilde{P} < \tilde{P}_{\text{peak}}$; these solutions are homoclinic to $\tilde{h}_m$. (a) The equilibrium profiles of a small droplet (with $\tilde{h}_{max} \ll \tilde{h}_{\text{node}}$, where the entire drop profile is influenced by the intermolecular forces) for both the constant (red dashed line) and height-dependent (blue solid line) surface tension models; the horizontal line crosses the droplets at the height $\tilde{h}_{\text{peak}}$, where their effective width is defined. The lower plot shows the solutions in the phase-plane of height and slope $\theta = \arctan(h_x)$; the green dots show the saddle node $\tilde{h}_m$ and the center $\tilde{h}_c$, and the horizontal dashed lines show the Young contact angle. (b) The equilibrium profiles for a large droplet (with $\tilde{h}_{max} > \tilde{h}_{\text{node}}$); here no difference between the models can be observed on a macroscopic scale, but a zoomed-in view shows the difference close to the contact line. In its corresponding phase plane we show both the saddle points $\tilde{h}_m$ and $\tilde{h}_\alpha$ as well as the center $\tilde{h}_c$ (the height is shown in log scale). For large drops, the equilibrium angle at the inflection point of the drop profile approaches the Young contact angle. In the height-dependent surface tension model the angle remains equal to the Young angle all the way down to the contact line, where it makes a sudden transition and meets the precursor film while in the classical model this transition is a gradual one and there is no compact support.

where we have used $\tilde{h}_m$ as the lower bound for calculating the droplet width; this is allowed due to the compact-support feature, whereas in the classical model the droplet profile only asymptotically meets the equilibrium film with a zero slope; there, we have to resort to $\tilde{h}_{\text{peak}}$ as the lower bound of integration for the effective width.

Figure 1-4 shows an example of equilibrium droplet solutions for two different droplet sizes; for very small drops, where the entire droplet profile is influenced by the intermolecular forces, we can see a considerable difference between the classical model with a constant surface tension and our model with a height-dependent surface tension. While both models leads to equilibrium solutions with equilibrium contact angles smaller than the macroscopic Young angle, our model predicts a more compact droplet profile, which meets the surrounding film at a non-zero angle; this is in contrast with the classical model predicting an asymptotic approach to the film with a zero angle. These differences become more pronounced in a phase-plane of height vs slope. As the drop size grows, the core of the drops will only be influenced by the bulk surface tension and approach a parabolic profile, thereby both models will predict the same macroscopic profile; a zoomed-in view in the vicinity of the contact line region, however, shows the differences: a compact profile vs the asymptotic approach to the surrounding film. The absence of compact support in the classical model does not allow solutions without a precursor film (Brenner and Bertozzi, 1993).

Figure 1-5 shows the variation of some of the droplet features as a function of its equilibrium pressure (or size) for both the classical model (with constant surface tension) and our model (with a height-dependent surface tension). The first observation is that the difference between the two models is most pronounced for very small droplets, where their entire profile is influenced by the intermolecular forces; as the droplets become larger, intermolecular forces can only be felt very close to the contact line and the difference between the two models is limited to the vicinity of this region and less relevant to macroscopic features such as width, maximum height, or even equilibrium film thickness, which is now determined by balancing the Laplace pressure due to the curvature of the core region of the drops. The equilibrium contact angle also becomes size dependent for very small droplets (Fig. 1-5(a)), where the entire
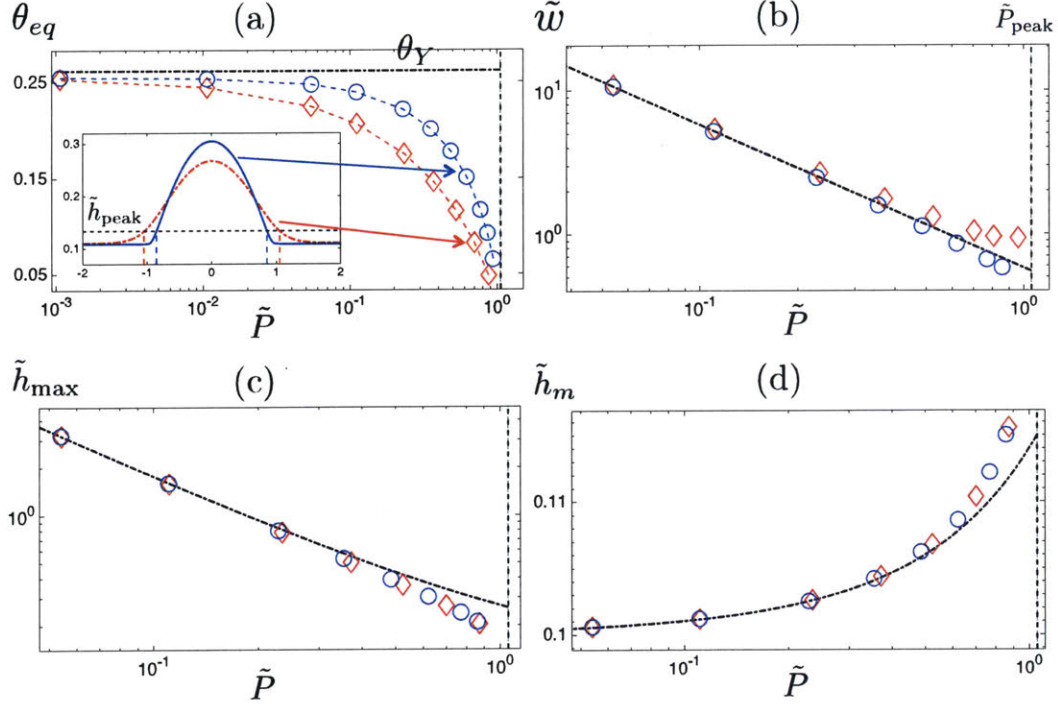
Figure 1-5: The variation of equilibrium droplet features with the liquid pressure in the droplet. The symbols show the result of numerical simulations with a constant surface tension (red diamonds), and a height-dependent surface tension (blue circles). The dash-dotted lines represent the theoretical predictions for small droplets, and the vertical dashed lines correspond to the $\tilde{P}_{\mathrm{peak}}$ beyond which no droplet solutions exist. (a) The equilibrium contact angle defined at the inflection point of the droplet profile; the dash-dotted line represents the Young contact angle. **The inset** shows two typical droplet profiles of equal mass (*but different equilibrium pressure* with the new model leading to smaller liquid pressures) for the constant surface tension (red dash-dotted line) and height-dependent surface tension (blue solid line) models. (b) Droplet width defined as the distance from center of the drop to its edge at $\tilde{h}_{\mathrm{peak}}$. The dash-dotted line represents $\tilde{w} = 1/(\sqrt{3}\tilde{P})$. In the constant surface tension case, the droplet core asymptotically meets the equilibrium film leading to a larger effective width. (c) Maximum droplet height. The dash-dotted line represents $\tilde{h}_{\mathrm{max}} = 1/(6\tilde{P}) + \delta + O(\delta^2)$. The height-dependence of surface tension results in lower equilibrium pressures, which in turn lead to larger $\tilde{h}_{\mathrm{max}}$ values in the small droplets. (d) Equilibrium film thickness. The dash-dotted line represents $\tilde{h}_m = \delta + \delta^2 P + \delta^3 (4P^2 - \mathrm{Bo})$.

droplet geometry is influenced by the intermolecular forces; this dependence however, is not due to the line tension effect, which would be relevant for axisymmetric drops (Amirfazli and Neumann, 2004; Schimmele et al., 2007; Weijs et al., 2011; Giro et al., 2017). The second observation is that for small droplets, the height-dependent surface tension model always leads to more localized profiles with larger contact angle and smaller effective width; for equal droplet mass, the height-dependence of surface tension leads to a lower equilibrium pressure, which according to the tangent construction shown in Fig. 1-2 leads to a larger maximum height ($\tilde{h}_{\max}$) and smaller equilibrium film thickness ($\tilde{h}_m$).

All the simulations in this paper are performed assuming an equilibrium film thickness of $h_f = 1$nm, and characteristic height $H = 10$nm, which is the typical range of dominance of vdW forces, leading to a non-dimensional equilibrium film height of $\delta = h_f/H = 0.1$, and Bo $= (L/l_\gamma)^2 = 2.2 \times 10^{-10}$, i.e., negligible gravity (capillary length $l_\gamma = 1.5$mm); while the influence of gravity in thin films is in principle insignificant, ignoring its role can lead to unphysical predictions (Thiele et al., 2001a).

1.4 Stability of Uniform Films

Here, we analyze the stability of uniform film solutions of Eq. (1.28) to infinitesimal and finite perturbations. Consider a uniform film of thickness $\tilde{h}_0$ that is perturbed infinitesimally by a superposition of Fourier modes as $\tilde{h} = \tilde{h}_0 + \epsilon \exp\left(\beta \tilde{t} + iq\tilde{x}\right)$, where β is the growth rate of the instability, $q = 2\pi/\lambda$ is the wavenumber, and $\epsilon \ll 1$. Substituting this decomposition into Eq. (1.22) and linearizing it to $O(\epsilon)$, we find:

$$\beta = \tilde{h}_0^3 q^2 \left(q_0 - \tilde{\kappa}(\tilde{h}_0)q^2 \right), \tag{1.37}$$

where $q_0 = -d^2\tilde{f}/d\tilde{h}^2\big|_{\tilde{h}_0}$. A uniform film becomes unstable if the growth rate is positive $\beta > 0$, or $q_0 > \tilde{\kappa}(\tilde{h}_0)q^2$. This implies that wave-numbers $q < \sqrt{q_0/\tilde{\kappa}(\tilde{h}_0)}$, or equivalently wavelengths $\lambda > \lambda_c = 2\pi\sqrt{\tilde{\kappa}(\tilde{h}_0)/q_0}$ will be unstable; surface tension damps the shorter wavelength deformations. The curve $q_0 = 0$ separates the linearly stable and unstable regions as shown in Figure 1-6; the instability phase diagram can be represented in the phase space of the initial uniform film thickness $\tilde{h}_0$ vs the equilibrium film thickness $\delta = h_f/H$ (Diez and Kondic, 2007) or $\tilde{h}_0$ vs Bo (Thiele et al., 2001a). The curve $q_0 = 0$ represents the boundary of the spinodal region in the free energy, where the second derivative of the bulk free energy becomes negative, $d^2\tilde{f}/d\tilde{h}^2\big|_{\tilde{h}_0} < 0$. This region is bounded by the heights $\tilde{h}_{\text{peak}}$ and $\tilde{h}_{\text{node}}$ as shown in Fig. 1-2. The region between these heights and the film heights corresponding to the tangent construction is called the binodal region, where the uniform wetted liquid films are not linearly unstable, but they can be nonlinearly unstable, i.e., if perturbed by a sufficiently large finite amplitude perturbation they can evolve to find a lower energy state. The boundaries of the binodal region are set by $\tilde{h}_m^*$ and $\tilde{h}_\alpha^*$ as shown in Fig. 1-2. The lower and upper branches all meet at a *critical point*, where the bulk free energy transitions from a double-well to a single-well structure; at the critical point, we have $d^2\tilde{f}/d\tilde{h}^2 = 0$, and $d^3\tilde{f}/d\tilde{h}^3 = 0$, leading to $\tilde{h} = (5/3)\delta$, $\delta_{cr} \approx 1.9 \times 10^4$, and $\text{Bo}_{cr} \approx 7.85$. To find the fastest growing mode, we take $d\beta/dq = 0$, which leads
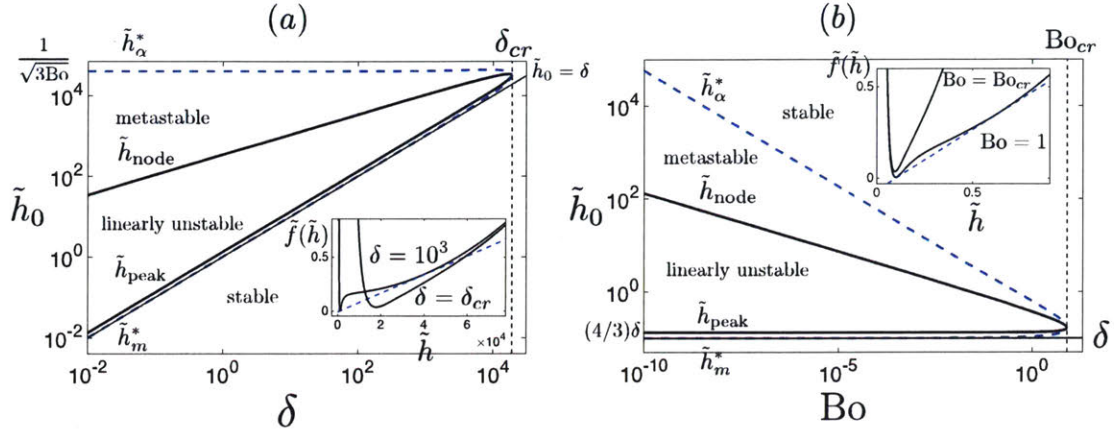
Figure 1-6: Stability phase diagram showing the regions where the uniform film is linearly unstable, metastable (nonlinearly unstable), and absolutely stable. (a) Shows the phase diagram as a function of the initial film height, $\tilde{h}_0 = h_0/H$, and the equilibrium film thickness, $\delta = h_f/H$. The full black solid line represents the marginal stability curve, where the instability growth rate, β is zero (i.e., $q_0 = -d^2\tilde{f}/d\tilde{h}^2|_{\tilde{h}_0} = 0$); inside the curve, the film is linearly unstable to infinitesimal perturbations, whereas outside it is linearly stable; the lower branch of the marginal stability curve is coincident with $\tilde{h}_{\text{peak}}$, whereas the upper branch represents $\tilde{h}_{\text{node}}$. The blue dashed line represents the curve of absolute stability; outside this curve, all films are absolutely stable, whereas inside it uniform films can become unstable due to finite perturbations, i.e., they are nonlinearly unstable. The upper and lower branches of the absolute stability curve represent the $\tilde{h}_\alpha^*$ and $\tilde{h}_m^*$ lines; these are the points tangent to the Maxwell double tangent construction. In other words, while the curve of marginal stability represents the spinodal region, where $d^2\tilde{f}/d\tilde{h}^2|_{\tilde{h}_0} \leq 0$, the curve of absolute stability represents the binodal or coexistence curve. The upper and lower branches meet at the *critical point*, where we have $d^2\tilde{f}/d\tilde{h}^2 = 0$, and $d^3\tilde{f}/d\tilde{h}^3 = 0$, leading to $\tilde{h} = (5/3)\delta$ and $\delta_{cr} \approx 1.9 \times 10^4$, where (as shown in the **inset**) a transition from a double-well to a single-well structure occurs in the free energy. The dashed blue line in the inset represents the tangent construction. (b) Shows the phase diagram as a function of the initial film thickness, $\tilde{h}_0$, and the Bond number. The same transition from a double-well to a single-well structure is observed at a critical Bond number of $\text{Bo}_{cr} \approx 7.85$ where the upper and lower branches of the stability curves meet.
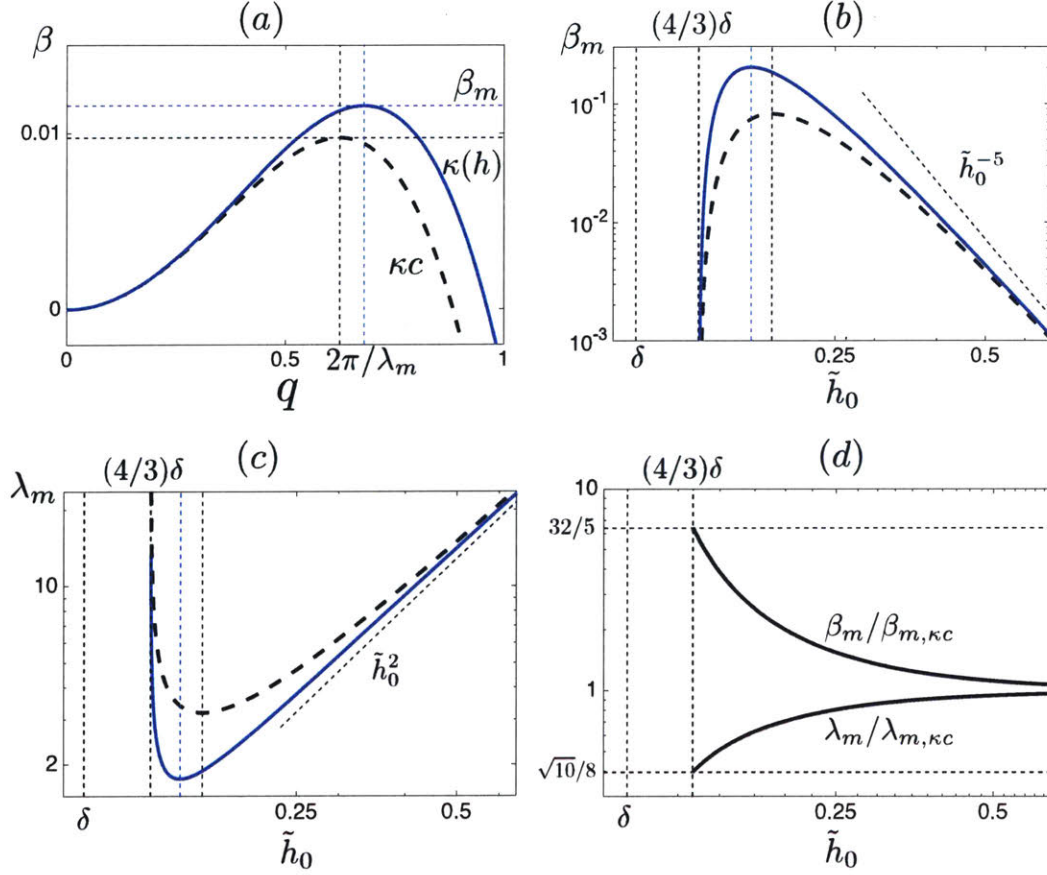
Figure 1-7: Linear stability analysis results. (a) Dispersion curve showing the instability growth rate β versus the wavenumber q for a film of thickness $\tilde{h}_0 = 4\delta$. All curves labeled with κc and $\kappa(h)$ represent the classical model with a constant surface tension and the new model with a height-dependent surface tension, respectively. The new model results in a shift to larger values for both the maximum growth rate β_m and its corresponding wavenumber, leading to a smaller wavelength of instability λ_m. (b) Scaling of the maximum growth rate with the thickness of the initial uniform film $\tilde{h}_0$. The vertical dashed line $(4/3)\delta$ represents the lower limit of linear instability. (c) Wavelength of the instability corresponding to the most unstable mode. (d) Ratio of predicted growth rate and instability wavelength between the new model and the classical model. It is apparent that the maximum ratio corresponds to the smallest film thickness $\tilde{h}_0 = (4/3)\delta$ where the film is linearly unstable; below the height of $\tilde{h}_0 = (4/3)\delta$ the film becomes linearly stable and the surface tension keeps decreasing until it reaches a value of zero for $\tilde{h}_0 = \delta$.

59

to the following expressions for the most unstable wavelength

$$\lambda_m = \sqrt{2}\lambda_c = 2\pi \sqrt{\frac{2\tilde{\kappa}(\tilde{h}_0)}{-d^2\tilde{f}/d\tilde{h}^2\big|_{\tilde{h}_0}}}, \qquad (1.38)$$

and its corresponding maximum growth rate

$$\beta_m = \frac{\tilde{h}_0^3}{4\tilde{\kappa}(\tilde{h}_0)} \left(\frac{d^2\tilde{f}}{d\tilde{h}^2}\bigg|_{\tilde{h}_0}\right)^2. \qquad (1.39)$$

We observe that both the instability wavelength and growth rate are affected by the height-dependence of the surface tension. We can denote the corresponding predictions of the classical model by $\lambda_{m,\kappa c} = 2\pi\sqrt{1/q_0}$ and $\beta_{m,\kappa c} = (\tilde{h}_0^3/4)q_0^2$, where the subscript κc represents constant surface tension. The new model therefore predicts a smaller instability wavelength, $\lambda_m/\lambda_{m,\kappa c} = \sqrt{\tilde{\kappa}(\tilde{h}_0)} \leq 1$, and a faster growth rate $\beta_m/\beta_{m,\kappa c} = 1/\tilde{\kappa}(\tilde{h}_0) \geq 1$, as shown in Fig. 1-7. For very large initial thicknesses, the effect of height-dependence of surface tension becomes insignificant and both models predict the same scaling for the maximum growth rate $\beta_m \sim \tilde{h}_0^{-5}$ (Fig. 1-7 (b)), showing that it drastically reduces as the film thickness increases. The height-dependence of surface tension, however, leads to a larger growth rate for small film thicknesses, predicting that the instability grows faster. The largest β_m corresponds to $\tilde{h}_0 = (28/15)\delta$ for the classical model and $\tilde{h}_0 \approx 1.7\delta$ for the new model. Both models predict a similar scaling for the most unstable wavelength at large thicknesses $\lambda_m \sim \tilde{h}_0^2$ (Fig. 1-7 (c)), whereas for smaller heights, where the effect of variability of surface tension becomes relevant, the new model predicts smaller wavelengths. The minimum λ_m corresponds to $\tilde{h}_0 = (5/3)\delta$ for the classical model and $\tilde{h}_0 \approx 1.52\delta$ for the new model. Note that these heights are different from those concerning the maximum growth rate β_m. Further the instability wavelength shows a much weaker dependence on the film thickness than the growth rate ($\tilde{h}_0^2$ vs $\tilde{h}_0^{-5}$). Within the linearly unstable region, the new model predicts the instability can grow up to six times faster than the predictions of the classical model (Fig. 1-7 (d)) while its corresponding instability wavelength can be less than half of that in the classical model; the growth rate is

60
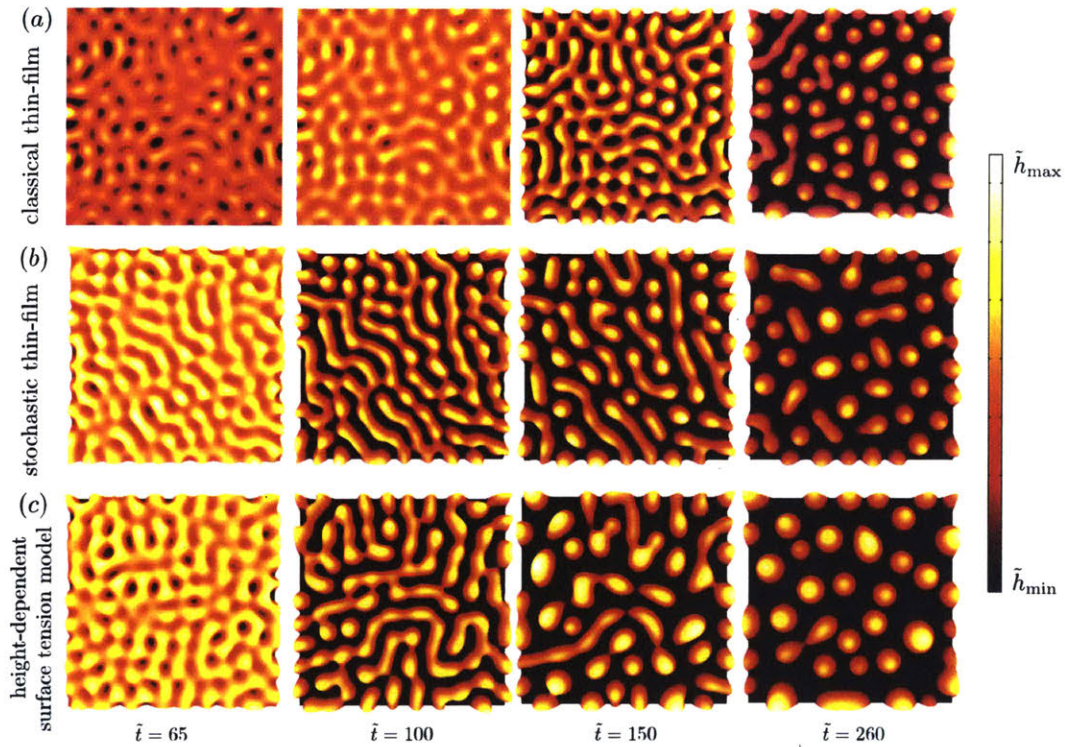
Figure 1-8: 2D simulations of dewetting in the spinodal regime with $\tilde{h}_0 = 2\delta$ in a domain of size $10\lambda_m$ by $10\lambda_m$; 2D profiles of $\tilde{h}(\tilde{x}, \tilde{y})$ with contour levels between $\tilde{h}_{\min}$ and $\tilde{h}_{\max}$ as specified are shown. (a) The classical thin film equation ($\tilde{h}_{\min} = 1.99\delta, 1.86\delta, \delta, \delta$, and $\tilde{h}_{\max} = 2.02\delta, 2.16\delta, 4\delta, 6.7\delta$, respectively). (b) The stochastic thin film equation (1.44) with constant surface tension at temperature $T = 50^\circ C$, i.e., $\sigma = 0.039$, ($\tilde{h}_{\min} = \delta$, and $\tilde{h}_{\max} = 2.8\delta, 4.3\delta, 5.1\delta, 7.5\delta$, respectively). (c) The new model with height-dependent surface tension ($\tilde{h}_{\min} = \delta$, and $\tilde{h}_{\max} = 2.8\delta, 4.3\delta, 5.1\delta, 7.5\delta$, respectively). Both thermal fluctuations and height-dependence of surface tension lead to a faster dewetting process, bringing the theoretical predictions closer to the experimental observations (Becker et al., 2003).

therefore a more sensitive measure of the height-dependence of surface tension.

To go beyond the linear stability analysis, we conducted 2D numerical simulations in the spinodal regime to examine the dewetting rate and morphologies obtained. Figure 1-8 shows that thermal fluctuations (see Eq. (1.44)) and height-dependence of surface tension both lead to a faster initial dewetting. Figure 1-9 shows the growth of perturbations in the nonlinear simulations of dewetting using the different models. The linear stability analysis for this film thickness predicts that the growth rate of the height-dependent surface tension model is twice faster than the classical model ($\beta_m/\beta_{m,\kappa c} = 2$). From the nonlinear simulations we find that the new model leads to
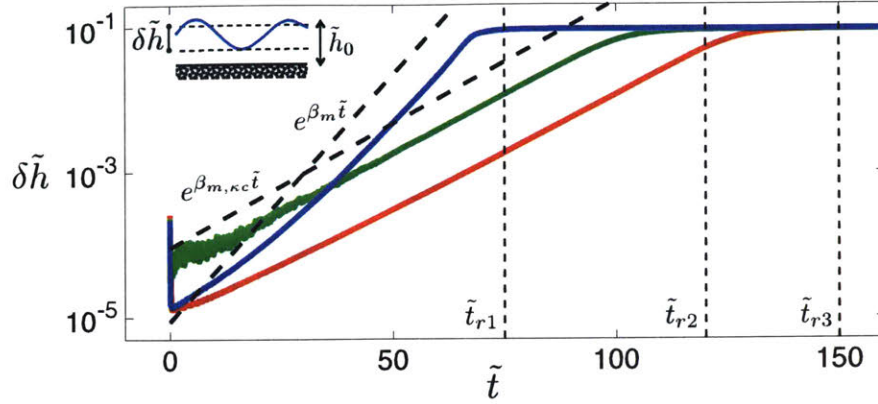
Figure 1-9: The growth of perturbations in the spinodal regime ($\tilde{h}_0 = 2\delta$ as in Fig. 1-8) for the classical model (solid red line), stochastic model (solid green line), and height-dependent surface tension model (solid blue line) as obtained from the nonlinear simulations. The imposed perturbations become damped at early times due to the surface tension, but then start to grow exponentially (as shown by the dashed-lines).
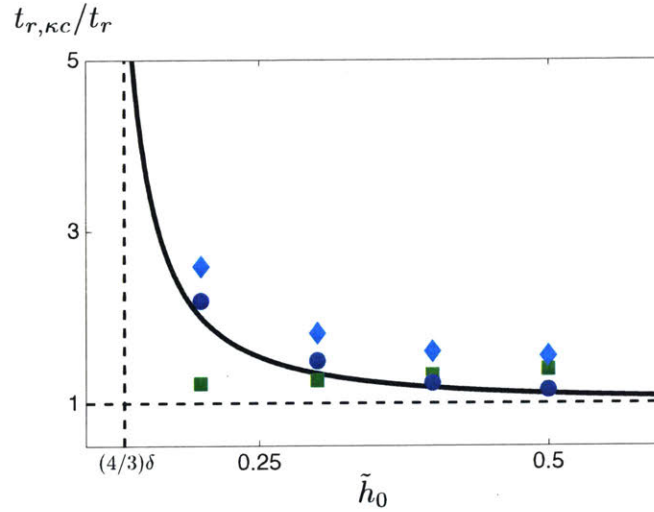
Figure 1-10: The ratio of the rupture times between the classical model ($t_{r,\kappa c}$) and a) the classical model with thermal noise (green squares), b) the height-dependent surface tension model without noise (blue circles), c) the height-dependent surface tension model with noise (cyan diamonds)). Both the thermal noise and height-dependence of surface tension lead to a faster rupture time compared to the classical model. While the effect of noise is almost independent of the initial film thickness (green squares), the height dependence of surface tension leads to an increasingly faster ruptures as the film thickness decreases (blue circles). This effect becomes even more amplified when thermal noise is added to the new model (cyan diamonds). The solid line represents the ratio of the growth rates between the classical and new model as predicted from the linear stability analysis (see Figure 6(d)).

a film rupture at $\tilde{t}_{r1} \approx 75$, whereas the classical model leads to a rupture time of $\tilde{t}_{r3} \approx$ 150, which is in agreement with the linear stability predictions. Thermal fluctuations at $T = 50^o C$, i.e., $\sigma = 0.039$ (see Eq. (1.44)), lead to a rupture around $\tilde{t}_{r2} \approx 125$, which is faster than the classical model. Figure 1-10 shows a more quantitative comparison of the rupture times between the classical model and the other models. The speed up observed due to the thermal noise is independent of the initial height of the film, whereas the height dependence of surface tension in the new model leads to increasingly faster rupture as the initial film height decreases. The prediction of a faster growth rate in our model deserves special attention. Earlier studies have pointed to temporal inconsistencies between theoretical predictions and experimental observations (Becker et al., 2003), with experiments showing a faster initial dewetting process by more than a factor of two compared to the theoretical predictions. Our new model therefore brings theoretical predictions closer to the earlier experimental observations. Our results in Fig. 1-10 further suggest that to disentangle the roles played by the height-dependence of surface tension and the thermal noise, experiments with different initial heights need to be conducted.

1.5 Coarsening: self-similar intermediate asymptotics

1.5.1 Coarsening phase diagram

The drops formed after the dewetting process are in a meta-stable state; they can still communicate through the ultra-thin films connecting them and thus coarsen in time to lower the overall energy of the system. Multiplying both sides of Eq. (1.22) by $\delta\Gamma/\delta\tilde{h}$, integrating in space and using the no-flux boundary conditions we can easily show (see also Thiele et al. (2001a); Glasner and Witelski (2003)):

$$\frac{d\Gamma}{d\tilde{t}} = -\int \mathcal{M}\left(\frac{\partial}{\partial\tilde{x}}\left(\frac{\delta\Gamma}{\delta\tilde{h}}\right)\right)^2 d\tilde{x} \leq 0, \tag{1.40}$$

demonstrating that the evolution governed by the thin film equation leads to a decreasing free energy and, therefore, a thermodynamically-admissible system.

We can further demonstrate this fact by considering the coarsening of two equally sized droplets of width $\tilde{w}_2$ and pressure $\tilde{P}_2$ (Glasner and Witelski, 2003). Assuming that the core of the droplets is only influenced by surface tension (neglecting gravity and intermolecular forces within the droplet core) leads to a parabolic droplet profile, from which we can estimate the energy associated with the two distinct drops as

$$\Gamma_2 = 2\int_{-\tilde{w}_2}^{\tilde{w}_2}\left((1/2)(\tilde{P}_2\tilde{x})^2\right)d\tilde{x} = (2/3)\tilde{P}_2^2\tilde{w}_2^3, \tag{1.41}$$

where $\tilde{w}_2 = 1/(\sqrt{3}\tilde{P}_2)$. Now if the two drops merge and form a single drop with a width $\tilde{w}_1$, we can use conservation of mass to show $\tilde{w}_1 = \sqrt{2}\tilde{w}_2$ and $\tilde{P}_1 = \tilde{P}_2/\sqrt{2}$; the rest of the domain $(4\tilde{w}_2 - 2\tilde{w}_1)$ will now be covered by an equilibrium film of thickness δ; we can therefore write the energy of this new system as

$$\Gamma_1 = \int_{-\tilde{w}_1}^{\tilde{w}_1}\left((1/2)(\tilde{P}_1\tilde{x})^2\right)d\tilde{x} + (4\tilde{w}_2 - 2\tilde{w}_1)\,\tilde{f}(\delta), \tag{1.42}$$

which can further be simplified to: $\Gamma_1 = (\sqrt{2}/3)\tilde{P}_2^2\tilde{w}_2^3 + (4 - 2\sqrt{2})\tilde{w}_2\tilde{f}(\delta)$; comparing
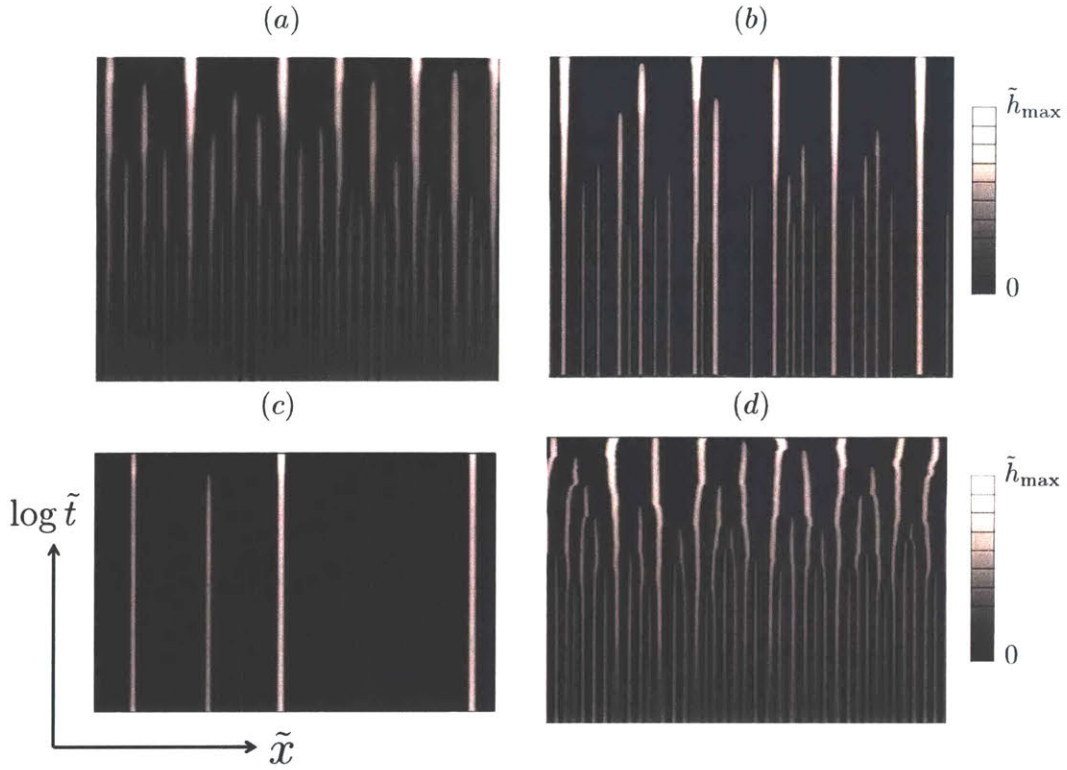
Figure 1-11: Space-time diagrams showing the evolution of drop height of the classical thin film equation (constant surface tension); the results of the height-dependent case are similar. The simulations are done in a domain of size $100\lambda_m$ and the frames shown here show a zoom-in of a size $40\lambda_m$. In all the cases, a line coming to an end indicates an Ostwald ripening event, in which a smaller drop feeds into larger neighboring drops through the ultra-thin film that connects them. (a) $\tilde{h}_0 = 4\delta$ representing the classical spinodal regime, where the number of drops is approximately set by the most unstable wavelength λ_m ($\tilde{h}_{max} = 35\delta$), (b) $\tilde{h}_0 = 10\delta$ representing a mixed mode instability regime in between spinodal and nucleation regimes; here, fewer drops than the spinodal regime form and the distance between the formed drops seems to be random ($\tilde{h}_{max} = 100\delta$), (c) $\tilde{h}_0 = 25\delta$ which is deep into the nucleation regime showing the formation of very few drops ($\tilde{h}_{max} = 700\delta$), (d) $\tilde{h}_0 = 4\delta$ and including thermal fluctuations ($T = 50^oC$, i.e., $\sigma = 0.039$) ($\tilde{h}_{max} = 25\delta$): thermal noise enhances the lateral motion of the drops; the coarsening mechanism however, still seems to be dominated by Ostwald ripening.

this equation with the energy of two drops, we can see that not only is the interfacial energy of a single drop lower than that of two droplets, but also the part covered by the equilibrium film further lowers the free energy since $\tilde{f}(\delta) = -1/6 < 0$.

Figure 1-11 shows space-time diagrams of the dewetting of thin liquid films of different thickness and their coarsening over time. The simulations presented here

are conducted on a large domain of size $100\lambda_m$ and the frames shown are a zoomed-in view of a window of size $40\lambda_m$; these simulations show the results corresponding to the classical model with a constant surface tension; the results of the height-dependent surface tension model are very similar. In all cases we start with a uniform film of thickness $\tilde{h}_0$ on which random perturbations of amplitude $10^{-4}\tilde{h}_0$ are imposed. While all the initial thicknesses are within the linearly unstable regime (see Fig. 1-6), they lead to entirely different morphologies.

For small initial film height of $\tilde{h}_0 = 4\delta$, we observe the characteristics of the spinodal dewetting, a term originally coined by Mitlin (1993) due to its similarity to the spinodal decomposition in binary mixtures (Cahn, 1961). In this regime, the distance between the drops is the same as the most unstable wavelength, i.e., we get ≈ 100 drops in a domain of size $100\lambda_m$ (Diez and Kondic, 2007). The coarsening here proceeds through Ostwald ripening (Ostwald, 1897), or collapse of smaller drops at the expense of growth of larger ones (Glasner and Witelski, 2003).

As the initial film height increases to $\tilde{h}_0 = 10\delta$, we can immediately see in Fig. 1-11 (b) that the number of drops formed upon dewetting and their spacing do not follow the predictions of the linear stability analysis anymore, i.e., fewer drops form and their spacing becomes random. This behavior has signatures of nucleation dewetting within the linearly unstable regime (Thiele et al., 2001b,a; Diez and Kondic, 2007) and shows a mixed mode instability, i.e., a behavior in-between spinodal and nucleation regimes. Such a transition has also been reported in phase separation dynamics within the Cahn–Hilliard framework (Novick-Cohen, 1985). Figure 1-12 shows corresponding 2D simulations of dewetting in this regime; in contrast with the spinodal regime, where holes appear around the same time with a uniform spacing, here the nucleation process begins with formation of a hole, which then laterally expands and forms a rim behind it (Seemann et al., 2001b, 2005; Fetzer et al., 2005; Bäumchen and Jacobs, 2010; Bäumchen et al., 2014). In this mixed mode regime, the growth rate is still large enough that shortly after growth of a hole, the depression behind the dewetting rim can lead to rupture; this behavior leads to the satellite-hole formation observed in the experiments (Becker et al., 2003; Neto et al., 2003) and in the 2D simulations
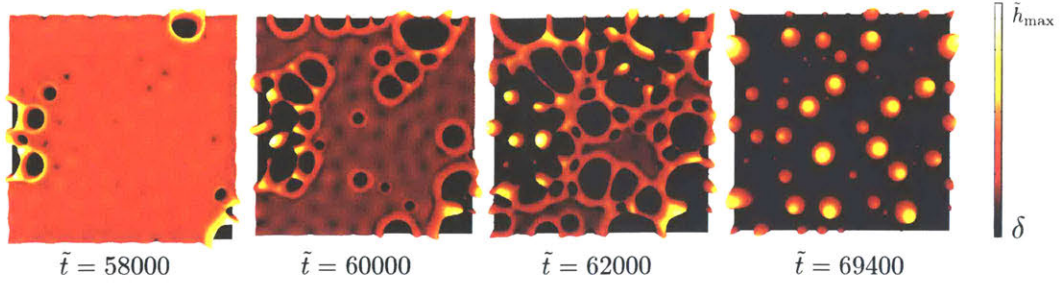
Figure 1-12: Nucleation dewetting for $\tilde{h}_0 = 10\delta$ for the constant surface tension model. In this regime, holes randomly appear and start expanding laterally, forming a growing rim behind them ($\tilde{h}_{\max} = 30\delta, 54\delta, 70\delta, 120\delta$, respectively). The depression behind the dewetting rim leads to the formation of satellite holes. The dewetting rims subsequently become unstable and lead to fingering and pinch off to form droplets (see Reiter and Sharma (2001); Bäumchen et al. (2014) for experimental details)

of Fig. 1-12. Figure 1-13 illustrates this nucleation process in a space-time diagram of a 1D simulation of the height-dependent surface tension model with $\tilde{h}_0 = 10\delta$.

As we keep increasing the initial film thickness further to $\tilde{h}_0 = 25\delta$ (Fig. 1-11(c)), we move deeper into the nucleation regime, where fewer drops form; in this case 5 drops formed in random locations in a domain of size $40\lambda_m$. In the nucleation regime two time scales compete: the time scale associated with the growth of linearly unstable modes and the time scale associated with the dewetting front (Thiele et al., 2001b; Diez and Kondic, 2007; Snoeijer and Eggers, 2010). As we showed before, the growth rate of the most unstable mode β_m scales as $\tilde{h}_0^{-5}$ leading to significant decreases in the growth rate for thicker films, thereby favoring growth via nucleation.

Since the dynamics of the coarsening process is slaved to the flux through the ultra-thin equilibrium films ($\tilde{h}_m \approx \delta$) connecting the drops and the mobility scales as $\tilde{h}^3$, the coarsening dynamics are extremely slow. Two time scales are involved in this process: a fast time scale over which individual coarsening events happen, and a slow time scale between the individual events (Glasner and Witelski, 2003). A full numerical simulation of the thin film equation therefore can be computationally very expensive. Glasner and Witelski (2003) used the separation of time scales in this problem to reduce the governing partial differential equation, Eq. (1.22), to a system of ordinary differential equations for the droplet pressures and locations. Coarsening can proceed via two general mechanisms: coalescence of droplets or Ostwald ripening

67
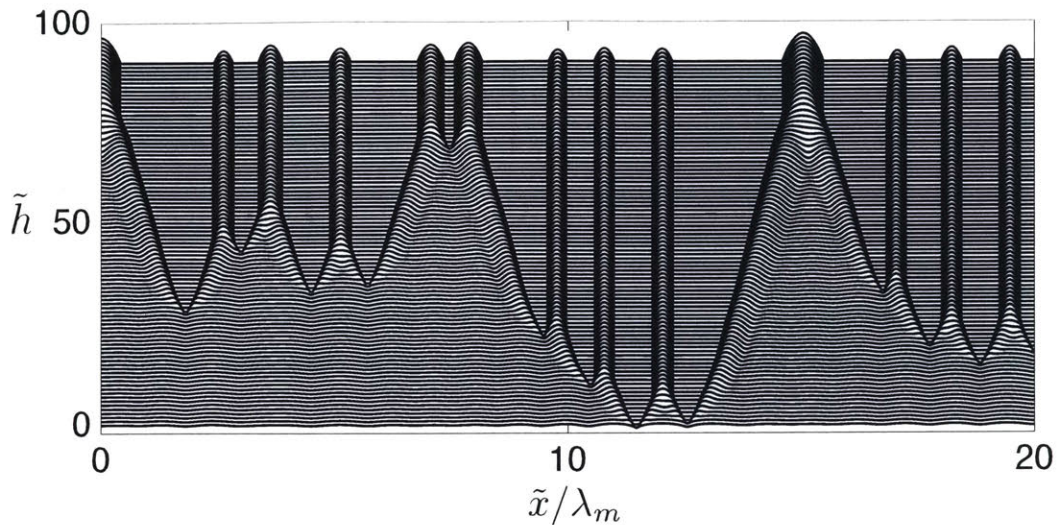
Figure 1-13: Space-time diagram of the nucleation process in the height-dependent surface tension model with $\tilde{h}_0 = 10\delta$ in a domain of size $20\lambda_m$ (each snapshot is shifted up by $10\delta = 1$). The lateral expansion of holes, growth of the rim behind the hole, and the subsequent instability of the dip behind a growing rim can all be seen in this illustration.

(Glasner and Witelski, 2005). Their mathematical model allowed them to simulate the coarsening of a very large number ($O(10^5)$) of drops. They observed a scaling of $N \sim \tilde{t}^{-2/5}$ for the number of drops in time and also observed a transition from Ostwald-ripening dominated (capillary-driven drainage and collapse) coarsening to coalescence-dominated coarsening as they increased the total mass of liquid in the domain.

In contrast with the findings of Glasner and Witelski (2005), we do not observe such a transition from Ostwald ripening dominated to coalescence-dominated coarsening (Fig. 1-11). The change in the instability mode from spinodal to nucleation leads to the formation of fewer drops as the total mass of the liquid in the domain increases, i.e., as the initial film height increases: the large distance between the drops favors coarsening through Ostwald ripening rather than coalescence. The reason Glasner and Witelski (2005) observe such a transition is that they keep the number of drops within a given domain fixed as they increase their mass; this naturally leads to wider drops that progressively get closer to each other, therefore favoring coalescence.

1.5.2 Influence of thermal fluctuations

Some experiments on thin-film dewetting (Limary and Green, 2002, 2003) and nanoparticle growth in thin films (Meli and Green, 2008; Woehl et al., 2014) have reported a crossover from diffusion-dominated to coalescence-dominated behavior. A potential source of this transition could be thermal noise, which may play a dominant role in thin-film systems (Mecke and Rauscher, 2005; Grün et al., 2006; Fetzer et al., 2007b; Willis and Freund, 2009; Belardinelli et al., 2016; Diez et al., 2016). In the presence of thermal noise, Grün et al. (2006) showed that the stochastic thin film equation can be derived starting from the phenomenology introduced by Landau and Lifshitz (1987), where the thermal fluctuations enter the Navier-Stokes equations as a symmetric random stress tensor $\mathbf{S}$, where $\langle \mathbf{S} \rangle = 0$, and $\langle S_{ij}(\mathbf{x}, t) S_{lm}(\mathbf{x}', t') \rangle = 2 k_b T \mu \delta(\mathbf{x} - \mathbf{x}') \delta(t - t')(\delta_{il}\delta_{jm} + \delta_{im}\delta_{jl})$. The hydrodynamic equations in the presence of thermal noise have been used in many studies including the dynamic critical phenomena of randomly stirred fluids (Forster et al., 1977), or the convective instabilities (Swift and Hohenberg, 1977). Using the long-wave approximation, then one can arrive at a stochastic thin film equation that includes a vertical integral in the off-diagonal term of the random stress S_{xz} (Grün et al., 2006; Diez et al., 2016):

$$\frac{\partial \tilde{h}}{\partial \tilde{t}} = \frac{\partial}{\partial \tilde{x}} \left(\tilde{h}^3 \frac{\partial \tilde{P}}{\partial \tilde{x}} \right) + \frac{\partial}{\partial \tilde{x}} \left(\int_0^{\tilde{h}} (\tilde{h} - z) S_{xz}(z) \, dz \right). \tag{1.43}$$

This equation can be further simplified to one without the integral term; to do so, Grün et al. (2006) use the equivalency of the corresponding Fokker-Planck equations of the probability densities, further showing that the distribution function satisfies the detailed balance and is given by $\mathcal{W}_{eq} = (1/Z) \exp(-\mathcal{H}[h]/T)$, where Z is the partition function and $\mathcal{H}[h] = \int f(h) + \gamma/2 (\nabla h)^2 dx$ is the effective interface Hamiltonian or free energy. An alternative way of arriving at the Langevin term is to consider the linear response of a near-equilibrium system and use the fluctuation-dissipation theorem together with equipartition of the thermal energy (Davidovitch et al., 2005). The stochastic thin film equation therefore can be written as follows:

$$\tilde{t} = 160 \qquad \tilde{t} = 180 \qquad \tilde{t} = 330 \qquad \tilde{t} = 545$$
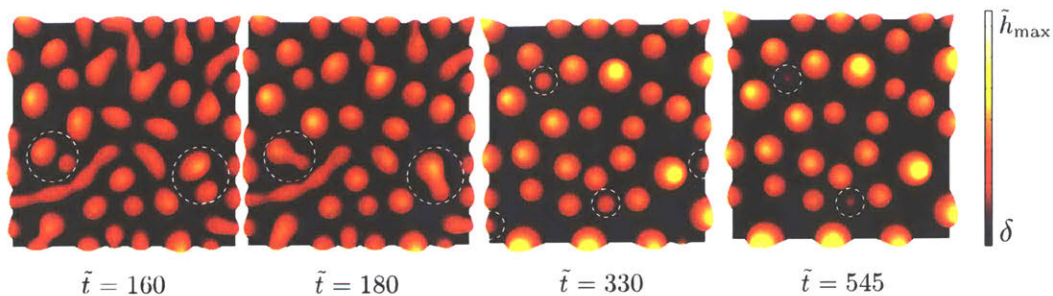
Figure 1-14: Two-dimensional simulations of coarsening dynamics at early and late times for the height-dependent surface tension model with $\tilde{h}_0 = 2\delta$ ($\tilde{h}_{\max} = 8.5\delta$ in the colorbar). At early times, coalescence events, as highlighted by the dashed white circles, are dominant. At late times (once the metastable drops have formed), however, Ostwald ripening, i.e., capillary drainage and collapse of drops, becomes the key coarsening mechanism; note that this latter process is diffusion-dominated and therefore much slower than coarsening through coalescence events.

$$\frac{\partial \tilde{h}}{\partial \tilde{t}} = \frac{\partial}{\partial \tilde{x}} \left(\tilde{h}^3 \frac{\partial \tilde{P}}{\partial \tilde{x}} \right) + \sigma \frac{\partial}{\partial \tilde{x}} \left(\tilde{h}^{3/2} \tilde{\xi}(\tilde{x}, \tilde{t}) \right), \tag{1.44}$$

in which $\tilde{P} = d\tilde{f}/d\tilde{h} - \sqrt{\tilde{\kappa}} \partial/\partial \tilde{x} \left(\sqrt{\tilde{\kappa}} \partial \tilde{h}/\partial \tilde{x} \right)$ with $\tilde{\kappa} = \kappa/\gamma$ and $\tilde{f} = f/(\gamma H^2/L^2)$, where H and L are characteristic height and length scales. The second term on the right hand side of the equation represents the thermal fluctuations (Mecke and Rauscher, 2005; Davidovitch et al., 2005; Grün et al., 2006) with $\sigma = \sqrt{k_B T/\gamma H^2}$, where k_B is the Boltzmann constant and T represents the temperature, and $\tilde{\xi}$ represents a spatiotemporal Gaussian white noise: $\langle \tilde{\xi} \rangle = 0$ and $\langle \tilde{\xi}(\tilde{x}, \tilde{t}) \tilde{\xi}(\tilde{x}', \tilde{t}') \rangle = \delta(\tilde{x} - \tilde{x}') \delta(\tilde{t} - \tilde{t}')$ with δ as the Dirac delta function and $\langle . \rangle$ implying ensemble average over realizations of the noise.

Introducing thermal noise to the system leads to enhanced lateral motion of the drops as seen in Fig. 1-11 (d), and this can promote coalescence. Our simulations for the stochastic thin film Eq. (1.44) within the spinodal regime, however, shows the dominance of Ostwald ripening despite the enhanced lateral motion of the drops. The crossover from the diffusion-dominated to coalescence-dominated behavior observed in the experiments (Limary and Green, 2002, 2003) therefore could be a consequence of the dimensionality of the problem, i.e., 2D in the experiments versus 1D in the simulations shown in Fig. 1-11. In two dimensions, each drop can be surrounded

and interact with multiple other drops, whereas in 1D each drop only interacts with its two neighbors. To investigate this, we have conducted 2D nonlinear simulations, which point to the dominance of coalescence events at short times and Ostwald ripening at long times as shown in Fig. 1-14, which corresponds to the height-dependent surface tension model; similar results are obtained for both the classical and stochastic models. Our observations are in agreement with the 2D simulations of Glasner (2008) using a reduced order model that suggest the dominance of the coalescence mechanism.

1.5.3 Coarsening statistics

The statistics of the coarsening process for (i) the spinodal regime, $\tilde{h}_0 = 4\delta$ (for both constant and height-dependent surface tension models as well as the classical stochastic thin film equation with thermal noise) and (ii) for the mixed-mode instability regime $\tilde{h}_0 = 10\delta$ (for the constant surface tension model) are shown in Fig. 1-15. In the spinodal regime, the number of drops follows the scaling $N \sim \tilde{t}^{-2/5}$ in time (Fig. 1-15 (a)) as computed by Glasner and Witelski (2003); incorporating the height-dependence of surface tension does not alter this scaling. Introducing thermal noise does not affect the scaling either—an observation that is consistent with recent studies (Nesic et al., 2015). In the mixed-mode instability regime ($\tilde{h}_0 = 10\delta$), fewer drops form, so our simulations have limited statistics and do not clearly reach the self-similar intermediate regime (Gratton and Witelski, 2009), but it seems that the results for this case are also in general agreement with the $\tilde{t}^{-2/5}$ scaling (Fig. 1-15 (a)). Due to mass conservation, it is easy to show that the mean width of drops should then follow the scaling $\tilde{t}^{1/5}$ as shown in Fig. 1-15 (b). An interesting feature of the variation of the mean width in time, particularly at late times, is the jumps observed as smaller drops shrink and feed into the larger drops.

As argued above, the thin film evolution equation predicts a monotonically decreasing free energy for the system (Eq.(1.40)). We can further check this by looking at the variation of the numerically calculated total energy of the system $E_t \equiv \Gamma = \int \tilde{f}(\tilde{h}) + (\tilde{\kappa}/2)(\tilde{h}_x)^2 d\tilde{x}$. In agreement with the predictions of Otto et al. (2006), we find a $\tilde{t}^{-1/5}$ scaling for the decrease of the free energy (Fig. 1-15(c)). An interesting observation here is that for the thicker film of $\tilde{h}_0 = 10\delta$, we observe a lower total free energy at early times that later converges to the $\tilde{t}^{-1/5}$ scaling. To understand the reason behind the difference at early times, it is instructive to look at the typical variation of the different components of the free energy during the entire dewetting process, as shown in Fig. 1-15 (d). Here, $E_b = \int \tilde{f}(\tilde{h})d\tilde{x}$ is the bulk free energy and $E_i = \int (\tilde{\kappa}(\tilde{h})/2)(\tilde{h}_x)^2 d\tilde{x}$ is the interfacial energy. As an initially uniform film becomes unstable, it must increase the interfacial energy to dewet and create droplets. This in-
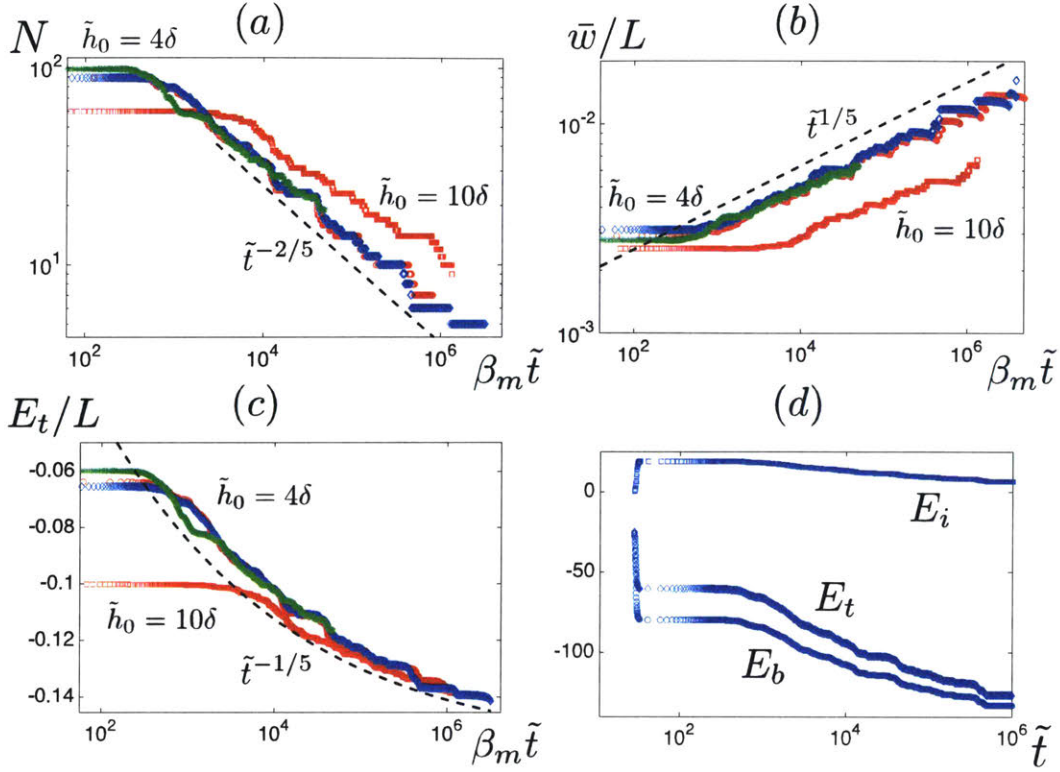
Figure 1-15: Coarsening statistics; red circles and squares correspond to the classical model with $\tilde{h}_0 = 4\delta$ and $\tilde{h}_0 = 10\delta$, respectively; blue diamonds show the results of the new model with $\tilde{h}_0 = 4\delta$; green stars correspond to the stochastic thin film model with $\tilde{h}_0 = 4\delta$. (a) Evolution of the number of drops in time shows the scaling $\tilde{t}^{-2/5}$ as suggested by Glasner and Witelski (2003). (b) Evolution of mean width of drops in time; as expected from conservation of mass and the scaling of the number of drops in time, the mean width scales as $\tilde{t}^{1/5}$ in time. (c) Evolution of the total energy in time shows a decrease in the energy with coarsening with a scaling of $\tilde{t}^{-1/5}$, which is expected for the 1D case (Otto et al., 2006); the $\tilde{h}_0 = 10\delta$ case results in fewer drops upon dewetting, therefore the majority of the domain is covered by the equilibrium film, which means the initial energy is lower than the $\tilde{h}_0 = 4\delta$ case; at long times the dynamics becomes self-similar and both follow the same scaling. (d) Evolution of the bulk E_b, interfacial E_i, and total $E_t = E_b + E_i$ energies for a typical simulation (here $\tilde{h}_0 = 4\delta$ and height-dependent surface tension model); at short times, creation of drops increases the interfacial energy, but the total energy is still lowered due to the reduction in the bulk energy; at long times, as drops coarsen, both the bulk and interfacial energy contribution decrease.

crease in the interfacial energy, however, is compensated by the reduction in the bulk free energy as the ultra thin films connecting the drops are in their near-equilibrium states. The drops connected by these ultra-thin films however are only metastable and after a long intermediate plateau state the system starts lowering its total energy through coarsening, which lowers both the interfacial energy as well as the bulk free energy due to the creation of new ultra-thin films. With this observation in mind, we can now go back to Fig. 1-15(c); here, the thicker film ($\tilde{h}_0 = 10\delta$) leads to the formation of fewer drops upon dewetting, meaning a lower interfacial and bulk free energies in the mixed-mode instability regime compared to the spinodal regime (formation of fewer drops means a higher fraction of the total surface is covered by the ultrathin films that have a lower bulk free energy). This is why right after dewetting, the thicker film case $\tilde{h}_0 = 10\delta$ leads to a lower total free energy compared to the $\tilde{h}_0 = 4\delta$ case in the spinodal regime. At long times, however, as the coarsening sets in, the dynamics become self-similar and the total system energies per unit length of the substrate corresponding to the different regimes all collapse on top of each other.

1.5.4 LSW mean-field description of coarsening: self-similar drop size distribution

In the late stages of a first-order phase transition of a binary alloy mixture, Ostwald ripening is quite common (Ostwald, 1897; Siggia, 1979; Voorhees, 1985). The curvature-dependence of the chemical potential leads to a flow from higher curvature regions (smaller clusters) to lower curvature regions (larger clusters). The result of this coarsening is a decrease in the total interfacial energy of the system. Lifshitz and Slyozov (1961) were the first to place experimental measurements of Ostwald ripening within a consistent theoretical framework: they considered a spherical cluster in a supersaturated solution and developed a mean-field description for the evolution of the size of the cluster at long times, $\langle r(t) \rangle \sim t^{1/3}$. This scaling is an intermediate-asymptotic behavior (Barenblatt, 1996) for a quasi-steady system in isolation, i.e., the interactions with other clusters are neglected, so it is expected to hold in the limit of dilute solutions. Lifshitz and Slyozov (1961) originally assumed the transport in the medium to be diffusion dominated; later, Wagner (1961) independently studied the Ostwald ripening process and considered the case where the attachment/detachment of particles from the clusters is the rate-limiting factor and derived a scaling $\langle r(t) \rangle \sim t^{1/2}$. Apart from the mode of mass transport considered, the two theories are essentially the same and are known as the LSW model for coarsening (Kahlweit, 1975). An alternative generalized view of the same problem is to consider all the clusters of size greater than $r_c \sim t^\beta$ to grow and all with a smaller size to shrink, where $\beta = 1/3$ in the diffusion-dominated case and $\beta = 1/2$ in the attachment/detachment-dominated case.

Theories of LSW-type appear in many diverse phenomena, such as stability of emulsions (Imhof and Pine, 1997; Taylor, 1998; Bibette et al., 1999; Solans et al., 2005; Gupta et al., 2016), droplet size distribution in liquid jet fragmentation (Eggers and Villermaux, 2008), coarsening of granular clusters (Aranson and Tsimring, 2006), phase separation in polymer blends (Geoghegan and Krausch, 2003), growth of silicone nanowires (Schmidt et al., 2010), quantum dots (Liu and Risbud, 1990),
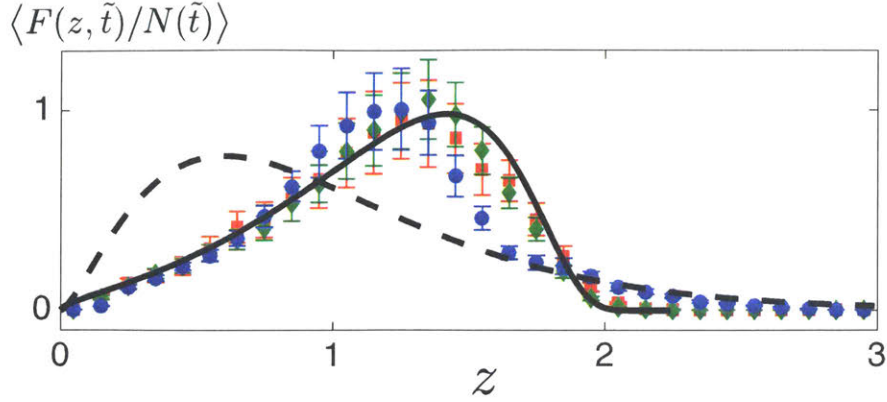
Figure 1-16: Droplet mass distribution for the spinodal regime with $\tilde{h}_0 = 4\delta$ obtained from ensemble averaging of 10 realizations in domains of size $250\lambda_m$ with $z = m/m_*$; vertical lines show the error bars computed from the standard deviation of the 10 realizations; red squares represent classical model with a constant surface tension; green diamonds represent the stochastic thin film model; blue circles represent the new model wth height-dependent surface tension; the solid line represents the mean-field LSW theory (Eq. (1.46)); the dashed line represents the Smoluchowski distribution (Eq. (1.47)).

growth of nanoparticles in colloidal solutions (Talapin et al., 2001), and grain growth in thin films (Thompson, 1990), or even loss of electrocatalyst coating in low temperature fuel cells (Shao-Horn et al., 2007). There is a close connection between the LSW theory and coarsening of drops connected by thin films. The drops formed upon dewetting are in a metastable quasi-equilibrium configuration, so one can treat a droplet connected to a near equilibrium film in isolation from the other drops. The transport through the surrounding thin film is diffusion-dominated since curvature becomes negligible in the film. Diffusion here is set by the interface potential and mobility reaches a constant value set by the film thickness, so the transport between droplets can formally be written as a diffusion equation similar to the LSW theory.

At long times, the clusters or drops follow a size distribution function $F(r, \tilde{t})$, or equivalently $F(m, \tilde{t})$ where $m = \int_{-\tilde{w}}^{\tilde{w}} \tilde{h} d\tilde{x}$ is the mass of a 1D drop, which satisfies the following continuity equation (Voorhees, 1985; Gratton and Witelski, 2009):

$$\frac{\partial F(m, \tilde{t})}{\partial \tilde{t}} + \frac{\partial}{\partial m}\left(F(m, \tilde{t})v(m)\right) = 0, \qquad (1.45)$$

where $v(m) = dm/d\tilde{t}$ determines the flux of particles. The number of drops can then be related to the distribution function as $N = \int_0^\infty F(m,\tilde{t})dm$. The problem then reduces to defining the flux $v(m)$. Gratton and Witelski (2009) showed that an equivalent LSW mean field model can be defined for a system of drops, where a drop is considered to be at a mean distance $\bar{L}(\tilde{t}) = L/N(\tilde{t})$ from two neighboring drops of mass m_*; since the mass transport between the drops takes place through the ultra-thin films with nearly zero curvature connecting them, the transport through the films becomes purely diffusive and its dynamics can be approximated as $\partial\tilde{h}/\partial\tilde{t} \sim \partial^2/\partial\tilde{x}^2(\mathcal{V}(\tilde{h}))$, where $d\mathcal{V}/d\tilde{h} = \tilde{h}^3 d^2\tilde{f}/d\tilde{h}^2$ (Glasner and Witelski, 2003). The mean flux between the drops can then be approximated as $v(m) = 2(\mathcal{V}(m_*) - \mathcal{V}(m))/\bar{L}$, where the mean-field potential is defined as $\mathcal{V}(m_*(\tilde{t})) = (1/N)\int_0^\infty \mathcal{V}(m)F(m,\tilde{t})dm$. The non-locality in this mean-field description comes from the mean quantities $\bar{L}$ and m_*, both of which evolve in time. At long times, we expect the distribution of the drop sizes to become self-similar, for which we can postulate $F(m,\tilde{t}) = g(m/m_*)/\tilde{t}^\alpha$ and $m_* = c\tilde{t}^\beta$. Using conservation of mass, one then arrives at the following ODE for the self-similar distribution function $g(z)$ (Gratton and Witelski, 2009):

$$\frac{dg}{dz} = \left(\frac{27/2 - 8z^{3/2}}{4z^{5/2} + 27z(1 - \sqrt{z})}\right)g, \tag{1.46}$$

where $0 \le z \equiv (m/m_*) \le 9/4$, and the solution of the above equation can be obtained in the analytical form to be $g(z) = C\left(\sqrt{z}e^{2/(-3+2\sqrt{z})}\right) / \left((3 - 2\sqrt{z})^{28/9}(3 + \sqrt{z})^{17/9}\right)$ with $C \approx 70$ as a normalization constant. From the conservation of mass, one can further find $m_* \approx 0.846\bar{m}$ (with $\bar{m} = M_{tot}/N(\tilde{t})$ being the total liquid mass divided by the instantaneous number of drops), which separates growing and shrinking drops, i.e., $v(m_*) = 0$. This mean-field treatment is expected to hold in the dilute limit, where local interactions between drops can be neglected and each drop only interacts with a background field.

The normalized distribution of the droplet mass ($\langle F(z,\tilde{t})/N(\tilde{t})\rangle$ with $z = m/m_*$) in the self-similar intermediate regime, where the LSW model is applicable is shown in Fig. 1-16. The results of the simulations closely follow Eq. (1.46) (solid line)

for small droplets. The close agreement we observe between the classical and new models, as well as in the presence of thermal fluctuations, indicates that in the self-similar coarsening regime the details of the thin-film interfacial dynamics are not critical. For larger size droplets, i.e. $z > 1$ $(m > m_*)$, however, we do observe deviations from the LSW model. While some deviations have also been observed by Gratton and Witelski (2009) in their dynamical system treatment of coarsening and is a known issue in the LSW model, there is a distinct skewness in the distribution of the droplets in the new model. The long tail observed in the distribution of droplet sizes in our model has also been reported in some experiments and Monte Carlo models of thin-film coarsening (Lo and Skodje, 2000; Limary and Green, 2002, 2003; Green, 2003; Meli and Green, 2008; Woehl et al., 2014) and is typically associated with coarsening through coalescence. This type of drop-size distribution is modeled with the Smoluchowski equation (Smoluchowski, 1917; Sholl and Skodje, 1996; Lo and Skodje, 2000; Eggers and Villermaux, 2008):

$$g(z) = \left(\frac{dW(Wz)^{d(\alpha+1-1/d)}}{\Gamma(\alpha+1)} \right) e^{-(Wz)^d}, \qquad (1.47)$$

where $W = \Gamma(\alpha + 1 + 1/d)/\Gamma(\alpha + 1)$ with Γ is the gamma function, and d represents the dimension of the system. When mass transport is dominated by diffusion around the periphery of the droplet, $\alpha = 3/2$; when diffusion away from the boundaries is the dominant transport mechanism, $\alpha = 1$, and when evaporation-condensation in the periphery of the drops is the main transport avenue, $\alpha = 1/2$ (Lo and Skodje, 2000). Here, we find the best fit for the tail of the distribution in a 1D system of droplets is obtained for the periphery-diffusion dominated case with $\alpha = 3/2$. It is interesting, however, that the change in the tail of the drop-size distribution in our model is not associated with a change in the coarsening mechanism, i.e., Ostwald ripening remains the dominant coarsening mechanism (Fig. 1-11); perhaps, it is the lower lateral motion of the larger-size droplets that leads to the asymmetry in the distribution. While our 1D simulation results cannot be directly compared with the experiments, the long-tailed distribution in our model calls into question whether the

reported distributions in the experiments are uniquely a signature of the coalescence-dominated coarsening and this motivates further detailed experimental observations.

1.6 Discussions: comparison with experimental data

While the scaling of the wavelength of instability and its growth rate with the film thickness can be derived from the linear stability analysis, the only way to make quantitative predictions about the dewetting is to have the precise form of the intermolecular forces. The dewetting pattern in the spinodal regime can give us the information needed to reconstruct the surface potential; one can extract the wavelength of instability for a given initial uniform film thickness and repeat this process for different film thicknesses; all the experiments need to be done within the spinodal regime, where a uniform distribution of holes can be observed (Seemann et al., 2001a). Figure 1-17 shows such a reconstruction for polystyrene films on a Si wafer with a 191 nm silicone oxide layer coating; the free energy is assumed to have a form $f(h) = -\mathcal{A}_{\mathrm{SiO}}/(12\pi h^2) + c/h^8$, where the first term represents the long-ranged attractive van der Waals forces and the second term represents the short-ranged repulsion; $\mathcal{A}_{\mathrm{SiO}}$ is the Hamaker constant for this system and c determines the strength of the repulsive term. We know that the depth of the potential is equal to the spreading parameter, $f(h_f) = \mathcal{S} = \gamma(\cos(\theta_{eq}) - 1)$, where h_f and θ_{eq} are the equilibrium film thickness and contact angle, respectively, which can be independently measured. We can therefore fit the experimental data for the instability wavelength using the least squares method with equilibrium film thickness and contact angle as two penalty conditions. Considering a constant surface tension of $\gamma = 30.8$ mN/m, we arrive at $\mathcal{A}_{\mathrm{SiO}} = 2.24 * 10^{-20}$ J, and $c = 7.24 * 10^{-76}$ Jm^6 that are close to the values obtained by Seemann et al. (2001a). In our model, surface tension can be defined as $\kappa(h) = \gamma(1 - f(h)/f(h_f))$, leading to $\kappa(h_f) = 0$. Following the same fitting procedure as above, we obtain precisely the same coefficient values as before; the new model however, predicts a faster instability growth rate compared to the constant surface tension model (see Fig. 1-17).

The prediction of a faster growth rate in our model compared to the classical model deserves special attention. Becker et al. (2003) used the potential reconstruction procedure outlined above to make quantitative predictions about their experimental

80
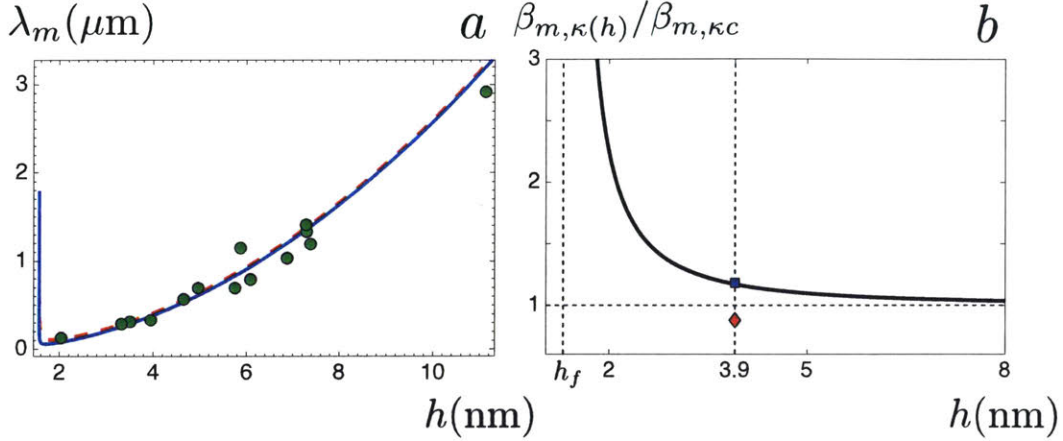
Figure 1-17: Reconstructing the interface potential using the experimental observations of spinodal dewetting by Seemann et al. (2001a) with a thin film of polystyrene film on a Si wafer coated with a 191 nm thick oxide layer: (a) shows the instability wavelength in the spinodal regime (green circles) for different initial uniform film thicknesses; the red dashed line is the fit to the data using the classical model with a constant surface tension; the blue solid line represents the fit obtained with the new model with a height-dependent surface tension; both fits also consider the equilibrium film thickness and contact angle as penalty conditions. The equilibrium contact angle as measured by the AFM is 7.5° and the equilibrium film thickness measured by x-ray reflectivity is $h_f = 1.3$ nm (Seemann et al., 2001a); (b) represents the ratio of instability growth rate in the new model to that of the classical model. It is clear that even for the same instability wavelength, height-dependence of the surface tension leads to a faster growth rate. For a typical PS film thickness of 3.9 nm, our model predicts the dewetting to be $\approx 20\%$ faster than the classical model, bringing the theoretical prediction closer to the experimental observations (Becker et al., 2003). The blue square symbol shows the ratio of the growth rate as obtained from the nonlinear simulations; it coincides with the result of the linear stability analysis. The red diamond symbol represents the ratio of growth rates obtained from the nonlinear simulations of the classical model with and without thermal noise ($T = 0^oC$ and $T = 53^oC$ in Eq. (1.44) with a constant surface tension); we find the growth rate in the presence of thermal noise to be less than the deterministic one by $\approx 10\%$.
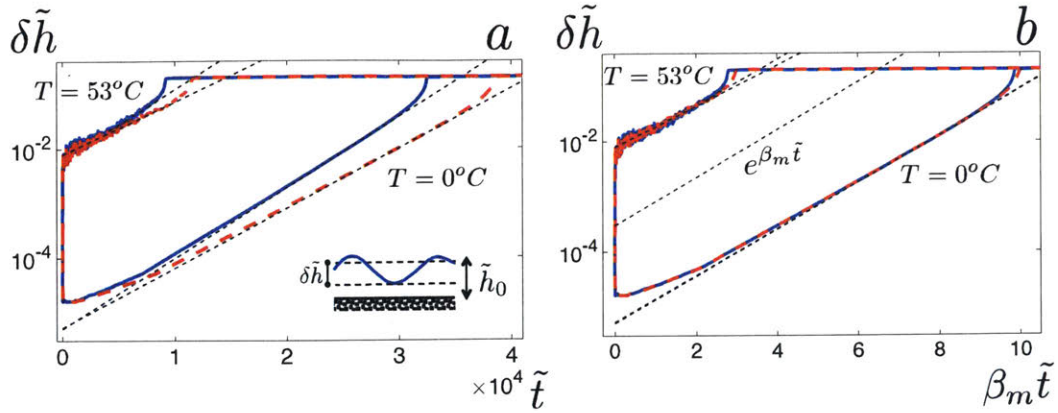
Figure 1-18: The growth of perturbations in a uniform film ($\delta\tilde{h} = \tilde{h}_0 - \min(\tilde{h}(\tilde{t}))$) as a function of (a) time $\tilde{t}$ and (b) rescaled time $\beta_m\tilde{t}$, obtained from the deterministic and stochastic nonlinear simulations with the experimentally reconstructed potential for a PS film of thickness 3.9 nm. In both the classical (red dashed line) and new model (blue solid line), in the absence of thermal noise, the initially imposed infinitesimal perturbations ($\delta\tilde{h}(\tilde{t} = 0) \approx 10^{-4}$) are initially damped by surface tension before the films become unstable to the fastest growing mode and then grow exponentially until rupture takes place, when the minimum film thickness reaches the equilibrium thickness $\tilde{h}_m$; the results of the two models overlay on top of each other when time is scaled with the growth rate ($\beta_m\tilde{t}$). At non-zero temperatures ($T = 53^\circ C$ here) thermal fluctuations do not allow the initially imposed perturbations to be damped by the surface tension, leading to a much faster rupture (≈ 3 times faster than the rupture in the deterministic case) even though for the constant surface tension model the growth rate in the presence of thermal noise is smaller than the deterministic case by more than $\approx 10\%$. Nonlinear simulations further show that while the dewetting occurs much faster in the presence of thermal fluctuations, the morphology of the drops do not seem to be affected, i.e., 10 drops form in a domain size of $10\lambda_m$ consistent with the predictions of linear stability analysis.

results; while they observed similar patterns in simulations and experiments, the temporal evolution did not match: experiments showed a faster initial dewetting process. It was later argued that thermal fluctuations are responsible for the mismatch and including them in the theory will bring the results closer to the experiments (Mecke and Rauscher, 2005; Grün et al., 2006; Fetzer et al., 2007b). Our results are therefore pointing to the right direction; for the experiments of Becker et al. (2003) with a 3.9 nm PS film, our model predicts $\approx \%20$ faster growth rate bringing the theory closer to the experimental results.

To further explore the dewetting rate, we need to go beyond the linear analysis

and perform nonlinear simulations. Figure 1-18 shows the growth of perturbations, $\delta\tilde{h} = \tilde{h}_0 - \min(\tilde{h}(\tilde{t}))$, in a linearly unstable uniform film of 3.9 nm thickness as obtained from the nonlinear simulations of Eq. (1.44). For the deterministic case ($\sigma = 0$), both the classical model with a constant surface tension and our model with a height-dependent surface tension show that initially the imposed perturbations are damped by the surface tension until the fastest growing mode kicks in and the perturbations start growing exponentially. Our model shows a faster growth rate by $\approx 20\%$ (which matches very well the linear predictions as shown with the blue square in Fig. 1-17 (b)); when the time-scale ($\tilde{t}$) is rescaled with the corresponding growth rates (β_m) the perturbation growth in both models perfectly overlay (Fig. 1-18 (b)). However, in the presence of thermal fluctuations, the initial damping of the imposed perturbations by the surface tension is not observed; instead, thermal fluctuations give rise to the immediate growth of the perturbations until the fastest growing mode kicks in and the growth continues exponentially; this leads to a rupture more than 3 times faster than the prediction of the deterministic equation. It is interesting to note, however, that in the classical model, the growth rate in the stochastic case is found to be $\approx 10\%$ smaller than that of the deterministic case (shown as a red diamond in Fig. 1-17 (b)). While the dewetting proceeds faster in the stochastic case, the corresponding dynamics and the resulting morphology seem to be similar to that of the deterministic case, e.g. we observe the formation of 10 drops in both cases in a domain size of $10\lambda_m$.

To gain further insight into the stochastic thin film equation, we can linearize it around the initial uniform film thickness $\delta\tilde{h}(\tilde{x}, \tilde{t}) = \tilde{h}(\tilde{x}, \tilde{t}) - \tilde{h}_0$:

$$\frac{\partial\delta\tilde{h}}{\partial\tilde{t}} = \tilde{h}_0^3 \left(\frac{d^2\tilde{f}}{d\tilde{h}^2}\bigg|_{\tilde{h}_0} \frac{\partial^2\delta\tilde{h}}{\partial\tilde{x}^2} - \kappa(\tilde{h}_0)\frac{\partial^4\delta\tilde{h}}{\partial\tilde{x}^4} \right) + \sigma\tilde{h}_0^{3/2}\frac{\partial\tilde{\xi}(\tilde{x}, \tilde{t})}{\partial\tilde{x}}, \qquad (1.48)$$

Using the Fourier transform $\widehat{\delta\tilde{h}}(q, \tilde{t}) = (2\pi)^2 \int_{-\infty}^{\infty} \delta\tilde{h}(\tilde{x}, \tilde{t})e^{-iq\tilde{x}}\, d\tilde{x}$, we can then write the linearized equation in the wave domain as:
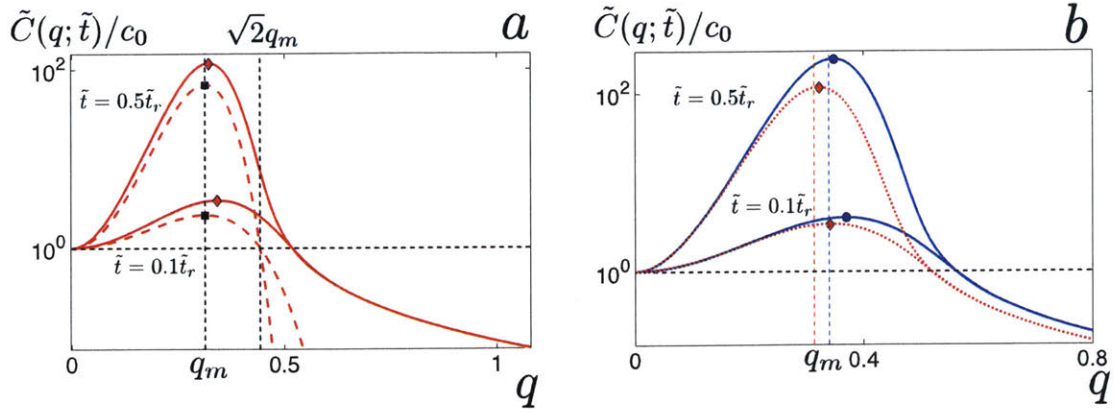
Figure 1-19: Structure factor with the experimentally reconstructed potential for a PS film of thickness 3.9 nm at times $\tilde{t} = 0.1\tilde{t}_r$ and $\tilde{t} = 0.5\tilde{t}_r$, where $\tilde{t}_r$ represents a characteristic rupture time for (a) the deterministic (red dashed line) and stochastic (red solid line) models with a constant surface tension (see also Mecke and Rauscher (2005)), and (b) stochastic model with a constant (red dotted line) and height-dependent (blue solid line) surface tension. The symbols show the location of the peaks of the structure factor; the peak is coincident with the most unstable wavenumber for the deterministic case, whereas it approaches this value from above in the presence of thermal noise.

$$\frac{\partial \widehat{\delta \tilde{h}}}{\partial \tilde{t}} = \tilde{h}_0^3 q^2 \left(\left. \frac{d^2 \tilde{f}}{d\tilde{h}^2} \right|_{\tilde{h}_0} - \tilde{\kappa}(\tilde{h}_0) q^2 \right) \widehat{\delta \tilde{h}} - i q \sigma \tilde{h}_0^{3/2} \widehat{\tilde{\xi}}, \tag{1.49}$$

$$\frac{\partial \widehat{\delta \tilde{h}}}{\partial \tilde{t}} = \beta(q) \widehat{\delta \tilde{h}} - i q \sigma \tilde{h}_0^{3/2} \widehat{\tilde{\xi}}, \tag{1.50}$$

where as for the deterministic case (Eq. (1.37)) $\beta = \tilde{h}_0^3 q^2 \left(\left. \frac{d^2 \tilde{f}}{d\tilde{h}^2} \right|_{\tilde{h}_0} - \tilde{\kappa}(\tilde{h}_0) q^2 \right)$. The Fourier transform of the height autocorrelation function then can be defined as (Mecke and Rauscher, 2005; Diez et al., 2016) $< \delta \tilde{h}(q, \tilde{t}) \delta \tilde{h}(q', \tilde{t}') > = (2\pi)^2 \delta(q + q') \tilde{C}(q; \tilde{t}, \tilde{t}')$, where:

$$\tilde{C}(q; \tilde{t}, \tilde{t}') = \tilde{C}_0(q) e^{\beta(q)(\tilde{t}+\tilde{t}')} + \frac{\sigma^2 \tilde{h}_0^3}{2} \frac{q^2}{\beta(q)} \left(e^{\beta(q)(\tilde{t}+\tilde{t}')} - e^{\beta(q)|\tilde{t}-\tilde{t}'|} \right), \tag{1.51}$$

where $\tilde{C}_0(q) = < |\widehat{\delta \tilde{h}}(q, 0)|^2 >$; for a white Gaussian noise, $\tilde{C}_0(q) = c_0$ becomes a constant. Figure 1-19 shows the normalized structure factor or power spectrum as a function of the wavenumber for the deterministic and stochastic thin film models.

84

In the absence of thermal noise, the peak of the structure factor, shown as black squares, is always the same as q_m, i.e., the most unstable wavenumber; further at long times and for large wavenumbers, we always see an exponential decay $e^{-2|\beta|t}$ as easily seen in the first term of Eq. (1.51). In the presence of thermal noise however, the behavior qualitatively changes at large wavenumbers, i.e., exponential decay is taken over by a power law decay q^{-2}. Further, the peak of the structure factor shown by the red diamonds approaches the deterministic most unstable wavenumber from above (Mecke and Rauscher, 2005; Fetzer et al., 2007b; Nesic et al., 2015). Height-dependence of surface tension shifts the most unstable wavenumber to larger values and leads to an increase in the growth rate (see Fig. 1-7 (a) and 1-17 (b)); this leads to a shift in the peak and magnitude of the structure factor as shown in Fig. 1-19 (b).

1.7 Conclusions

We have shown, using a consistent thermodynamic framework, that the intermolecular forces between liquid–gas and liquid–solid interfaces of a thin film in the partial wetting regime lead to an expression for the system free energy with a height-dependent surface tension. In the long-wave approximation, this free energy resembles the Cahn–Hilliard formulation for the free energy of binary alloys (Cahn and Hilliard, 1958). We have shown that this new form of free energy leads to a generalized disjoining pressure that is consistent with recent calculations (Dai et al., 2008).

Using our model, we have revisited the dewetting and coarsening of thin liquid films on solid substrates in the partial wetting regime. We have first shown that the equilibrium droplet solutions obtained in the new model have compact support and meet the contact line with a non-zero equilibrium angle, whereas equilibrium droplets in the classical model only asymptotically meet the surrounding precursor film with a zero angle. While the classical model cannot admit solutions without a precursor film (Brenner and Bertozzi, 1993), our model does not require the precursor film, allowing us to recover the true partial wetting regime (Brochard-Wyart et al., 1991).

Analyzing the stability of uniform liquid films, we have shown that in the spinodal dewetting regime, our model predicts a faster growth rate β_m for the most unstable mode, and a smaller corresponding instability wavelength λ_m than those predicted by the classical model with a constant surface tension. While the instability wavelength is only weakly dependent on the height-dependence of the surface tension, we have shown that the instability growth rate can be up to six times faster than the predictions of the classical model. This faster growth rate brings the theoretical predictions closer to the experimental observations (Becker et al., 2003).

Experimental observations by Limary and Green (2003) indicate a crossover in the coarsening from Ostwald ripening-dominated to coalescence-dominated as the film thickness increases. They infer the coarsening mechanism from the droplet-size distribution, i.e., they associate the Ostwald ripening and coalescence processes with LSW-type and Smoluchowski-type distributions, respectively (Limary and Green,

2002, 2003; Green, 2003). Our nonlinear simulations of the dewetting and subsequent coarsening on large domains $L \sim 100\lambda_m$ have shown that the coarsening process at intermediate times becomes self-similar (Glasner and Witelski, 2003) and independent of the details of the models used, i.e., we observe the same scalings for the classical model (with and without thermal noise) and in our new model with height-dependent surface tension. We have shown that the crossover reported in the experiments cannot be observed in 1D simulations of the thin-film equation. This is in contrast to the predictions of Glasner and Witelski (2005), who used a reduced-order model of thin-film equation and predicted a crossover. As the thickness of the initial uniform film increases the instability mechanism changes from spinodal, (i.e., equally-distanced droplets after dewetting) to nucleation, (i.e., randomly-spaced droplets). This change in the instability mechanism is a result of the competition of two time scales: the growth rate of the instability, which scales as $\beta_m \sim \tilde{h}_0^{-5}$, versus the rate of lateral expansion of dewetted holes (Thiele et al., 2001b; Diez and Kondic, 2007). This change of instability mechanism from spinodal to nucleation prevents the crossover from Ostwald ripening-dominated to coalescence-dominated coarsening. We have also shown that while thermal noise enhances lateral motion of droplets, it does not lead to a crossover in the coarsening mechanism. We therefore conclude that the crossover observed in the experiments is a result of the 2D nature of the experiments versus the initial 1D simulations presented here and in earlier studies. To investigate this hypothesis, we have conducted 2D nonlinear simulations, which indeed indicate the dominance of coalescence events at early times following the dewetting and a crossover to Ostwald-ripening at late times in the coarsening process.

We also have shown that the droplet-size distribution in the self-similar coarsening regime follows a LSW-type distribution (Lifshitz and Slyozov, 1961; Wagner, 1961; Voorhees, 1985; Gratton and Witelski, 2009) and becomes model-independent at least for small droplets. For larger drops, we have found that the new model leads to a long-tailed drop-size distribution, which follows the Smoluchowski Eq. (1.47) in 1D for peripheral diffusion-dominated transport. Our observation of a skewed distribution associated with an Ostwald-ripening-dominated coarsening calls into question

the associations made before between the long-tailed distribution and coalescence-dominated coarsening in the earlier experiments (Limary and Green, 2002, 2003; Green, 2003) and motivates further detailed experimental observations.

An important open question is how to characterize the predicted height-dependence of surface tension in typical dewetting experiments. As we have shown, the characteristic instability wavelength, which is most readily observed in the experiments, is only weakly dependent on the height-dependence of surface tension and perhaps not a reliable indicator. The instability growth rate, however, varies more significantly due to the height-dependence of surface tension and could serve as a distinguishing factor. Experimental measurements of growth rate are exceptionally challenging, particularly in the spinodal regime and for very thin liquid films for which the height-dependence of surface tension becomes relevant. Further, the viscosity of thin polymer films changes drastically from its bulk values due to a shift in the glass transition temperature (Herminghaus et al., 2001), making it potentially difficult to distinguish between consequences of the changes in surface tension from those in viscosity. Spreading of droplets in the partial-wetting regime can therefore serve as an alternative test for the height-dependence of surface tension; we have shown that our new model allows investigations of the spreading process without the need for precursor films (Pahlavan et al., 2015). Visualization of the contact-line motion at micro/nano-scales (Chen et al., 2014; Qian et al., 2015; McGraw et al., 2016; Deng et al., 2016) could therefore lead the way in refining and validating models for interfacial flows.

Chapter 2

Moving contact lines in partial wetting

When a liquid touches a solid surface, it spreads to minimize the system's energy. The classic thin-film model describes the spreading as an interplay between gravity, capillarity and viscous forces, but cannot see an end to this process as it does not account for the non-hydrodynamic liquid–solid interactions. While these interactions are important only close to the contact line, where the liquid, solid and gas meet, they have macroscopic implications: in the partial-wetting regime, a liquid puddle ultimately stops spreading. We show that by incorporating these intermolecular interactions, the free energy of the system at equilibrium can be cast in a Cahn–Hilliard framework with a height-dependent interfacial tension. Using this free energy, we derive a mesoscopic thin-film model that describes statics and dynamics of liquid spreading in the partial-wetting regime. The height-dependence of the interfacial tension introduces a localized apparent slip in the contact-line region and leads to compactly-supported spreading states. In our model, the contact line dynamics emerge naturally as part of the solution and are therefore non-locally coupled to the bulk flow. Surprisingly, we find that even in the gravity-dominated regime, the dynamic contact angle follows the Cox–Voinov law.

A glass of water poured on a table spreads for a while and finally stops. This process seems simple enough to be described by a reduced-order model, and indeed the

classic thin-film model is a step in this direction (Oron et al., 1997; Craster and Matar, 2009). This model can be derived from the Stokes equations using the lubrication approximation, but it contains no information about the interactions between the liquid and the underlying solid surface. While these interactions are of non-hydrodynamic origin and only become significant at heights less than $\sim 100\,\mathrm{nm}$ (Israelachvili, 2011), they have pronounced macroscopic implications: the classic model, which does not incorporate these intermolecular interactions, predicts that the liquid never stops spreading, in stark contrast with the basic observation of a static puddle that forms in the partial-wetting regime.

A liquid is said to be partially wetting to a surface when it forms a contact angle in the range of $0 < \theta_Y \leq \pi/2$ at equilibrium. This equilibrium contact angle is well described by the Young equation, $\cos\theta_Y = (\gamma_{sg} - \gamma_{sl})/\gamma$, where γ_{sg}, γ_{sl} and γ are solid–gas, solid–liquid, and liquid–gas interfacial energies (de Gennes, 1985). To extend the classical description to the partial-wetting regime, one can supplement it with non-hydrodynamic interactions as a boundary condition at the contact line (Oron et al., 1997; Craster and Matar, 2009; Bonn et al., 2009). When capillary forces are the dominant driving mechanism, the dynamic contact angle, θ_d, follows the Cox–Voinov law, $\theta_d^3 = \theta_Y^3 + 9\mathrm{Ca}\ln(l_M/l_\mu)$ (Voinov, 1976; Cox, 1986; Bonn et al., 2009; Snoeijer and Andreotti, 2013), where $\mathrm{Ca} = \eta U/\gamma$ is the capillary number with liquid viscosity η and contact line velocity U; l_M and l_μ are characteristic macroscopic and microscopic length scales in the problem. Despite its success in matching experimental data, invoking this boundary condition does not address the question of how the non-hydrodynamic forces determine the emerging dynamics at the macroscopic scale.

90

2.1 A nonlinear Cahn–Hilliard equation

Here, we work within the long-wave approximation to derive a generalized meso-scopic thin-film equation that captures the dynamics of the moving contact line self-consistently as part of the solution, making it non-locally coupled to the rest of the system. Within the framework of non-equilibrium thermodynamics, a conservation equation for the height of the liquid film h can be written as (Hohenberg and Halperin, 1977; Cahn, 1961; Mitlin, 1993):

$$\frac{\partial h}{\partial t} = \nabla \cdot \left(\mathcal{M}(h) \nabla \left(\frac{\delta \Gamma}{\delta h} \right) \right), \tag{2.1}$$

where $\mathcal{M}(h)$ is the mobility, Γ is the free energy, and $\delta \Gamma / \delta h = \partial \Gamma / \partial h - \nabla \cdot [\partial \Gamma / \partial (\nabla h)]$ is the variational derivative of the free energy with respect to height. In Chapter 1, we showed how the free energy at equilibrium can be derived based on arguments using the calculus of variations and the requirement of a non-zero contact angle at the wall representing the true partial wetting regime.

Here, we present a summary of the derivations presented in Chapter 1 to arrive at the free energy at equilibrium. We start by deriving the free energy Γ of a non-volatile liquid puddle on a solid surface. At equilibrium, the variation of the free energy is zero, $\delta \Gamma = 0$. Writing the free energy as $\Gamma = \int \Phi(h, \nabla h) \, dX$ and using the calculus of variations, we arrive at the following two equations for the specific free energy Φ (Yeh et al., 1999; Starov et al., 2007; Arfken et al., 2013):

$$\frac{\partial \Phi}{\partial h} - \nabla \cdot \left(\frac{\partial \Phi}{\partial \nabla h} \right) = 0, \tag{2.2}$$

$$\left[\Phi - \nabla h \cdot \left(\frac{\partial \Phi}{\partial \nabla h} \right) \right]_{h=0} = 0, \tag{2.3}$$

known as the Euler–Lagrange and Augmented Young equations, respectively. Equation (2.2) determines the shape of the liquid surface at equilibrium and reduces to the Young–Laplace equation in the simplest form, while Eq. (2.3) serves as the boundary condition at the contact line.

Macroscopic contributions taken into account, we can write the free energy as $\Phi(h, \nabla h) \equiv \Phi_M(h, \nabla h) = 1/2\rho g h^2 + (\gamma_{sl} - \gamma_{sg}) + \gamma \sqrt{1 + (\nabla h)^2}$, in which ρ is the liquid density and g is the gravitational acceleration. The classic thin-film model can be recovered by putting the macroscopic free energy into the conservation Eq. (2.1). Substituting Φ_M into the Augmented Young equation, we recover the Young equation (de Gennes, 1985). An often-overlooked constraint on the free energy is that as the height of the liquid film goes to zero, one should recover the solid–gas interfacial energy, $\lim_{h \to 0} \Phi = 0$ (de Gennes, 1985; de Gennes et al., 2004). It is straightforward to see that the only way to satisfy this constraint with the macroscopic free energy is to have $\gamma + \gamma_{sl} = \gamma_{sg}$, corresponding to the complete-wetting regime.

Microscopic intermolecular forces close to the contact line must therefore be considered to arrive at a self-consistent description of the free energy for partial-wetting systems. These interactions are commonly known as surface forces (Derjaguin et al., 1987) or disjoining/conjoining pressure (Israelachvili, 2011). Taking the intermolecular forces $\Phi_\mu(h)$ into account, we can write the free energy as $\Phi(h, \nabla h) \equiv \Phi_M(h, \nabla h) + \Phi_\mu(h)$. Substituting into the Augmented Young equation, we arrive at what is commonly known as the Derjaguin-Frumkin equation, $\cos \theta_Y = \cos \theta_\mu + \Phi_\mu(0)/\gamma$, relating the Young contact angle to the surface forces (Yeh et al., 1999; Starov et al., 2007). The Young angle is defined at the macro scale, whereas θ_μ is the microscopic contact angle (de Gennes, 1985; Yeh et al., 1999; Pompe and Herminghaus, 2000), which needs to be zero for the free energy to be continuous. The combination of a non-zero Young contact angle and a zero microscopic contact angle indicates the existence of an ultra-thin liquid film around the main drop, the so-called pseudo-partial-wetting regime (Brochard-Wyart et al., 1991; Reiter et al., 1999; de Gennes et al., 2004). While precursor films are commonly observed in the complete-wetting regime (Kavehpour et al., 2003; Hoang and Kavehpour, 2011; Popescu et al., 2012), they are not in non-volatile partial-wetting liquids (Brochard-Wyart et al., 1991; de Gennes et al., 2004; Snoeijer and Andreotti, 2013). We therefore need a description of the system's free energy that allows for non-zero microscopic contact angles.

Traditionally, surface forces are expressed as a function of film height only, since

they are derived for parallel liquid–solid interfaces (Oron et al., 1997; Craster and Matar, 2009; Israelachvili, 2011). Close to the contact line, however, the liquid and solid interfaces are not parallel and one should account for the interface slope to arrive at a proper description of the intermolecular forces (Miller and Ruckenstein, 1974; Hocking, 1993; Kalliadasis and Chang, 1996; Wu and Wong, 2004; Dai et al., 2008). The free energy should therefore be written as $\Phi(h, \nabla h) \equiv \Phi_M(h, \nabla h) + \Phi_\mu(h, \nabla h)$. Consistent with the derivations of (Dai et al., 2008) and using the long-wave approximation, we propose to decompose the surface forces as $\Phi_\mu(h, \nabla h) = \phi_{\mu,1}(h) + \phi_{\mu,2}(h)(\nabla h)^2/2$. Substituting the free energy, Φ, into the Augmented Young equation and requiring the continuity of the free energy, it is straightforward to show that all constraints are satisfied without imposing any *a priori* condition on θ_μ if $\phi_{\mu,1}(0) = \mathcal{S}$ and $\phi_{\mu,2}(0) = -\gamma$, where $\mathcal{S} = \gamma_{sg} - \gamma_{sl} - \gamma$ is the spreading coefficient (de Gennes et al., 2004). The microscopic contact angle therefore emerges naturally as part of the solution, consistent with the predictions of nonlocal density functional theory (Snoeijer and Andreotti, 2008). We can therefore write the free energy as:

$$\Gamma = \int \left[f(h) + \kappa(h) \frac{(\nabla h)^2}{2} \right] dX. \tag{2.4}$$

This free energy expression resembles the Cahn–Hilliard formulation (Cahn and Hilliard, 1958), in which the free energy can be decomposed into bulk $f(h) = \rho g h^2/2 - \mathcal{S} + \phi_{\mu,1}(h)$ and interfacial $\kappa(h)(\nabla h)^2/2$ contributions, where $\kappa(h) = \gamma + \phi_{\mu,2}(h)$ can be interpreted as a height-dependent interfacial tension. A nonlinear KPZ-type term can be generated using this free energy (Kardar et al., 1986; Kardar, 2007). The constraints on $\phi_{\mu,1}(0)$ and $\phi_{\mu,2}(0)$ imply that $f(0) = 0$ and $\kappa(0) = 0$. Vanishing of the interfacial tension as the film height tends to zero is required to arrive at compactly-supported spreading states (Benzi et al., 2011; Cueto-Felgueroso and Juanes, 2012), and our derived form of the free energy naturally meets this requirement. Another constraint on $\phi_{\mu,1}(h)$ can be incorporated through a tangent construction on the bulk free energy, which ensures that the two coexisting phases at equilibrium have the same chemical potential (Rowlinson and Widom, 1982; Bray,
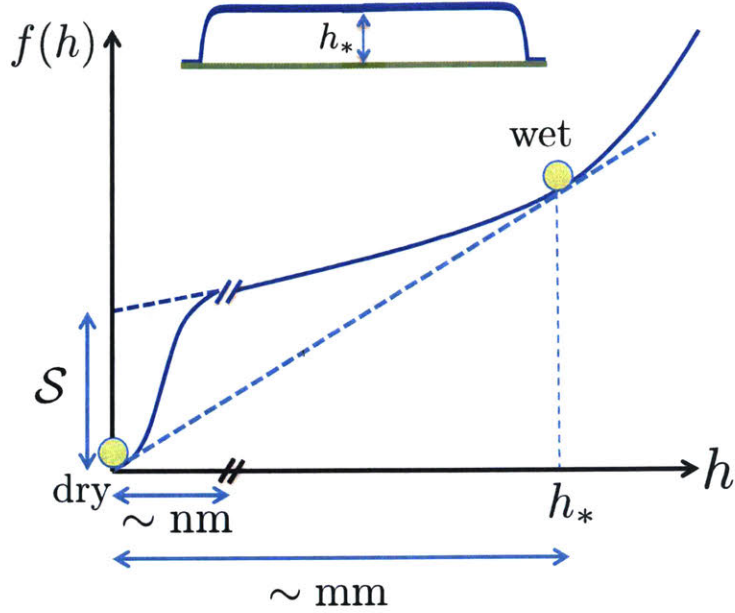
Figure 2-1: Schematic of the tangent construction on the bulk free energy, $f(h)$, leading to the coexistence of wet, $h = h_*$, and dry, $h = 0$, states. In the absence of intermolecular forces, the bulk free energy does not reduce to the solid–gas interfacial energy as $h \to 0$ unless $\mathcal{S} = 0$, which implies complete wetting (de Gennes et al., 2004).

1994), i.e. $df/dh|_{h=0} = df/dh|_{h=h_*} = \rho g h_*$ (Fig. 2-1), where $h_* = 2\,l_\gamma \sin(\theta_Y/2)$ is the height of the liquid puddle that is set by a balance between gravity and surface tension, and $l_\gamma = \sqrt{\gamma/\rho g}$ is the capillary length (de Gennes et al., 2004). To describe the functional form of $\phi_\mu(h)$, we use a surface force that consists of long-ranged attractive van der Waals forces and short-ranged repulsive forces, similar to an integrated Lennard-Jones potential (Israelachvili, 2011). Other such combinations (Sharma, 1993b,c; Pismen and Pomeau, 2000; Thiele et al., 2001b) can also be used. We therefore write $\phi_{\mu,i}(h) = \alpha_i \left[(1 + \beta_i)d_0^2/(h + d_0)^2 - \beta_i d_0^8/(h + d_0)^8\right]$, where $d_0 = \sqrt{\mathcal{A}/6\pi\gamma} \approx 0.2\,\text{nm}$ is a molecular length scale with $\mathcal{A}$ being the Hamaker constant (de Gennes et al., 2004; Israelachvili, 2011). The coefficients $\alpha_1 = \mathcal{S}$, $\beta_1 = (1 - d_0/h_*)/3$ and $\alpha_2 = -\gamma$, $\beta_2 = 1/3$ are determined through imposing the constraints on $\phi_{\mu,i}(0)$, the tangent construction, and requiring a non-zero slope at the contact line. The denominator has been regularized by adding d_0, allowing us to recover the solid–liquid interfacial energy when the film height is zero (Sharma, 1993b; de Gennes et al., 2004; Dai et al.,

2008).

Substituting the derived free energy from Eq. (2.4) back into the conservation Eq. (2.1) and nondimensionalizing the parameters as $\tilde{h} = h/h_*$, $\tilde{x} = x/R_f$, $\tilde{t} = t/(3\mu R_f^2/\rho g h_*^3)$, $\tilde{f} = f/\rho g h_*^2$, $\tilde{\kappa} = \kappa/\gamma$ and dropping the tilde for convenience, the generalized thin film equation takes the form:

$$\frac{\partial h}{\partial t} = \nabla \cdot \left\{ \mathcal{M}(h) \nabla \left[\frac{\partial f}{\partial h} - \frac{1}{\mathrm{Bo}} \sqrt{\kappa(h)} \nabla \cdot \left(\sqrt{\kappa(h)} \nabla h \right) \right] \right\}, \qquad (2.5)$$

in which $\mathrm{Bo} = R_f^2/l_\gamma^2$ is the Bond number, where R_f is the characteristic lateral length of the liquid, taken to be its final equilibrium radius. Vanishing of the interfacial tension $\kappa(h)$ at the contact line indicates that the order of the equation is reduced by one, pointing to a singular perturbation problem. This picture is consistent with the description suggested by de Gennes (de Gennes et al., 1990), indicating the dominance of intermolecular forces very close to the contact line, leading to a natural cut-off scale that removes the moving-contact-line singularity.

2.2 A localized slip boundary condition

Starting from the Stokes equation, using the lubrication approximation, and assuming no slip at the wall and zero shear stress at the liquid–gas interface, $\tau = 0$ (neglecting the viscosity of the gaseous phase), the mobility in Eq. (2.1) is easily derived to be $\mathcal{M}(h) = h^3$. The no-slip boundary condition, however, will lead to the moving-contact-line singularity (Huh and Scriven, 1971b; Dussan V. and Davis, 1974). To resolve the singularity, the Navier slip boundary condition is generally used, introducing a slip velocity proportional to the shear stress in the liquid adjacent to the wall, $u_s = b_s \nabla u$ (Neto et al., 2005; Lauga et al., 2007), where b_s is the slip length, which depends on the liquid–solid interaction (Granick et al., 2003; Huang et al., 2008; Bocquet and Charlaix, 2010). The slip condition leads to a mobility of the form $\mathcal{M}(h) = h^3 + 3\, b_s h^2$. In immiscible flows however, slip is localized to the contact-line region (Koplik et al., 1988; Thompson and Robbins, 1989; Freund, 2003; Qian et al., 2003, 2004, 2006; Ren and E, 2007; Ren et al., 2010) and to match the observations of molecular simulations, *ad hoc* functions with decaying slip away from contact line have been proposed (Dussan V., 1976; Zhou and Sheng, 1990; Hadjiconstantinou, 1999).

The free energy derived in Eq. (2.4) incorporates a height-dependent interfacial tension $\kappa(h)$. A gradient in the interfacial tension leads to the Marangoni effect (Scriven and Sterling, 1960; Levich and Krylov, 1969), which causes a non-zero shear stress at the liquid–gas interface, driving a net flow. The gradient in surface tension typically is caused by either temperature gradients (Cazabat et al., 1990) or a gradient in the concentration of surfactants (Craster and Matar, 2009). The resulting Marangoni flow can be utilized to pattern surfaces (Kim et al., 2016a; Darhuber and Troian, 2005), contribute to the spreading of bacteria on surfaces (Angelini et al., 2009), and its influence can be readily seen in the tears of wine (Hosoi and Bush, 2001).

In analogy with the Marangoni effect, we propose that the height dependence of the interfacial tension leads to a non-zero interfacial shear stress at the liquid–gas

interface. Therefore, we generalize the stress boundary condition at the interface to account for this additional stress:

$$([P]\mathbf{I} - [\mathbf{T}]) \cdot \mathbf{n} = (\gamma\mathcal{K} + \Phi)\,\mathbf{n} + \frac{\lambda^2}{\epsilon\gamma}\frac{\partial P}{\partial s}\left|\frac{\partial\kappa}{\partial s}\right|\mathbf{t}, \qquad (2.6)$$

where λ is a molecular length scale defined as $\lambda = \sqrt{\mathcal{A}/\gamma}$ with $\mathcal{A}$ as the Hamaker constant (de Gennes et al., 2004), and s represents the arc length of the interface. The new term on the right hand side represents the proposed tangential stress due to the height-dependence of surface tension. Note that we cannot simply set this term to be equal to the gradient in surface tension as is done for the case of Marangoni stresses in interfacial flows (Craster and Matar, 2009); otherwise, even at equilibrium there would be a flow due to the height-dependece of surface tension. The variation of the interfacial tension is limited to the contact line region where intermolecular forces dominate. Away from the contact line ($d\kappa/dh = 0$) or at equilibrium ($\partial P/\partial s = 0$), the stress balance reduces to the usual one (Oron et al., 1997; Craster and Matar, 2009). Only during spreading does this non-zero interfacial stress come into play, which is similar to the idea of "flow-induced Marangoni effect" (Shikhmurzaev, 1997, 2007; Sibley et al., 2012).

After non-dimensionalization, the tangential component of the stress boundary condition becomes:

$$\epsilon\tilde{h}_{\tilde{x}}\left[\tilde{\tau}_{xx} - \tilde{\tau}_{zz}\right] - \left(1 - \epsilon^2\tilde{h}_{\tilde{x}}^2\right)\left[\tilde{\tau}_{zx}\right] = \tilde{\lambda}^2\frac{\partial\tilde{P}}{\partial\tilde{x}}\left|\frac{\partial\tilde{\kappa}}{\partial\tilde{x}}\right|, \qquad (2.7)$$

The normal component of the stress boundary condition at the interface then becomes:

$$\left[\tilde{P}\right]\left(1 + \epsilon^2\tilde{h}_{\tilde{x}}^2\right) - \epsilon\left(\epsilon^2\tilde{h}_{\tilde{x}}^2\left[\tilde{\tau}_{xx}\right] - 2\epsilon\tilde{h}_{\tilde{x}}\left[\tilde{\tau}_{zx}\right] + \left[\tilde{\tau}_{zz}\right]\right) = -\frac{\tilde{h}_{\tilde{x}\tilde{x}}}{\sqrt{1 + \epsilon^2\tilde{h}_{\tilde{x}}^2}} + \tilde{\Phi}\left(1 + \epsilon^2\tilde{h}_{\tilde{x}}^2\right),$$

$$(2.8)$$

where $\tilde{\Phi} = \Phi/\left(\gamma H/L^2\right)$.

Using the above non-dimensionalization and long-wave approximation, $\epsilon \ll 1$,

and negligible inertia, $\epsilon \text{Re} \ll 1$, and surface tension-dominated flow, $\tilde{C}a = O(1)$, we find that the slip and kinematic boundary conditions remain unchanged under the lubrication approximation. The stress boundary condition however, simplifies further; the tangential component becomes:

$$[\tilde{\tau}_{zx}] = -\tilde{\lambda}^2 \frac{\partial \tilde{P}}{\partial \tilde{x}} \left| \frac{\partial \tilde{\kappa}}{\partial \tilde{x}} \right|, \tag{2.9}$$

and the normal component reduces to $[\tilde{P}] = -\tilde{h}_{\tilde{x}\tilde{x}} + \tilde{\Phi}$.

We can then integrate the x-momentum and apply the tangential stress and Navier slip boundary conditions to obtain the $x-$velocity component:

$$\tilde{u} = \frac{1}{\tilde{C}a} \frac{\partial \tilde{P}}{\partial \tilde{x}} \left(\frac{\tilde{z}^2}{2} - (\tilde{z} + \beta) \left(\tilde{\lambda}^2 \left| \frac{\partial \tilde{\kappa}}{\partial \tilde{x}} \right| + \tilde{h} \right) \right). \tag{2.10}$$

Integrating the continuity equation and using the kinematic boundary condition, we arrive at $(1/\tilde{C}a)\partial\tilde{h}/\partial\tilde{t} + \partial/\partial\tilde{x} \int_0^{\tilde{h}} \tilde{u}\,d\tilde{z} = 0$. Replacing the x-velocity component in the above equation we therefore arrive at the evolution equation for the height of the film:

$$\frac{\partial \tilde{h}}{\partial \tilde{t}} = \frac{\partial}{\partial \tilde{x}} \left\{ \left[\frac{\tilde{h}^3}{3} + \left(2\beta + \tilde{\lambda}^2 \frac{d\tilde{\kappa}}{d\tilde{h}} \left| \tilde{h}_{\tilde{x}} \right| \right) \frac{\tilde{h}^2}{2} + \left(\beta\tilde{\lambda}^2 \frac{d\tilde{\kappa}}{d\tilde{h}} \left| \tilde{h}_{\tilde{x}} \right| \right) \tilde{h} \right] \frac{\partial \tilde{P}}{\partial \tilde{x}} \right\}. \tag{2.11}$$

Comparing this equation with the gradient formulation of Eq. (1.22), we now can write the mobility as:

$$\mathcal{M} = \tilde{h}^3/3 + \left(2\beta + \tilde{\lambda}^2(d\tilde{\kappa}/d\tilde{h})|\tilde{h}_{\tilde{x}}| \right) \tilde{h}^2/2 + \left(\beta\tilde{\lambda}^2(d\tilde{\kappa}/d\tilde{h})|\tilde{h}_{\tilde{x}}| \right) \tilde{h} \tag{2.12}$$

The effective slip that we obtained in our proposed "flow-induced Marangoni effect" bears similarities with the ideas of slip due to the gradient of chemical potential close to the contact line (Ruckenstein and Dunn, 1977; Pismen and Rubinstein, 2001) and the generalized Navier boundary condition (Qian et al., 2003, 2004, 2006; Ren and E, 2007; Ren et al., 2010), where it is proposed that in the vicinity of the contact line, the uncompensated Young force, i.e. $\gamma(\cos\theta_Y - \cos\theta_d)$, where θ_d is the
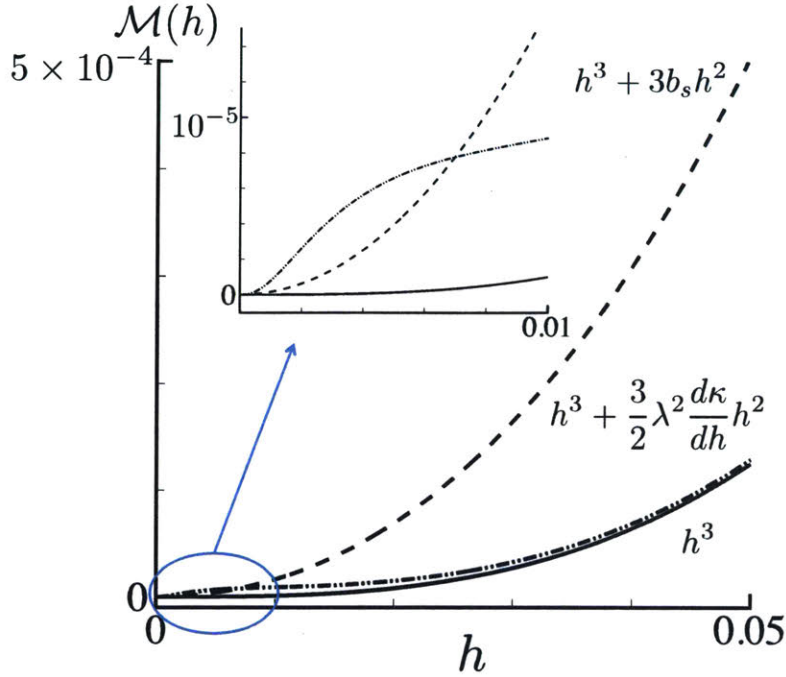
Figure 2-2: Comparison of the mobility with and without slip ($\mathcal{M}(h) = h^3$ solid line, $\mathcal{M}(h) = h^3 + 3b_s h^2$, $b_s = 10d_0$ dashed line, $\mathcal{M}(h) = h^3 + (3/2)\lambda^2(d\kappa/dh)h^2$, $\lambda = 10d_0$, $\theta_Y = \pi/12$ dash-dotted line). While Navier slip is global, our proposed slip model is localized to the contact-line region, where it dominates the Navier slip, consistent with molecular simulations (Koplik et al., 1988; Thompson and Robbins, 1989; Freund, 2003; Qian et al., 2003, 2004, 2006; Ren and E, 2007; Ren et al., 2010).

non-equilibrium dynamic contact angle, exerts an additional tangential stress on the fluid–fluid interface, leading to a generalized slip, which is dominated by this uncompensated Young force close to the contact line and recovers the Navier slip far away.

The height-dependent surface tension therefore introduces an effective slip mechanism that removes the moving contact line singularity (Huh and Scriven, 1971b; Dussan V. and Davis, 1974). While the Navier slip is global and defined in single-phase flows and only depends on the local velocity gradient, this new slip mechanism concerns multiphase flows and is localized in the contact-line region, consistent with earlier observations (Koplik et al., 1988, 1989; Thompson and Robbins, 1989; Freund, 2003; Qian et al., 2003, 2004, 2006; Ren and E, 2007; Ren et al., 2010). Our proposed model therefore addresses two main requirements regarding slip at the contact line: 1)

it is localized to the contact line region, and 2) it depends on the non-hydrodynamic interactions close to the contact line and introduces an energy scale (Snoeijer and Andreotti, 2013) (Fig. 2-2).

Further, the dependence of our proposed slip mechanism on the slope $|\tilde{h}_{\tilde{x}}|$ implies the dependence of the slip magnitude on the dynamic contact angle, i.e. a larger dynamic contact angle leads to a larger slip; this leads to a dynamic slip length that is larger the farther away from equilibrium the system is; it also implies that as the system approaches equilibrium, a larger equilibrium contact angle will lead to a larger slip, which is also consistent with earlier observations (Huang et al., 2008; Sendner et al., 2009; Bocquet and Charlaix, 2010). These are all interesting and important consequences that go far beyond the phenomenology of the Navier slip.

In our model, the slip velocity can be written as:

$$\tilde{u}_s = -\beta \frac{1}{\tilde{\mathrm{Ca}}} \frac{\partial \tilde{P}}{\partial \tilde{x}} \tilde{h} - \beta \frac{1}{\tilde{\mathrm{Ca}}} \frac{\partial \tilde{P}}{\partial \tilde{x}} \left(\tilde{\lambda}^2 \frac{d\tilde{\kappa}}{d\tilde{h}} \left| \frac{d\tilde{h}}{d\tilde{x}} \right| \right) , \tag{2.13}$$

where the first term is due to the regular Navier slip, and the second is the term localized to the contact line region and is the analog of the uncompensated Young force: it is also caused by a tangential stress at the fluid–fluid interface and goes to zero at equilibrium (Bonn et al., 2009). Further, while Navier slip removes the divergence of shear stress close to the contact line, it leads to a logarithmic pressure singularity; this singularity however can be removed in the presence of a non-constant surface tension (Sibley et al., 2014). Therefore, we expect our model to remove both the shear stress and pressure singularities in the classical hydrodynamic description of the moving contact lines.

2.3　Macroscopic dynamics

We solve Eq. (2.5) using standard finite differences (Diez et al., 2000) and adaptive mesh refinement. The disparate length scales involved in this problem make the numerical computations prohibitively expensive. Since we are mainly interested in the macroscopic predictions of our model, we regularize the microscopic length d_0 by multiplying it by a magnifying factor 10^4, therefore bringing the peak of the energy function shown in Fig. 2-1 from the nano to the micro scale. For simplicity, we set the Navier slip length to zero, $b_s = 0$, and consider only the localized effective slip in the contact-line region, $\lambda = 10d_0$ (Fig. 2-2). We take the capillary length to be $l_\gamma = 1.5$mm, which is typical of silicone oil.

We now address the original question of how a liquid puddle spreads on a solid surface. We expect a partial-wetting liquid to spread initially to minimize the system's free energy and to stop spreading when it reaches equilibrium. For small liquid volumes, i.e. when Bo $\lesssim$ 1, capillarity is the dominant driving force, leading to the Tanner's law for spreading, which predicts that the wetted area, $A(t)$, scale as $t^{1/5}$ (Tanner, 1979) (Fig. 2-3). As the volume of the liquid increases, i.e. Bo $\gg$ 1, gravity becomes the dominant driving force in the bulk while surface tension effects remain limited to the vicinity of the moving contact line (Lopez et al., 1976; Huppert, 1982a; Hocking, 1983). Balancing the gravity and viscous forces acting at the macroscopic scale, one arrives at a scaling of $t^{1/4}$ for the wetted area. In this regime, the spherical-cap approximation is no longer valid, but similarity solutions for the quasi-static spreading can still be obtained (Huppert, 1982a; Hocking, 1983). In both the capillary and gravity-dominated regimes, the final approach to equilibrium is exponential (Hocking, 1983; de Ruijter et al., 1999), deviating markedly from the quasi-static self-similar power-law behavior. Our model predicts this final approach to a compactly-supported spreading state (Fig. 2-3).

While the macroscopic spreading rate is a good measure for examining the validity of our model, it is not very sensitive to the contact line dynamics, which arrest the spreading drop as it approaches equilibrium. In the capillary-dominated regime,
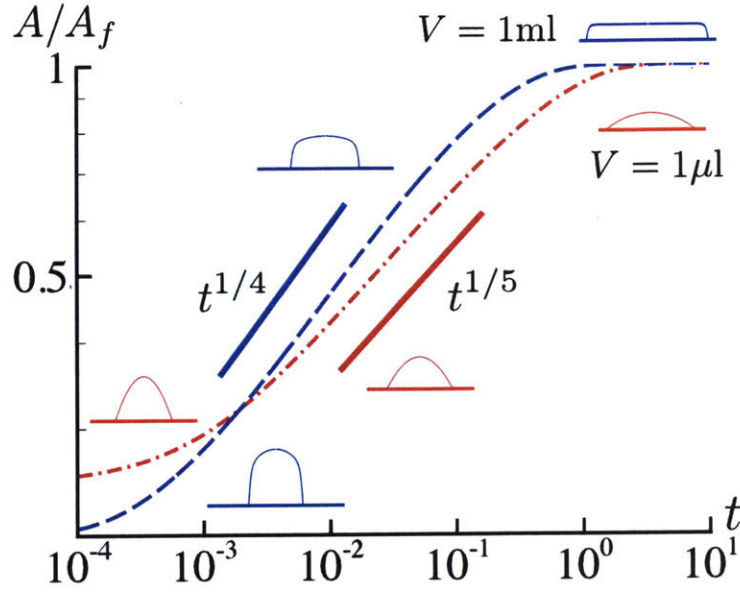
Figure 2-3: The rate of spreading is influenced by the volume of liquid. For small volumes (Bo $\lesssim$ 1, red dash-dotted line), capillary forces are dominant and the drop takes the shape of a spherical cap while viscosity resists the spreading, leading to the Tanner's law $A \sim t^{1/5}$. For large volumes (Bo $\approx$ 360, blue dashed line), gravity dominates, leading to a $t^{1/4}$ scaling; the liquid puddle takes the shape of a pancake at equilibrium. A_f is the final equilibrium area and $\theta_Y = \pi/12$.

the Cox–Voinov law describes the dependence of the dynamic contact line on the spreading rate (Voinov, 1976; Cox, 1986; Bonn et al., 2009; Snoeijer and Andreotti, 2013). Our model indeed displays an excellent agreement with the Cox–Voinov law for different equilibrium contact angles θ_Y [Fig. 2-4(b)]. Consistent with earlier observations (Chen, 1988; Reznik and Yarin, 2002), the dynamic contact angle exhibits a dependence on the liquid volume. This dependence is expected, as the macroscopic length l_M in the Cox–Voinov law is related to the radius of the drop (Eggers and Stone, 2004; Bonn et al., 2009), which scales with its volume ($R_f \sim V^{1/3}$ in the capillary-dominated regime and $\sim (V/h_*)^{1/2}$ in the gravity-dominated regime). The surprising observation, however, is that the Cox–Voinov law provides an excellent description of the dynamic contact angle even in the gravity-dominated regime. This observation is supported by early experiments in the complete-wetting regime (Redon et al., 1992). The macroscopic length scale, l_M, increases with volume and thus with the Bond number, but saturates to a constant value (proportional to the capillary
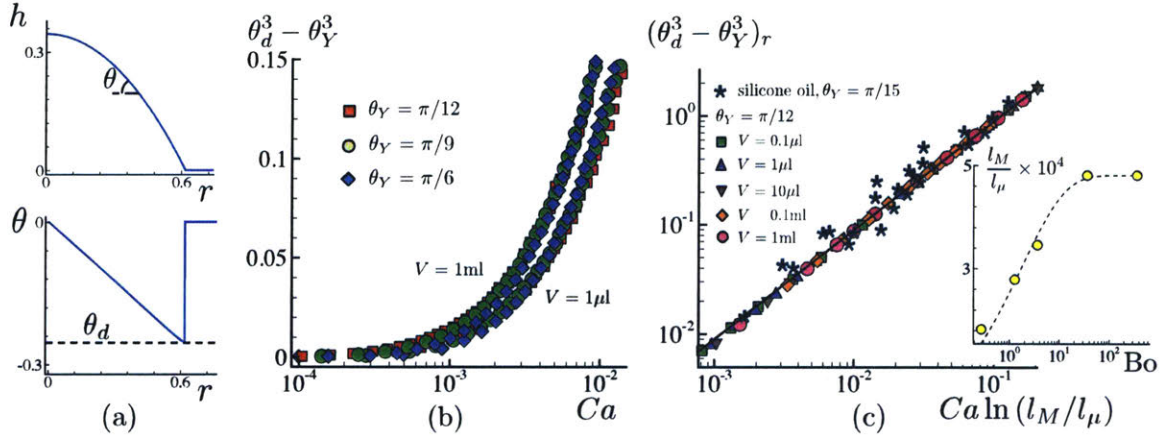
Figure 2-4: (a) The dynamic contact angle is defined at the inflection point of the drop profile (top), where its slope (bottom) reaches a plateau ($\tan\theta = (h_*/R_f)(dh/dr)$). (b) The dynamic contact angle, θ_d, follows the Cox–Voinov law $\theta_d^3 - \theta_Y^3 = 9\mathrm{Ca}\ln(l_M/l_\mu)$, but increases with the volume of the liquid. (c) The non-local influence of bulk flow can be conflated into the macroscopic length scale, l_M, leading to a collapse of the dynamic contact angle data for the different volumes onto a single curve (solid line represents the Cox–Voinov law). The stars represent the classic experiments of (Hoffman, 1975b; Fermigier and Jenffer, 1991b) corresponding to the silicone oil-air interface in a capillary tube ($l_M/l_\mu \approx 1.25 \times 10^3$). The rescaled contact angle data from the model accounts for the fact that the microscopic length scale l_μ is magnified by 10^4 in the simulations: $(\theta_d^3 - \theta_Y^3)_r = \theta_d^3 - \theta_Y^3 + (9\ln 10^4)\mathrm{Ca}$, (inset: an approximate fit $l_M/l_\mu = 4.8 \times 10^4 \times (1 - \exp(-0.75\mathrm{Bo}^{1/2}))$ is shown as the dashed line)

length) beyond the transition from capillary-dominated to gravity-dominated regime (at Bo $\approx$ 30). Taking the effective slip length to be the microscopic length scale $l_\mu = \lambda$, we find the macroscopic length scale l_M by fitting the dynamic contact angle data to the Cox–Voinov law ($l_M \approx 100\,\mu$m in the gravity-dominated regime). Taking the dependence of the macroscopic length scale on the volume into account, we observe a remarkable collapse of all the dynamic contact angle data corresponding to different volumes onto a single curve [Fig. 2-4(c)].

In summary, we have shown that incorporating non-hydrodynamic interactions between the liquid and solid in a self-consistent manner leads to a free energy that can be cast in a Cahn–Hilliard formulation with a height-dependent interfacial tension. This height-dependence allows compactly-supported spreading states with no precursor film (Benzi et al., 2011; Cueto-Felgueroso and Juanes, 2012), in contrast

with the classic thin-film model that does not admit such solutions (Brenner and Bertozzi, 1993). The height-dependence of the interfacial tension further introduces an effective slip that is localized to the contact-line region, where it dominates the Navier slip, consistent with the observations of molecular simulations (Koplik et al., 1988; Qian et al., 2003). Our thin-film model predicts that the dynamic contact angle follows the Cox–Voinov law both in the capillary-dominated and gravity-dominated regimes. This feature illustrates the ability of our mesoscopic model to capture nonlocal effects on the contact line dynamics, which exert a fundamental control on pattern formation in immiscible porous media flows (Martys et al., 1991; Geromichalos et al., 2002; Levaché and Bartolo, 2014).

2.4 Bridging the gap across the scales

The classical hydrodynamic description of the immiscible flows breaks down at the contact line where the two immiscible fluids meet the solid surface, predicting divergent stresses and leading to the conclusion that "even Heracles cannot sink a solid" (Huh and Scriven, 1971b; Dussan V. and Davis, 1974; Kirkinis and Davis, 2013). This early observation led to a long endeavor in search for the physical non-hydrodynamic mechanisms that resolve this paradox (Bonn et al., 2009; Snoeijer and Andreotti, 2013). Two descriptions at different scales prevail, i.e. the hydrodynamic and molecular descriptions.

The hydrodynamic description assumes that the microscopic contact angle θ_μ (see Figure 2-5) is not influenced by the flow and is equal to Young contact angle defined as $\cos\theta_Y = (\gamma_{sg} - \gamma_{sl})/\gamma$, where γ_{sg}, γ_{sl} and γ are solid-gas, solid-liquid, and liquid-gas interfacial energies (Young, 1805; de Gennes, 1985). Note that we use θ_Y and θ_{eq} interchangeably throughout this thesis. Experimental observations however indicate that microscopic features of the contact line are indeed influenced by the flow (Ramé et al., 2004; Eggers and Stone, 2004) and cannot be assumed constant a priori. The moving contact line singularity is also removed by introducing slip (Lauga et al., 2007). While slip is observed in single-phase flows at nanometric scales and can be well described using Navier law (Barrat and Bocquet, 1999; Zhu and Granick, 2001), its physical origin is different in immiscible flows as it is very localized to the contact line region (Koplik et al., 1988, 1989; Thompson and Robbins, 1989; Hadjiconstantinou, 1999; Qian et al., 2003, 2004, 2006; Ren and E, 2007; Ren et al., 2010; Qian et al., 2015). Using these simplifying assumptions, hydrodynamic theory then relates the dynamic contact angle θ_d away from the contact line to θ_μ using asymptotic matching, resulting in the Cox-Voinov law $\theta_d^3 = \theta_\mu^3 + 9\mathrm{Ca}\ln(l_M/l_\mu)$ (Voinov, 1976; Cox, 1986; Bonn et al., 2009; Snoeijer and Andreotti, 2013), where $\mathrm{Ca} = \mu U/\gamma$ is the capillary number with liquid viscosity μ and contact line velocity U; l_M and l_μ are characteristic macroscopic and microscopic length scales in the problem . The dynamic contact angle is then used as an effective boundary condition cutting off the inner region
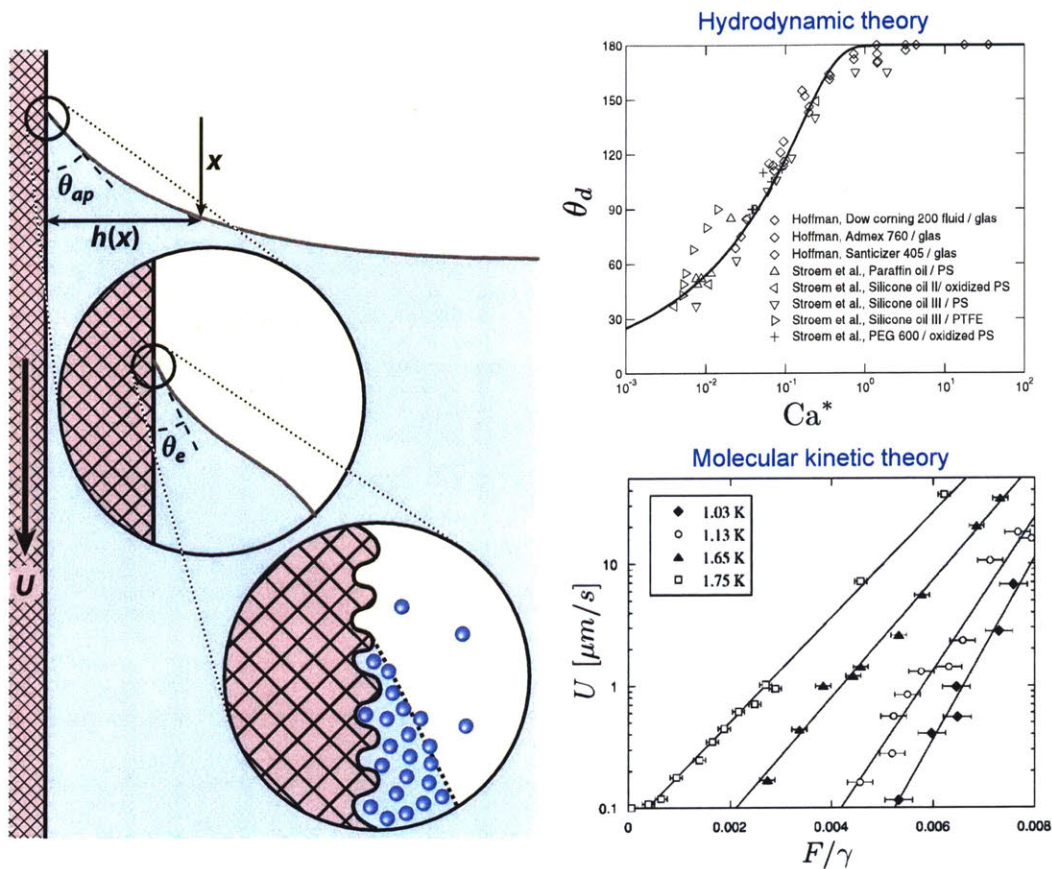
Figure 2-5: Moving contact lines are intrinsically multiscale: the left column shows a schematic of the contact line structure next to a moving plate (Snoeijer and Andreotti, 2013); macroscopically, the interface bends due to the viscous flow leading to an apparent or dynamic contact angle ($\theta_{\mathrm{ap}} = \theta_d$); in the vicinity of contact line, however, the angle is assumed to be equal to its equilibrium value $\theta_e = \theta_{eq}$; this assumption, however, has been shown not to be accurate (Thompson and Robbins, 1989; Ramé et al., 2004; Eggers and Stone, 2004); at the nanometric scale, the interface becomes diffused and the surface roughness may also become relevant. The macroscopic angle is well described by the hydrodynamic theory as described by the Cox–Voinov law and matches the experimental observations (Bonn et al., 2009). On the molecular scale, however, the molecular kinetic theory (Blake and Haynes, 1969; Blake, 2006) describes the motion of contact line as an activated process driven by the unbalanced Young force, leading to an exponential dependence of contact line velocity on the contact line force as exemplified here for the case of liquid helium being dragged on a cesium substrate (Prevost et al., 1999).

close to the contact line from the solution (Sui et al., 2014). While this approach is tempting due to its simplicity, it suffers from the above mentioned inconsistencies.

At nano-scale, behavior of the contact line can be described using the molecular
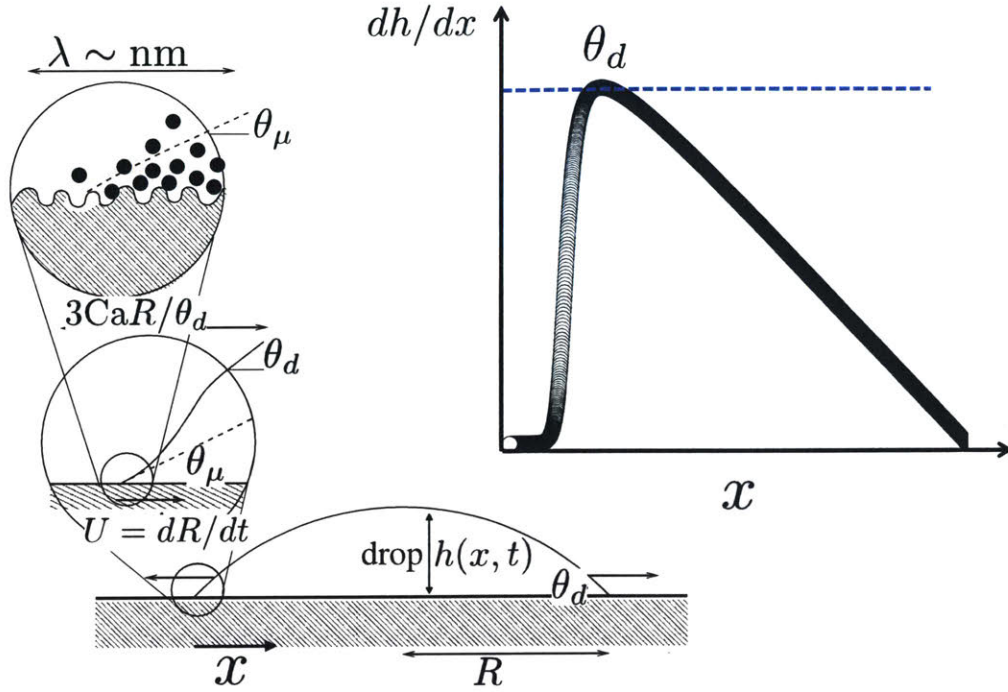
Figure 2-6: A schematic of the drop profile in the hydrodynamic framework (Bonn et al., 2009). Here, only one inflection point, where curvature becomes zero, exists in the profile, at which the dynamic contact angle θ_d is defined. The microscopic contact angle θ_μ is assumed to be equal to the equilibrium value.

kinetic theory that is based on the idea of a local activated process (Blake and Haynes, 1969; Blake, 2006; Seveno et al., 2009; Ramiasa et al., 2013). This theory results in a very different scaling of the contact angle with the contact line velocity, i.e. $\sinh(\cos\theta_Y - \cos\theta_w) \sim$ Ca, which for small capillary numbers can be linearized to recover the scaling obtained by balancing dissipation mechanisms at the contact line using the idea of uncompensated Young force $(\cos\theta_Y - \cos\theta_w) \sim$ Ca (Brochard-Wyart and de Gennes, 1992). These scalings are also observed in molecular dynamic simulations (Qian et al., 2003, 2004, 2006; Ren and E, 2007; Ren et al., 2010). The idea of an activated motion in the vicinity of the contact line has also been recently tested using AFM experiments (Guan et al., 2016).

Realizing the fact that the hydrodynamic and molecular descriptions act at different scales, patching the two by assuming $\theta_\mu = \theta_w$ seems to be a reasonable proposal (Petrov and Petrov, 1992; Lhermerout et al., 2016). In this work however, we put
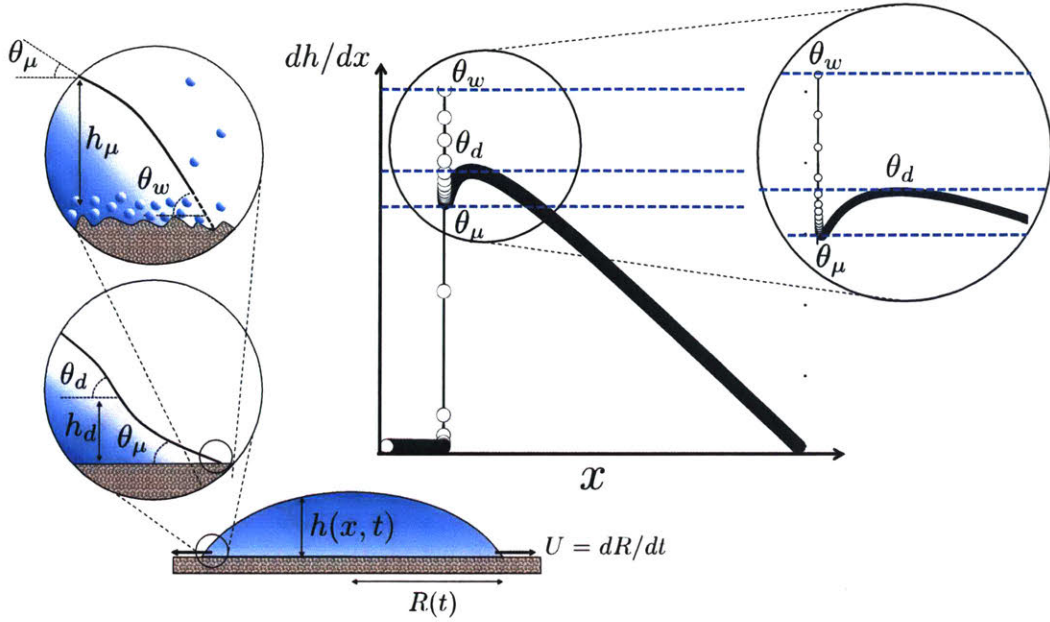
Figure 2-7: A schematic of the multiscale structure of the profile close to the moving contact line as obtained in our model. Here, two inflection points appear in the interface structure in the vicinity of the contact line. The first zoomed-in view of the profile shows the macroscopic inflection point, where the dynamic angle θ_d is defined. The dynamic angle connects to the microscopic angle, which is assumed to be equal to the equilibrium angle in the hydrodynamic picture. The second zoomed-in view shows that the microscopic angle in our model is a second inflection point connecting the macroscopic and microscopic frameworks. The contact line meets the wall at a non-zero angle θ_w. This picture is consistent with the recent AFM observations of the moving contact lines at the nano-scale (Chen et al., 2014).

forward a mesoscopic model that bridges the gap between these two descriptions. We show in a self-consistent manner that proper description of the system naturally leads to the emergence of a "missing link" between the two descriptions consistent with the Atomic Force Microscopy observations (Chen et al., 2014). Our model shows that θ_μ follows a similar scaling with Ca as θ_d does, thereby velocity-dependence of θ_μ is screened leading to an excellent match between the Cox-Voinov law with $\theta_\mu = \theta_Y$ and experimental observations (Hoffman, 1975b; Bonn et al., 2009). On the other hand, θ_w follows a scaling similar to that proposed in the molecular kinetic theory (Blake and Haynes, 1969; Blake, 2006), which indeed points to the fact that our mesoscopic model can capture the underlying physics of the moving contact line across the scales.

We now start looking at predictions of this equation through simulations of ax-

isymmetric drop spreading, varying the equilibrium contact angle and volume of the liquid. To resolve the detailed structure of the contact line, we use adaptive mesh refinement together with standard finite difference techniques Diez et al. (2000). In the classical hydrodynamic picture (Fig. 2-6), viscous forces lead to the bending of the interface in the vicinity of the contact line, creating an inflection point, where the curvature is zero. The dynamic, or apparent angle is typically defined at this point. The microscopic angle is further assumed to be equal to the equilibrium value $\theta_\mu = \theta_{eq} = \theta_Y$. Our model, in which the effective surface tension becomes height-dependent, however, leads to a more complex structure of the interface in the vicinity of the moving contact line. Here, two inflection points appear in the structure (Fig. 2-7). One of the inflection points is due to the viscous bending of the interface, where the dynamic angle is defined θ_d, consistent with the hydrodynamic theory. While in the hydrodynamic picture, the profile smoothly meets the surrounding precursor film with a zero angle (Fig. 2-6), the height-dependence of surface tension allows the profile to meet the surrounding film at a non-zero angle (Alizadeh Pahlavan et al., 2018a). The presence of this non-zero angle at the contact line leads to a more complex structure of the contact line, in which the microscopic angle θ_μ becomes a second inflection point, connecting the macroscopic part of the profile (θ_d) to the microscopic part (θ_w).

This second inflection point therefore provides a "missing link" between the macroscopic and microscopic pictures as also observed recently in AFM experiments probing moving contact lines at the nano-scale (Chen et al., 2014). This observation allows us to go beyond the ad-hoc patching of the two descriptions as proposed by Petrov and Petrov (1992) to a reconciled picture, where the two descriptions naturally arise at different length scales. This new picture is also consistent with the arguments of de Gennes et al. (1990), where he proposed that the intermolecular forces introduce a natural cut-off length, removing the contact line singularity even without slip. In our model, the length scales corresponding to the new inflection point, where θ_μ is defined, provide this cut-off length scale. On length scales larger than h_μ, the hydrodynamic description applies, and the point h_μ serves as a boundary condition for

this description; since $h_\mu > 0$, the contact line singularity is therefore removed from the hydrodynamic description. On scales smaller than h_μ, the molecular description becomes applicable and the contact line moves with a diffusive motion as we discuss later.

To gain further insight into the dynamics of the moving contact line, we can probe the evolution of the heights of the inflection points, where the dynamic and microscopic angles are defined. Here, we allow a precursor film to surround the drop to avoid numerical issues with the positivity preserving of the solution (Zhornitskaya and Bertozzi, 1999); the presence of this film does not influence the structure of the contact line (Alizadeh Pahlavan et al., 2018a). Far from equilibrium, as a drop starts spreading, two inflection points exist in the structure of the contact line (Fig. 2-8 (a)). Here, we observe that while the microscopic height h_μ remains nearly constant in time, the dynamic height h_d decreases in time as drop spreads and gets closer to its equilibrium position. The rate of spreading of the drop decays in time, indicating that the viscous forces weaken in time. Viscous forces lead to the bending of the interface and appearance of the hydrodynamic inflection point, where θ_d is defined (Cox, 1986; Bonn et al., 2009). As the viscous forces become weaker, this viscous bending point becomes closer and closer to the contact line, finally leading to the dynamic branch merging with the microscopic branch. This is a point, where the two inflection points merge. We identify this first regime as the *hydrodynamic regime*, where viscous forces are dominant and a well-defined dynamic angle exists at a macroscopic length scale.

Beyond the merger of the two branches, no inflection points exist in the contact line structure as shown in (c). Here, the point of minimum non-zero curvature can be identified as the continuation of the merged dynamic-microscopic branches. This branch finally meets the h_w branch very close to the equilibrium, where the curvature becomes nearly constant everywhere as shown in (d). We identify this second regime as the *molecular regime*, in which the three length scales identified above all enter the nanometric length scale, indicating that viscous, surface tension, and intermolecular forces become of the same order.

We can further probe the evolution of the contact angles as drop spreads and
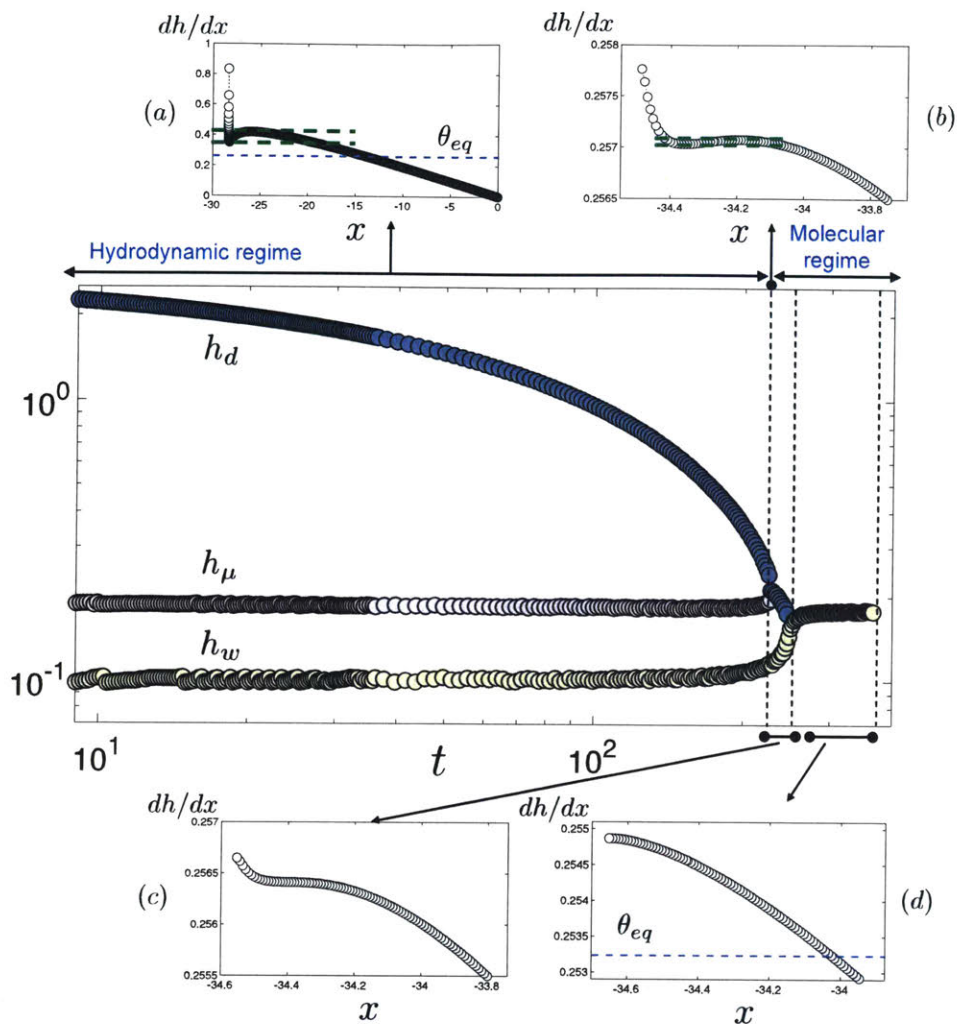
Figure 2-8: Evolution of the heights corresponding to the dynamic, microscopic, and wall angles as defined by h_d, h_μ, and h_w, respectively (Fig. 2-7). (a) In the first regime, far from equilibrium, two inflection points can be identified. In this hydrodynamic regime, the dynamic angle can be identified at a macroscopic distance from the contact line. As drop spreads, the viscous forces weaken farther away from the contact line, leading to a decrease in the dynamic height, which eventually leads to the merger of the dynamic and microscopic branches as shown in (b). Beyond the merger of the two branches, no inflection points exist in the contact line structure as shown in (c). Here, the point of minimum non-zero curvature can be identified as the continuation of the merged dynamic-microscopic branches. This branch finally meets the h_w branch very close to the equilibrium, where the curvature becomes nearly constant everywhere as shown in (d). In this molecular regime, the only identifiable angle is the wall contact angle. This picture therefore suggests that while both hydrodynamic and molecular mechanisms are at play during the entire evolution, the dominant mechanism evolves in time: (i) the dynamics farther away from the equilibrium, when viscous forces are strong on macroscopic scalae, is described by the hydrodynamic picture; (ii) at late times, when viscous forces become weak and only matter at microscopic scales, the balance is between viscous and intermolecular forces, leading to a molecular regime.

compare and contrast it with the hydrodynamic and molecular descriptions. Figure 2-9 (a) shows that all three identified contact angles, dynamic θ_d, microscopic θ_μ, and wall θ_w evolve in time and are distinct functions of the spreading rate as identified by the capillary number.

We expect the dynamic angle to follow the hydrodynamic description as described by the Cox–Voinov law. Figure 2-9 (b) shows that the data corresponding to four different equilibrium contact angles can be collapsed on a curve using the scaling $\theta_d^3 - \theta_{eq}^3 \sim$ Ca. In the hydrodynamic framework, the microscopic angle is considered to be fixed and equal to the equilibrium angle, leading to the description $\theta_d^3 - \theta_\mu^3 = \theta_d^3 - \theta_{eq}^3 \sim$ Ca. Our observations indicate that the microscopic angle is not fixed and deviates from the equilibrium angle. In fact, we find that the microscopic angle follows the same cubic scaling as the dynamic angle, only with a smaller prefactor indicating a weaker deviation from the equilibrium value, i.e. $\theta_\mu^3 - \theta_{eq}^3 \sim$ Ca. Therefore, even with this non-constant microscopic angle, we can recover the Cox–Voinov scaling, i.e. $\theta_d^3 - \theta_\mu^3 \sim \theta_d^3 - \theta_{eq}^3 \sim$ Ca. This observation explains why using a fixed equilibrium angle at the wall in the hydrodynamic picture as represented by the Cox–Voinov model works well.

We, however, find that the wall angle θ_w follows a scaling different from that of the hydrodynamic theory. In the vicinity of contact line the effective surface tension goes to zero. This implies that the thin film equation governing the flow (Eq. (2.5)) can be approximated as:

$$\frac{\partial h}{\partial t} \sim \nabla^2 \left(\frac{df}{dh} \right), \tag{2.14}$$

which is effectively a diffusion equation, in which diffusion is set by the intermolecular forces. This is similar to the idea of diffusive motion of the contact line in the diffuse interface methods (Seppecher, 1996; Anderson et al., 1998; Jacqmin, 1999, 2000; Chen et al., 2000; Qian et al., 2003, 2004; Yue et al., 2004; Briant et al., 2004a; Qian et al., 2006; Ding and Spelt, 2007; Khatavkar et al., 2007; Yue et al., 2010; Xu and Qian, 2010; Yue and Feng, 2011; Sibley et al., 2013; Kusumaatmaja et al., 2016), which lead
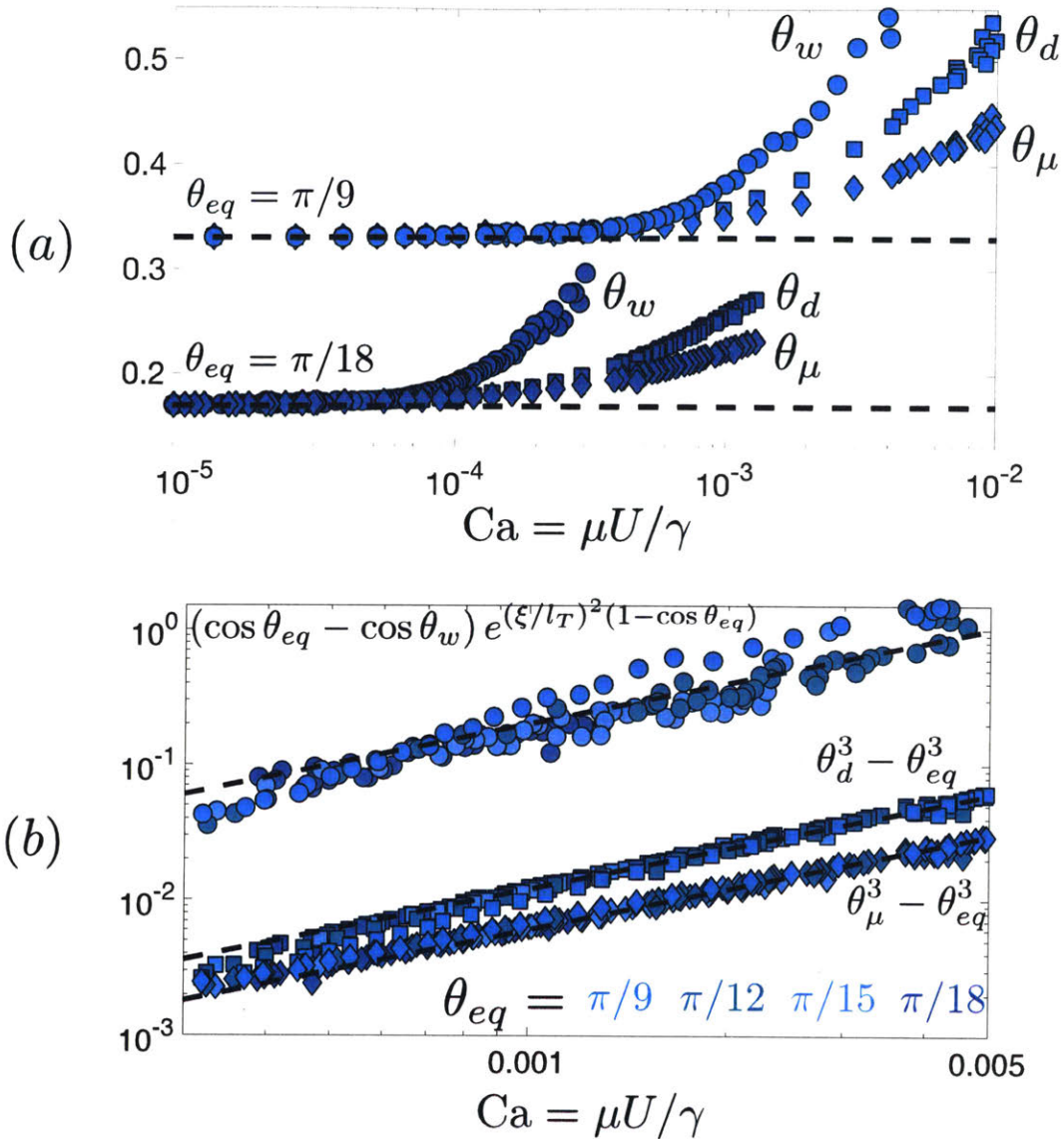
Figure 2-9: Evolution of the dynamic θ_d, microscopic θ_μ, and wall θ_w contact angles as a function of contact line speed Ca. (a) The three angles follow distinct branches and as spreading comes to a stop near equilibrium, they all become equal to the equilibrium contact angle. Note that as described in Fig. fig:InflectionPoints, the dynamic and microscopic branches merge when the two inflection points disappear. (b) We observe that the dynamic and microscopic angles both follow a cubic scaling consistent with the hydrodynamic description and Cox–Voinov law and collapse the data corresponding to four different equilibrium contact angles. The wall angle, however, follows a different scaling and can be collapsed using the scaling of the molecular kinetic theory using $(\xi/l_T)^2 \approx 40$.

to a scaling

$$\cos\theta_{eq} - \cos\theta_w \sim \mathrm{Ca}\zeta/l_s \tag{2.15}$$

where ζ is the diffuse interface width and l_s is the slip length, which here is taken to be of the order of the diffusion length l_D (Snoeijer and Andreotti, 2013).

The diffusive description of the moving contact line is analogous to the linearized version of the molecular kinetic theory, which considers the contact line motion as a thermally activated process. Here, we briefly review the derivation of the molecular kinetic theory (Blake and Haynes, 1969; Blake, 2006; De Coninck and Blake, 2008; Duvivier et al., 2013; Snoeijer and Andreotti, 2013). The liquid molecules in the vicinity of the contact line need to overcome an energy barrier E^* to move. In a thermally activated process, the frequency of crossing the energy barrier is set by the reaction rate theory (Hänggi et al., 1990): $\nu = \nu_0 \exp\left(-E^*/k_BT\right)$, where $\nu_0 \sim k_BT/\hbar$ is the attempt frequency with $\hbar$ as the Planck's constant. The contact line velocity can therefore be estimated as $U = \xi(\nu_+ - \nu_-)$, where ξ is the activation length, and $\nu_\pm$ are the crossing frequencies in the forward and backward directions. Disorder is always present on real surfaces, therefore relating the activation length to the pinning sites and the energy barrier to the "rugged energy landscape" of the surface (Giacomello et al., 2016; Perrin et al., 2016, 2018b,a). Away from equilibrium, the contact line is driven by the unbalanced Young force $F = \gamma\xi(\cos\theta_{eq} - \cos\theta_w)$, tilting the energy barrier $\nu_\pm = \nu_0 \exp\left(-(E^* \pm F\xi/2)/k_BT\right)$. The contact line velocity can therefore be written as:

$$U = 2\nu_0\xi \exp\left(-\frac{E^*}{k_BT}\right) \sinh\left(\left(\frac{\xi}{l_T}\right)^2 (\cos\theta_{eq} - \cos\theta_w)\right), \tag{2.16}$$

where $l_T = \sqrt{k_BT/\gamma}$ is the thermal length scale.

To relate the molecular kinetic theory to the macroscopic properties of the liquid, we can use the Eyring's equation for the viscosity of simple liquids (Blake and

De Coninck, 2011; Snoeijer and Andreotti, 2013):

$$\mu = \frac{k_B T}{\nu_0 \xi^3} \exp\left(\frac{E_\mu}{k_B T}\right), \tag{2.17}$$

where E_μ represents the liquid-liquid interaction energy. Using this definition of the liquid viscosity together with the linearized version of the molecular theory Eq. (2.16) we then arrive at:

$$\text{Ca} = (\cos\theta_{eq} - \cos\theta_w)\exp\left(\frac{E_\mu - E^*}{k_B T}\right), \tag{2.18}$$

in which $E_\mu \sim 2\gamma\xi^2$ and $E^* \sim \gamma\xi^2(1 + \cos\theta_{eq})$ (Blake and De Coninck, 2011), leading to

$$\text{Ca} = (\cos\theta_{eq} - \cos\theta_w)\exp\left(\left(\frac{\xi}{l_T}\right)^2(1 - \cos\theta_{eq})\right), \tag{2.19}$$

which can be interpreted as an effective boundary condition on the molecular scale. It is easy to see that both Eqs. (2.15) and (2.19) can be written in a general simplified form as:

$$(\cos\theta_{eq} - \cos\theta_w)/\chi \sim \text{Ca}, \tag{2.20}$$

which relates the contact line velocity to the driving unbalance Young force with χ representing a friction coefficient.

We use the scaling of the molecular theory for the wall contact angle data as shown in Fig. 2-9, which indeed seems to collapse the data corresponding to four different equilibrium contact angles. This observation is consistent with the diffusive dynamics of the wall angle in diffuse interface methods as well as in molecular dynamic simulations (Thompson and Robbins, 1989; Qian et al., 2003, 2004, 2006; Ren and E, 2007; Ren et al., 2010).

Our model therefore reconciles the hydrodynamic and molecular frameworks and bridges the gap in our understanding of the moving contact lines. We observed that both descriptions are valid throughout the spreading process with the dynamic and microscopic angles following the hydrodynamic description of Cox–Voinov law and the wall angle following the molecular theory. At early times, the viscous forces are dominant, leading to a macroscopic dynamic height corresponding to the viscous

bending of the interface. This height keeps decreasing in time as drop gets closer to its equilibrium state and the spreading slows down, weakening the viscous forces. At late times, this macroscopic height merges with the microscopic height, which is accompanied by the merger of the two inflection points in the contact line structure. At late times, no inflection points exists in the structure and only the wall angle is defined next to the contact line. In this molecular regime, the intermolecular forces become of the same order as surface tension and viscous forces.

Part II

Wetting transition, entrainment and instability

Chapter 3

Wetting transitions in confined environments

Here, we propose a phase diagram for wetting transition, entrainment, and instabilities in confined domains. We discuss the parallels between the interfacial instabilities in confined and unconfined geometries and point out to the differences. Overall, we show that the topic of pattern formation in confined domains in the presence of moving contact lines is largely unexplored and promises to be an exciting field of research with a very rich underlying physics. This chapter serves to review the exiting experimental observations and theoretical models and motivate new studies to address the unexplored areas.

119

3.1 Withdrawing a plate from a liquid bath: liquid entrainment

When a solid plate is withdrawn from a liquid bath that is perfectly wetting to the solid surface, a film of the liquid is entrained on the plate. This process was first described by Landau and Levich (1942) and Derjaguin (1943). They showed that the entrained film thickness scales as $h_f/L \sim \mathrm{Ca}^{2/3}$, where L is a macroscopic characteristic length scale and $\mathrm{Ca} = \mu U/\gamma$ with μ and γ as the liquid viscosity and interfacial tension and U as the plate velocity. Later, Taylor (1961a) and Bretherton (1961) observed that the liquid film thickness around a moving bubble in a capillary tube follows the scaling proposed by Landau, Levich, and Deraguin (LLD). The LLD scaling is relevant to many coating processes, suggesting that the coating layer thickness can be controlled by tuning the velocity, surface tension, or viscosity (Ruschak, 1985; Quéré, 1999; Weinstein and Ruschak, 2004; Stone, 2010). The LLD scaling is strictly valid for very low capillary numbers as it is obtained via a matched asymptotic expansion as shown by Bretherton (1961); Wilson (1982) and needs to be modified for thick films, where gravitational drainage becomes important (White and Tallmadge, 1965), or for high velocities, where inertia becomes relevant (Quéré, 1999; Aussillous and Quéré, 2000). At very low velocities also there is a cut-off to the validity of the LLD scaling, when intermolecular forces become relevant and set the film thickness (Quéré et al., 1989). In confined flows also the LLD scaling has been found to be of high importance, from the pressure drop across a meniscus in a Hele–Shaw cell (Park and Homsy, 1984) to handling of drops, bubbles, and foams in microfluidics (Baroud et al., 2010; Cantat, 2013). All these processes rely on an important assumption that the liquid completely wets the solid surface, i.e. no contact line is present. In many situations, however, the liquid partially wets the surfaces. This observation leads to a basic question: how does partial wetting affect the liquid coating and entrainment process?

In the partial wetting regime, the liquid forms a non-zero angle with the solid surface. Slowly removing a plate from a liquid bath that partially wets the plate, the

contact line moves slightly up the plate and remains stationary at its new equilibrium position, i.e. simply the apparent contact angle decreases (Sedev and Petrov, 1991). Using the thin-film framework, Eggers (2004) used asymptotic matching to show that the curvature of the inner solution near the contact line cannot be matched with the curvature of the outer solution if the plate velocity increases beyond a certain critical value. The absence of steady state solutions indicates the onset of the wetting transition and liquid entrainment. The critical capillary number is found to be (Eggers, 2004):

$$\text{Ca}_{cr} = \frac{\theta_{eq}^3}{9} \left[\ln \left(\frac{\text{Ca}_{cr}^{1/3} \theta_{eq}}{18^{1/3} \pi [\text{Ai}(s_{max})]^2 \lambda \alpha} \right) \right]^{-1}, \tag{3.1}$$

where θ_{eq} is the equilibrium contact angle, Ai is the Airy function, $s_{max} = -1.0188$, α is the plate inclination with respect to the liquid bath, and λ is the slip length. All length scales are non-dimensionalized by the capillary length scale $l_\gamma = \sqrt{\gamma/\rho g}$, where ρ is the liquid density and g is the gravitational acceleration. Here, the onset of entrainment coincides with the apparent contact angle becoming zero, which is consistent with the observations of Sedev and Petrov (1991). Whether the apparent contact angle becomes zero at the onset of entrainment, however, has been a subject of debate. de Gennes (1986) balanced the viscous dissipation and capillary driving force near the contact line and concluded that the entrainment occurs discontinuously at a non-zero apparent angle. Eggers (2005), however, pointed to an inconsistency in the approximations made by de Gennes (1986) and argued that the transition is continuous. Further, Snoeijer and Eggers (2010) showed that the dewetting speed of a receding contact line as predicted by the model proposed by de Gennes is greater than the critical entrainment velocity, suggesting the incorrect conclusion that a receding contact line cannot exist. The experimental observations of Delon et al. (2008) for the plate withdrawal, however, indicate that the entrainment occurs at a non-zero apparent angle. They suggested that the transition is pre-critical, i.e. occurs at a capillary number Ca*, which is smaller than the Ca$_{cr}$ predicted by the hydrodynamic theory. The origin of this pre-critical transition is not yet fully resolved as different mechanisms have been suggested: Snoeijer et al. (2006) observed that a capillary ridge

forms before the critical point and suggest that the formation of this ridge leads to the pre-critical transition; the inherent roughness of the plates has also been suggested to lower the critical capillary number (Golestanian and Raphaël, 2003; Perrin et al., 2016); Maleki et al. (2007) suggest that one needs to be cautious about the definition of apparent angle as different definitions can lead to different conclusions. Further, the dimensionality of the problem can also be an important factor in whether a zero angle is observed at the onset of entrainment as shown for the case of sliding drops, for which near the corner the 3D nature of the flow needs to be considered (Limat and Stone, 2004; Snoeijer et al., 2007b). A remarkable observation is that the transient dynamics of the contact line before the entrainment precisely follows the predictions of the quasi-static hydrodynamic theory all the way up to the Ca_{cr} even though no static meniscus can be observed experimentally for $Ca^* < Ca < Ca_{cr}$.

3.2 Plunging a plate into a liquid bath: air entrainment

In the Landau–Levich problem the dynamics of the surrounding air phase can be safely neglected. In the reverse case of a plate plunging into a liquid bath, however, the air dynamics becomes important. In fact, the thin-film model used to predict the critical capillary number in the receding contact angle case, predicts that the advancing contact line is stable for any arbitrary velocity. While the experimentally observed wetting transition for advancing contact lines is observed at much higher velocities than the receding contact lines, the failure of the thin-film framework to predict the transition stems from the fact that the dynamics of the air phase is neglected. To get an estimate of the critical capillary number, therefore, the dynamics of both phases need to be included. One approach to achieve this goal is to solve for the flow fields in both phases, i.e. solve the full Stokes or Navier–Stokes equations with appropriate boundary conditions at the interface between the two fluids as well as the fluid-solid boundary and contact line. This approach is computationally expensive, but can reproduce the experimental observations for the air entrainment for instance (Vandre et al., 2012, 2013). Alternatively, one can use Cox's asymptotic theory for two-phase flow, which predicts how viscous forces lead to the bending of the interface to get an estimate of the apparent contact angle (Cox, 1986; Bonn et al., 2009):

$$g(\theta(x), M) - g(\theta_\mu, M) = \mathrm{Ca}\ln{(x/\lambda)}, \tag{3.2}$$

where $\tan{(\theta(x))} = dh/dx$ is the slope of the interface at a distance x from the contact line and $M = \mu_{rec}/\mu_{adv}$ is the ratio of the viscosity of the receding phase to that of the advancing phase (Vandre et al., 2013). The microscopic contact angle θ_μ is usually assumed to be equal to its equilibrium value, i.e. $\theta_\mu = \theta_{eq}$. It is however, recognized that the microscopic angle can deviate from the equilibrium angle due to the flow and there is an ongoing debate about its dependence on the front velocity (Thompson and Robbins, 1989; Qian et al., 2003, 2006; Blake, 2006; Ren and E, 2007; Bonn et al.,

2009; Ren et al., 2010; Perrin et al., 2016; Lhermerout et al., 2016; Alizadeh Pahlavan et al., 2018c). The function g accounts for the viscous forces in both phases and has the following form:

$$g(\theta(x), M) = \tag{3.3}$$
$$\int_0^\theta \frac{M \left[x^2 - (\sin x)^2\right] \left[(\pi - x) + \sin x \cos x\right] + \left[(\pi - x)^2 - (\sin x)^2\right] (x - \sin x \cos x)}{2 \sin x \left[M^2 \left(x^2 - (\sin x)^2\right) + 2M \left[x(\pi - x) + (\sin x)^2\right] + \left[(\pi - x)^2 - (\sin x)^2\right)\right]}.$$

In the limit of zero viscosity contrast, i.e. air-liquid systems, the function g simplifies considerably to:

$$g(\theta) = \int_0^\theta \frac{x - \sin x \cos x}{2 \sin x}, \tag{3.4}$$

which can safely be approximated as $\theta^3/9$ for $\theta < 3\pi/4$, leading to the celebrated Cox–Voinov relation for advancing contact lines (Voinov, 1976):

$$\theta^3 - \theta_\mu^3 = 9\mathrm{Ca}\ln(x/\lambda). \tag{3.5}$$

The critical capillary number can therefore be estimated as the point, where the apparent contact angle approaches π:

$$\mathrm{Ca}_{cr} = (g(\pi, M) - g(\theta_\mu, M))/\ln(l_M/\lambda), \tag{3.6}$$

where l_M is a macroscopic length scale at which the apparent angle is defined. As discussed above for the case of receding contact lines in the context of Landau–Levich problem, whether the transition occurs when the apparent contact angle reaches π or before that is a subject of debate. This definition, however, seems to lead to reasonable estimates of the critical capillary number for the air entrainment experiments (Vandre et al., 2012, 2013). Another point that needs to be emphasized is that the general Cox's relationship or the Cox–Voinov relation are strictly valid for advancing contact lines, where the outer curvature of the inner solution in the vicinity of the contact line approaches zero, allowing for an unambiguous matching with the outer solution (Eggers, 2005); in the case of receding contact lines, as discussed above, the outer

124

curvature of the inner solution is a non-zero value, which prevents matching of the inner to the outer solution beyond a critical capillary number.

An alternative approach to find the critical capillary number is to use the lubrication approximation to simplify the equations of motion (Oron et al., 1997; Craster and Matar, 2009). The lubrication approximation goes back to the early works of Reynolds (1886) and is a very powerful technique in fluid mechanics, allowing to get valuable information about the flow at a much reduced computational cost compared with the full solution of equations of motion. The downside of this approach is that it is limited to small slopes to be consistent with the assumption of mainly uni-directional flow field. It should be noted that the lubrication approximation usually works well even outside its regime of strict validity, for instance in flows involving stagnation points, due to its weak ellipticity (Krechetnikov, 2010). For large slopes, the lubrication approximation can be generalized by assuming that the flow locally can be approximated as a flow in a wedge instead of the usual Poiseuille flow approximation (Snoeijer, 2006). For the general case of arbitrary viscosity contrast between the two phases, the interface can be described as (Chan et al., 2013):

$$\frac{d^2\theta}{ds^2} = \frac{3\mathrm{Ca}}{h(h + 3\lambda)} f(\theta, M),$$ (3.7)

where θ is the local interface slope, s is the arc length along the interface, and the function f can be written as:

$$f(\theta, M) = \frac{2(\sin\theta)^3 \left[M^2 f_1(\theta) + 2M f_3(\theta) + f_1(\pi - \theta) \right]}{3 \left[M f_1(\theta) f_2(\pi - \theta) - f_1(\pi - \theta) f_2(\theta) \right]},$$ (3.8)

where $f_1(\theta) = \theta^2 - (\sin\theta)^2$, $f_2(\theta) = \theta - \sin\theta\cos\theta$ and $f_3(\theta) = \theta(\pi - \theta) + (\sin\theta)^2$. In the limit of zero viscosity contrast, Snoeijer (2006) has shown that the generalized lubrication approximation is equivalent to the Cox's asymptotic theory (Eq. (3.2)). However, this equivalence is strictly valid for the advancing contact lines. In the case of receding contact lines, the generalized lubrication approximation needs to be used, which reproduces the experimental observations (Snoeijer et al., 2007a; Snoeijer and Andreotti, 2013).

125

While the Cox's theory and the generalized lubrication approximation have been qualitatively successful in predicting the experimentally observed critical capillary number for the onset of air entrainment, the agreement is not quite satisfactory yet. In particular, the dependence of the critical point on the viscosity ratio is not quite consistent with the experimental observations (Chan et al., 2013). Changing the ambient air pressure is known to lead to a change in the critical capillary number of the entrainment (Benkreira and Khan, 2008), or suppress splashing in a drop impacting a solid surface (Xu et al., 2005). The gas viscosity, however, is not a strong function of the pressure. Slip length is therefore thought to be responsible for the dependence on the air pressure (Marchand et al., 2012; Snoeijer and Andreotti, 2013). Recently, it has been shown that to get a quantitaive prediction of the onset of transition, kinetic effects in the gas phase need to be accounted for via solving the Boltzmann equation coupled with the hydrodynamic model for the liquid phase (Sprittles, 2017).

3.3 Influence of confinement on the wetting transition

In the predictions of the critical capillary number for receding (Eq. (3.1)) and advancing (Eq. (3.6)) contact lines, the ratio of a microscopic to a macroscopic length scale in the problem appears inside log terms. This observation implies that confinement can indeed influence the onset of transition if the macroscopic length scale, i.e. confinement scale becomes smaller than the capillary length scale. For instance, Vandre et al. (2012) have shown that the onset of air entrainment can be delayed by confining the meniscus to a small gap of order of few hundred microns. Such small spacings are in fact very typical of many coating applications and indeed point to the importance of confinement effects. In the context of Couette flow geometry, few studies have analyzed the role of confinement on the entrainment features (Jacqmin, 2004; Sbragaglia et al., 2008; Gao and Lu, 2013; Kim and Nam, 2017), where it has been observed that in liquid-liquid displacement the transition occurs discontinuously at a non-zero apparent angle, whereas in the air-liquid systems the transition remains continuous. In fact, the role of the macroscopic geometry on the onset of wetting transition can be simply understood by considering the example of a fiber being withdrawn from a liquid bath (Shing Chan et al., 2011). For very large fiber radii, the critical capillary number can be written as follows:

$$\mathrm{Ca}_{cr} = \frac{\theta_{eq}^3}{9}\left[\ln\left(\frac{(3\mathrm{Ca}_{cr})^{1/3}\theta_{eq}l_\gamma}{2^{5/6}3\pi[\mathrm{Ai}(s_{max})]^2\lambda}\right)\right]^{-1}, \tag{3.9}$$

where the slip length λ is the molecular length scale and the capillary length is the macroscopic length scale (see Eq. (3.1) and (Eggers, 2005)). In the opposite limit of very small fibers, however, the critical capillary number can be written as:

$$\mathrm{Ca}_{cr} = \frac{\theta_{eq}^3}{9}\left[\ln\left(\frac{(3\mathrm{Ca}_{cr})^{1/3}\theta_{eq}r_0}{2^{1/3}3\pi[\mathrm{Ai}(s_{max})]^2\lambda}\right)\right]^{-1}, \tag{3.10}$$

where the fiber radius r_0 is now the macroscopic length scale. In the case of wetting transition in a capillary tube, the radius would be that of the tube (Zhao et al., 2018).

More recently, Setu et al. (2015) have investigated the effect of confinement on wetting transition using a demixed colloid-polymer mixture, which has an ultralow interfacial tension, leading to a small capillary length and therefore a much smaller separation of microscopic and macroscopic length scales (Aarts et al., 2004), allowing for a direct visualization of length scales on the order of the diffuse interface thickness. In this limit, they found that the effect of confinement scale on the critical capillary number is no longer logarithmic, but in fact linear. They argue that this change in scaling is due to the fact that in "superconfinement", the influence of contact line friction dominates the volumetric contributions of the viscous dissipation in the bulk.

Here, we are mainly interested in the influence of confinement on the morphology of the wetting transition and its ensuing instability features. Figure 3-1 represents a phase diagram of the displacement patterns in confinement (in a channel, or a capillary tube), where a less viscous fluid displaces a more viscous fluid, and its analogy to the wetting transitions in open systems, i.e. plate withdrawal from or plunging into a liquid bath discussed above. In the confined domains, displacement of more wetting defending fluid by a less wetting invading fluid is called drainage. The reverse process of displacement of a less wetting fluid by a more wetting fluid is known as imbibition. We focus on the case of a less viscous fluid displacing a more viscous one, which is known to lead to interfacial instabilities. Some of the discussions, however, do extend to the stable displacement processes. We will discuss the influence of viscosity contrast in passing when relevant. While most of the morphologies presented here are experimentally observed, some are theoretical predictions that remain to be verified. We need to understand the details of the displacement morphologies beyond the transition to be able to describe and predict their ensuing instabilities— a very important topic, which we will discuss next.
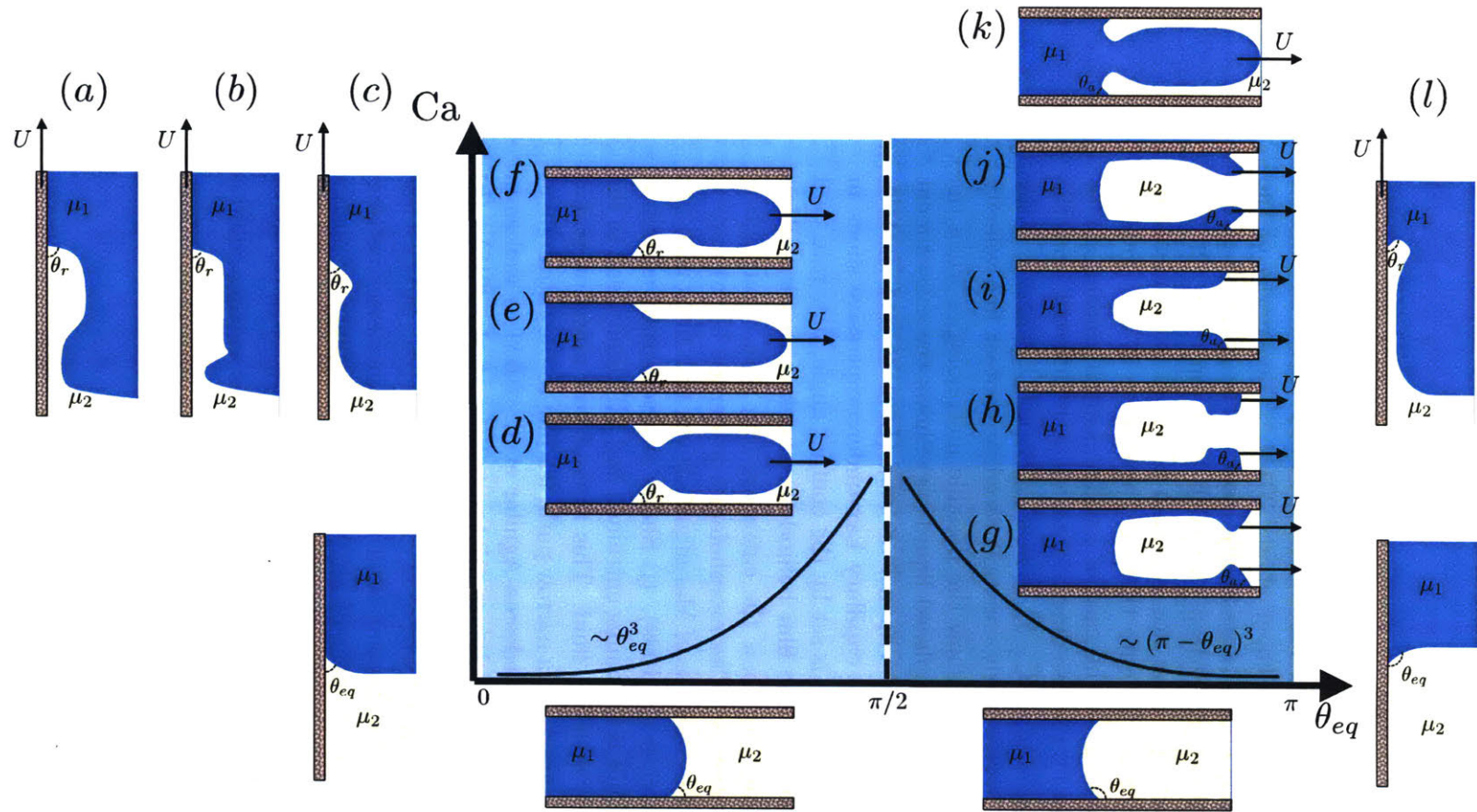
Figure 3-1: Phase diagram of dynamical wetting transitions in confined immiscible flows when a less viscous fluid displaces a more viscous liquid and its analogy to the unconfined case. (a-c) A liquid film becomes entrained on a solid plate withdrawn from a liquid bath if the plate velocity is higher than a critical velocity; $Ca_{cr} \sim \theta_{eq}^3$ (Eq. (3.1)). The entrained liquid film can have different morphologies depending on the plate velocity (Galvagno et al., 2014; Gao et al., 2016): (a) shows the formation of a capillary ridge, which is thought to be responsible for the pre-critical nature of the observed transition (Snoeijer et al., 2006); while the thickness of the entrained film next to the liquid bath is described by the Landau–Levich scaling $h_f \sim l_\gamma Ca^{2/3}$, the capillary ridge thickness is set by the contact angle and is independent of the plate velocity; the structure of the ridge is remiscient of an Lax-undercompressive shock front, in which the front and back of the shock travel at different speeds leading to the broadening of the ridge (Bertozzi et al., 1998, 1999) (b) shows a thick liquid film with a stationary dimple next to the liquid bath (Snoeijer et al., 2008); as the plate velocity increases, the dimple finally detaches from the liquid bath and capillary ridges of the form shown in (a) form; this observation is also remiscient of undercompressive shock formation and separation in Marangoni-driven thin films (Münch, 2003; Sur et al., 2003; Münch and Evans, 2005). (c) Shows the formation of a dewetting rim next to the contact line (Maleki et al., 2007). (d-f) Forced wetting transition in a channel or a tube, where a film of the defending liquid gets entrained on the wall. This observation is typical of the drainage regime, when a less wetting fluid displaces a more wetting liquid.

Figure 3-1: (d) shows the dewetting rim profile beyond the onset of transition (Zhao et al., 2018). The entrained film thickness follows the modified Taylor–Bretherton scaling (Aussillous and Quéré, 2000; Klaseboer et al., 2014). The growth of the dewetting rim next to the receding contact line finally leads to the pinch-off of the invading phase and formation of a bubble/drop (Alizadeh Pahlavan et al., 2018e). Morphologies presented in (e) and (f) have not yet been observed experimentally, but our preliminary modeling results indicate that they can arise in the presence of a body force, e.g. gravity, similar to the case of Landau–Levich coating shown in (a-c). Note that in all cases (a-f), the receding contact angle is different from the equilibrium angle and can be expressed as $\theta_r^3 - \theta_{eq}^3 = 9\mathrm{Ca}^* \ln 2\theta_{eq}w/3\lambda$, where w is the width of the rim and $\mathrm{Ca}^* \sim \theta_{eq}^3$ is the nearly constant receding contact line velocity (Snoeijer and Eggers, 2010). Cases (g-k) show the possible morphologies when the invading fluid is more wetting than the displaced liquid. (g) Shows the entrainment of the invading liquid on the walls of the channel or tube (Levaché and Bartolo, 2014). (h) Shows an entrained film with a capillary Lax-undercompressive shock in front. The thickness of the capillary shock is set by the contact angle, flow rate, and viscosity contrast between the fluids. The film behind the shock, however, follows the typical Landau–Levich scaling. (i) Show the entrained film with a rarefaction wave-undercompressive shock structure. The morphologies presented in (h) and (i) are reminiscent of those observed in the case of Marangoni-driven thin films with two competing driving forces (Bertozzi et al., 1999). (j) Shows an overturned entrained thin film, where the defending liquid is becoming entrained and will finally lead to the pinch-off of a drop/bubble of the invading fluid. This type of flow morphology has been observed in gravity-driven flows down a narrow path, leading to the entrainment of the air phase and pinch-off of a drop (Ledesma-Aguilar et al., 2011) as well as in confined channels using demixed colloid-polymer mixtures (Setu et al., 2015). (k) Shows the morphology when the invading interface overturns transitions from the imbibition regime to the drainage regime (Setu et al., 2013; Odier et al., 2017). Case (l) represents the entrainment of a non-wetting fluid in the Landau–Levich setting; this is a common observation in entrainment of air on hydrophilic plates (Snoeijer and Andreotti, 2013). Cases (g-j) can be thought of as analogues of Landau–Levich problem, where a less viscous and more wetting liquid is being entrained on the plate, whereas case (k) is similar to case (l), where a more viscous and less wetting liquid is being entrained on the wall.

The typical interface morphologies in the Landau–Levich problem of withdrawing a plate from a liquid bath in the partial wetting regime are shown in Fig. 3-1(a-c). In the Landau–Levich problem, we expect a uniform coating of thickness $h_f \sim l_\gamma \mathrm{Ca}^{2/3}$, where the capillary number is defined based on the plate velocity U. In the partial wetting regime, however, the morphology becomes more complex. Snoeijer et al. (2006) observed that the wetting transition to coating the plate occurs pre-critical, i.e. before the capillary number reaches the critical capillary number predicted in Eq. (3.1). They observed that this pre-critical transition is always accompanied by the formation of a capillary ridge that separates from the bath and travels upwards along the plate as shown in Fig. 3-1(a). The thickness of this capillary ridge depends on the contact angle and shows features of the Lax-undercompressive shock front observed in Marangoni-driven thin films (Bertozzi et al., 1998, 1999), i.e. the front moves at a faster speed than the back of the shock leading to the broadening of the ridge in time. This ridge is then connected to the liquid bath via a Landau–Levich film. They later argued that the capillary ridge profile belongs to a class of thick-film solutions shown in Fig. 3-1(b), which connect to the bath via a dimple, whose thickness is set by the Landau–Levich scaling (Snoeijer et al., 2008). The structure shown in Fig. 3-1(a) is then observed in the class of thick films, when the plate velocity is suddenly increased leading to the detaching of the capillary shock and formation of a Landau–Levich film behind it. This pinch-off like process is again similar to the observations in the Marangoni-driven thin films (Münch, 2003; Sur et al., 2003; Münch and Evans, 2005). The structure shown in pane (c) is the usual Landau–Levich film, which meets the wall with a dewetting rim (Maleki et al., 2007). In the confined flow cases (d-f), which can occur in a channel or a capillary tube, we expect to observe similar morphologies to those discussed in the case of Landau–Levich in open systems. In particular, Zhao et al. (2018) observed a wetting transition in a capillary tube, leading to the entrainment of the defending liquid on the tube wall and formation of a dewetting rim as shown in pane (d). An important difference with the case of open systems here is that the growth of the dewetting rim next to the receding contact line eventually leads to the pinch-off of a bubble/drop of the

invading fluid (Alizadeh Pahlavan et al., 2018e), whereas in an open system such an event will not occur. The thickness of the entrained film here follows the modified Taylor–Bretherton scaling (Aussillous and Quéré, 2000; Klaseboer et al., 2014), which is essentially the same as that of the Landau–Levich problem (Stone, 2010). Note also that while we have focused on the unstable displacement, i.e. a less viscous fluid displacing a more viscous one, the morphology shown in pane (d) is expected to be observed for arbitrary viscosity contrasts. The critical capillary number of course increases as the invading fluid becomes more viscous. In the singular limit of the defending fluid being air, air films become entrained on the wall beyond a critical capillary number. This will be further discussed below.

Figure 3-1(e-f) show flow morphologies that have not yet been reported experimentally; they are however, motivated by the observed morphologies in the open system (panes a-c) as well as our preliminary theoretical predictions in the presence of a uniform body force, e.g. gravity. In particular, pane (e) shows an undercompressive shock next to the receding contact line without a ridge. Pane (f) shows an undercompressive-Lax shock pair, i.e. a capillary ridge next to the contact line. Similar to the case of Landau–Levich problem shown in pane (a), here the thickness of ridge is set by the contact angle; this ridge is then connected to a Landau–Levich type film. The existence and features of the morphologies presented in panes (e-f) have important consequences on the stability properties of the interface as will be discussed further below. Further, in case (d), the contact line speed and contact angle seem to follow the predictions in the open system, i.e. contact angle can be expressed as $\theta_r^3 - \theta_{eq}^3 = 9\mathrm{Ca}^* \ln 2\theta_{eq} w/3\lambda$, where w is the width of the rim and $\mathrm{Ca}^* \sim \theta_{eq}^3$ is the nearly constant receding contact line velocity (Snoeijer and Eggers, 2010). It remains to be seen whether these remain true for cases (e-f). Further, all our discussions on cases (a-f) assumed that the fluid 1 is air, i.e. $\mu_1 \approx 0$ and its dynamics can be safely neglected. It remains to be seen how finite viscosity contrasts, for which the dynamics of both phases need to be considered will change the predictions.

Figure 3-1(g-k) represent the flow morphologies observed when the invading fluid is more wetting and less viscous than the defending fluid. It should be noted that

132

whether any of the morphologies (g-j) or (k) will be observed depends sensitively on the viscosity contrast between the fluids as well as the contact angle. Here, we focus on the case of an arbitrary high viscosity contrast, i.e. a much less viscous fluid displacing a more viscous fluid. We also consider the limit where the invading fluid forms a non-zero, but very small angle with the interface. Under these conditions, all the presented morphologies are likely to be observed, while increasing the viscosity or the contact angle of the invading fluid can result in only a subset of these morphologies, and in particular only pane (k) to be observed.

Figure 3-1(g) shows the flow morphology observed first by Levaché and Bartolo (2014) in a rectangular Hele–Shaw cell, where thin films of the invading fluid become entrained on the walls of the cell. These thin films have since been observed in micromodel experiments (Zhao et al., 2016; Odier et al., 2017) as well as in smooth and rough radial Hele–Shaw cells (Alizadeh Pahlavan et al., 2018b,d). In particular, we have shown that depending on the upstream boundary conditions, one of the three morphologies (g-i) will be chosen. Pane (g) represents a leading Lax shock structure; pane (h) represents a Lax-undercompressive shock structure, and pane (i) represents a rarefaction wave-undercompressive shock structure. As we will discuss later, the front instability is very sensitive to the flow morphology observed here, which serves as the base state.

Pane (j) shows an overhanging thin-film front, which occurs when the defending fluid becomes entrained on the wall. Morphologies similar to this have been observed in open systems (Ledesma-Aguilar et al., 2011), where a narrow stream of liquid flowing on an inclined plate entrains air at its advancing contact line, leading to the pinch-off of the droplets. In confined flows also a situation similar to the pane (j) has been observed in experiments using demixed colloid-polymer mixtures with ultra-low interfacial tensions (Setu et al., 2015). In this case also similar to the unconfined case, the entrainment occurs due to the wetting transition at the advancing contact line. This situation is similar to that depicted in pane (l) with the fluids 1 and 2 being flipped, i.e. a less-wetting fluid 1 being dragged into the fluid 2. Note that in pane (j), we have assumed that two wetting transitions occur. The first one

being the entrainment of the invading fluid and the second one being the entrainment of the defending fluid. While the entrainment condition depends on the boundary conditions, it is unlikely that both entrainments occur for the same speed, i.e. either one of the cases (g-i) will be observed or the case represented in pane (k), showing the entrainment of the defending fluid. Case (j) can however be observed in the presence of a variable velocity, or in a situation similar to that presented in (Setu et al., 2015), where the ultra-low interfacial tension leads to a small capillary length and therefore make gravitational forces relevant even in "superconfinement". We also expect to be able to observe such a flow configuration in the context of our radial Hele–Shaw cell experiments, where the invading liquid coats one of the walls; for high enough injection rates, one would then expect to observe the entrainment of the defending fluid and overturning and pinch-off of the invading liquid. This hypothesis remains to be experimentally confirmed.

Finally, pane (k) represents the entrainment of the defending liquid on the walls. This flow configuration has been observed in Hele–Shaw experiments using demixed colloid-polymer mixtures (Setu et al., 2013) as well as in micromodel experiments in unstable imbibition regime for very high injection rates (Odier et al., 2017) leading to the switching of the flow from the thin-film mode represented in panes (g-j) to the flipped meniscus in pane (k). The morphology here is analogous to the entrainment of air on a hydrophilic plate plunging into a liquid bath as shown in pane (l) (Marchand et al., 2012; Chan et al., 2013; Vandre et al., 2013, 2014). In this case, the flow morphology is similar to that represented in pane (d) (Zhao et al., 2018); therefore, we expect a rapid growth of the dewetting rim and pinch-off of bubbles/drops.

134

3.4 Interfacial instabilities beyond wetting transition

So far, we analyzed the morphology of two-phase flow displacement across the gap in a channel or a capillary tube. When a less viscous fluid displaces a more viscous fluid, the interface is subject to a lateral instability (Bensimon et al., 1986; Homsy, 1987). In the case of a non-wetting fluid displacing a wetting fluid, i.e. in the absence of contact lines, this leads to the classic Saffman–Taylor instability (Saffman and Taylor, 1958; Saffman, 1986). This instability is one of the archetypes of pattern formation and has been extensively analyzed to address questions related to the instability wavelength selection (Pitts, 1980; Tabeling et al., 1987; Kessler et al., 1988; van Saarloos, 2003) or its sensitivity to perturbations (Couder et al., 1986b,a; McCloud and Maher, 1995).

In the Saffman–Taylor instability, the displacement is either considered to be complete, i.e. the invading fluid completely displaces the defending fluid across the gap, or thin films of the defending wetting liquid are considered to coat the walls according to the Taylor–Bretherton scaling (Park and Homsy, 1984). In either case, contact line dynamics is neglected, i.e. it is either assumed to move with the same velocity as the rest of the meniscus, as is observed before the wetting transition, or no contact line is present and the entire wall is coated with a thin film of the defending liquid.

The presence of moving contact lines in the partial wetting regime, however, leads to a wealth of different flow morphologies across the gap as we discussed before (Fig. 3-1). Given that most of these complexities have only been recently discovered, their influence on the ensuing interfacial instabilities is an open question with important consequences for the flow behavior on macroscopic scales. Here, we briefly summarize the recent experimental observations on this topic and the analogy between confined and open systems.

In open systems, in the context of a plate being withdrawn from a liquid bath or plunging into a liquid bath (Fig. 3-2 (b, e, g)), when the plate velocity becomes higher than the corresponding critical entrainment velocity, as the liquid or air are coating

the plate, contact lines form an angle with respect to the plate to lower their normal component of velocity and therefore delay the onset of wetting transition (Blake and Ruschak, 1979; Snoeijer and Andreotti, 2013). The same phenomenon occurs in the case of drops moving down inclined plates (Fig. 3-2 (a)), where a corner forms in the back of the drop (Podgorski et al., 2001; Rio et al., 2005; Peters et al., 2009). While the normal contact line velocity in these problems turn out to be different and sensitive to the macroscopic geometry, the dynamic contact angles seem to be universal (Delon et al., 2008). As the plate velocity or the drop velocity increases further, a pearling transition occurs leading to drops or bubbles emitting from the tip of the corner (Simpkins and Kuck, 2000).

Very recently He and Nagel (2018) have studied the plate withdrawal and plunging problem using high-speed interferometric imaging to reconstruct the thickness in the cornered structure of the entrained films and discovered that a more complex fingering-like pattern emerges within the entrained corner (Fig. 3-2 (c, f)). Stability analysis of the Landau–Levich problem has shown that the base profile before the onset of transition is stable to lateral perturbations (Golestanian and Raphaël, 2001; Snoeijer et al., 2007a). In fact the generalized lubrication approximation predicts that two branches of solutions exist in this problem (Snoeijer et al., 2007a; Chan et al., 2012). Both branches are quasi-static solutions with the lower branch being the stable one and the upper branch the unstable one. Remarkably, as the plate velocity goes beyond the critical velocity, the contact line follows the lower branch all the way to the critical point and then follows onto the unstable upper branch, which is accompanied by the coating of the wall. This observation indicates that the contact line dynamics is quasi-static all the way to the entrainment. As far as we know, however, the stability of the unstable branch, i.e. stability of the front beyond the wetting transition, to lateral perturbations has not yet been analyzed. The observations by He and Nagel (2018) as well as a separate study by Deblais et al. (2016), which focuses on controlling the instability using polymeric solutions, indeed indicate that there is a rich physics in the pattern formation beyond the onset of transition that needs to be understood. These observations are also relevant to other problems

involving moving contact lines, such as droplet splashing on solid surfaces (Riboux and Gordillo, 2014, 2015); in this context, the role of air pressure on the splashing has been clearly demonstrated (Xu et al., 2005) and points to the kinetic effects of the gas phase, which needs to be taken into account in combination with the hydrodynamics of the liquid phase to arrive at a consistent description (Sprittles, 2017).
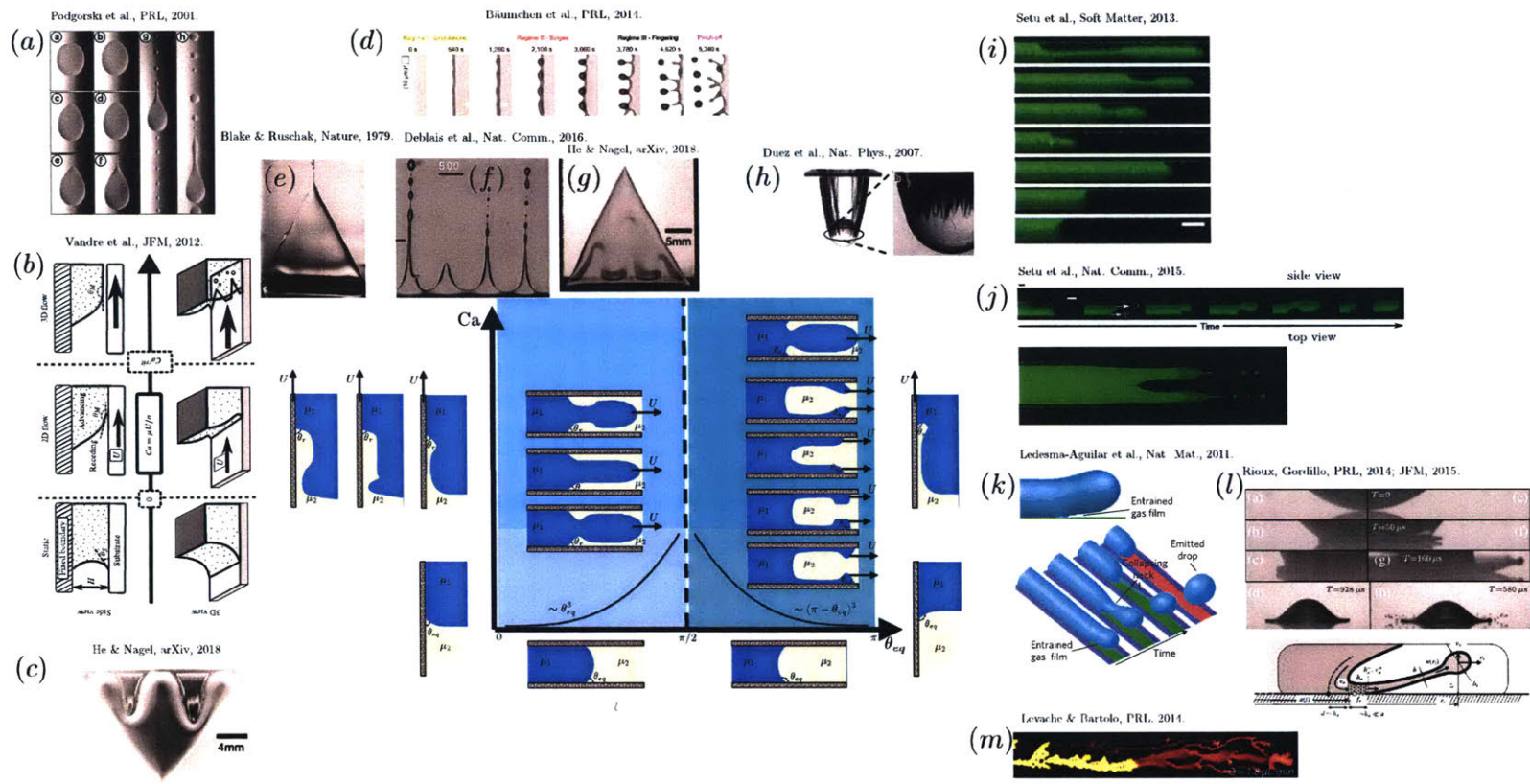
Figure 3-2: Phase diagram of the dynamical wetting transition and its ensuing interfacial instabilities in confined immiscible flows and analogies to the unconfined flows. (a) represents the morphologies of a drop in the partial wetting regime on an inclined plate (Podgorski et al., 2001; Le Grand et al., 2005). As the inclination angle increases and therefore the drop velocity increases, a corner forms in the back, which will eventually lead to the emission of tiny droplets from the back of the drop. This observation is similar to the formation of corners in the Landau–Levich problem, when a plate is withdrawn from a liquid bath (Blake and Ruschak, 1979) as shown in pane (e). The formation of corner is to delay the onset of wetting transition as the velocity normal to the contact line is decreased (Snoeijer and Andreotti, 2013). (b) represents the entrainment of the air phase in a confined meniscus, where the bottom wall drag the meniscus inwards. Beyond a critical capillary number, air becomes entrained and this coinceds with the contact line becoming three-dimensional due to a lateral instability, in which small v-shaped cusps form through which small air bubbles emit into the liquid phase (Simpkins and Kuck, 2000; Vandre et al., 2012).

Figure 3-2: (c) shows that in the entrainment of air when a plate plunges into a liquid bath, three-dimensional structures form due to the lateral instability of the entrained film (He and Nagel, 2018). Pane (g) from the same study shows the lateral instability in the entrained liquid film withdrawn from a liquid bath. Pane (f) shows a similar instability for polymer solutions (Deblais et al., 2016). Pane (d) represents the lateral instability, i.e. fingering, of a receding contact line of a nanometric thin film dewetting from a solid substrate (Bäumchen et al., 2014). Pane (h) shows the lateral instability of the front during the impact of a superhydrophobic ball on a liquid bath (Duez et al., 2007; Snoeijer and Andreotti, 2013). Pane (i) shows the confocal microscope imaging of the cross section of a Hele–Shaw cell, where an ultra-low interfacial tension demixed colloid-polymer mixture shows a change of curvature as capillary number increases and finally forms a finger in the middle of the channel (Ledesma-Aguilar et al., 2007a,b; Setu et al., 2013). Pane (j) shows the entrainment of the defending liquid next to an advancing contact line and eventual pinch-off of a drop of the invading fluid due to the entrainment in the side view as well as the lateral instability of the front in the top view (Setu et al., 2015). Air entrainment in open systems can also lead to the drop pinch-off as shown in pane (k) (Ledesma-Aguilar et al., 2011). Pane (l) shows that a similar idea of the air entrainment next to an advancing contact line is responsible for some cases of splashing events observed after impact of drops on solid surfaces (Riboux and Gordillo, 2014, 2015). Pane (m) shows the lateral interfacial instability observed in a rectangular Hele–Shaw cell upon entrainment of thin films of the invading fluid (Levaché and Bartolo, 2014).

In both confined and unconfined systems, a variety of different morphologies can be observed across the channel gap as shown in Figure 3-1. The morphology across the gap has important consequences on the front instability to lateral perturbations. In particular, in Fig. 3-1, we showed that three types of base morphologies can be observed in both drainage and imbibition regimes in confinement as well as in the Landau–Levich problem in the open systems. These three general types of solutions are 1) Lax shock, 2) Lax-undercompressive shock, and 3) rarefaction wave-undercompressive wave (Alizadeh Pahlavan et al., 2018b). These three types of structures have been also observed in the context of Marangoni-driven thin films, where two driving forces compete (Ludviksson and Lightfoot, 1971; Cazabat et al., 1990; Bertozzi et al., 1998; Sur et al., 2003; Münch, 2003) and have also been observed in the context of two-phase flow solutions in porous media flows (van Duijn et al., 2007). Apart from the rich dynamics of the base states of these solutions, they also have unusual stability features. The Lax shock structure is also observed in the context of thin films flowing down inclined plates and is known to be unstable to lateral perturbations (Huppert, 1982b; Brenner, 1993; Bertozzi and Brenner, 1997; Diez and Kondic, 2001). However, in the Lax-undercompressive double shock structure, it was predicted by Bertozzi et al. (1998, 2001b) that consistent with the experimental observations, the leading undercompressive shock is stable to perturbation. The trailing Lax shock can still become unstable. This observation points to the unusual stability of undercompressive shock fronts that has in fact been utilized in various contexts, including ion sputtering of surfaces (Chen et al., 2005; Perkinson et al., 2016; Bertozzi, 2016). Given that the different flow morphologies listed above can in fact be observed in the context of coating in open systems, i.e. Landau–Levich problem, it remains to be seen whether the observed front stability properties remains the same as those in the Marangoni-driven thin films. In particular, the observations of front instability by He and Nagel (2018) may suggest that their base profile is either of type I, with a Lax shock front, or type II, where the trailing Lax shock has become unstable.

Presence of confinement, however, can dramatically change the front stability properties. In fact, we have recently shown that in the context of imbibition, where

thin films of the invading fluid get entrained on the walls, the same three type of structures described above in the context of Marangoni-driven thin films can be observed. The crucial difference, however, is that we discovered that the undercompressive shock front under confinement becomes unstable to perturbations (Alizadeh Pahlavan et al., 2018b). This leads to a viscous fingering-like front instability in radial Hele–Shaw cells, which is reminiscent of the classical Saffman–Taylor instability. We have, however, found that the scaling of the most unstable wavelength with the flow rate is different from that observed in the Saffman–Taylor instability, indicating that the observed instability belongs to a different class of pattern forming processes. We discuss these observations further in Chapter 6.

The presence of moving contact lines, therefore lead to a very rich morphological patterns across the channel gap, which further lead to an even richer variety of interfacial instabilities in the moving fronts. These instabilities are not expected to be generally described by the same scalings as those of the classical Saffman–Taylor instability and therefore call for careful investigation. This opens the door to new classes of pattern forming processes, which remain to be observed and theoretically explained. In particular, in the imbibition regime, where beyond the wetting transition thin films of the invading fluid become entrained on the walls, we have observed that the instability is quite distinct from the Saffman–Taylor instability. In the drainage regime, the finger front is similar to that considered in the Saffman–Taylor instability (Park and Homsy, 1984); it remains to be seen, however, how the coupling with the structure of the rim next to the dewetting contact line may alter the instability features. In fact, Setu et al. (2013) have suggested that when the interface becomes flipped (Fig. 3-2 (i)), the curvatures may inhibit the front instability, which is otherwise predicted in the Saffman–Taylor framework. Further, the dewetting rim is prone to a pinch-off instability, which will then lead to the detachment of bubbles/drops, which will then travel downstream (Zhao et al., 2018). The receding contact line can also become unstable and lead to a fingering-like instability as shown in Fig. 3-2 (d). Understanding of these instabilities is not only an exciting fundamental scientific challenge, but also relevant to many applications in controlled pattern formation

in microfluidics (Wong et al., 2011; Wexler et al., 2015; Kreder et al., 2016; Bazyar et al., 2018) and biophysics (Hollister, 2005), printing of electronics (Kumar, 2015; Gu et al., 2018), and self-assembly (Huang et al., 2005; van Hameren et al., 2006; Thiele, 2014).

Chapter 4

Forced wetting transition in a capillary tube

Immiscible fluid-fluid displacement in partial wetting continues to challenge our microscopic and macroscopic descriptions. Here, we study the displacement of a viscous fluid by a less viscous fluid in a circular capillary tube in the partial wetting regime. In contrast with the classic results for complete wetting, we show that the presence of a moving contact line induces a wetting transition at a critical capillary number that is contact angle dependent. At small displacement rates, the fluid-fluid interface deforms slightly from its equilibrium state and moves downstream at a constant velocity, without changing its shape. As the displacement rate increases, however, a wetting transition occurs: the interface becomes unstable and forms a finger that advances along the axis of the tube, leaving the contact line behind, separated from the meniscus by a macroscopic film of the viscous fluid on the tube wall. We describe the dewetting of the entrained film, and show that it universally leads to bubble pinch-off, therefore demonstrating that the hydrodynamics of contact line motion generate bubbles in microfluidic devices, even in the absence of geometric constraints.

The displacement of one fluid by another immiscible fluid in small, confined geometries is an important process in many natural and industrial settings, including water infiltration into soil (Cueto-Felgueroso and Juanes, 2008b), enhanced oil recovery (Orr and Taber, 1984), ink-jet printing (Jang et al., 2009), and microfluidics (Whitesides,

2006). A particularly challenging aspect of describing fluid-fluid displacement in the presence of a solid is the movement of the contact line between the two fluid phases and the solid surface (*i.e.*, the three-phase contact line), which violates the no-slip boundary condition commonly assumed in classical fluid mechanics (Huh and Scriven, 1971b; Bertozzi, 1998; Briant et al., 2004b; Briant and Yeomans, 2004; Bonn et al., 2009; Pahlavan et al., 2015). Recent experiments in quasi-2D geometries (Levaché and Bartolo, 2014; ?) have demonstrated that the presence of moving contact lines lead to a wealth of pattern formation regimes. Due to the planar nature of these experiments, however, the contact line could not be directly visualized.

A capillary tube provides an ideal experimental system for studying fluid-fluid displacement, as it allows for unobstructed visualization of the contact line dynamics. While the displacement of a less viscous fluid by a more viscous one has been extensively studied in the context of capillary rise (Washburn, 1921; Fries and Dreyer, 2008; Zhmud et al., 2000; Siebold et al., 2000) and forced imbibition (Hoffman, 1975a, 1983; Fermigier and Jenffer, 1991a), experiments on the displacement of a more viscous fluid by a less viscous one have been relatively scarce. In his seminal work, G. I. Taylor found that as the air invades into a capillary tube initially filled with a *perfectly wetting*, viscous fluid, it leaves a film of the defending fluid coating the tube walls in its wake, whose thickness is controlled by the finger velocity.

Here, we revisit the Taylor–Bretherton problem (Taylor, 1961b; ?) in the *partial wetting* regime by studying the invasion of air into a capillary tube filled by a viscous fluid, and show that contact line motion leads to novel flow behaviors. At low displacement rates, the fluid-fluid interface moves downstream at a constant velocity, without changing its shape. As the flow rate increases beyond a critical value, however, a forced wetting transition occurs and a liquid film is deposited on the tube wall. The deposited film is unstable and dewets from the wall, leading to the formation of a growing dewetting rim that ultimately causes bubble pinch-off.

We conduct fluid-fluid displacement experiments in precision-made borosilicate glass capillary tubes with inner diameter $d = 750$ μm (Hilgenberg GmbH, Germany). We wash the capillary tubes with methanol and isopropyl alcohol, followed by ul-
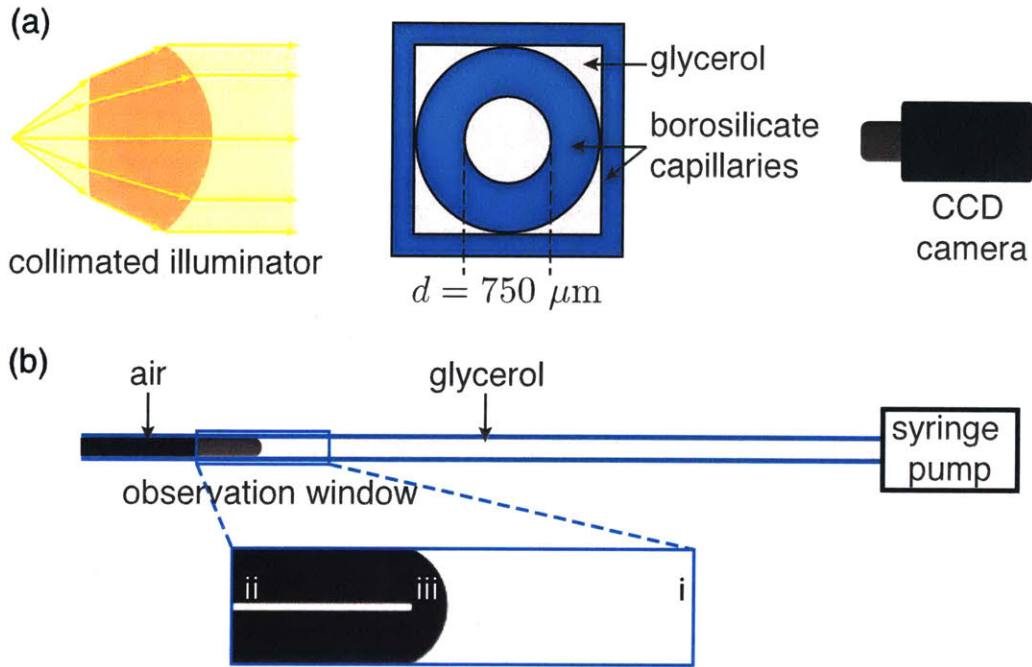
Figure 4-1: We study fluid-fluid displacement in circular capillary tubes. (a) The capillary tube is open to the atmosphere on one end and connected to a syringe pump on the other. To achieve viscously unfavorable displacement, we withdraw glycerol from the capillary tube so that air displaces glycerol. (b) We use precision-made borosilicate glass capillary tubes with inner diameter $d = 750$ μm. The circular capillary tube is housed in a slightly larger square capillary tube filled with glycerol, which has the same refractive index as borosilicate glass. The combination of a collimated light source and a glycerol-filled square borosilicate glass housing eliminates light refraction through the capillary tube, which enables clear, undistorted visualization of the fluid-fluid interface via a CCD camera. We identify three distinct regions in the experimental images: (i) bright sections of the image represent areas of the tube that are fully saturated with glycerol; (ii) sections with a bright line in the middle represent areas of the tube that are fully saturated with air; (iii) completely dark sections of the images represent areas of the tube that are partially saturated with glycerol.

trasonic cleaning in a de-ionized water bath for 10 minutes. Following cleaning, we dry the capillary tubes in a convection oven at 70 °C for 10 hours. The capillary tubes are wetting to glycerol after the washing process, having a static receding contact angle $\theta_{eq} = 25 \pm 5°$. To alter the wettability of the capillary tubes, we apply heat-assisted chemical vapor deposition (CVD) of trichloro(1H,1H,2H,2H-perfluorooctyl)silane (Sigma-Aldrich, USA) in a vacuum oven. The silane-coated capillary tubes are less wetting to glycerol, having a static receding contact angle $\theta_{eq} = 68 \pm 5°$. We use each capillary tube only once to ensure precise control over its wettability.

The capillary tube is open to the atmosphere on one end and connected to a glycerol-filled glass syringe (1710-LT-SYR, Hamilton Robotics, USA) on the other end (Fig. 4-1). The glass syringe is secured to a programmable syringe pump (PHD 2000, Harvard Apparatus, USA). To achieve viscously unfavorable displacement, we withdraw glycerol from the capillary tube so that air displaces glycerol. By withdrawing the incompressible glycerol instead of injecting the compressible air, we eliminate compressibilty from our experimental system. The circular capillary tube is housed in a slightly larger square capillary tube filled with glycerol, which has the same refractive index as borosilicate glass. The capillary tubes are illuminated with a collimated fiber optic light (ACE1, SCHOTT, USA) and imaged with a CCD camera (acA3800, Basler, USA). We identify three distinct regions in the experimental images: (i) bright sections of the image represent areas of the tube that are fully saturated with glycerol—the incoming light passes through the capillary tubes without any refraction; (ii) sections with a bright line in the middle represent areas of the tube that are fully saturated with air—the incoming light is refracted towards the center of the tube due to its circular geometry; (iii) completely dark sections of the images represent areas of the tube that are partially saturated with glycerol—the incoming light is refracted away by the fluid-fluid interface.

Figure 4-2 shows an experimental phase diagram of the fluid-fluid interface profiles obtained under the two distinct wettability conditions and a wide range of capillary numbers (Ca). We define Ca $= \mu U/\gamma$, where $\mu = 1400$ mPa · s is the viscosity

146
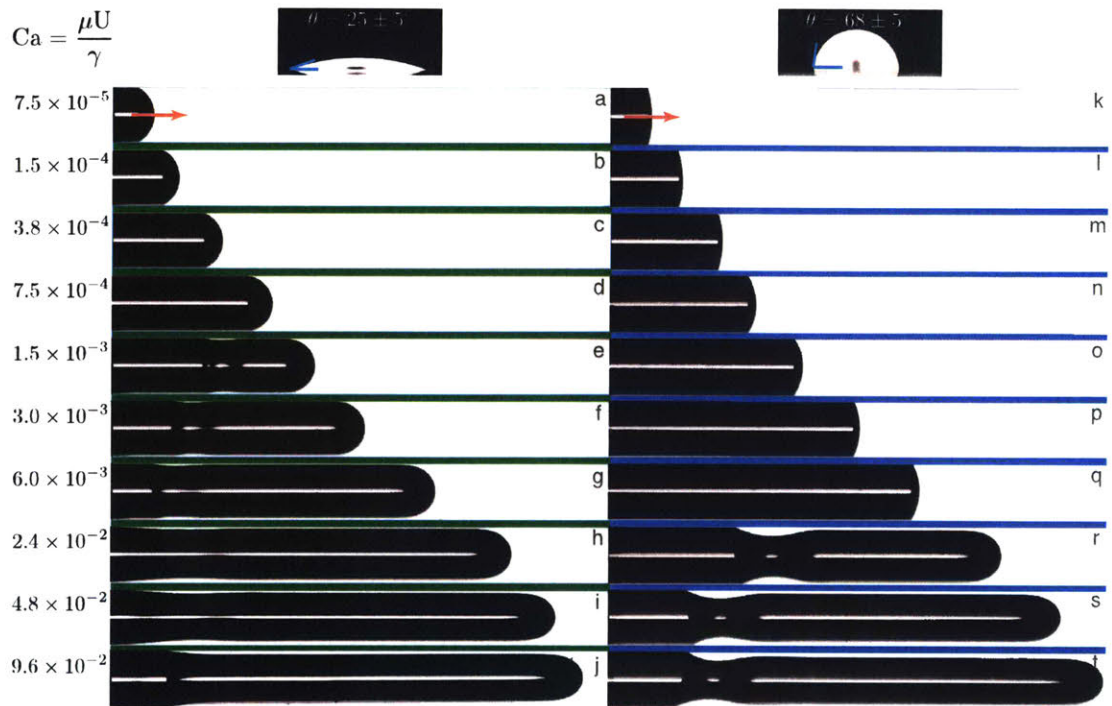
Figure 4-2: Fluid-fluid interface of air (black) displacing glycerol (white) under increasing capillary numbers (top to bottom) in a wetting capillary tube with $\theta_{eq} = 25 \pm 5°$ (left column) and a weakly wetting capillary tube with $\theta_{eq} = 68 \pm 5°$ (right column). The orange arrows indicate the direction of interface displacement. At small Ca, the meniscus deforms slightly from its equilibrium shape, but remains as a spherical cap. At large Ca, however, a wetting transition occurs and the invading air forms a single finger that advances along the center of the tube, leaving a macroscopic trailing film of the viscous liquid on the tube walls. The critical capillary number Ca* at which film formation occurs is controlled by the wettability (pane r vs. pane e).

of glycerol at 20°C, $U = 4Q/(\pi d^2)$ is the displacement velocity, with Q being the imposed flow rate, and $\gamma = 65 \pm 2$ mN/m is the glycerol-air interfacial tension. The left column shows the results corresponding to the more wetting case ($\theta_{eq} = 25°$). At low Ca numbers, the fluid-fluid interface deforms slightly from its equilibrium state and travels downstream at a constant velocity, without changing its shape (Fig. 4-2a-d). Deformation of the fluid-fluid interface corresponds to a decrease in the apparent contact angle, which reaches zero at a critical capillary number Ca*. This value of Ca* marks the onset of the wetting transition, beyond which the defending liquid is forced to wet the tube walls as a thin film and the air advances as a finger through the center of the tube (Fig. 4-2e-j). We find that the onset of the wetting transition is strongly dependent on the wettability of the capillary tube: Ca* is over an order of magnitude larger in the less wetting tube (Fig. 4-2, right column) compared to that in the more wetting tube (Fig. 4-2r vs. Fig. 4-2e).

4.1 Onset of wetting transition

The flow dynamics before the wetting transition (Ca<Ca*) is governed by the two-way coupling between the fluid-fluid interface shape and the flow field within each fluid phase, as described by the Stokes equations. The Laplace pressure jump across the fluid-fluid interface is balanced by a normal viscous stress discontinuity. In the framework of the generalized lubrication approximation (Snoeijer, 2006; Chan et al., 2013), we can use the local approximation of the Stokes flow in a wedge, for which exact analytical solutions exist (Huh and Scriven, 1971b), and greatly reduce the complexity of this problem to an equation for the shape of the interface in the frame co-moving with the fluid-fluid interface (Levaché and Bartolo, 2014). While this approximation is strictly valid for flow in a 2D setting, our results show that it provides good estimates for flow in an axisymmetric tube as well. In this framework, we arrive at the following differential equation describing the interface shape:

$$\frac{d^2\theta}{ds^2} = \frac{3\mathrm{Ca}f(\theta, R)}{h(h + 3\lambda_s)},$$

(4.1)

148

where θ is the local interface slope, s is the arc length along the interface, $R = \mu_g/\mu_l$ is the viscosity ratio between the gas and liquid, and $\lambda_s = O(\mathrm{nm})$ is the slip length that removes the moving contact line singularity (Huh and Scriven, 1971a). In the limit of zero viscosity ratio (i.e. neglecting the air viscosity), we have $f(\theta, 0) = -(2/3)(\sin\theta)^3/(\theta - \sin\theta\cos\theta)$. We can then describe the fluid-fluid interface shape deformation for an arbitrary displacement rate by solving Eq. (4.1) using the boundary conditions $\theta|_{s=0} = \theta_{eq}$, $h|_{s=0} = 0$ at the contact line, and $\theta|_{s=l} = \pi/2$, $h|_{s=l} = d/2$ at the tube center, where l is the half-arc length of the interface.

We find excellent agreement between the experimental data and the theoretical predictions for the fluid-fluid interface shape before the wetting transition (Fig. 4-3). The deformation of the interface from equilibrium is accompanied by a decrease in the apparent contact angle θ_{app}. At the point of wetting transition, $\theta_{\mathrm{app}} \to 0$, and the liquid becomes effectively wetting to the walls, leaving an entrained liquid film (Fig. 4-3b). A similar behavior is also observed in the forced wetting transition dynamics of receding contact lines in unconfined systems when a fiber or plate is withdrawn from a liquid bath. When the liquid is perfectly wetting to the substrate, it immediately leaves a film behind, known as the Landau–Levich film (Levich and Landau, 1942; Quéré, 1999; Stone, 2010). When the liquid is only partially wetting, however, a critical plate velocity is needed for the liquid to coat the substrate (Eggers, 2004; Snoeijer et al., 2006; Bonn et al., 2009; Snoeijer and Andreotti, 2013). In the reverse process of forced wetting transition in advancing contact lines, air is entrained, but at much higher contact line velocities (Duez et al., 2007; Ledesma-Aguilar et al., 2011; Marchand et al., 2012; Vandre et al., 2012; Ledesma-Aguilar et al., 2013; Vandre et al., 2014; Setu et al., 2015; Sprittles, 2017).
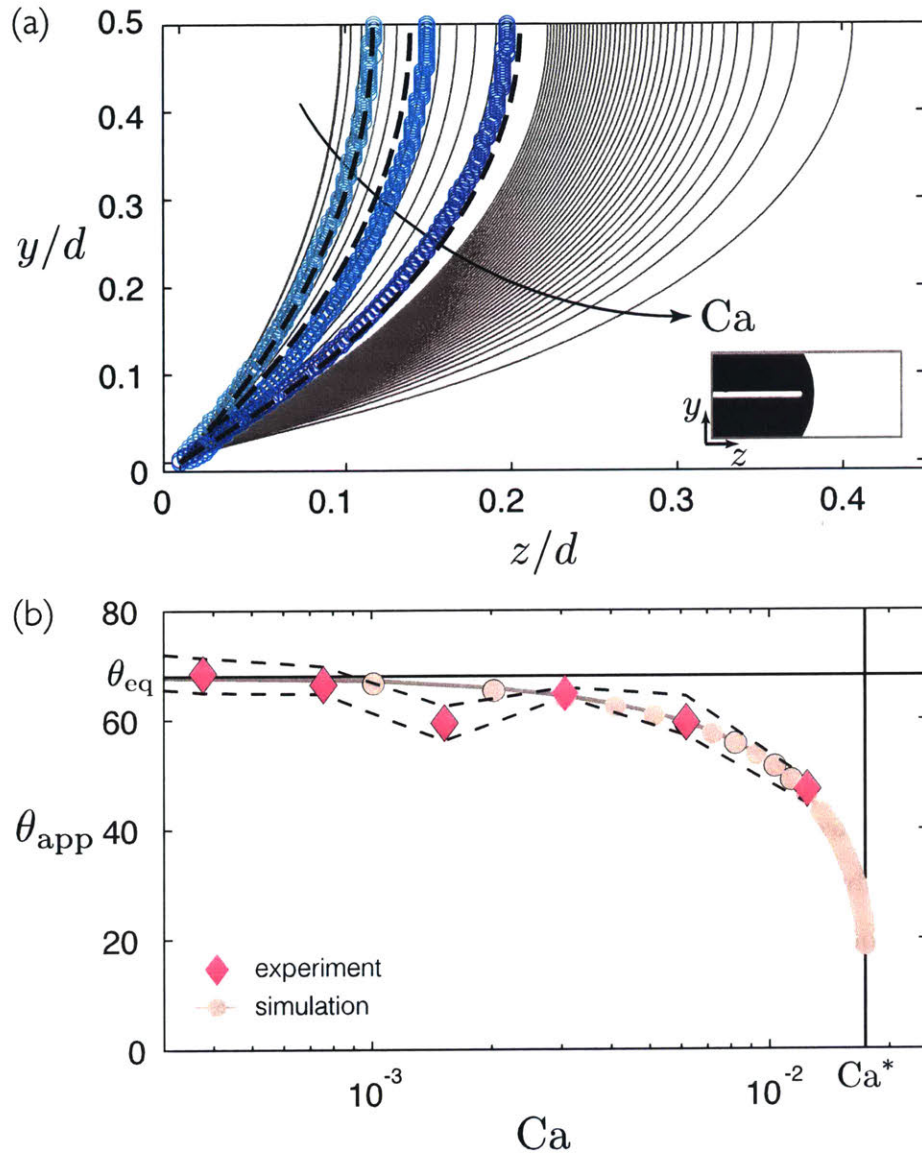
149

Figure 4-3: (a) Fluid-fluid interface profiles for Ca<Ca* in the less wetting capillary tube ($\theta_{eq} = 68°$). As Ca increases, the fluid-fluid interface deforms further from its equilibrium shape. The symbols and dashed lines correspond to the experimental and numerical results for Ca $= 0.003, 0.006, 0.012$, respectively. (b) Deformation of the fluid-fluid interface can be quantified by the apparent contact angle θ_{app}, which decreases asymptotically towards zero as the Ca approaches the critical capillary number Ca*. This marks the onset of the wetting transition. The diamond and circle symbols represent the experimental data and theoretical predictions, respectively. The dashed lines above and below the data points represent the experimental uncertainty.

4.2 Dynamic beyond the transition: growth of the dewetting rim and pinch-off

Below the wetting transition, the contact line moves with the same velocity as the interface tip. Above the critical point (Ca>Ca*), however, the interface becomes

unstable and a finger is formed. In this regime, the contact line travels at a constant, but smaller, velocity compared to that of the finger tip, which gives rise to a macroscopic film of the viscous defending fluid in the wake of the the finger. It is remarkable that, for Ca>Ca*, the contact line speed becomes independent of Ca (Fig. 4-4). This indicates that the dynamics downstream (near the finger tip) and upstream (close to the contact line) become effectively decoupled. We further observe that the contact line speed beyond the wetting transition is strongly dependent on the wettability—the contact line speed is more than an order of magnitude higher in the less wetting tube compared to that in the more wetting tube. These observations lead us to hypothesize that the dynamics of the entrained film next to the contact line can be analyzed independently of the finger tip dynamics.

The contact line behind the entrained film recedes from the tube wall at a constant rate, leading to the formation of a dewetting rim (see, *e.g.*, Fig. 4-2r). While the dynamics of hole formation and the associated dewetting rims has been extensively studied in the context of thin film on flat substrates (Redon et al., 1991; Snoeijer and Eggers, 2010; Edwards et al., 2016), much less is known about the influence of confinement on the dewetting dynamics. In particular, as we show below, an important distinguishing factor in dewetting in confined geometries is that it leads to a pinch-off instability in finite time.

We can use the long-wave approximation to derive a model that describes the dynamics of the dewetting rim in an axisymmetric capillary tube. Consider a liquid film of height h coating the walls of a cylindrical capillary tube of radius r. The fluid flow inside the film is governed by the axisymmetric Navier-Stokes equations in a cylindrical domain, $\rho\frac{D\mathbf{u}}{Dt} = -\nabla P + \mu\nabla^2\mathbf{u}$, where ρ is the liquid density, $D/Dt = \partial/\partial t + \mathbf{u}\cdot\nabla$ is the material derivative, $\mathbf{u} = (u, w)$ are the fluid velocity components in the radial and axial directions (r, z), respectively; P represents the liquid pressure, and μ is the liquid viscosity. We consider the liquid to be incompressible, such that $\nabla\cdot\mathbf{u} = 0$. These governing equations of motion are subject to the no slip and no penetration boundary conditions on the walls, zero shear stress at the liquid-air interface, and normal stress jump across the interface due to the Laplace pressure.
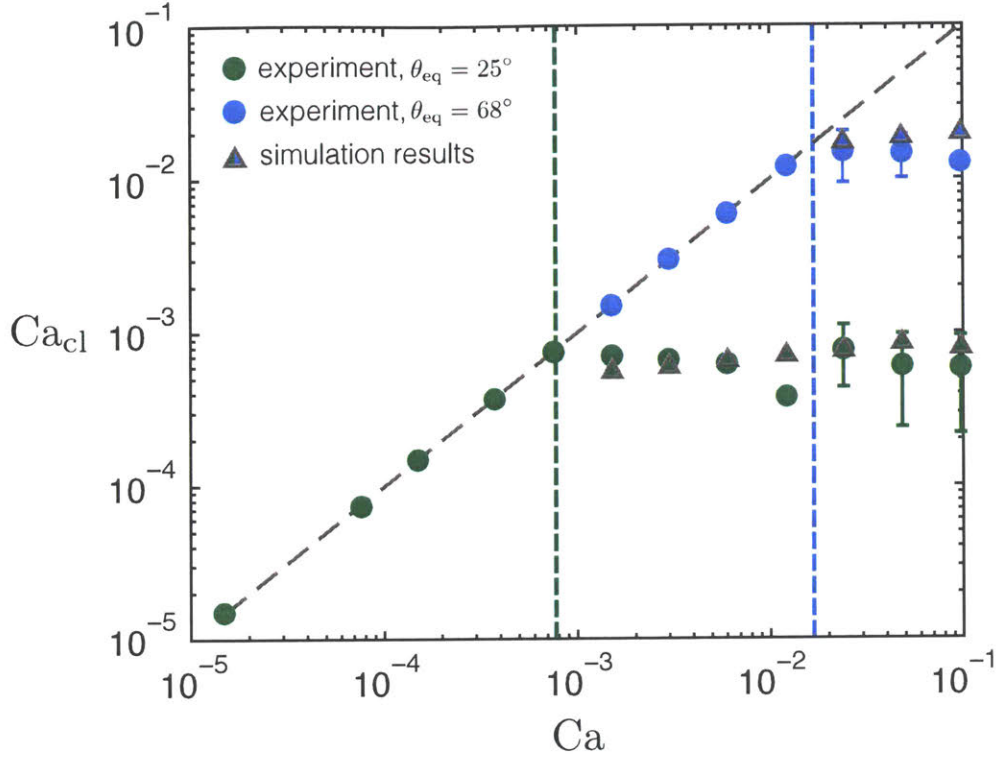
151

Figure 4-4: The contact line capillary number $Ca_{cl} = \mu U_{cl}/\gamma$ as a function of the macroscopic capillary number $Ca = \mu U/\gamma$, where U_{cl} and U are the contact line velocity and the displacement velocity, respectively. The green and blue circles represent the experimental measurements in the more wetting tube ($\theta_{eq} = 25°$) and in the less wetting tube ($\theta_{eq} = 68°$), respectively. The triangles show the corresponding theoretical predictions of Eq. (5.1). The vertical dashed lines represent the critical capillary numbers Ca^* as predicted by Eq. (4.1). For $Ca < Ca^*$, the fluid-fluid interface deforms slightly while remaining a spherical cap, and the contact line and the interface tip travel at the imposed displacement velocity $U = 4Q/\pi d^2$ (gray dashed line). For $Ca > Ca^*$, the air forms a finger that advances along the center of the tube, leaving behind a film of the more-viscous defending liquid. The incomplete displacement of the defending liquid results in an interface tip velocity that is faster than the imposed displacement velocity. The contact line that trails behind travels at a velocity that, remarkably, is independent of the imposed flow rate. Instead, the contact line velocity is controlled by the wettability of the capillary tube.

We non-dimensionalize the governing equations by the following scalings: $\tilde{y} = y/r$, $\tilde{z} = z/r$ with y and z as the coordinates normal and tangential to the walls of the tube, $\tilde{u} = u/U_0$, $\tilde{w} = w/W_0$, $\tilde{t} = (\gamma/\mu)t/(16r)$, $\tilde{P} = \epsilon Pr/\mu W_0$, where $W_0 = Q/\pi(r^2 - (r-h)^2)$, $U_0 = \epsilon W_0$, $\epsilon = r/L$, with L as a characteristic length scale, and Q as a characteristic flow rate. We can then simplify the non-dimensional governing

equations using the long-wave approximation, i.e. assuming $\epsilon \ll 1$ and $\epsilon \mathcal{R} \ll 1$, where $\mathcal{R} = \rho W_0 r / \mu$ is the Reynolds number. In the simplified form of the Navier-Stokes equations, the liquid pressure turns out to be constant across the liquid film and only a function of the axial direction z. Using this observation, we can integrate the z component of the momentum to find $\tilde{w} = (1 - \tilde{y})^2 \tilde{P}_{\tilde{z}}/4 + c_1 \ln{(1 - \tilde{y})} + c_2$, where the constants c_1 and c_2 can be determined using the no-slip boundary condition on the wall and zero shear stress on the liquid-air interface.

The liquid pressure is set by the Laplace pressure jump across the interface, and is augmented by the disjoining pressure in the vicinity of the contact line, where the film height becomes nanometric (Bonn et al., 2009; Pahlavan et al., 2015; Craster and Matar, 2009; Gauglitz and Radke, 1988):

$$\tilde{P}_{\tilde{z}} = \frac{\partial}{\partial \tilde{z}} \left(\Pi(\tilde{h}) - \tilde{\kappa} \right), \tag{4.2}$$

where $\Pi(\tilde{h}) = 6(1 - \cos\theta_{\mathrm{eq}})(\delta^2/\tilde{h}^3)(1 - \delta/\tilde{h})$ is the disjoining pressure with δ as the precursor film thickness, and $\tilde{\kappa} = 1/(1 - \tilde{h}) + \tilde{h}_{\tilde{z}\tilde{z}}$ is the curvature.

We can then integrate the axial component of the liquid velocity across the film thickness to obtain the liquid flux through the film, $\tilde{q}(\tilde{z}, \tilde{t}) = 2\pi \int_0^{\tilde{h}} \tilde{w}(1 - \tilde{y})d\tilde{y}$, which after replacing the velocity simplifies to $\tilde{q} = -\mathcal{M}(\tilde{h})\tilde{P}_{\tilde{z}}$ with the mobility:

$$\mathcal{M}(\tilde{h}) = 1 - 4(1 - \tilde{h})^2 + 3(1 - \tilde{h})^4 - 4(1 - \tilde{h})^4 \ln{(1 - \tilde{h})} \tag{4.3}$$

Using conservation of mass, we then have:

$$\frac{\partial}{\partial \tilde{t}} \left[\pi(1 - (1 - \tilde{h})^2) \right] + \frac{\partial \tilde{q}}{\partial \tilde{z}} = 0, \tag{4.4}$$

where we can replace the liquid flux in this equation to arrive at:

$$(1 - \tilde{h})\frac{\partial \tilde{h}}{\partial \tilde{t}} - \frac{\partial}{\partial \tilde{z}} \left(\mathcal{M}(\tilde{h})\tilde{P}_{\tilde{z}} \right) = 0, \tag{4.5}$$

153

which can finally be expanded to:

$$\frac{\partial \tilde{h}}{\partial \tilde{t}} = \frac{1}{(1 - \tilde{h})} \frac{\partial}{\partial \tilde{z}} \left(\mathcal{M}(\tilde{h}) \frac{\partial}{\partial \tilde{z}} \left[\Pi(\tilde{h}) - \tilde{\kappa} \right] \right). \tag{4.6}$$

In the absence of the disjoining pressure, this model has similarities to the class of models describing the evolution of films coating cylindrical fibers or interior of tubes (Quéré, 1999; Craster and Matar, 2009; Camassa and Ogrosky, 2015), and in the thin-film limit simplifies to the models describing the Rayleigh–Plateau instability of thin liquid films in cylindrical tubes (Hammond, 1983; Gauglitz and Radke, 1988). It is interesting to note that, in this limit, the model is equivalent to one describing the Rayleigh–Taylor instability of a thin film on the underside of a horizontal plate, where gravity plays the destabilizing role of the azimuthal curvature in the tube (Oron et al., 1997).

The thickness of the entrained liquid film depends on the finger tip velocity and has been determined using a matched-asymptotic analysis by Bretherton (?), who found that $h_f \sim \text{Ca}_f^{2/3}$ as $\text{Ca} \to 0$, with $\text{Ca}_f = \mu U_f / \gamma$ representing the finger capillary number. This scaling was later empirically extended to higher capillary numbers: $h_f / r = 1.34 \text{Ca}_f^{2/3} / (1 + 1.34 \times 2.5 \text{Ca}_f^{2/3})$ (Aussillous and Quéré, 2000; Klaseboer et al., 2014). This relationship, in combination with conservation of mass $Q = \pi (r - h_f)^2 U_f$, determine both the entrained film thickness and the finger velocity. We use this thickness as the downstream boundary condition for Eq. (5.1).

The growth of the dewetting rim is well-captured by our theoretical predictions (Fig. 4-5a). At early times, the growth of the dewetting rim is linear in time due to the constant-speed retraction of the contact line (Fig. 4-4). At late times, however, this mechanism is overtaken by the surface tension driven Rayleigh–Plateau instability caused by the azimuthal curvature, leading to an accelerated growth and bubble pinch-off (Fig. 4-5b). The continual movement of the contact line repeats the process of ridge growth and pinch-off, leading to the formation of a train of mono-dispersed bubbles.

The pinch-off time depends on both the capillary number and the wettability of
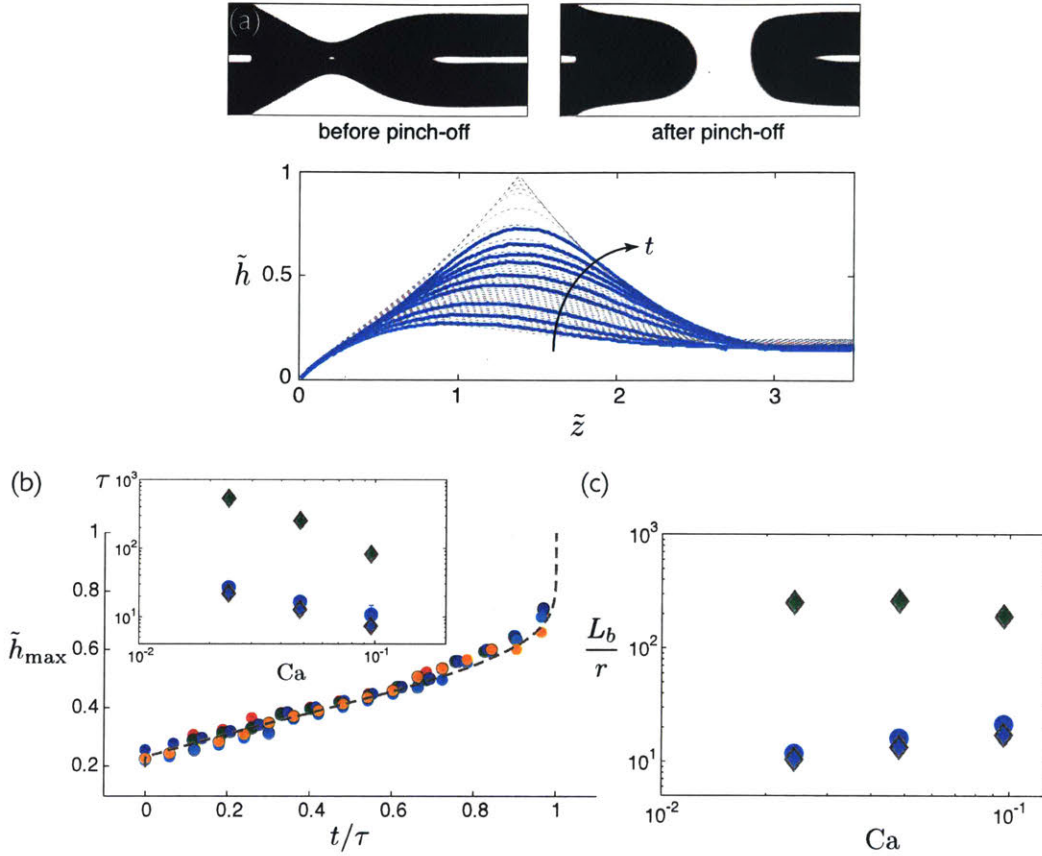
Figure 4-5: (a) Top: Experimental images of the fluid-fluid interface profile just before and after pinch-off. Bottom: The dewetting rim profile in the frame co-moving with the receding contact line for Ca = 0.096 and $\theta_{\text{eq}} = 68^o$. The dashed and solid lines correspond to the numerical and experimental data, respectively. (b) The maximum height of the rim $\tilde{h}_{\text{max}}$ grows linearly at early times and nonlinearly accelerates close to the pinch-off time τ. The color-coded circles represent different experimental realizations of rim growth that led to pinch-off, while the dashed line represents the theoretical prediction of Eq. (5.1). The inset shows the pinch-off time as a function of the capillary number and the wettability condition, where the green and blue symbols correspond to $\theta_{\text{eq}} = 25°$ and $68°$, respectively. The theoretical predictions (diamonds) matches closely to the experimental data (circles) for $\theta_{\text{eq}} = 68°$. Given the limited experimental window, we did not directly observe pinch-off in the more wetting tube since its τ is predicted to be over an order of magnitude larger than that in the less wetting tube. (c) The bubble length L_b as a function of the capillary number and the wettability condition, where the green and blue symbols correspond to $\theta_{\text{eq}} = 25°$ and $68°$, respectively. The theoretical predictions (diamonds) agree well with the experimental data (circles) for $\theta_{\text{eq}} = 68°$.

the capillary tube (Fig. 4-5b, inset). For a given wettability, higher Ca leads to faster pinch-off due to the thicker film deposited on the tube wall ($h_f \sim \text{Ca}_f^{2/3}$). For a given

Ca, higher θ_{eq} leads to faster pinch-off due to the higher contact line velocity (Fig. 4-4) as the contact line velocity of the dewetting rim scales as θ_{eq}^3 (Snoeijer and Eggers, 2010; Edwards et al., 2016). The large difference in contact line velocity, in turn, leads to a pinch-off time that is over an order of magnitude larger in the more wetting tube ($\theta_{eq} = 25°$) compared to that in the less wetting tube ($\theta_{eq} = 68°$).

The dependence of the pinch-off time on the wettability leads to a dependence of the generated bubble length L_b on the contact angle: for a given flow rate, a higher contact angle leads to faster pinch-off and therefore a smaller bubble (Fig. 4-5c). The impact of the flow rate on the bubble size is less straightforward. Higher Ca leads to a faster travelling finger, which increases the length of the bubble, but also to a thicker entrained film, which reduces the pinch-off time. The competition between these two effects lead to a weak dependence of the bubble length on the flow rate, leaving the wettability as the dominant factor controlling the bubble size.

Pinch-off induced bubble formation has a wide range of applications in microfluidic devices (Whitesides, 2006; Agresti et al., 2010). Most existing microfluidic bubble generators rely on flow channels with geometric constrictions (Link et al., 2004; Garstecki et al., 2004b; Dollet et al., 2008b; Roman et al., 2017) or an external cross-flow (Thorsen et al., 2001; Anna et al., 2003; Garstecki et al., 2006b; van Steijn et al., 2009b) to initiate bubble pinch-off (Baroud et al., 2010; Seemann et al., 2012; Anna, 2016). Recently, it has been shown that "superconfinement" can trigger a jet instability from a moving interface in the absence of geometric features, but through a mechanism that relies on thermal fluctuations in systems with ultralow surface tension (Setu et al., 2015). Our experiments demonstrate that pinch-off will occur in smooth, uniform capillaries as a result of wettability-mediated contact line motion. We have shown that wettability and flow rate control the pinch-off time, and therefore can be used to tune the size of mono-dispersed bubbles.

156

Chapter 5

Restoring universality to the breakup of a bubble

The pinch-off of a bubble is an example of the formation of a singularity, which exhibits a characteristic separation of length and time scales in the vicinity of the singularity. Because of this scale separation, one expects universal dynamics that collapse into self-similar behavior determined by the balance between viscous, inertial, and capillary forces. Here, we show that the breakup dynamics of a bubble confined in a capillary tube undergo a sequence of two distinct self-similar regimes, even though the dominant balance between viscous and surface-tension forces remains unchanged throughout the process. The crossover from one regime to another is due to the change in the dominant contributions to the dissipation mechanism— from the spatially-localized moving contact line singularity that translates axially at early times to the temporally-localized radial necking that controls bubble pinch-off singularity at late times. While the pinchoff of a bubble from an orifice in the classic configuration corresponding to an unbounded reservoir is known to be non-universal, here we demonstrate that the early-time self-similar regime that develops in the laterally-confined system effectively erases the system?s memory and restores universality to bubble breakup. This universality of bubble pinch-off dynamics has important consequences for the control of bubbles and drops in microfluidic devices, and for understanding multiphase-flow phenomena in porous media.

From dripping faucets to children blowing soap bubbles, we observe the formation of drops and bubbles on a daily basis. This seemingly simple phenomenon, however, has long puzzled and attracted scientists, from the early descriptions of da Vinci, Savart, Plateau, and Rayleigh (Savart, 1833; Plateau, 1849; Rayleigh, 1879) to advanced experimental techniques that yield precise observations of the interface evolution leading to pinch-off (Rayleigh, 1891; Worthington, 1908; Edgerton et al., 1937; Shi et al., 1994; Thoroddsen et al., 2008; Eggers, 1997). In the immediate vicinity of the pinch-off point the local curvature and velocity diverge. The resulting separation of temporal and spatial scales is often expected to lead to self-similar behavior and universal dynamics describing the formation of a singularity (Eggers, 1993; Eggers and Villermaux, 2008). This observation has important consequences for applications such as ink-jet printing (Basaran, 2002; Wijshoff, 2010), medical imaging (Lindner, 2004; Rodríguez-Rodríguez et al., 2015), and micro/nanoparticle production (Park et al., 2010; Amstad et al., 2015), as well as for understanding geologic processes such as $CO2$ sequestration (Lackner, 2003; Szulczewski et al., 2012), volcanic eruptions (Blake, 1981; Huppert and Woods, 2002; Parmigiani et al., 2016; Schmid et al., 2017; Cashman et al., 2017), and venting of methane from seafloor sediments (Skarke et al., 2014; Ruppel and Kessler, 2017; Andreassen et al., 2017).

Most previous studies of singularities during bubble or drop formation have focused on unbounded domains (Peregrine et al., 1990; Longuet-Higgins et al., 1991; Tjahjadi et al., 1992; Oguz and Prosperetti, 1993; Brenner et al., 1994; Papageorgiou, 1995; Day et al., 1998; Lister and Stone, 1998; Cohen et al., 1999; Rothert et al., 2001; Doshi et al., 2003; Sierou and Lister, 2003; Bergmann et al., 2006; Keim et al., 2006; Eggers et al., 2007; Gekle et al., 2008, 2009; Schmidt et al., 2009). Many natural phenomena and industrial processes, however, often involve flows under confinement (Gañán Calvo and Gordillo, 2001; Anna et al., 2003; Link et al., 2004; Stone et al., 2004; Garstecki et al., 2004a; Squires and Quake, 2005; Gordillo et al., 2005; Garstecki et al., 2005a; Utada et al., 2005; Cubaud et al., 2005; Garstecki et al., 2005b, 2006a; Fuerstman et al., 2007; Gañán-Calvo et al., 2007; van Hoeve et al., 2011; Huerre et al., 2014; Katsikis et al., 2015; Gai et al., 2016; Anna, 2016), where dimensionality

of the confined geometry is known to strongly influence the breakup (Garstecki et al., 2005c; Burton and Taborek, 2007; Dollet et al., 2008a; van Steijn et al., 2009a). These studies often assume that a continuous liquid phase coats all the surfaces. In many situations, however, one encounters partially wetting liquids, which naturally lead to the presence of contact lines, where fluid phases meet the solid surface. The difficulty in dealing with moving contact lines stems from the divergence of stress and pressure (a singularity) in the classical hydrodynamic description, which would imply that an infinite force is needed to move the contact line (Huh and Scriven, 1971b; Bonn et al., 2009). To resolve this paradox, non-hydrodynamic processes at the molecular scale must be incorporated (Snoeijer and Andreotti, 2013; Pahlavan et al., 2015).

Here, we study the breakup of a bubble in confinement in the partial wetting regime. We show that the moving contact line singularity dominates the viscous dissipation at early times, leading to an axially-dominated flow and the emergence of an early-time self-similar regime, which then crosses over to a late-time regime, where the flow is mainly radial and the viscous dissipation is dominated by the pinch-off singularity. While the observation of different self-similar regimes is expected when the balance of forces between inertia, viscosity and surface tension changes (Lister and Stone, 1998; McKinley, 2005; Castrejón-Pita et al., 2015), here we show that in our system the crossover between self-similar regimes occurs even though the entire evolution is controlled by a balance between viscous and surface-tension forces. We further show that the presence of the early-time regime has important consequences on the breakup dynamics, erasing the system's memory and restoring the universality of bubble breakup, which is lost in the case of breakup in unbounded domains(Doshi et al., 2003).

We study the bubble generation process in precision-made borosilicate glass capillary tubes (diameter $d = 280, 750$ μm). We wash the capillary tubes with Isopropyl alcohol and Ethanol, followed by an ultrasonic cleaning step in a de-ionized water bath for one hour. The capillary tubes are then dried using compressed nitrogen gas. We use glycerol (viscosity $\mu = 1.4$ Pa.s) and 90% glycerol-water mixture (viscosity $\mu = 0.2$ Pa.s) with surface tension $\gamma = 65$ mN/m) as the liquid phase. Both liquids

are partially wetting to the tube with a contact angle of ≈ 25 degrees. The receding contact line speed is proportional to the equilibrium contact angle cubed ($\sim \theta_{eq}^3$) (Snoeijer and Eggers, 2010; Zhao et al., 2018); therefore, to accelerate the pinch-off process, we make the tubes less wetting to the liquid through a heat-assisted chemical vapor deposition step of trichloro(1H,1H,2H,2H-perfluorooctyl)silane (Sigma-Aldrich, USA) in a vacuum oven, which leads to a contact angle of ≈ 65 degrees.

The capillary tube is open to the atmosphere at the left end and is connected to a syringe pump at the right end. The tube is initially filled with glycerol and then the glycerol is withdrawn at a specified flow rate Q from the right end of the tube using a syringe pump (CETONI low pressure pump neMESYS). At low flow rates, the meniscus deforms slightly and moves downstream at a constant velocity $4Q/(\pi d^2)$. When the flow rate is higher than a critical value, however, a wetting transition occurs: the meniscus loses its quasi-static geometry and air starts invading the tube in the form of a finger, leaving a film of the viscous liquid on the walls (Zhao et al., 2018). Fig. 5-1 shows that the entrained liquid film immediately starts to dewet along the tube walls. As the contact line recedes, the rim behind it grows and the bubble neck shrinks until it finally pinches off and forms a bubble. To achieve refractive-index matching and an undistorted view of the displacement process, we house the circular capillary tube inside a square tube (both tubes are made of borosilicate glass) and fill the gap between the two with glycerol. When the capillary tube is filled with glycerol, light goes through the system without any refraction (white color in Fig. 5-1). When air penetrates the tube, it leads to the refraction of light to the center of the tube; therefore air appears in black color with a straight white line in the middle. The capillary tube is backlit with a LED light source (constellation 120E, Veritas), which shines directly on a white light diffuser behind the setup. Imaging is done from the front side using a high-speed camera (Phantom Micro 320) at a typical frame-rate of $10 - -25$ kfps. A 4X lens is mounted on the camera leading to a resolution of 1.7 μm/pixel.
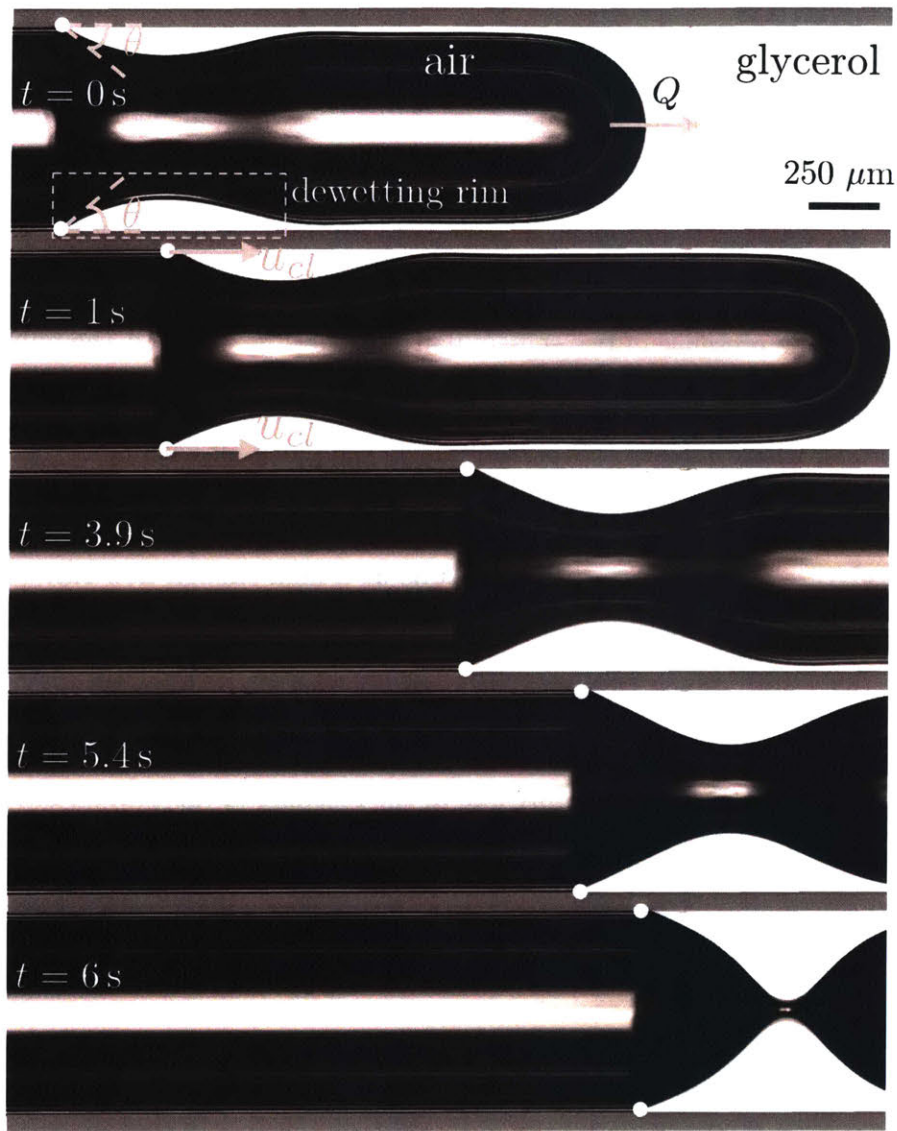
Figure 5-1: Displacement of a partially-wetting liquid from a tube: as the glycerol (white) is withdrawn from the right end of the micro-capillary tube with a constant flow rate Q, air (black) invades the tube from the left end at atmospheric pressure, and entrains a thin film of the glycerol on the tube walls (the white color in the middle of the tube is due to light refraction). The entrained liquid film then starts receding from the tube wall with a velocity u_{cl}, forming a growing dewetting rim behind the contact line, where the liquid, solid, and air meet at a non-zero contact angle θ. As the liquid rim grows, the bubble neck diameter shrinks and ultimately leads to the breakup and formation of a bubble.

5.1 Approach to singularity: two distinct self-similar regimes

In the case of bubble formation in a large quiescent tank, the balance of radial viscous flow and surface tension causes the bubble neck diameter to shrink linearly in time (Burton et al., 2005; Thoroddsen et al., 2007). In contrast, here, during the process of bubble pinch-off in a micro-capillary tube, the evolution of the diameter of the bubble neck indicates the presence of two self-similar regimes (Fig. 5-2 (a)): the bubble neck diameter initially follows a $\tau^{1/5}$ scaling before transitioning to the familiar linear scaling regime, where $\tau = (t_0 - t)$ is the time to the pinch-off with t_0 as the breakup time.

When glycerol is withdrawn from the tube at a high-enough flow rate $(Q > Q_c)$ (Zhao et al., 2018), air penetrates the tube from the left side leaving a film of the liquid on the walls. Since the liquid is partially wetting to the tube $(\theta_{eq} \approx 65°)$ it starts dewetting from the tube wall, forming a growing dewetting rim (Fig. 5-3). Initially, the flow in the film is mainly due to the receding of the contact line, leading to the flow to be mainly parallel to the tube axis. This observation allows us to describe the dynamics of the growing dewetting rim using a long-wave approximation (Zhao et al., 2018):

$$\frac{\partial \tilde{r}}{\partial \tilde{\tau}} = \frac{1}{16^2} \frac{1}{\tilde{r}} \frac{\partial}{\partial \tilde{z}} \left(\mathcal{M}(\tilde{r}) \frac{\partial}{\partial \tilde{z}} \left[\Pi(\tilde{r}) - \tilde{\kappa} \right] \right), \tag{5.1}$$

where $\tilde{r}(\tilde{z}, \tilde{\tau})$ is the radius of the neck of the bubble, $\mathcal{M}(\tilde{r}) = 1 - 16\tilde{r}^2 + 48\tilde{r}^4 - 64\tilde{r}^4 \ln 2\tilde{r}$ is the mobility, $\Pi(\tilde{r}) = 6(1 - \cos\theta_{eq})(\delta^2/(1/2 - \tilde{r})^3)(1 - \delta/(1/2 - \tilde{r}))$ is the disjoining pressure with δ as the precursor film thickness, and $\tilde{\kappa} = 1/\tilde{r} - \tilde{r}_{\tilde{z}\tilde{z}}$ is the curvature. Here, all length scales are non-dimensionalized by the tube diameter d, and the dimensionless time to the pinch-off is defined as $\tilde{\tau} = \tau/t^*$, where $\tau = (t_0 - t)$ is the time to the pinch-off with t_0 as the breakup time and $t^* = \mu d/\gamma$ is the visco-capillary time scale. Near the point of pinch-off, we postulate that the shape of the profile becomes self-similar: $\tilde{R}(\xi) = \tilde{r}(\tilde{z}, \tilde{\tau})/\tilde{\tau}^\alpha$, and $\xi = (\tilde{z} - \tilde{z}_0)/\tilde{\tau}^\beta$ (inset of Fig. 5-2
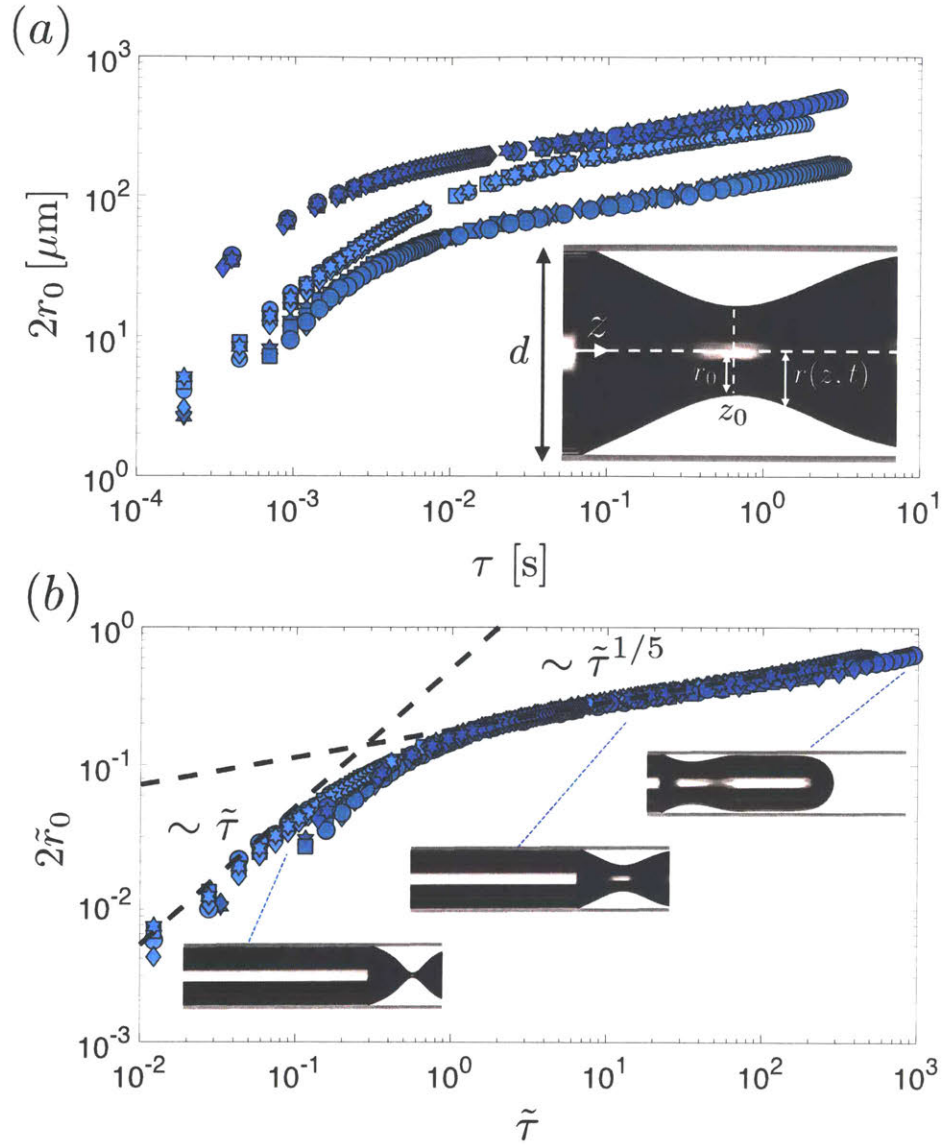
Figure 5-2: Evolution of the neck diameter versus time $\tau = (t_0 - t)$ to pinch-off at t_0. (a) Data from 12 different experiments are shown: light blue symbols correspond to $d = 750$ μm and $\mu = 1.4$ Pa.s; the cyan symbols correspond to $d = 280$ μm and $\mu = 1.4$ Pa.s; the dark blue symbols correspond to $d = 750$ μm and $\mu = 0.2$ Pa.s. Each color represents data corresponding to 4 different flow rates with $\text{Ca} = \mu U/\gamma \in [0.008, 0.02]$, where $U = 4Q/(\pi d^2)$ and Q is the liquid flow rate. While changing the flow rate does not influence the evolution of the bubble neck diameter ($2r_0$), changing μ or d shifts the curves. (b) When time and length scales are non-dimensionalized with the visco-capillary time scale $t^* = \mu d/\gamma$ and the tube diameter d, respectively, the data corresponding to all 12 experiments collapse onto a single curve ($\tilde{\tau} = \tau/t^* = \gamma\tau/(\mu d)$, and $\tilde{r}_0 = r_0/d$). Here, two self-similar regimes can be observed: an early-time regime, which follows a $1/5$ power-law scaling in time, and a late-time regime very close to the point of breakup, which follows a linear scaling in time.

163

(a)). We can neglect the disjoining pressure in the vicinity of the singularity, which is far away from the contact line. Substituting this ansatz back into Eq. (5.1), we arrive at an ordinary differential equation for the neck profile:

$$(-\alpha\tilde{R} + \beta\xi\tilde{R}')\tilde{\tau}^{\alpha-1} = \frac{1}{16^2}\frac{1}{\tilde{R}}\left(\left[-\frac{2}{\tilde{R}^3}\tilde{R}'^2 + \frac{1}{\tilde{R}^2}\tilde{R}''\right]\tilde{\tau}^{-2(\alpha+\beta)} + \tilde{R}''''\tilde{\tau}^{-4\beta}\right), \quad (5.2)$$

where primes indicate differentiation. For all the terms to balance in time we need to have $\alpha = \beta = 1/5$, which leads to $\tilde{R}(\xi) = \tilde{r}(\tilde{z},\tilde{\tau})/\tilde{\tau}^{1/5}$, and $\xi = (\tilde{z} - \tilde{z}_0)/\tilde{\tau}^{1/5}$. This is consistent with the scaling of the neck diameter as a function of time to pinch-off in the early-time self-similar regime shown in Fig. 5-2(b).

The equation governing the dewetting rim in the early self-similar regime is therefore the following:

$$(-\tilde{R} + \xi\tilde{R}') = \frac{5}{16^2}\frac{1}{\tilde{R}}\left(\left[-\frac{2}{\tilde{R}^3}\tilde{R}'^2 + \frac{1}{\tilde{R}^2}\tilde{R}''\right] + \tilde{R}''''\right), \quad (5.3)$$

which represents the balance of viscous forces on the left-hand side with the surface tension forces on the right-hand side. This type of ordinary differential equations typically leads to an infinite family of solutions, where only one is found to be stable (Papageorgiou, 1995; Brenner et al., 1996). To obtain the self-similar solution of the ODE, we solve the original partial differential equation (5.1) numerically and extract the self-similar solution from the late-time solution of the PDE very close to the point of pinch-off. The self-similar solution obtained using this technique is shown as the dashed line in Fig. 5-4(b) and shows an excellent agreement with the experimental data at the early-time self-similar regime, where the long-wave model is valid.

The early-time self-similar regime is an example of self-similarity of the first kind, in which the scaling exponents can be determined based on dimensional analysis (Barenblatt, 1996), as was done above. The crossover to the late-time self-similar regime, however, hints to the breakdown of the long-wave model very close to the pinch-off. While both regimes are governed by a balance of surface tension and viscous forces, the crossover occurs due to a change in the nature of the viscous flow in the dewetting film from axially dominated to radially dominated as the dominant
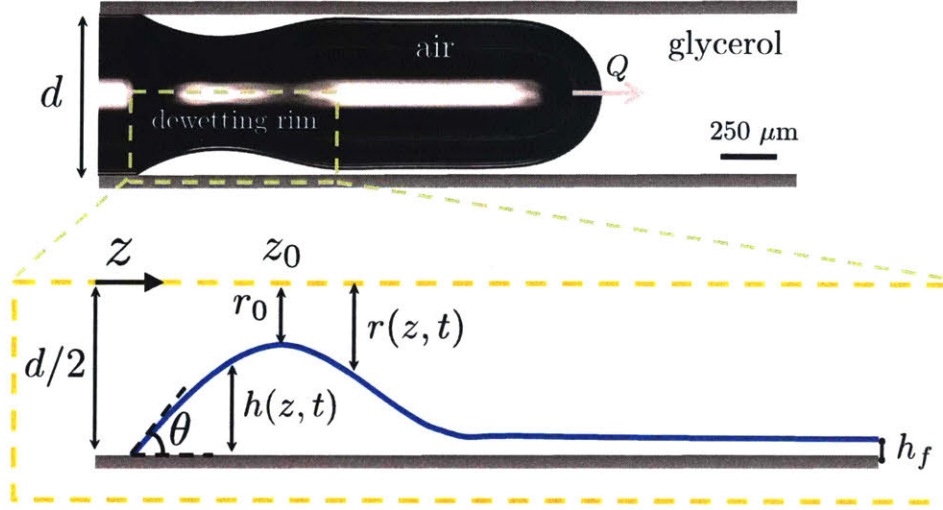
164

Figure 5-3: Schematics of the dewetting rim: as the contact line recedes from the tube wall, liquid accumulates behind it and the rim keeps growing. The dynamics of this growing rim can be described using a long-wave approximation (Eq. (5.1)). The film thickness downstream of the rim is set by the Taylor-Bretherton scaling $h_f/(d/2) = 1.34\mathrm{Ca}_f^{2/3}/(1 + 1.34 \times 2.5\mathrm{Ca}_f^{2/3})$, where $\mathrm{Ca}_f = \mu U_f/\gamma$ with U_f as the air finger velocity(Taylor, 1961a; Bretherton, 1961; Aussillous and Quéré, 2000; Klaseboer et al., 2014). This relationship combined with the conservation of mass: $Q = \pi(d/2 - h_f)^2 U_f$ determine both the finger velocity and the film thickness.

viscous dissipation changes from the moving contact line singularity to the pinch-off singularity.

5.2   Crossover in self-similarity

To estimate the crossover time between the two regimes, we compare their corresponding radial velocities. In the early-time regime, the growth rate of the dewetting rim is proportional to the velocity of the receding contact line, i.e. $dr_0/d\tau \sim U_{cl} \sim (\gamma/\mu)\theta_{eq}^3$, which is nearly constant for a given wettability (Snoeijer and Eggers, 2010; Zhao et al., 2018). In the late-time regime, the bubble neck close to the point of singularity can be approximated as an axisymmetric cylinder, and the flow in the viscous fluid can be approximated as radial. The normal viscous stress generated by the radial flow is balanced by surface tension, leading to $dr_0/dt = -\gamma/(2\mu)(1 - 2r_0/r_c)$ (Bolaños-Jiménez et al., 2009), where $r_c \approx r_c(t = 0)$) is the axial radius of curvature. The radius of the
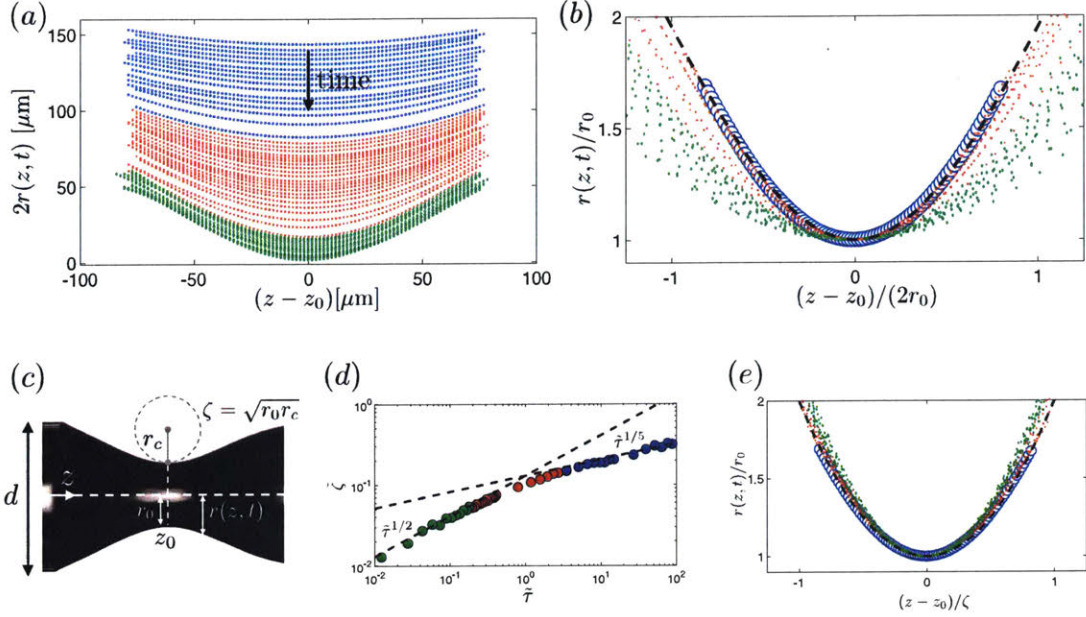
Figure 5-4: Self-similarity of the neck profile: (a) The evolution of the bubble neck profile in time (data corresponding to $d = 750$ μm, $\mu = 1.4$ Pa.s, and Ca = 0.008); blue and green symbols represent the data corresponding to the early and late-time self-similar regimes, and red symbols represents the transition between the two. (b) Scaling the neck profile with the minimum neck diameter collapses the data corresponding to the early-time self-similar regime, where $\tilde{R}(\xi) = \tilde{r}(\tilde{z}, \tilde{\tau})/\tilde{\tau}^{1/5}$, and $\xi = (\tilde{z} - \tilde{z}_0)/\tilde{\tau}^{1/5}$. The dashed line, overlaying the blue symbols corresponding to the early-time self-similar regime, represents the self-similar solution of the long-wave model. The data corresponding to the late-time self-similar regime, however, deviate from the predictions of the long-wave model. (c) The definition of parameters used to characterize the bubble neck profile. (d) The evolution of the lateral length scale defined as $\tilde{\zeta} = \sqrt{\tilde{r}_0 \tilde{r}_c}$ versus time to pinch-off. In the early-time regime, $\tilde{\zeta} = \sqrt{\tilde{r}_c \tilde{r}_0} \sim \tilde{\tau}^{1/5}$, consistent with the predictions of the long-wave model. In the late-time regime, however, $\tilde{r}_0 \sim \tilde{\tau}$ and $\tilde{\zeta} \sim \tilde{\tau}^{1/2}$, which indicates that the axial radius of curvature becomes constant, i.e. the neck profile becomes a parabola that simply translates in time (Doshi et al., 2003; Eggers and Fontelos, 2015). (e) Scaling the lateral length scale with that obtained in (d) leads to the collapse of the bubble neck profiles during the entire pinch-off process (shown in (a)) onto a single parabolic curve: $r/r_0 = 1 + [(z - z_0)/\zeta]^2$ (dashed line).

neck can therefore be approximated as $r_0(t) = r_{00}[1 - r_c/(2r_{00})]e^{\gamma t/(\mu r_c)} + r_c/(2r_{00})$ where $r_{00} = r_0(t = 0)$, leading to $dr_0/d\tau \sim (\gamma/\mu)e^{-\tau/t^*}$ as the radial velocity in the late-time regime (Bolaños-Jiménez et al., 2009). Note that very close to the point of pinch-off, we have $r_0 \ll r_c$, leading to $dr_0/d\tau = \gamma/(2\mu)$, which is the familiar linear scaling in time (Doshi et al., 2003; Burton and Taborek, 2008). Equating the two radial velocities corresponding to the early- and late-time regimes we obtain an estimate of the crossover time $\tau_c \sim t^* = \mu d/\gamma$, indicating that the visco-capillary time scale sets the point of transition between the two regimes. Fig. 5-2(b) shows that, indeed, using the visco-capillary time scale and the tube diameter as the characteristic time and length scales leads to the collapse of the data corresponding to 12 different experiments with different tube diameters ($d = 280, 750 \ \mu$m), liquid viscosities ($\mu = 0.2, 1.4$ Pa.s), and flow rates ($\mathrm{Ca} = \mu U/\gamma \in [0.008, 0.02]$).

The long-wave model predicts that both the bubble neck diameter and its lateral extent scale as $\tilde{\tau}^{1/5}$. Fig. 5-4(a) shows the evolution of the bubble neck profile in time (for the experiment with $d = 750 \ \mu$m, $\mu = 1.4$ Pa.s, and $\mathrm{Ca} = 0.008$), where the blue and green symbols correspond to the early- and late-time regimes, respectively, and red corresponds to the transition between the two regimes. In Fig. 5-4(b), we show that, indeed, scaling both the neck diameter and lateral dimension with the the minimum neck diameter collapses the profiles in the early-time regime (blue symbols). The self-similar solution of the long-wave model (black dashed line) fits the data in this regime. This observation further confirms the validity of the long-wave model in the early-time self-similar regime. The data in the late-time regime (green symbols), however, cannot be completely collapsed using the scalings in Fig. 5-4(b), and deviate from the predictions of the long-wave theory.

In the local neighborhood of the minimum neck radius, we expect the profile to follow a parabolic profile with $r(z, t) = r_0(t) + (z - z_0)^2/r_c(t)$, where r_0 is the minimum neck radius, and r_c is the axial radius of curvature. Scaling the profile with $r_0(t)$, we then obtain $r/r_0 = 1 + (z - z_0)^2/\zeta^2$, where $\zeta = \sqrt{r_c r_0}$ represents the axial extent of the parabola.

In the early-time self-similar regime, we showed that both the minimum neck

radius as well as its axial length follow the scaling $\tilde{\tau}^{1/5}$. Therefore, we expect $\tilde{\zeta} = \sqrt{\tilde{r}_c \tilde{r}_0} \sim \tilde{\tau}^{1/5}$ in this regime. This scaling is indeed observed in Fig. 5-4(d) in the early-time self-similar regime.

Very close to the point of pinch-off in the late-time self-similar regime, we can approximate the bubble neck as a cylinder, which effectively acts as a sink sucking the liquid radially towards the tube center, leading to a balance of normal viscous stresses and the surface tension $\partial r / \partial \tau = \gamma / (2\mu)$ (Doshi et al., 2003; Eggers and Fontelos, 2015). Therefore, the neck profile is simply translated in time without changing its shape. Assuming the scale-invariance of the dynamics close to the singularity, and using the ansatz $\tilde{R}(\xi) = \tilde{r}(\tilde{z}, \tilde{\tau}) / \tilde{\tau}^\alpha$, and $\xi = (\tilde{z} - \tilde{z}_0) / \tilde{\tau}^\beta$, the governing equation for the neck profile becomes:

$$-\alpha \tilde{\tau}^{\alpha-1} \tilde{R} + \beta \tilde{\tau}^{\alpha-1} \xi \tilde{R}' = -1, \tag{5.4}$$

where prime indicates differentiation. For all the terms to balance in time we need to have $\alpha = 1$. The value of the exponent β, however, cannot be determined from dimensional analysis, indicating that the self-similarity is of the second kind (Barenblatt, 1996).

Here, we briefly review how to determine the value of the exponent β in the second self-similar regime (Eggers, 2012). The solution of Eq. (5.4) is described by $\tilde{R} = 1 + a\tilde{\xi}^{1/\beta}$, in which a is a constant of integration that depends on the outer solution away from the singularity. Close to the pinch-off time, the neck profile away from the singularity becomes effectively frozen in time, which leads to a constraint on the behavior of the self-similar solution: $\tilde{r}(\tilde{z} \to \tilde{z}_0 \pm \epsilon, \tilde{\tau} \to \epsilon) = \tilde{\tau}^\alpha \tilde{R}((\tilde{z} - \tilde{z}_0) / \tilde{\tau}^\beta) = \text{const}$, and therefore we need to have $\tilde{R}(\xi \to \pm\infty) \sim \xi^{\alpha/\beta}$. The regularity condition also implies that $1/\beta$ must be a positive integer and even and $a > 0$. We can therefore have a discrete family of solutions for β, i.e. $\beta_i = 1/(2i)$ with $i = 1, 2, \dots$. This is similar to the breakup of a drop, where also an infinite family of solutions is obtained (Papageorgiou, 1995; Brenner et al., 1996).

To find out which one of these solutions is selected, we need to address the stabil-

ity of these solutions. Briefly, we use a change of variables $T = -\ln \tilde{\tau}$, rewriting the equation governing the self-similar profile as $R_T = R - \beta\xi R' - 1$, which is a dynamical system representation of the original equation, for which the original self-similar solution will be a fixed point. We can therefore perturb the self-similar solution as $\tilde{R}(\xi, T) = \bar{R}(\xi) + \epsilon e^{nT}P(\xi)$, where n is the eigenvalue and P is the eigenfunction. The stability analysis (Eggers, 2012) shows that the stable solution is described by $\beta = 1/2$, i.e. $\tilde{R}(\xi) = 1 + a\xi^2$. This implies that the neck profile can be described as $\tilde{r}(\tilde{z}, \tilde{\tau}) = \tilde{\tau}(1 + a[(\tilde{z} - \tilde{z}_0)/\tilde{\tau}^{1/2}]^2) = \tilde{\tau} + a(\tilde{z} - \tilde{z}_0)^2$, which is a parabola that is simply translated in time.

We therefore have $\tilde{\zeta} \sim \tilde{\tau}^{1/2}$ as the scaling of the lateral length scale, which is supported by the experimental data in the late-time regime (Fig. 5-4(d)). Using ζ as the lateral length scale, we can therefore collapse the neck profiles over the entire pinch-off process (Fig. 5-4(e)), which is overlaid by the parabola $R(\xi) = 1 + \xi^2$.

5.3 Universality of the pinch-off

While in the early-time self-similar regime, both the neck radius and its axial radius of curvature are time-dependent, in the late-time regime the axial radius of curvature of the neck profile becomes independent of time. This can be shown easily noting that in the late-time regime $\tilde{r}_0 \sim \tilde{\tau}$ (Fig. 5-2(b)), and $\tilde{\zeta} = \sqrt{\tilde{r}_c \tilde{r}_0} \sim \tilde{\tau}^{1/2}$ (Fig. 5-4(c)), leading to $\lim_{\tilde{\tau} \to 0} \tilde{r}_c(\tilde{\tau}) = \tilde{r}_{cf} = \text{const}$. The temporal invariance of the axial radius of curvature of the bubble neck might suggest that the separation of scales is lost and the singularity formation becomes non-universal. In other words, the lateral extent of the neck profile retains an imprint of the details of the experimental system and the memory of the initial/boundary conditions will persist all the way to the point of pinch-off (Doshi et al., 2003; Eggers and Fontelos, 2015).

In our system, however, this late-time self-similar regime is preceded by an early-time self-similar regime of the first kind, which sets the lateral length scale of the late-time regime at the crossover between the two regimes. This characterization is captured in Fig. 5-4(c) and Fig. 5-5, which shows a crossover in the scaling of the

169
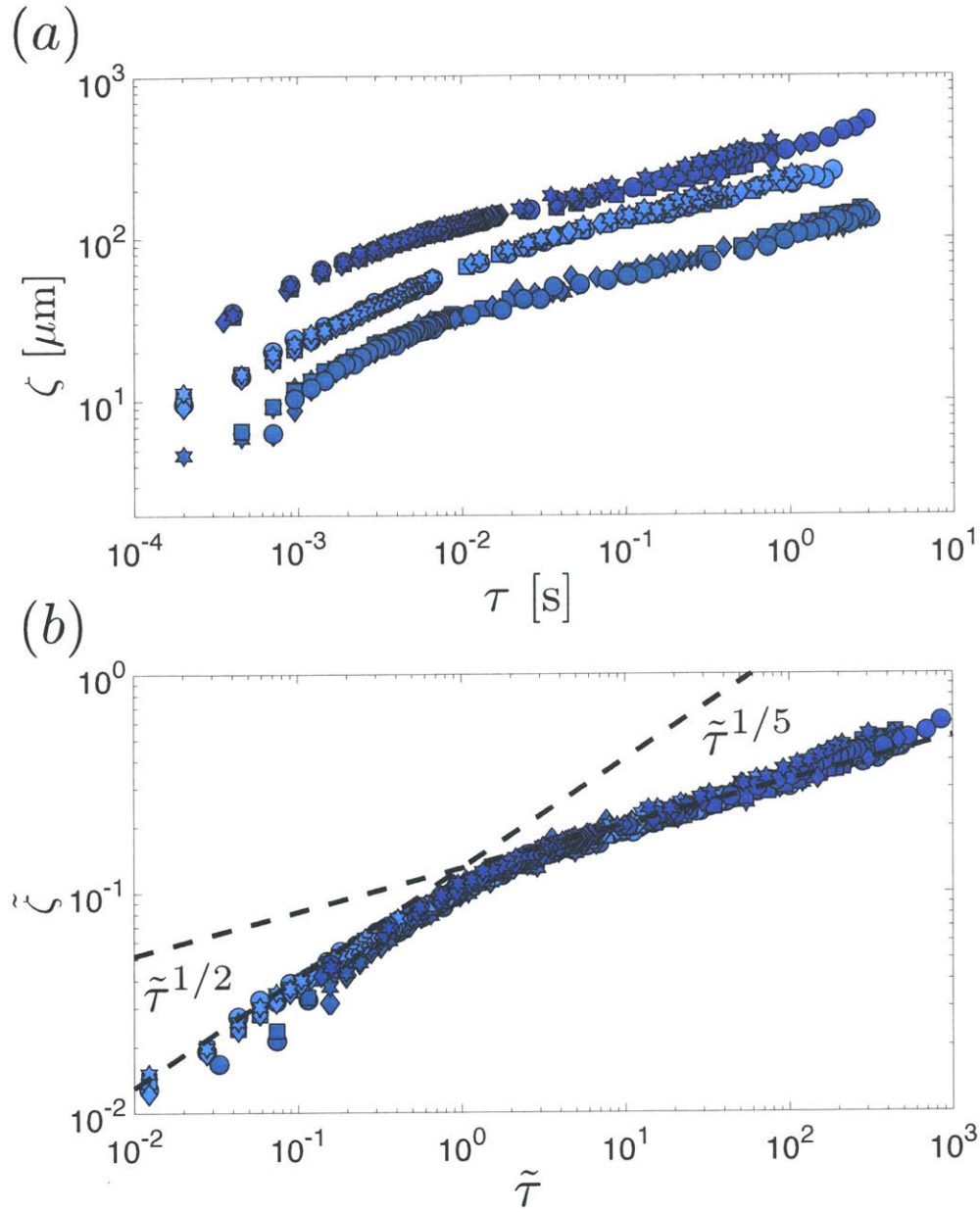
Figure 5-5: The evolution of the lateral length scale of the bubble neck ($\zeta = \sqrt{r_0 r_c}$) in time: (a) dimensional, and (b) non-dimensional. Data from 12 different experiments are shown: light blue symbols correspond to $d = 750$ μm and $\mu = 1.4$ Pa.s; the cyan symbols correspond to $d = 280$ μm and $\mu = 1.4$ Pa.s; the dark blue symbols correspond to $d = 750$ μm and $\mu = 0.2$ Pa.s. Each color represents data corresponding to 4 different flow rates with Ca $= \mu U / \gamma \in [0.008, 0.02]$, where $U = 4Q/(\pi d^2)$ and Q is the liquid flow rate. While changing the flow rate does not influence the evolution of the lateral length scale ($\tilde{\zeta}$), changing μ or d shifts the curves.

lateral length scale at $\tilde{\tau} \approx 1$. The self-similar solution of Eq. (5.3) shows that in the early-time regime, $\tilde{r}_0 \approx 0.09\tilde{\tau}^{1/5}$, and $\tilde{r}_c \approx 0.19\tilde{\tau}^{1/5}$, leading to $\tilde{\zeta} = \sqrt{\tilde{r}_c\tilde{r}_0} \approx 0.13\tilde{\tau}^{1/5}$ as the scaling of the lateral length scale. In the late-time regime, we also have $\tilde{\zeta} = \sqrt{\tilde{r}_c\tilde{r}_0} \approx \tilde{\tau}^{1/2}\sqrt{\tilde{r}_{cf}}/2$. Therefore, at the point of crossover, $\tilde{\tau} \approx 1$, the early-time self-similar regime sets the lateral length scale of the late-time regime ($\tilde{\zeta} \approx 0.13$), leading to $\tilde{r}_{cf} \approx 0.07$. Fig. 5-6 shows a plot of the axial radius of curvature as a function of time to the pinch-off. Here, we observe that, indeed, the data corresponding to all the 12 experiments collapse on a single curve, with the asymptotic universal radius of curvature of $\tilde{r}_{cf} \approx 0.07$. This observation indicates that the early-time self-similar regime effectively erases the system's memory and restores the universality to bubble breakup in a viscous liquid.

We therefore conclude that the combined effect of confinement and the contact line motion leads to the emergence of an early-time self-similar regime of the first kind, which at late times crosses over to a regime of self-similarity of the second kind. While the balance remains between viscous and surface tension forces in both regimes, the crossover occurs due to a change in the dominant viscous dissipation from the spatially-localized moving contact line singularity at early times to the temporally-localized bubble pinch-off singularity at late times. This change in the dominant viscous dissipation is accompanied by a change in the direction of the flow from axially-dominated in the early-time regime to radially-dominated in the late-time regime. The late-time regime is also observed in the breakup of bubbles in unbounded domains, where flow is mainly radial and the lateral length scale of the bubble is sensitive to the details of the experimental system, making the breakup non-universal (Doshi et al., 2003). Here, in the case of bubble breakup in confined domains, however, we observe that the lateral length scale is set by the early-time self-similar regime, effectively erasing the system's memory and restoring the universality to the breakup process.

The restoration of universality has important consequences for the control of bubble/drop/emulsion generation in microfluidics with a myriad of applications in medicine (Lindner, 2004) and material science (Park et al., 2010; Rodríguez-Rodríguez
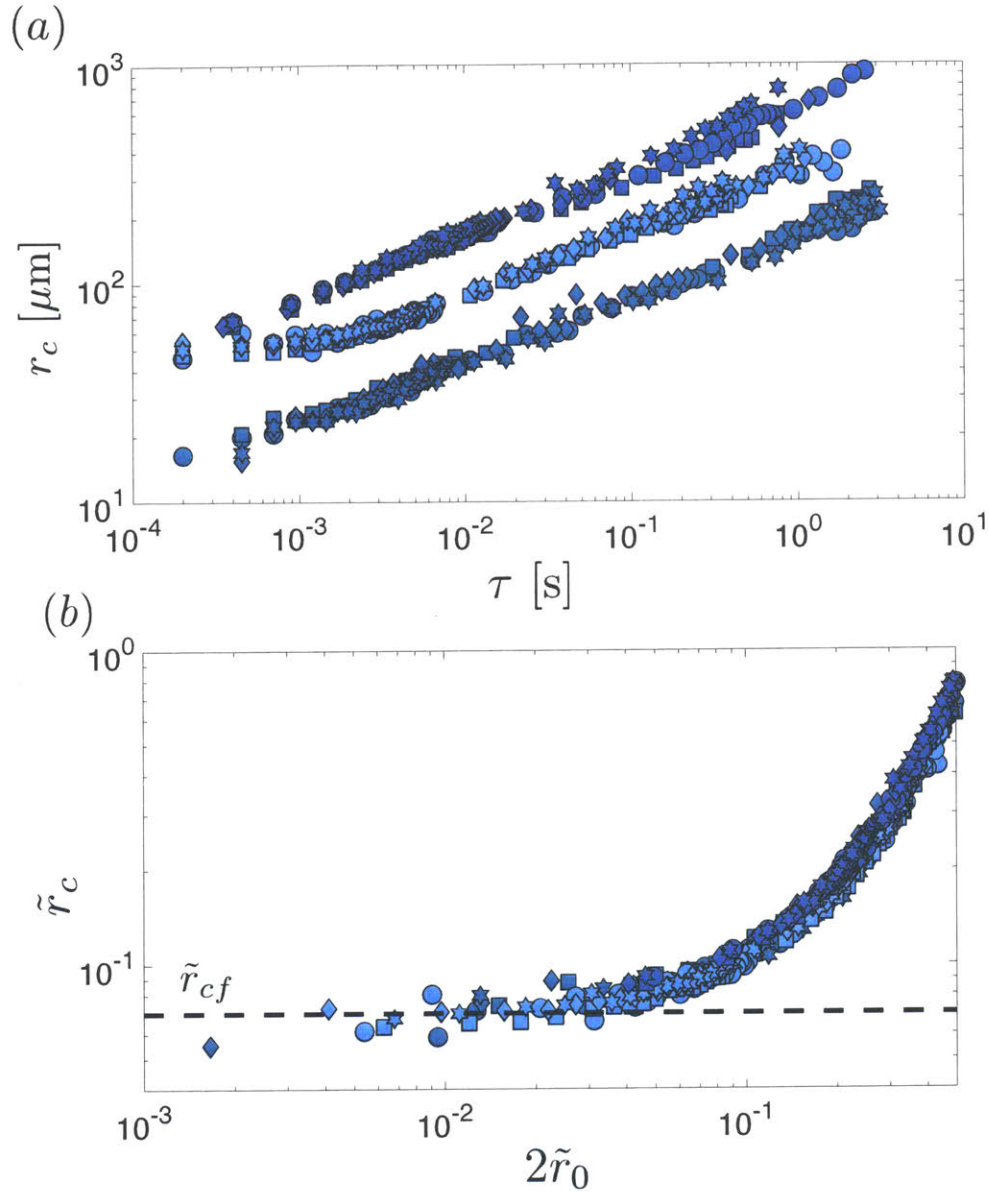
Figure 5-6: The evolution of the axial radius of curvature versus time to the pinch-off shows that as we get close to the point of pinch-off, the curvature asymptotes to a constant value (symbols are the same as in Fig. 5-2). (a) The time evolution of axial radius of curvature is independent of the flow rate, but changes when the liquid viscosity or the tube diameter are varied. (b) The data corresponding to all 12 experiments collapse on a single curve when non-dimensional axial radius of curvature is plotted against the non-dimensional minimum neck diameter. The non-dimensional axial radius of curvature asymptotes to a universal constant $\lim_{\tilde{\tau} \to 0} \tilde{r}_c(\tilde{\tau}) = \tilde{r}_{cf} \approx 0.07$ at late-times near the pinch-off event.

et al., 2015) as well as for understanding of multiphase flows in natural geologic phenomena (Parmigiani et al., 2016; Ruppel and Kessler, 2017), where confinement and liquid-solid interaction play a key role. While we have focused on the case of bubble breakup in a viscous liquid, we expect the early-time self-similar regime (perhaps with a different scaling exponent) to persist for any other fluid-fluid displacement process involving moving contact lines.

Chapter 6

Revisiting the Saffman–Taylor instability in imbibition: emergence of a new scaling

In their seminal work, Saffman and Taylor showed that when a less viscous fluid displaces a more viscous immiscible one in a Hele-Shaw cell, the interface between the two fluids becomes unstable and fingers of the invading fluid protrude into the defending fluid. Here, we revisit the Saffman-Taylor instability in the imbibition regime, when the invading fluid is more wetting to the substrate, using both experiments in radial Hele-Shaw cells and theory. We show that thin films of the invading fluid become entrained and propagate on the walls, leading to an entirely different dynamics from the classical Saffman-Taylor instability. We propose a model to describe the evolution of these films and show that they lead to a front instability akin to the fingering of thin films flowing on inclined plates. We show that the wavelength of instability follows a scaling different from the scaling of Saffman–Taylor, implying that this thin-film front instability belongs to a new class of pattern forming processes.

Revisiting the Saffman-Taylor instability, (Levaché and Bartolo, 2014) have recently reported the observation of new instability regimes in imbibition, when the invading fluid is more wetting to the substrate. Beyond a critical displacement rate, a forced wetting transition was observed, where thin films of the invading fluid became

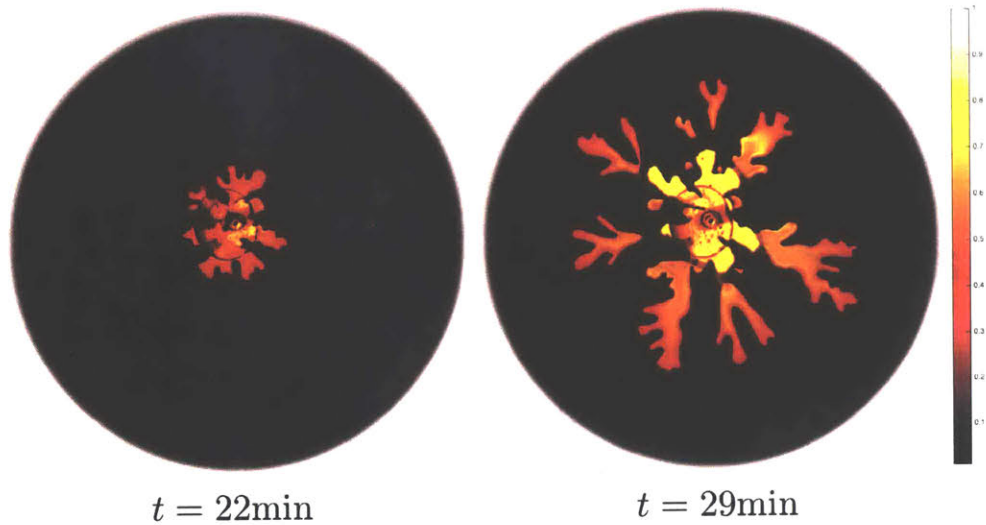$$t = 22\text{min} \qquad\qquad t = 29\text{min}$$

Figure 6-1: The radial Hele-Shaw cells are first filled with the Krytox GPL105 liquid and then dyed water is injected in the middle. Water is more wetting, $\theta_{eq} \approx 30^o$ and less viscous $\mu = \mu_2/\mu_1 = 1000$ and becomes entrained and propagates along the substrate next to the injection port. The color map here shows the light intensity. Over time, the films swell, and form a bridge when touch the other wall of the cell. The bridge formation is evident by the increase in the light intensity in particular close to the injection port. In this work, we are mainly interested in the dynamics of the entrained thin films before the bridge forms. Since these films propagate in front of the bridged section, they determine the morphology of the instability.

entrained on the walls, moving ahead of the main meniscus. The dynamics, evolution, and instability of these entrained thin films, however, remains unexplained. Here, using a combination of experiments in radial Hele-Shaw cells and theoretical modeling, we study the dynamics of these films and show how they lead to an unstable front. Our work therefore goes beyond the classical Saffman-Taylor instability by proposing a new pathway to the front instability in immiscible flows in Hele-Shaw cells. Figure 6-1 shows the typical dynamics of the entrainment and propagation of the thin films in the unstable imbibition regime.

The flow schematics is presented in Fig. 6-2, which shows thin films of water (fluid 1) with height h coat the surface of the Hele-Shaw cell and displace the oil phase (fluid 2). We focus on the unstable imbibition regime, in which the oil phase is much more viscous than water $M = \mu_2/\mu_1 \gg 1$ and water is more wetting to the surface than oil $\theta_{eq} \ll 1$.
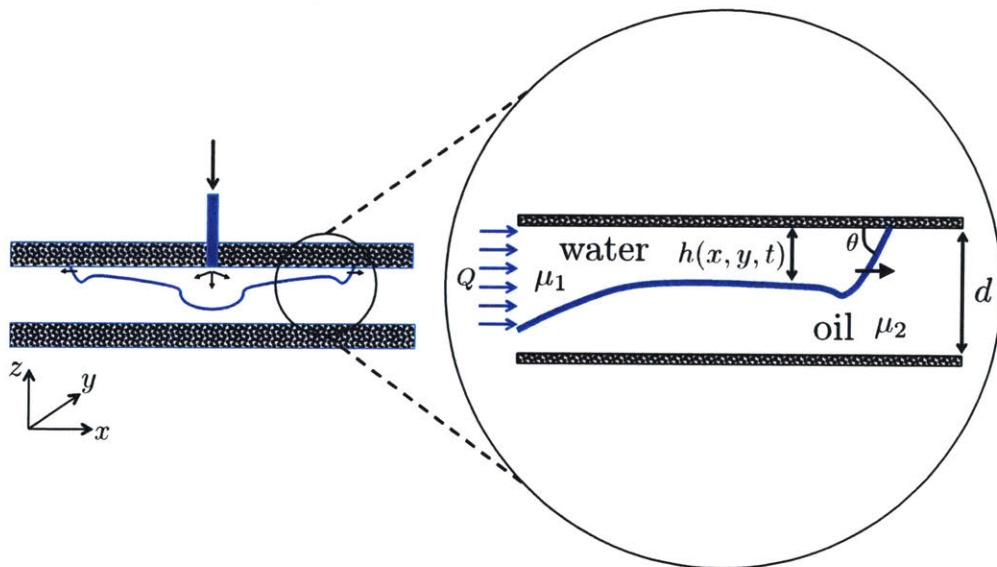
Figure 6-2: Schematic of the entrained thin film flowing in a rectangular Hele-Shaw cell with the width of the cell going into the plane.

6.1 Theoretical Formulation

Here, we use a long-wave approximation to derive a model describing the dynamics of the thin-film front. The fluid flow inside the film is governed by the Navier-Stokes equations

$$\rho_\alpha \frac{D\mathbf{u}_\alpha}{Dt} = -\nabla P_\alpha + \nabla \cdot \mathbf{T}_\alpha, \tag{6.1}$$

where ρ_α is the liquid density, $D/Dt = \partial/\partial t + \mathbf{u} \cdot \nabla$ is the material derivative, $\mathbf{u} = (u, v, w)$ are the fluid velocity components in (x, y, z) directions, respectively; P_α represents the liquid pressure, and $\mathbf{T}_\alpha$ is the stress tensor, with $\alpha = 1$ representing the invading fluid and $\alpha = 2$ representing the displaced fluid. The stress tensor can be further decomposed into two parts, $\mathbf{T} = \boldsymbol{\tau} + \mathbf{M}$, where $\boldsymbol{\tau}$ is the deviatoric stress and $\mathbf{M}$ represents the stress due to external body forces, taken to be zero in this work. The deviatoric stress is a function of the strain rate $\boldsymbol{\epsilon} = \left(\nabla \mathbf{u} + \nabla \mathbf{u}^T\right)/2$, and for a Newtonian liquid can be simply written as $\tau_{ij} = \mu \left(\partial u_i/\partial x_j + \partial u_j/\partial x_i\right)$. These governing equations of motion are subject to the no slip and no penetration boundary conditions on the walls $\mathbf{u}(z = 0, d) = 0$, continuity of shear stress at the fluid-fluid interface $\tau_{zx,1}(h) = \tau_{zx,2}(h)$ and $\tau_{zy,1}(h) = \tau_{zy,2}(h)$, normal stress jump across the interface $P_1 - P_2 = \mathcal{N} + \Pi$, where $\mathcal{N}$ represents the Laplace pressure jump and Π represents the disjoining pressure due to the intermolecular interactions. Further, we need to enforce the continuity of the velocity normal to the interface $w_1(h) = w_2(h)$ and the kinematic boundary condition at the fluid-fluid interface: $D(z - h)/Dt = 0$, leading to:

$$w_1(h) = \frac{\partial h}{\partial t} + u_1 \frac{\partial h}{\partial x} + v_1 \frac{\partial h}{\partial y} \tag{6.2}$$

$$w_2(h) = \frac{\partial h}{\partial t} + u_2 \frac{\partial h}{\partial x} + v_2 \frac{\partial h}{\partial y}. \tag{6.3}$$

We non-dimensionalize the equations in the following way: $(\tilde{x}, \tilde{y}) = (x, y)/L$, $\tilde{z} = z/H$, $\tilde{h} = h/H$, $(\tilde{u}, \tilde{v}) = (u, v)/U$, $\tilde{w} = w/(\epsilon U)$, $\tilde{t} = t/(L/U)$, $\tilde{P} = P/\left(\mu_1 U L/H^2\right)$, and $\tilde{\tau} = \tau/\left(\mu_1 U/H\right)$, where $\epsilon = H/L$ and H and L represent a characteristic height

and length, respectively.

In the long-wave approximation, $\epsilon \ll 1$, and assuming inertia to be negligible $\epsilon^2 \text{Re} \ll 1$ with Reynolds number defined as $\text{Re} = \rho_1 UL/\mu_1$, we can considerably simplify the Navier–Stokes equations of motion, leading to $0 = -\partial\tilde{P}_1/\partial\tilde{x} + \partial^2\tilde{u}_1/\partial\tilde{z}^2$ and $0 = -\partial\tilde{P}_2/\partial\tilde{x} + M\partial^2\tilde{u}_2/\partial\tilde{z}^2$ for the x-component of the momentum equation, where $M = \mu_2/\mu_1$ is the ratio of the displaced to invading fluid viscosity. Similarly, the y-component of the momentum equation simplifies to $0 = -\partial\tilde{P}_1/\partial\tilde{y} + \partial^2\tilde{v}_1/\partial\tilde{z}^2$ and $0 = -\partial\tilde{P}_2/\partial\tilde{y} + M\partial^2\tilde{v}_2/\partial\tilde{z}^2$. The z-component of the momentum equation simplifies showing a constant pressure in the gap $0 = -\partial\tilde{P}_1/\partial\tilde{z}$ and $0 = -\partial\tilde{P}_2/\partial\tilde{z}$. We can therefore integrate the x- and y-components of the momentum equation to obtain the velocity components (u_α, v_α).

We consider the liquid to be incompressible, such that $\nabla \cdot \mathbf{u} = 0$, which integrated across the gap leads to:

$$\frac{\partial}{\partial\tilde{x}}\left[\int_0^{\tilde{h}} \tilde{u}_1\,d\tilde{z} + \int_h^{\tilde{d}} \tilde{u}_2\,d\tilde{z}\right] + \frac{\partial}{\partial\tilde{y}}\left[\int_0^{\tilde{h}} \tilde{v}_1\,d\tilde{z} + \int_h^{\tilde{d}} \tilde{v}_2\,d\tilde{z}\right] = 0, \qquad (6.4)$$

which can be written as $\nabla \cdot \mathbf{u}_T = 0$ with $\mathbf{u}_T$ representing the total velocity across the gap.

Further, the incompressibility constraint together with the kinematic boundary conditions leads to the evolution equation of the interface height:

$$\frac{\partial\tilde{h}}{\partial\tilde{t}} + \frac{\partial}{\partial\tilde{x}}\int_0^{\tilde{h}} \tilde{u}_1 d\tilde{z} + \frac{\partial}{\partial\tilde{y}}\int_0^{\tilde{h}} \tilde{v}_1 d\tilde{z} = 0. \qquad (6.5)$$

Replacing the velocity components in the height evolution equation and incompressibility constraint, we finally arrive at (Merkt et al., 2005):

$$\frac{\partial h}{\partial t} + \nabla \cdot \left(\mathcal{M}_2(h)\mathbf{u_T} + \mathcal{M}_1(h)\nabla(\mathcal{N} + \Pi(h))\right) = 0, \qquad (6.6)$$

$$\mathbf{u_T} = A(h)\left(\nabla P_1 + \mathcal{M}_3(h)\nabla(\mathcal{N} + \Pi(h))\right), \qquad (6.7)$$

$$\nabla \cdot \mathbf{u_T} = 0, \qquad (6.8)$$

179

where we have dropped the tildes for brevity, P_1 represents the pressure field in fluid 1 and $\nabla = (\partial/\partial x, \partial/\partial y, 0)$ is the plane gradient operator. The normal pressure jump $\mathcal{N} = P_1 - P_2 = -\nabla^2 h/\tilde{\mathrm{Ca}}$, where $\epsilon^3/\mathrm{Ca} \equiv 1/\tilde{\mathrm{Ca}}$ and $\mathrm{Ca} = \mu_1 U/\gamma$. We have further scaled the time and length scales $(\hat{x}, \hat{y}, \hat{t}) = \tilde{\mathrm{Ca}}^{1/3}(x, y, t)$ to scale out the explicit dependence on the capillary number and dropped the hat over lines for brevity. The normal pressure jump is then simply defined as $\mathcal{N} = -\nabla^2 h$. The disjoining pressure $\Pi(h)$ represents the influence of intermolecular forces on the fluid-fluid interface in the vicinity of the contact line when the film height becomes of the order of few nanometers (Israelachvili, 2011).

The mobilities are defined as follows:

$$\mathcal{M}_1(h) = \frac{h^3(d-h)^3}{3D}\Big(d + h(M-1)\Big), \tag{6.9}$$

$$\mathcal{M}_2(h) = 1 - \mathcal{M}_3(h), \tag{6.10}$$

$$\mathcal{M}_3(h) = \frac{(d-h)^2}{D}\Big(Mh(4d-h) + (d-h)^2\Big), \tag{6.11}$$

$$A(h) = -\frac{D}{12M\Big((M-1)h+d\Big)}, \tag{6.12}$$

$$D(h) = (d-h)^4 + Mh\Big(h^3(M-2) + 4dh^2 - 6d^2h + 4d^3\Big), \tag{6.13}$$

with $M = \mu_2/\mu_1$. Figure 6-3 shows the mobility functions $\mathcal{M}_1(h)$ and $\mathcal{M}_3(h)$ for three different viscosity contrasts $M = \mu_2/\mu_1 = 0.001, 1, 1000$.
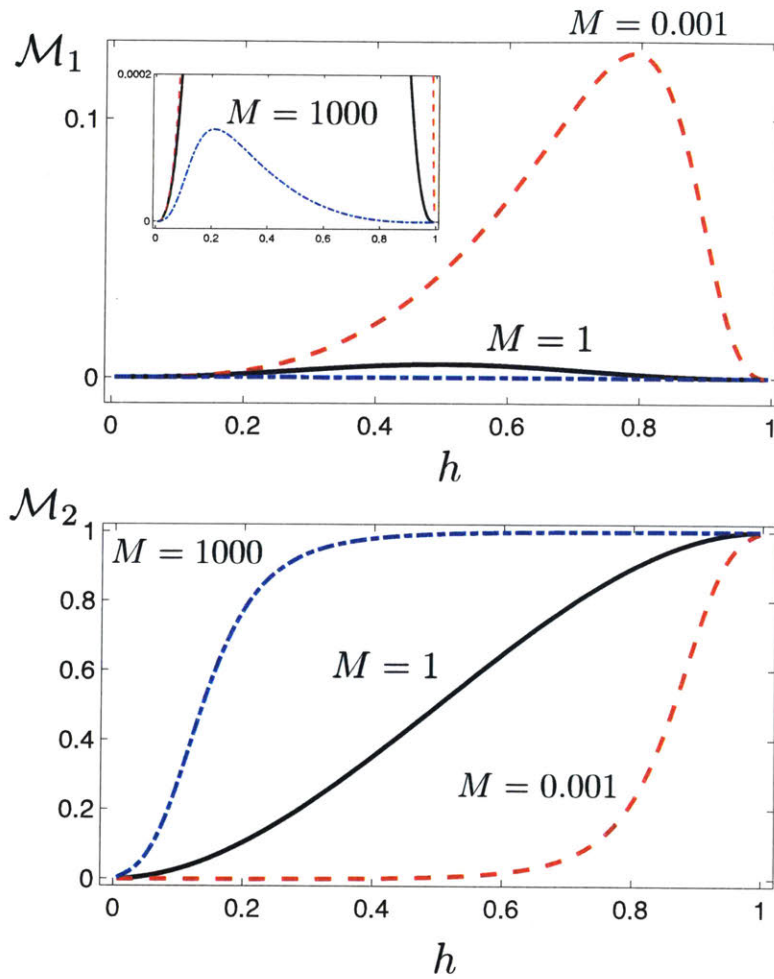
Figure 6-3: Mobilities as defined in the governing equations. $\mathcal{M}_1$ goes to zero in the vicinity of the top and bottom walls and its peak magnitude is a strong function of the viscosity contrast $M = \mu_2/\mu_1$. The mobility function $\mathcal{M}_2$ is a non-convex flux function, which as we will show later leads to three type of solutions.

6.1.1 Free energy description

To gain further insight into the evolution equation, we can rewrite it in terms of the free energy of the system as:

$$\frac{\partial h}{\partial t} + \nabla \cdot \left(\mathcal{M}_2(h)\mathbf{u_T} + \mathcal{M}_1(h)\nabla \left(\frac{\delta \Gamma}{\delta h} \right) \right) = 0, \tag{6.14}$$

where the free energy Γ is defined as:

$$\Gamma = \int f(h) + \frac{1}{2}(\nabla h)^2 \, d\mathbf{x}, \tag{6.15}$$

in which $f(h) = f_b(h) + f_t(h)$ with $f_b(h) = -6\,(1 - \cos\theta_{eq})\,(\delta^2/h^2)\,(1/2 - \delta/(3h))$ and $f_t(h) = -6\,(1 - \cos\theta_{eq})\,(\delta^2/(d-h)^2)\,(1/2 - \delta/(3(d-h)))$ representing the interaction energies with the bottom and top channel surfaces, and disjoining pressure is defined as $\Pi(h) = df/dh$. As shown in Fig. 6-4 we can find the equilibrium states of the system described by this free energy using the Maxwell tangent construction (Rowlinson and Widom, 1982).

Merkt et al. (2005) derived the same model to investigate dewetting of nanometric two-layer films in a channel, where they argued that their results on the instability of thin films is insensitive to the presence of an external mean flow and focused on the case without an external flow. In this work, however, we focus on the front instability of a thin-film front in a macroscopic channel, in which the effect of intermolecular forces become important only in the vicinity of the contact line. Mavromoustaki et al. (2010, 2011) also used the same model in the absence of intermolecular forces, i.e. in the regime of complete wetting, to analyze the front instability of gravity-driven thin film flows in an inclined channel. They focused the case, where a viscous liquid displaces a less viscous liquid or air and analyzed the 1D base state solutions (Mavromoustaki et al., 2010) as well as the front instability (Mavromoustaki et al., 2011). To do the latter, however, they assumed that the flow perpendicular to the streamwise direction can be set to zero, simplifying the equations of motion. As we will show in our work, such an assumption leads to incorrect results for the case

182
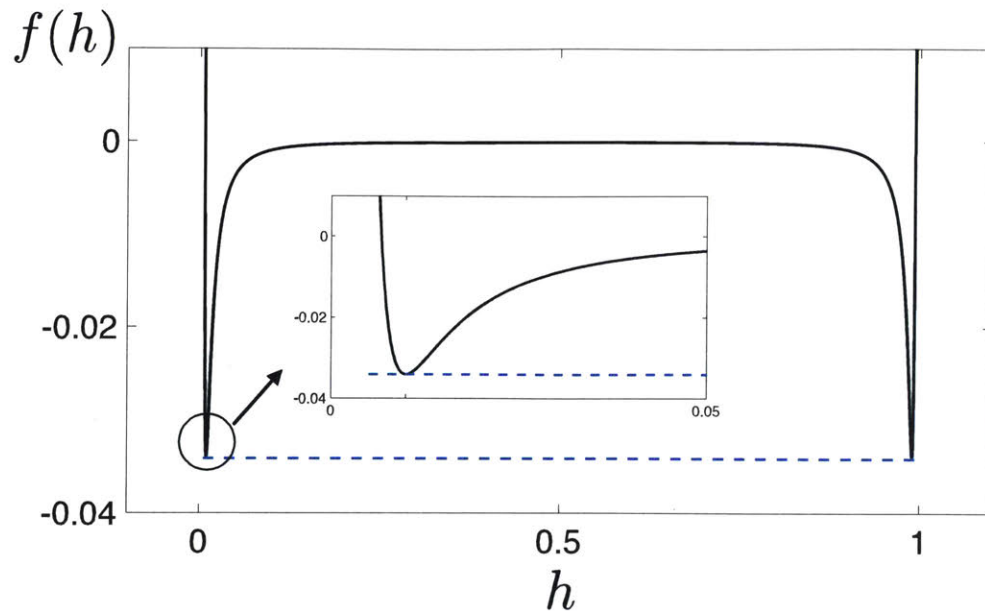
Figure 6-4: Bulk free energy (black solid line) and the common tangent construction (dashed blue line) showing the two equilibrium states. The inset shows the zoomed-in view of one of the energy wells. This form of free energy indicates that uniform films with heights in the region, where $d^2 f/dh^2 < 0$ are metastable and will phase separate to minimize the free energy.

studied here, i.e. it predicts an unstable front to be stable. The governing equations presented here have a similar form to those commonly used to describe immiscible flows in porous media or Hele-Shaw cells using generalized multiphase form of the Darcy's law (Riaz and Tchelepi, 2004; Cueto-Felgueroso and Juanes, 2012, 2014).

6.1.2   1D solutions

We begin by analyzing the behavior of the solutions obtained from solving Equation (6.8) in one dimension. In a 1D setting, the incompressibility constraint $\nabla \cdot \mathbf{u}_T = 0$ reduces to $du_T/dx = 0$ or $u_T = q_0 = \text{const}$. The evolution equation for the film height therefore simplifies to:

$$\frac{\partial h}{\partial t} + \frac{\partial}{\partial x}\left(\mathcal{M}_2(h)q_0 + \mathcal{M}_1(h)\frac{\partial}{\partial x}\left(-\frac{\partial^2 h}{\partial x^2} + \frac{df}{dh}\right)\right) = 0. \qquad (6.16)$$

Figure 6-5 shows the three type of solutions obtained from solving Eq.(6.16). These three types are: 1) Lax shocks, 2) Lax-undercompressive shocks, and 3) rarefaction wave-undercompressive shocks. These solution types have been observed in the context of thin films with competing driving forces, e.g. gravity and Marangoni forces (Bertozzi et al., 1998, 1999). Here, we review the conditions for the emergence of these solution types. Capillary shock profiles are solutions to hyperbolic conservation laws such as Eq. (6.16), which connect the upstream height h_u to the downstream height h_d; in the absence of higher order regularizing terms, we have:

$$\frac{\partial h}{\partial t} + \frac{\partial}{\partial x}\left(\mathcal{M}_2(h)q_0\right) = 0. \qquad (6.17)$$

the solutions of which represent a jump discontinuity across the shock. When the characteristics of the Eq. 6.17 from both downstream and upstream of the shock approach each other, the shock is called compressive, or Lax shock, satisfying the entropy condition $c(h_u) > s > c(h_d)$, where $c(h) = q_0 d\mathcal{M}_2/dh$ is the characteristic speed and $s = q_0(\mathcal{M}_2(h_u) - \mathcal{M}_2(h_d))/(h_u - h_d)$ given by the Rankine–Hugoniot jump condition represents the shock speed (Lax, 1957, 1973; LeVeque, 1990; Bertozzi et al., 1999). In the presence of higher order regularizing terms of Eq. 6.16, traveling wave solutions can be thought of as smoothed shock solutions, which travel with the same speed as the shock solutions. We observe this first type of shock profiles when the upstream height is larger than the downstream height, but smaller than a critical value (Fig. 6-5(a)). This type of solutions, i.e. Lax capillary shocks, are typical of thin film
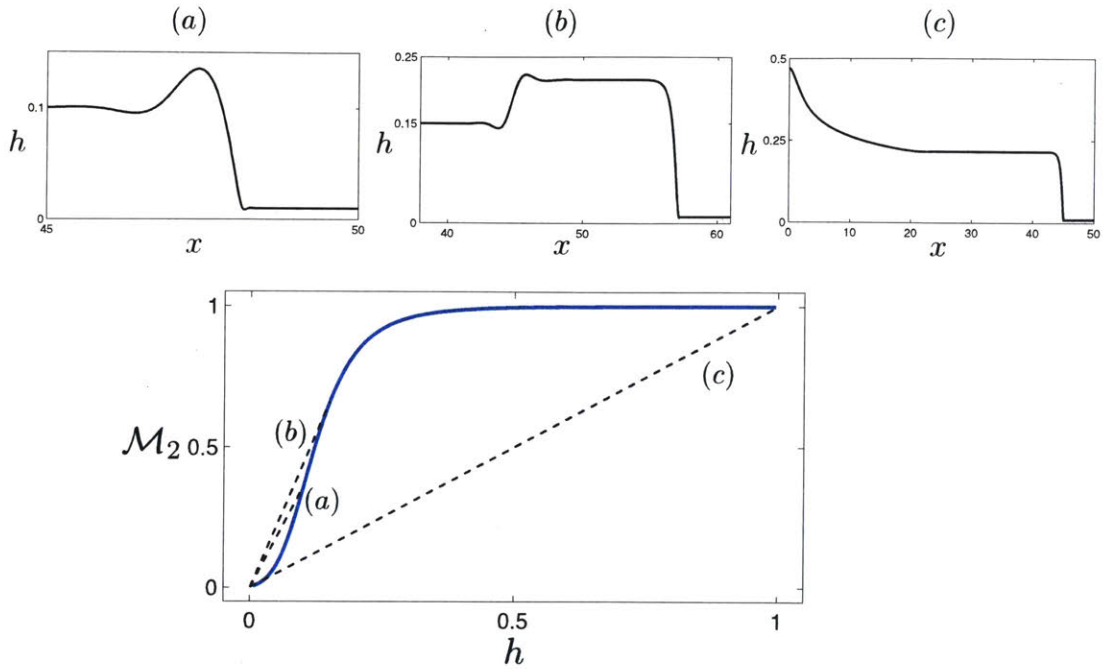
Figure 6-5: Three types of solutions of the Eq. (6.16) with $M = 1500$, $q_0 = 0.001$ and $\theta_{eq} = 0$ (complete wetting regime): (a) Lax shock, (b) Lax-undercompressive shock, (c) rarefaction wave-undercompressive shock. The bottom image shows the corresponding non-convex mobility function with the secant lines connecting the upstream and downstream heights.

flows with a single driving mechanism, such as gravity-driven flows (Huppert, 1982b), or Marangoni-driven flows, in which gravity effects can be neglected (Cazabat et al., 1990). These shocks are the ones we may encounter in our daily lives, from traffic jams (Lighthill and Whitham, 1955; Richards, 1956) to the dynamics of bacterial colonies and stock market dynamics (Helbing, 2001).

When the upstream height becomes larger than the critical value, a different structure appears, consisting of two shocks, which travel at different speeds (Fig. 6-5(b)). The trailing shock is a Lax shock, connecting the upstream height h_u to an intermediate plateau height $h_p > h_u$ and the leading shock represents an undercompressive shock connecting h_p to the downstream height h_d. This leading shock violates the Lax entropy condition as the shock travels faster than the characteristics both in front and behind it $s > c(h_d)$ and $s > c(h_p)$, meaning that the characteristics coming from downstream pass through the shock. In the context of scalar conservation laws,

until two decades ago it was thought that the only physically relevant shocks are Lax shocks (Bertozzi, 2016). The observation of undercompressive shocks in the context of thin-film flows was therefore a proof to their existence (Bertozzi et al., 1998, 1999), where it was shown that the presence of a non-convex flux function, i.e. two competing driving forces, as well as a high-order regularizing term, i.e. surface tension are required to observe these shocks. Undercompressive shocks have been observed in other contexts as well, such as phase boundaries in fluids or solids (Slemrod, 1983; Abeyaratne and Knowles, 1991), or ion sputtering of solid surfaces (Chen et al., 2005; Perkinson et al., 2016).

For upstream heights larger than the undercompressive plateau height $h_u > h_p$, we obtain a third type of solution (Fig. 6-5(c)), which consists of a trailing rarefaction wave, for which $h(x,t) = h_R(\xi = x/t)$ leading to $\xi = d\mathcal{M}_2/dh_R$ when substituted in Eq. 6.17, and a faster leading undercompressive shock wave with $s > c(h_p)$, where $s = q_0(\mathcal{M}_2(h_p) - \mathcal{M}_2(h_d))/(h_p - h_d)$ and $c(h_p)$ represents the trailing rarefaction wave speed.

6.2 Linear stability analysis

We analyze the stability of thin-film fronts in a confined channel as shown schematically in Fig. 6-2. In particular, we are interested in the stability analysis of type three solutions shown in Fig. 6-5 (c), which correspond to the experimental conditions: in the experiments once the cell is saturated with the defending liquid, we inject the invading liquid. We are therefore interested in analyzing the stability of the undercompressive shock front in Fig. 6-5 (c).

We first need to find the base state solutions of Eq. 6.16. To do so, we move from the (x, t) reference frame to the frame of reference of the traveling wave (ξ, t) with $\xi = x - st$, where s is the traveling wave (shock) velocity:

$$\frac{\partial h}{\partial t} - s\frac{\partial h}{\partial \xi} + \frac{\partial}{\partial \xi}\left(\mathcal{M}_2(h)q_0 + \mathcal{M}_1(h)\frac{\partial}{\partial \xi}\left(-\frac{\partial^2 h}{\partial \xi^2} + \frac{df}{dh}\right)\right) = 0. \tag{6.18}$$

Integrating Eq. (6.18) from $-\infty$ to ∞, we then obtain the traveling wave speed as:

$$s = q_0\frac{\mathcal{M}_2(h_u) - \mathcal{M}_2(h_d)}{h_u - h_d}, \tag{6.19}$$

in which h_u and h_d are upstream and downstream heights, respectively.

The base states are steady traveling waves $(h_0(\xi))$, which further simplifies Eq. (6.18) and allows for one integration from $-\infty$ to ξ to obtain:

$$-s(h_0 - h_u) + q_0\left(\mathcal{M}_2(h_0) - \mathcal{M}_2(h_u)\right) + \mathcal{M}_1(h_0)\frac{\partial}{\partial \xi}\left(-\frac{\partial^2 h_0}{\partial \xi^2} + \frac{df}{dh_0}\right) = 0. \tag{6.20}$$

Note that here we have assumed a film of thickness h_d exists in front of the main front. The use of this film is mainly for numerical simplicity; as we showed in Chapter 2 in the context of spreading of drops, a height-dependence surface tension can remove the need to use precursor films. In the context of thin films flowing down inclined plates, it has been shown that both precursor and slip models lead to similar results (Spaid and Homsy, 1996), justifying our use of a precursor film here. Further the instability wavelength should not be sensitive to the height of the precursor film

(Troian et al., 1989).

Using the incompressibility constraint $\nabla \cdot \mathbf{u}_T = 0$, we can further obtain the base state equation for the pressure field:

$$\frac{dP_{1,0}}{d\xi} = \frac{q_0}{A(h_0)} - \mathcal{M}_3(h_0)\frac{d}{d\xi}\left(-\frac{d^2h_0}{d\xi^2} + \frac{df}{dh_0}\right). \tag{6.21}$$

Once we have obtained the base state by solving Eqs. (6.20) and (6.21), we can analyze their stability to transverse perturbations. Our experiments are done in a radial Hele-Shaw cell, in which the speed of a stable front decays linearly and its perimeter grows linearly with the distance to the injection port. In the context of Saffman–Taylor instability Paterson (1981) found $\lambda \sim q^{-1/2}$ in a radial geometry similar to the original stability analysis of Saffman and Taylor (1958) in a rectangular geometry. Therefore, we also expect the scaling of the instability wavelength to be independent of the geometry and in the following we focus on a rectangular geometry, which in particular simplifies the task of identifying and comparing the instability wavelength obtained in the linear stability analysis with those of the nonlinear simulations in rectangular domains.

We perturb the base state solutions as follows:

$$(h, P_1) = (h_0(\xi), P_{1,0}(\xi)) + \epsilon\left(\hat{h}(\xi,t), \hat{P}_1(\xi,t)\right)e^{iky}, \tag{6.22}$$

where k is the wavenumber of the perturbation in the y direction and $(h_0(\xi), P_{1,0}(\xi))$ represent the base state solutions obtained from Eqs. (6.20), and(6.21). Plugging the perturbed variables into the governing equations (6.8) and (6.6) and keeping the $O(\epsilon)$ terms, we arrive at the following evolution equation for the perturbed height field:

$$\frac{\partial\hat{h}}{\partial t} + \left(C_1 + \mathcal{M}_{1,0}k^4\right)\hat{h} - \left(C_2 + C_3k^2\right)\frac{\partial\hat{h}}{\partial\xi} - 2k^2\mathcal{M}_{1,0}\frac{\partial^2\hat{h}}{\partial\xi^2} +$$
$$C_3\frac{\partial^3\hat{h}}{\partial\xi^3} + \mathcal{M}_{1,0}\frac{\partial^4\hat{h}}{\partial\xi^4} - \frac{\partial\hat{P}_1}{\partial\xi}\frac{dh_0}{d\xi}A_0\mathcal{M}'_{2,0} = 0, \tag{6.23}$$

where primes indicate differentiation with respect to h and the coefficients $C_{1,2,3}$ are

defined as follows:

$$C_1 = \mathcal{M}'_{1,0}\frac{d^4 h_0}{d\xi^4}$$

$$-\frac{1}{A_0}\frac{dh_0}{d\xi}\left[q_0 A'_0 \mathcal{M}'_{2,0} + A_0\left(q_0\mathcal{M}''_{2,0} + \left(A_0\mathcal{M}'_{3,0}\mathcal{M}'_{2,0} - \mathcal{M}''_{1,0}\right)\frac{d^3 h_0}{d\xi^3}\right)\right], \quad (6.24)$$

$$C_2 = s + q_0\mathcal{M}'_{2,0} - \mathcal{M}'_{1,0}\frac{d^3 h_0}{d\xi^3}, \quad (6.25)$$

$$C_3 = \frac{dh_0}{d\xi}\left(\mathcal{M}'_{1,0} - A_0\mathcal{M}'_{2,0}\mathcal{M}_{3,0}\right), \quad (6.26)$$

where the subscript 0 indicates base state.

Similarly, the perturbed equation for the pressure field becomes:

$$\hat{h}\left(C_4/A_0^2 + A_0\mathcal{M}_{3,0}k^4\right) + \frac{\partial \hat{h}}{\partial \xi}\left(C_5 - C_6 k^2\right)/A_0 - 2\frac{\partial^2 \hat{h}}{\partial \xi^2}A_0\mathcal{M}_{3,0}k^2 +$$

$$\frac{\partial^3 \hat{h}}{\partial \xi^3}C_6/A_0 + \frac{\partial^4 \hat{h}}{\partial \xi^4}A_0\mathcal{M}_{3,0} + \frac{\partial \hat{P}_1}{\partial \xi}A'_0\frac{dh_0}{d\xi} + \frac{\partial^2 \hat{P}_1}{\partial \xi^2}A_0 - k^2 A_0\hat{P}_1 = 0, \quad (6.27)$$

where the coefficients $C_{4,5,6}$ are defined as follows:

$$C_4 = A_0^3\mathcal{M}'_{3,0}\frac{d^4 h_0}{d\xi^4} +$$

$$\frac{dh_0}{d\xi}\left[-q_0(A'_0)^2 + q_0 A_0 A''_0 + A_0^2\left(A'_0\mathcal{M}'_{3,0} + A_0\mathcal{M}''_{3,0}\right)\frac{d^3 h_0}{d\xi^3}\right], \quad (6.28)$$

$$C_5 = q_0 A'_0 + A_0^2\mathcal{M}'_{3,0}\frac{d^3 h_0}{d\xi^3}, \quad (6.29)$$

$$C_6 = A_0 A'_0\frac{dh_0}{d\xi}\mathcal{M}_{3,0} + A_0^2\mathcal{M}'_{3,0}\frac{dh_0}{d\xi}. \quad (6.30)$$

To analyze the growth of perturbations, we need to solve Eqs.(6.23) and (6.27). There are two common ways to achieve this; the first method is to define $\hat{h} = \bar{h}\exp(\sigma t)$, where σ is the perturbation growth rate. Then equations (6.23), and (6.27) define an eigenvalue problem with $\bar{h}$ and $\hat{P}$ as the eigenfunctions and σ as the eigenvalue. These set of equations can therefore be compactly represented as follows:

$$\begin{pmatrix} A_1 & B_1 \\ A_2 & B_2 \end{pmatrix}\begin{pmatrix} \bar{h} \\ \hat{P} \end{pmatrix} = \begin{pmatrix} \sigma & 0 \\ 0 & 0 \end{pmatrix}\begin{pmatrix} \bar{h} \\ \hat{P} \end{pmatrix}, \quad (6.31)$$

189
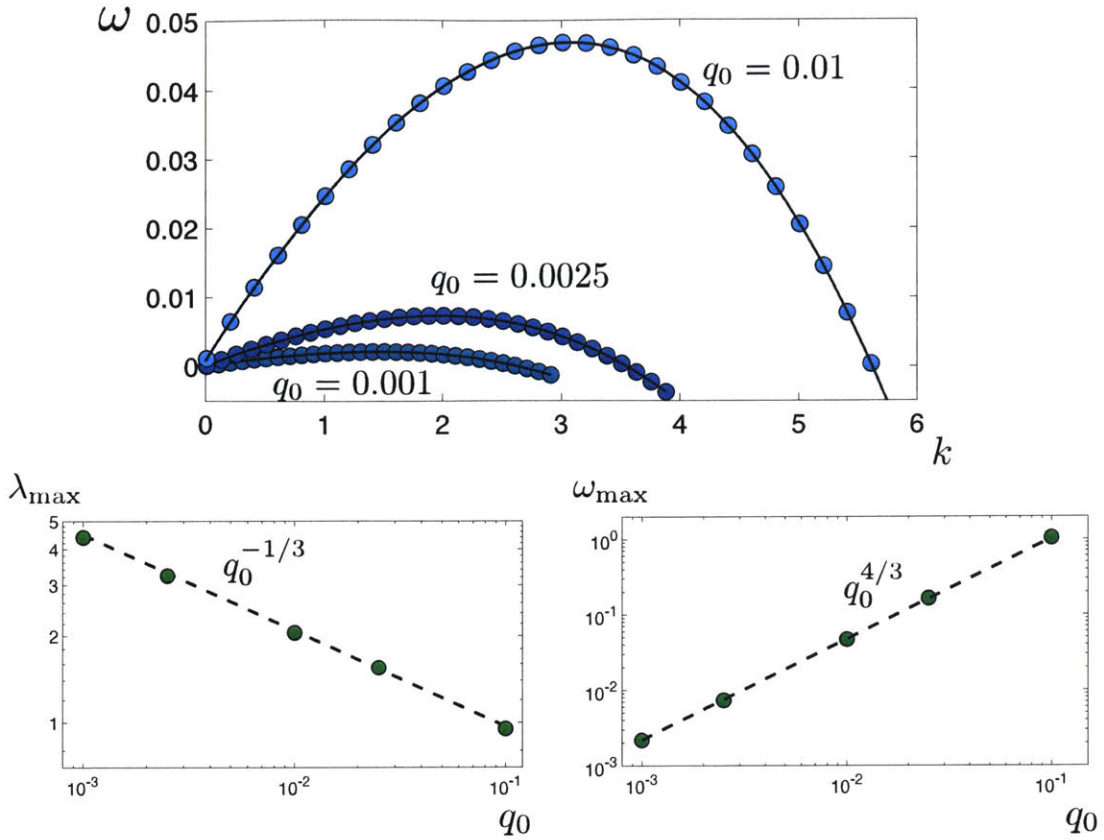
Figure 6-6: Dispersion curve obtained using linear stability analysis through solving Eqs.(6.23) and (6.27). The maximum growth rate determines the fastest growing mode and its associated wavelength of instability as shown in the two bottom figures. The scalings observed here are distinct from the scalings obtained in the classical Saffman–Taylor instability.

where $A_{1,2}$ and $B_{1,2}$ are discretization operators related to the perturbation equations. These equations therefore allow us to investigate the stability of the thin-film front in the unstable imbibition regime and give us the most unstable wavelength and its growth rate.

The alternative way to analyze the growth of the perturbation, which we use here, is to directly solve for the coupled partial differential equations (6.23) and (6.27) and monitor the growth of perturbations in time, defining the growth rate σ as (Matar and Kumar, 2007; Mavromoustaki et al., 2011):

$$\omega = \lim t \to \infty \frac{1}{2t} \ln \frac{E(t)}{E(t=0)}, \tag{6.32}$$

190

where the perturbation energy is defined as:

$$E(t) = \frac{\int_0^L \hat{h}^2 d\xi}{\int_0^L h_0{}^2 d\xi}.$$ (6.33)

The result of this linear stability analysis is shown in Fig. 6-6, which shows the rate of growth of the perturbations imposed on the front of the undercompressive shock structure shown in Fig. 6-5(c). As we mentioned before, the speed of undercompressive shocks is higher than the characteristic speeds in front or behind the shock. Therefore, any perturbations in front of the shock pass through the shock and becomes amplified if the shock is unstable to perturbations (Bowen et al., 2005). Figure 6-6 shows that indeed the undercompressive shock front is unstable to perturbations. This is a novel and surprising observation as undercompressive shocks in thin-film flows have been considered to lead to stable fronts (Bertozzi et al., 1998, 1999, 2001b; Bowen et al., 2005; Bertozzi, 2016). The underlying reason for the instability of the undercompressive shocks here is the confinement, which leads to the coupling of the pressure fields of the two liquids. In fact, assuming the flow in the y direction to be zero, i.e. zero transverse flow assumption, leads to the decoupling of the pressure fields and therefore stability of the front. As we have observed in the experiments, the thin-film front is indeed unstable; therefore, the zero transverse flow assumption, which is also used by Mavromoustaki et al. (2011) in their stability analysis, leads to the incorrect conclusion of the front stability.

The second important observation in Fig. 6-6 is the scalings of the most unstable wavelength and growth rate with the flow rate. Here, we observe that $\lambda_{\max} \sim q_0^{-1/3}$ and $\omega_{\max} \sim q_0^{4/3}$, which is distinct from the classical $\lambda_{\max} \sim q_0^{-1/2}$ and $\omega_{\max} \sim q_0^{3/2}$ scalings of the Saffman–Taylor instability (Saffman and Taylor, 1958; Paterson, 1981; Bensimon et al., 1986; Homsy, 1987). This observation indeed points to the fact that the thin-film front instability in our experiments belong to a new class of pattern forming processes.
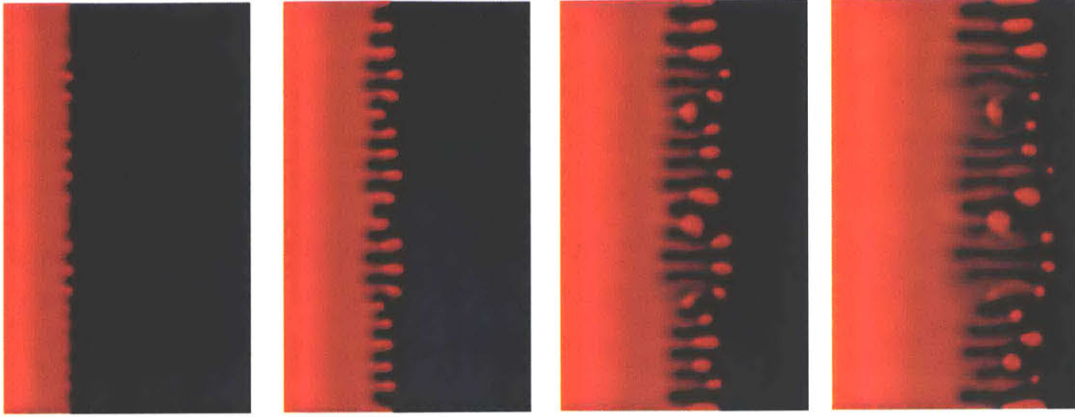
Figure 6-7: Nonlinear simulation of the coupled Eqs. (6.6) and (6.8) with $q_0 = 0.005$, $M = 1500$, and in the complete wetting regime. The snapshots from left to right are equally spaced in time and show the time evolution of the instability.

6.3 Nonlinear simulations

To go beyond the onset of instability, we need to conduct full nonlinear simulations of the coupled equations (6.6) and (6.8). In a rectangular domain, we can clearly see the development of fingers over time as shown in Fig. 6-7. At the onset of instability, a well-defined wavelength forms leading to a regular spacing between the fingers. As the fingers grow farther from their root, we observe an overshoot in the height at the finger tips, which ultimately leads to the pinch-off in some of the fingers. The presence of the dimple or overshoot at the tip of the fingers is reminiscent of the capillary ridge formation in driven thin films (Troian et al., 1989), which are the underlying reason for the front instability in those systems (Brenner, 1993; Bertozzi and Brenner, 1997). The linear stability analysis presented above showed that the perturbations to the shock front grow in time leading to the formation of a bump at front. This observation suggests that the undercompressive shock base states undergo a transition to a Lax shock type structure en route to instability. At later times, fingers further interact and merge with each other, leading to a ramified and complex front morphology.
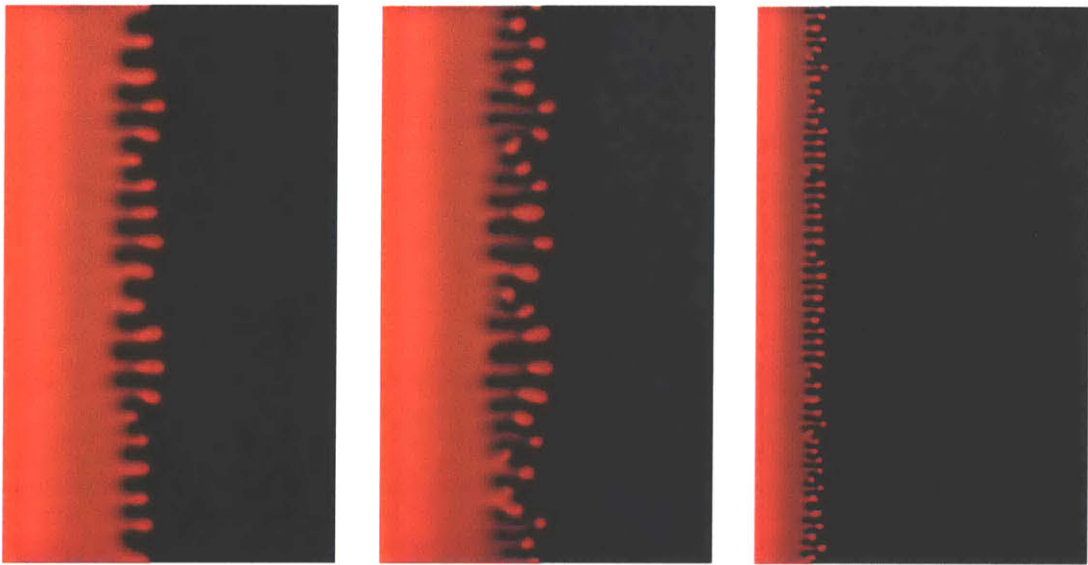
Figure 6-8: The effect of flow rate on the front instability, from left to right $q_0 = 0.005, 0.01, 0.1$. The wavelength of instability for $q = 0.01$ is $\lambda_{\max} \approx 2$ and for $q = 0.1$ is $\lambda_{\max} \approx 1$, which are in excellent agreement with the results of the linear stability analysis presented in Fig. 6-6.
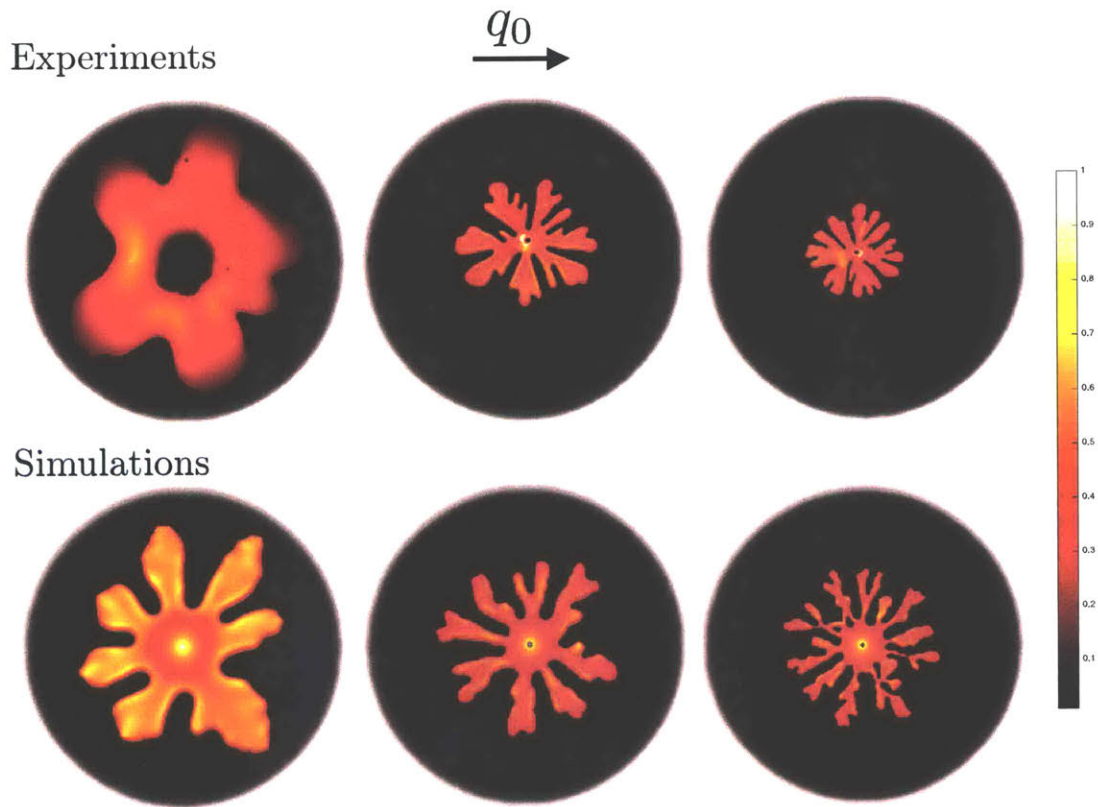
Figure 6-9: Comparison between experiments and simulations for increasing flow rates from left to right. The color indicates the normalized film height, where white color would represent full displacement. In the experiments, water is died with fluorescein and the light intensity is then converted to the film thickness using the Beer–Lambert law.

6.4   Discussion

Figure 6-9 shows a comparison between experimental results on the thin-film front instability and the simulations. Note that here in the simulations, we have considered the invading fluid to be partially wetting with $\theta_{eq} = \pi/6$, which is representative of the experimental conditions. While comparing the exact instability wavelength in the radial geometry is a harder task than in the rectangular geometry, we do observe a general qualitative agreement between the experiments and simulation results.

Chapter 7

Wetting and disorder: imbibition in a rough fracture

So far, we focused on the influence of contact line motion on interfacial instabilities in confined domains. Most real surfaces, such as those one encounters in porous media flows, however, are rough (Bonn et al., 2009; AlRatrout et al., 2018). Therefore, an understanding of the interplay between wetting phenomena and roughness is a necessity to be able to understand and describe immiscible flows in most applications.

Influence of roughness on wettability of solid surfaces has been the focus of many studies within the past two decades given the relevance of roughness and hierarchical topographical features of the surface in creating superhydrophobic surfaces (Quéré, 2008; Bonn et al., 2009; Rothstein, 2010; Wong et al., 2011). Surface roughness promotes the natural wettability of a surface, i.e. it makes a wetting surface even more wetting and a non-wetting surface even more non-wetting. This change in the effective wettability of the surface can be described using Wenzel (1936) or Cassie and Baxter (1944) laws. These laws, however, can only describe the average wettability of a surface and do not represent hysteresis associated with the presence of disorder on the medium (Bonn et al., 2009).

In the context of hydrophilic surfaces, roughness leads to a decrease in the effective contact angle as proposed by (Wenzel, 1936): $\cos \theta^* = r \cos \theta_{eq}$, where θ_{eq} is the intrinsic contact angle on a smooth surface of the same material and r is the ratio

of the actual surface area to the projected area, where $r < 1$. As the contact angle decreases, however, there is a transition from the Wenzel state, where the liquid drop is surrounded by the dry solid surface to a regime called hemiwicking, where thin films of the main drop wick into the grooves of the rough surface (Quéré, 2008). The transition to this second regime occurs when $\theta_{eq}\langle\theta_{cr}$, where $\cos\theta_{cr} \approx 1/r$. For a smooth solid surface, where $r = 1$, therefore this transition will not occur, whereas for a porous matrix, where $r \gg 1$, this transition happens when $\theta_{eq}\langle\pi/2$, i.e. the Washburn law. Once these thin films emerge from the main drop, they change the effective wettability of the medium as seen by the drop front, i.e. the grooves in advance of the drop are filled with the same liquid. This results in a change in the effective contact angle, leading to $\cos\theta^* \approx 1 - \cos\theta_{eq}$. Note that we have assumed that the liquid fills the grooves of the rough surface, and effectively no part of the surface remains in contact with air; in reality, this need not be true and the situation will likely depend on the contact angle. Balancing the driving surface tension forces with the viscous dissipation in the film, one arrives at a diffusive dynamics for the hemiwicking films akin to the dynamics predicted by the Washburn law.

The brief discussion presented above shows that the presence of roughness leads to complicating behavior even at equilibrium. Far less is known about the dynamics of wetting in the presence of rough surfaces. In particular, roughness is believed to have a crucial role in the onset of wetting transition (Golestanian and Raphaël, 2001; Zhao et al., 2014; Perrin et al., 2016) and dynamics beyond that (Krechetnikov and Homsy, 2005; Seiwert et al., 2011). Further, in confined flows roughness not only affects the contact line motion, but also the local permeability field. While the influence of heterogeneous permeability in immiscible flows has been widely studied (Chen et al., 2017; Hu et al., 2018), much less is known about the interplay between contact line motion and the disorder of the medium. Here, we present the results of an experimental study using a radial Hele–Shaw cell, in which one of the surfaces is roughened. Using the Hele–Shaw cell allows us to monitor the flow inside in real time while roughness can be thought of as a zeroth order correction on analogy between Hele–Shaw cells and porous media flows, in which the medium is inherently disordered
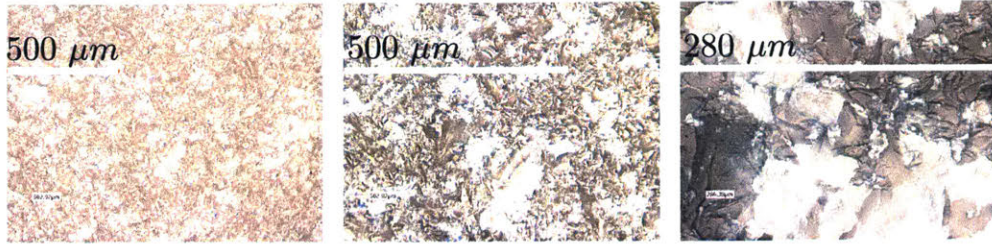
and heterogeneous.

Figure 7-1: Depth-composed optical image of the sand-blasted glass disk under different magnifications $10X$, $20X$, and $50X$. The white line in each image is a scale-bar.

7.1 Characterization of surface roughness

We scan the surfaces using a laser scanning confocal microscope (Keyence VK-X250, Keyence Corp.) with a 20X objective lens with a numerical aperture of 0.46, giving a lateral spatial resolution of 694nm and a vertical (height) resolution of 100nm. The total scanned area on each spot is $0.379\,\mathrm{mm}^2$,. Once the height of the surface is mapped, the mean can be subtracted $h(x,y) = z(x,y) - \langle z(x,y)\rangle$, where $\langle ...\rangle$ denotes spatial averaging over the sample area.

To roughen the glass discs, we use sandblasting, which is known to lead to randomly rough semi-Gaussian surfaces (Persson, 2013). The resulting surface is a self-affine fractal (Pelliccione and Lu, 2008). Figure 7-1 shows depth-composition images of a spot on the rough glass disc using different magnifications. Visually, it is clear that the roughness persists on different scales as expected from a self-affine fractal.

To gain a more quantitative sense of the roughness of the surfaces, we use the laser scanning confocal microscope (Keyence VK-X250, Keyence Corp.) to reconstruct the height of the surface. This height is then used to compute various features of the roughness as shown in Fig. 7-2. The root mean square (RMS) roughness defined as $w = \sqrt{\langle h^2(x,y)\rangle} \approx 10\mu m$. The autocorrelation function further is defined as $R(u,v) = \langle h(x+u,y+v) \cdot h(x,y)\rangle/w^2$, which measures the correlation of the height at a location (x,y) with that at $(x+u,y+v)$. The sandblasting procedure leads to an isotropically rough surface as indicated by the 2D FFT of the topography field shown in Fig. 7-2 (d). This observation indicates that the autocorrelation function can be radially averaged to arrive at the function shown in Fig. 7-2 (c), which indicates

that the correlation length is on the order of few hundred microns $\approx 300\mu m$. Given that the gap between the two plates of Hele–Shaw cell in our experiments are of the same order, i.e. $b = 100\mu m$, we can safely consider the roughness uncorrelated on the lateral scale of the glass disc $d = 6.5"$, i.e. there are no long-ranged correlations present in the topography.

The power spectral density $\mathrm{PSD}(k) = (|\langle h(x,y)\exp{(-i\mathbf{k}\cdot\mathbf{x})}\rangle|^2)/(4\pi^2)$, as shown in Fig. 7-2 (e) confirms the self-affine fractal nature of the surface, where a clear power law can be observed. The power law region can be described as $\mathrm{PSD}(k) \sim k^{-2H-2}$, where H is the Hurst or roughness exponent. Fitting the function, we find $H \approx 0.63$.
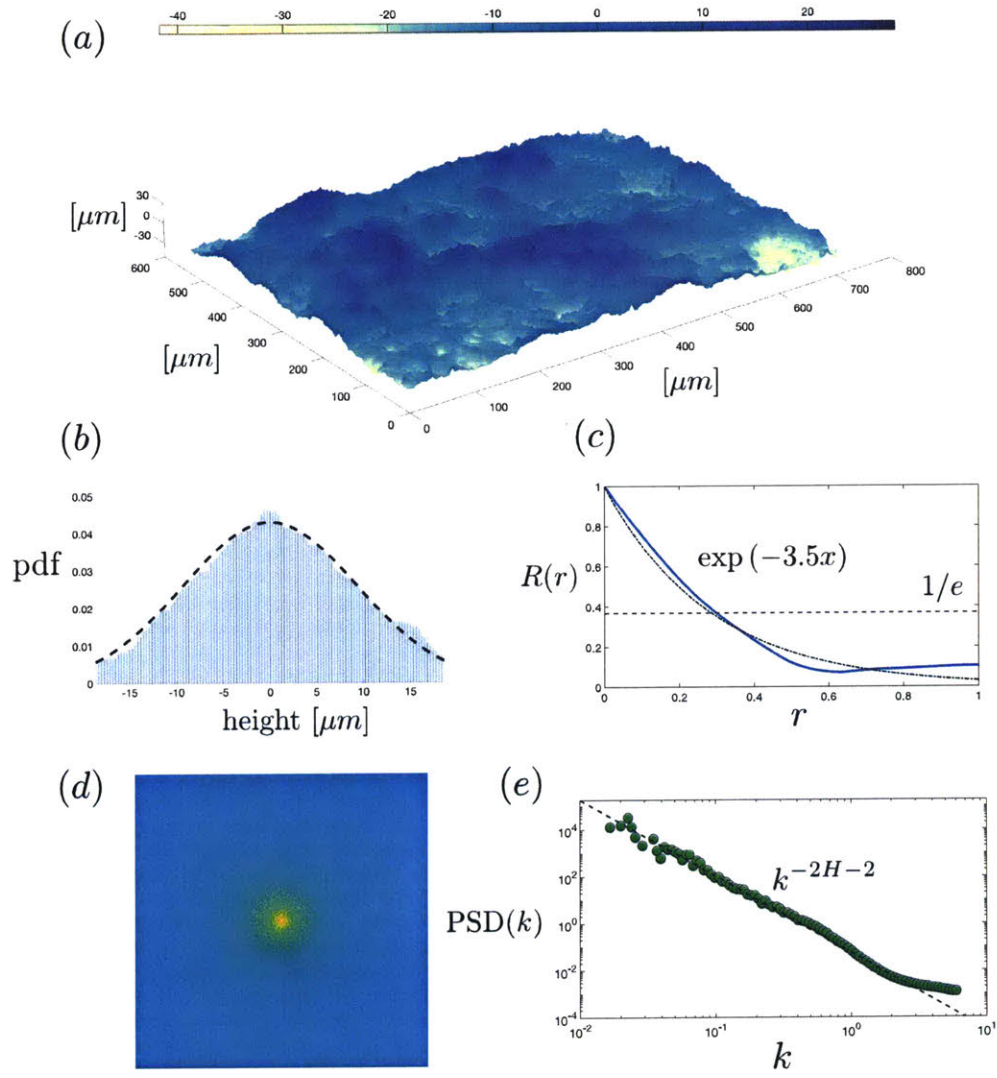
Figure 7-2: (a) Two-dimensional surface profilogram obtained with a 20X objective. (b) Shows the normalized pdf of the roughness height overlaid with a Gaussian distribution curve with a root mean square roughness of $\approx 10\mu m$. (c) Shows the radially-averaged autocorrelation function, overlaid with an exponentially decaying function. (d) 2D Fast Fourier Transform of the surface topography, showing the isotropic nature of the rough surface. (e) Power spectral density of the roughness as a function of the wavenumber k .

7.2 Experimental observations

Influence of disorder on the front dynamics in stable imbibition regime, when a more viscous and more wetting fluid displaces a less viscous and less wetting fluid has been widely studied within the past two decades (Alava et al., 2004; Ortín and Santucci, 2017). The main question in this context has been the universality of the interface in the stable imbibition and its connection to other problems related to surface growth. A cornerstone to describing the interface motion in disordered media is the Kardar-Parisi-Zhang (KPZ) equation (Kardar et al., 1986):

$$\frac{\partial h}{\partial t} = F + \nu \nabla^2 h + \frac{\lambda}{2}(\nabla h)^2 + \eta(x, h), \qquad (7.1)$$

where $\langle \eta(x, h) \rangle = 0$ and $\langle \eta(x, h)\eta(x', h') \rangle = \delta^d(x - x')\Delta(h - h')$, where $\langle .. \rangle$ indicates averaging over different realization of noise. This equation predicts that in the vicinity of the depinning transition, the size of pinned region diverges, i.e. the depinning transition is a critical point and the correlation length $\xi \sim (F - F_c)^{-\nu}$.

Figure 7-3 shows the experimental phase diagram for stable and unstable imbibition experiments. Each pair are done using the same cell, meaning that the front in both cases experiences exactly the same disorder. The influence of disorder on the front, however, is very different in the two cases. In stable imbibition, contact line pinning distorts the interface, whereas nonlocal viscous driven pressure field tends to smooth the interface. In unstable imbibition, however, both disorder and viscous pressure tend to perturb the interface, leading to a more ramified front at higher injection rates. Note that in unstable imbibition, thin films of the invading liquid coat the rough surface and propagate along the surface, whereas in the stable imbibition experiments the displacement across the gap is complete.

To gain a more quantitative understanding of the differences between the different patterns, we calculate the fractal dimension associated with the patterns as shown in Fig. 7-4. The stable imbibition patterns all have rather space-filling patterns that lead to high fractal dimensions close to two. The high injection rate unstable imbibition is consistent with the DLA dimension, whereas the low injection rate is consistent with
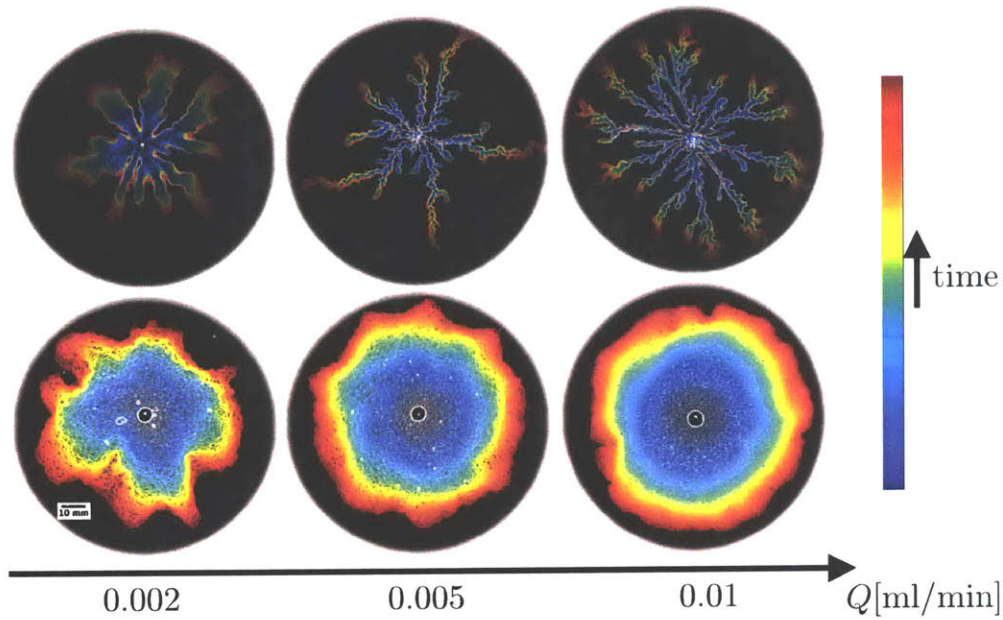
Figure 7-3: Phase diagram of stable (bottom row) and unstable (top row) imbibition in rough Hele–Shaw cells as a function of flow rate. Each cell is first filled with a highly viscous oil (Krytox, GPL106), and then fluorescein dyed water ($800mg/L$) is injected in the middle. The figures show color-coded time-lapse images of the front. The stable imbibition fronts roughen in time as the front velocity decreases the farther away from injection port it goes. Viscous forces dominate over capillary and pinning forces at higher injection rates in stable imbibition. The situation is however different in unstable imbibition, where disorder perturbs the unstable front, leading to a more ramified structure.
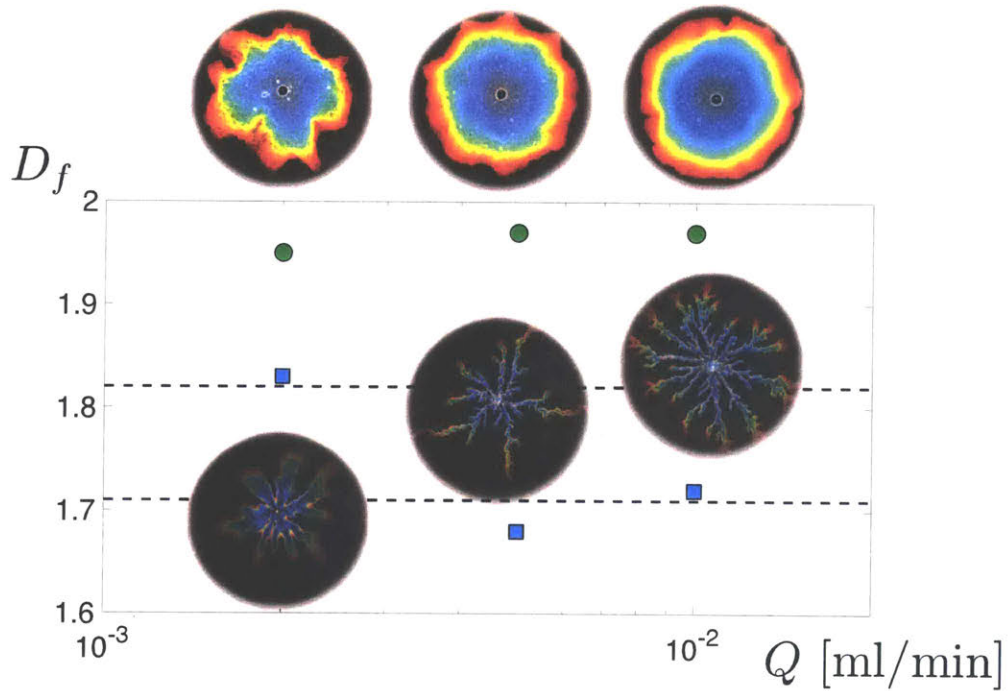
Figure 7-4: Fractal dimension of the stable and unstable imbibition experiments. The dashed lines indicate the fractal dimension of the diffusion limited aggregation, $D_f = 1.71$ (Witten and Sander, 1981), and invasion percolation $D_f = 1.82$ (Wilkinson and Willemsen, 1983). The viscous fingering pattern at high injection rate is consistent with the DLA dimension. It is interesting to note that at low injection rates, the unstable pattern seem to have a fractal dimension close to that of the invasion percolation, which is derived for the drainage regime. Here, in the unstable imbibition regime, contact line pinning seems to play the same role as the heterogeneous capillary pressure field does in the drainage regime.

the invasion percolation dimension. These are surprising observations given that here in unstable imbibition, thin film fronts propagate on the rough surface rather than the full displacement that is typically considered in the standard models for invasion percolation and DLA.

Finally, we briefly discuss the implications of the disorder in the cell on the pressure signal measured at the inlet of the cell. Figure 7-5 shows the evolution of the pressure field at the inlet as water is being injected into the cell. Water is less viscous than oil $M = \mu_o/\mu_w \approx 1500$; therefore, viscous pressure in the water phase can be safely neglected; as water displaces oil and the front gets closer to the outlet, the viscous pressure resistance in front of the leading edge decreases, justifying the decrease in the pressure. The interesting observation here, however, is that as the interface gets closer to the edge capillary and pinning forces become more important due to the radial decrease of the velocity. The oscillations in the pressure signal here therefore point to the stick-slip motion of the front and reflect the disorder in the medium. Another interesting observation is that while the propagating thin film coats the top rough surface next to the injection port, the film may touch the other smooth surface at some point in time due to the disorder in the medium or swelling of the film or any other local perturbations. When the film touches the other surface, it forms a liquid bridge that has a lower pressure than its surrounding liquid due to its Laplace curvature; this negative Laplace pressure difference is due to the small contact angle of the invading liquid $\theta_{eq} \approx \pi/6$. In Fig. 7-5, we can see the signature of this bridge formation in the pressure signal, which shows a sudden decrease in the pressure.
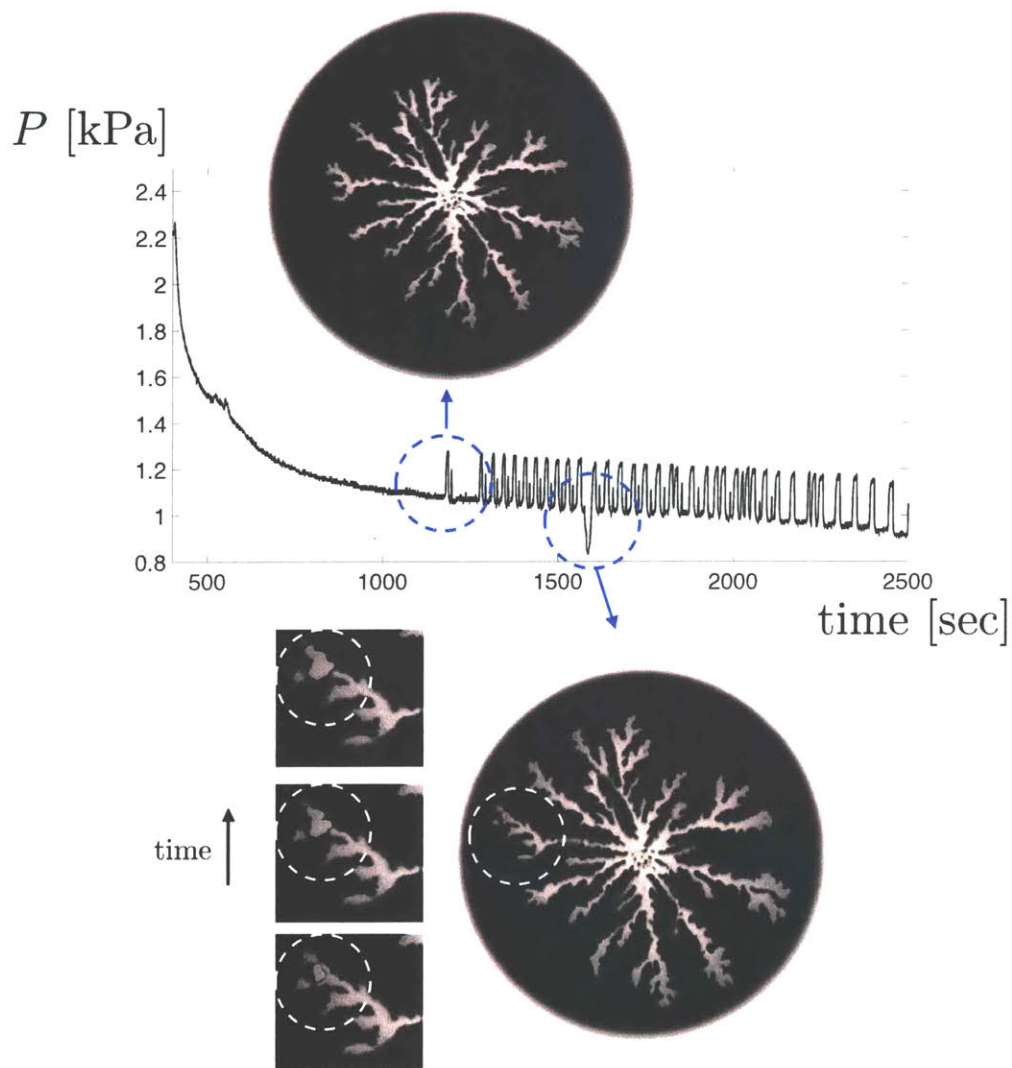
Figure 7-5: Pressure signal at the inlet to the cell during injection of water into the oil-filled cell $Q = 0.01$ml/min. As the less viscous liquid displaces the more viscous one, the inlet pressure decreases in time. Far away from the inlet, where viscous forces become comparable to the capillary and pinning forces, oscillations in the pressure signal begin to emerge. This oscillations correspond to the stick-slip motion of the front due to the pinning and depinning transitions. The bottom figure shows the dip in the pressure signal associated with the formation of a liquid bridge between the top rough surface and the bottom smooth surface. Note that before this point, the water film only propagate along the top rough surface next to the injection port and have not touched the bottom smooth surface. Once the bridge forms, it sucks more water into it due to its negative Laplace pressure and its size grows.

7.3   Hemiwicking dynamics

As we discussed above, if $\cos\theta_{eq} > 1/r$, thin films of the wetting liquid wick into the roughness of the surface and propagate ahead of the main front (Quéré, 2008). For real surfaces, there is no exact method to determine the ratio of the actual area to the projected area r; methods such as profilometry always have a lower cut-off length due to the resolution. One way to get an estimate of the ratio r in the Wenzel regime is to measure the apparent contact angle and relate that to r via Wenzel equation. Even then, we know that due to the hysteresis, the apparent contact angle is not uniquely defined and varies between and advancing and receding values depending on the history. Therefore, the only practical way to know if the hemi-wicking regime is achieved is through experimental observations. Figure 7-6 shows an example of formation of these films in rough Hele–Shaw cells. The presence of these films effectively lead to the wettability change of the medium as the contact angle of the main thin-film front changes.

The dynamics of the hemi-wicking films has been analyzed using scaling arguments and miromodel experiments, where the surface is designed to have a specific topography rather than being randomly rough (Bico et al., 2001; Ishino et al., 2007; Kim et al., 2016b). They balanced the capillary driving force with the viscous pressure drop in the wicking film to get an estimate of the front velocity, arriving at the conclusion that the dynamics of the front is diffusive, i.e. $L \sim \sqrt{t}$. In our case, however, the viscous dissipation occurs in both the invading and defending liquids. At early times, the viscous dissipation in the more viscous defending liquid dominates that of the invading liquid. Using a variant of the arguments of Kim et al. (2016b), and balancing the driving capillary force $F_d = \gamma(r\cos\theta_{eq} - 1)$ with the viscous force $F_r \sim \mu_o U L_o(1/w + (r-1)/\lambda)$, we find that at early times $L \sim t$, i.e. the dynamics is linear rather than diffusive. Here μ_o is the oil viscosity, L_o is the length of the oil film in front of the water film, which we consider to be approximately constant at early times, w is the RMS roughness of the surface, λ is the correlation length of the rough surface. At late times, however, as the L_o goes to zero and the viscous dissipation in
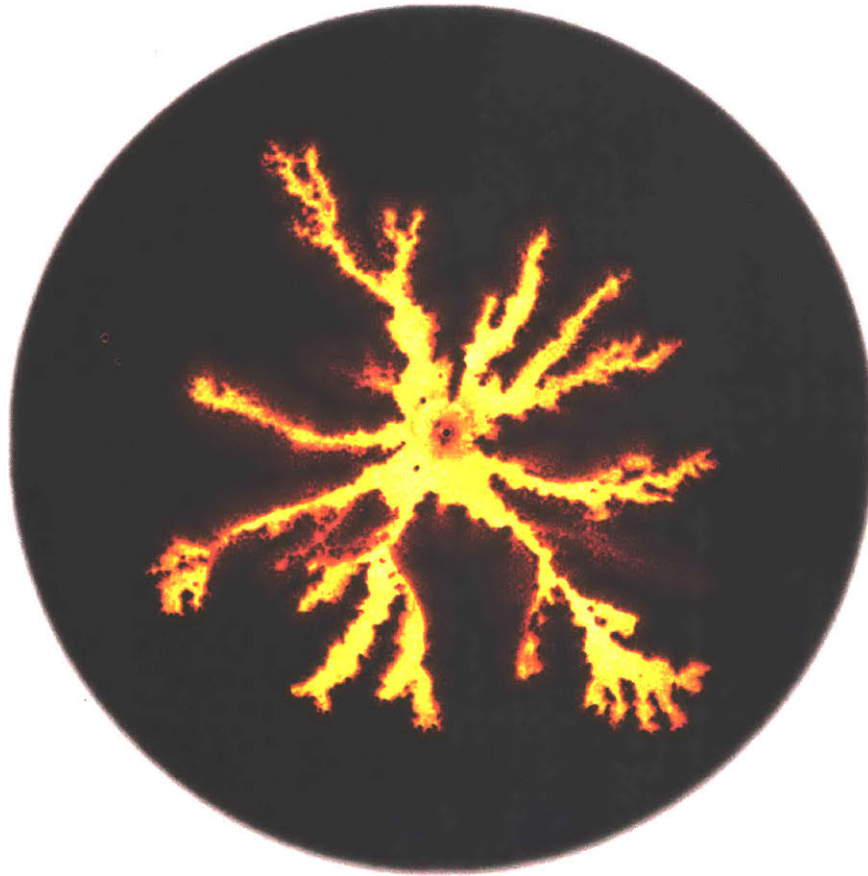
Figure 7-6: Formation of secondary thin films ahead or the main thin film front: this phenomenon is called hemi-wicking and changes the effective contact angle of the medium, i.e. the main thin film front now forms a contact angle $\cos \theta^* \approx 1 - \cos \theta_{eq}$ (Quéré, 2008).

the invading fluid dominates, the dynamics of the front becomes diffusive again. The crossover length scales as $L_c \sim \mu_o/(\mu_i + \mu_o)R$, where μ_i is the invading liquid viscosity and R is the radius of the cell. Note that when $\mu_o \gg \mu_i$, the dynamics effectively remains in the linear regime for the entire process. This scaling argument therefore points to a new regime of hemi-wicking.

Bibliography

Dirk G. A. L. Aarts, Matthias Schmidt, and Henk N. W. Lekkerkerker. Direct visual observation of thermal capillary waves. *Science*, 304(5672):847–850, 2004.

R. Abeyaratne and J. Knowles. Implications of viscosity and strain-gradient effects for the kinetics of propagating phase boundaries in solids. *SIAM Journal on Applied Mathematics*, 51(5):1205–1221, 1991.

J. J. Agresti, E. Antipov, A. R. Abate, K. Ahn, A. C. Rowat, J-C. Baret, M. Marquez, A. M. Klibanov, A. D. Griffiths, and D. A. Weitz. Ultrahigh-throughput screening in drop-based microfluidics for directed evolution. *Proc. Natl. Acad. Sci. USA*, 107 (14):4004–4009, 2010.

Mikko Alava, Martin Dubé, and Martin Rost. Imbibition in disordered media. *Advances in Physics*, 53(2):83–175, 2004.

Mikko J. Alava, Phani K. V. V. Nukala, and Stefano Zapperi. Statistical models of fracture. *Advances in Physics*, 55 (3-4):349–476, 2006. doi: 10.1080/00018730300741518. URL https://doi.org/10.1080/00018730300741518.

A. Alizadeh Pahlavan, L. Cueto-Felgueroso, A. E. Hosoi, G. H. McKinley, and R. Juanes. Thin films in partial wetting: stability, dewetting and coarsening. *Journal of Fluid Mechanics*, 845:642–681, 2018a.

Amir Alizadeh Pahlavan, Luis Cueto-Felgueroso, Gareth H. McKinley, and Ruben Juanes. Revisiting the Saffman–Taylor experiment in unstable imbibition. *submitted*, 2018b.

Amir Alizadeh Pahlavan, Luis Cueto-Felgueroso, Gareth H. McKinley, and Ruben Juanes. Moving contact lines in partial wetting: bridging the gap across the scales. *submitted*, 2018c.

Amir Alizadeh Pahlavan, Luis Cueto-Felgueroso, Gareth H. McKinley, and Ruben Juanes. Emergence of a thin-film front in a rough fracture. *submitted*, 2018d.

Amir Alizadeh Pahlavan, Howard A. Stone, Gareth H. McKinley, and Ruben Juanes. Restoring universality to the breakup of a bubble. *submitted*, 2018e.

Ahmed AlRatrout, Martin J. Blunt, and Branko Bijeljic. Wettability in complex porous materials, the mixed-wet state, and its relationship to surface roughness. *Proceedings of the National Academy of Sciences*, 115(36):8901–8906, 2018.

A. Amirfazli and A.W. Neumann. Status of the three-phase line tension: a review. *Advances in Colloid and Interface Science*, 110(3):121–141, 2004.

E. Amstad et al. Production of amorphous nanoparticles by super-sonic spray-drying with a microfluidic nebulator. *Science*, 349(6251):956–960, 2015. ISSN 0036-8075. doi: 10.1126/science.aac9582. URL http://science.sciencemag.org/content/349/6251/956.

D. M. Anderson, G. B. McFadden, and A. A. Wheeler. Diffuse-interface methods in fluid mechanics. *Annu. Rev. Fluid Mech.*, 30(1):139–165, January 1998.

K. Andreassen et al. Massive blow-out craters formed by hydrate-controlled methane expulsion from the arctic seafloor. *Science*, 356(6341):948–953, 2017. ISSN 0036-8075. doi: 10.1126/science.aal4500. URL http://science.sciencemag.org/content/356/6341/948.

Thomas E. Angelini, Marcus Roper, Roberto Kolter, David A. Weitz, and Michael P. Brenner. Bacillus subtilis spreads by surfing on waves of surfactant. *Proceedings of the National Academy of Sciences*, 106(43):18109–18113, 2009. doi: 10.1073/pnas.0905890106. URL http://www.pnas.org/content/106/43/18109.

S. L. Anna. Droplets and bubbles in microfluidic devices. *Annual Review of Fluid Mechanics*, 48(1):285–309, 2016.

S. L. Anna, N. Bontoux, and H. A. Stone. Formation of dispersions using "flow focusing" in microchannels. *Applied Physics Letters*, 82(3):364–366, 2003.

I. S. Aranson and L. S. Tsimring. Patterns and collective behavior in granular media: Theoretical concepts. *Reviews of Modern Physics*, 78:641–692, Jun 2006. doi: 10.1103/RevModPhys.78.641. URL http://link.aps.org/doi/10.1103/RevModPhys.78.641.

G. B. Arfken, H. J. Weber, and F. E. Harris, editors. *Mathematical Methods for Physicists*. Academic Press, Boston, seventh edition, 2013. ISBN 978-0-12-384654-9. doi: http://dx.doi.org/10.1016/B978-0-12-384654-9.00030-X. URL http://www.sciencedirect.com/science/article/pii/B9780123846549000030X.

P. Aussillous and D. Quéré. Quick deposition of a fluid on the wall of a tube. *Physics of Fluids*, 12(10):2367–2371, 2000.

P. Aussillous and D. Quéré. Quick deposition of a fluid on the wall of a tube. *Phys. Fluids*, 12(10), 2000.

Per Bak, Chao Tang, and Kurt Wiesenfeld. Self-organized criti-
cality: An explanation of the 1/f noise. *Phys. Rev. Lett.*, 59:
381–384, Jul 1987. doi: 10.1103/PhysRevLett.59.381. URL
https://link.aps.org/doi/10.1103/PhysRevLett.59.381.

G. I. Barenblatt. *Scaling, Self-similarity, and Intermediate Asymptotics: Dimensional
Analysis and Intermediate Asymptotics.* Cambridge University Press, 1996.

Charles N. Baroud, Francois Gallaire, and Remi Dangla. Dynamics of microflu-
idic droplets. *Lab Chip*, 10:2032–2045, 2010. doi: 10.1039/C001191F. URL
http://dx.doi.org/10.1039/C001191F.

Jean-Louis Barrat and Lydéric Bocquet. Large slip effect at
a nonwetting fluid-solid interface. *Phys. Rev. Lett.*, 82:4671–
4674, Jun 1999. doi: 10.1103/PhysRevLett.82.4671. URL
http://link.aps.org/doi/10.1103/PhysRevLett.82.4671.

O. A. Basaran. Small-scale free surface flows with breakup: Drop formation and
emerging applications. *AIChE Journal*, 48(9):1842–1848, 2002.

C. Bauer and S. Dietrich. Quantitative study of laterally inhomogeneous wetting
films. *The European Physical Journal B - Condensed Matter and Complex Sys-
tems*, 10(4):767–779, 1999. ISSN 1434-6028. doi: 10.1007/s100510050907. URL
http://dx.doi.org/10.1007/s100510050907.

O Bäumchen and K Jacobs. Slip effects in polymer thin films.
Journal of Physics: Condensed Matter, 22(3):033102, 2010. URL
http://stacks.iop.org/0953-8984/22/i=3/a=033102.

Oliver Bäumchen, Renate Fetzer, Mischa Klos, Matthias Lessel, Ludovic Marquant,
Hendrik Hähl, and Karin Jacobs. Slippage and nanorheology of thin liquid poly-
mer films. *Journal of Physics: Condensed Matter*, 24(32):325102, 2012. URL
http://stacks.iop.org/0953-8984/24/i=32/a=325102.

Oliver Bäumchen, Ludovic Marquant, Ralf Blossey, Andreas Münch, Barbara Wag-
ner, and Karin Jacobs. Influence of slip on the rayleigh-plateau rim instability in
dewetting viscous films. *Physical Review Letters*, 113:014501, Jul 2014.

Hanieh Bazyar, Pengyu Lv, Jeffery A. Wood, Slawomir Porada, Detlef Lohse, and
Rob G. H. Lammertink. Liquid–liquid displacement in slippery liquid-infused mem-
branes (slims). *Soft Matter*, 14:1780–1788, 2018.

Jacob Bear. *Dynamics of fluids in porous media.* Courier Corporation, New York,
1972.

Jurgen Becker, Gunther Grun, Ralf Seemann, Hubert Mantz, Karin Jacobs,
Klaus R. Mecke, and Ralf Blossey. Complex dewetting scenarios cap-
tured by thin-film models. *Nature Materials*, 2(1):59–63, 01 2003. URL
http://dx.doi.org/10.1038/nmat788.

D. Belardinelli, M. Sbragaglia, M. Gross, and B. Andreotti. Thermal fluctuations of an interface near a contact line. *Physical Review E*, 94:052803, Nov 2016. doi: 10.1103/PhysRevE.94.052803. URL https://link.aps.org/doi/10.1103/PhysRevE.94.052803.

Eshel Ben-Jacob and Peter Garik. The formation of patterns in non-equilibrium growth. *Nature*, 343:523 EP –, 02 1990. URL http://dx.doi.org/10.1038/343523a0.

Eshel Ben-Jacob, Inon Cohen, and Herbert Levine. Cooperative self-organization of microorganisms. *Advances in Physics*, 49(4):395–554, 2000. doi: 10.1080/000187300405228. URL https://doi.org/10.1080/000187300405228.

H. Benkreira and M.I. Khan. Air entrainment in dip coating under reduced air pressures. *Chemical Engineering Science*, 63(2):448–459, 2008.

David Bensimon, Leo P. Kadanoff, Shoudan Liang, Boris I. Shraiman, and Chao Tang. Viscous flows in two dimensions. *Rev. Mod. Phys.*, 58:977–999, Oct 1986.

R. Benzi, M. Sbragaglia, M. Bernaschi, and S. Succi. Phase-field model of long-time glasslike relaxation in binary fluid mixtures. *Phys. Rev. Lett.*, 106:164501, Apr 2011. doi: 10.1103/PhysRevLett.106.164501. URL http://link.aps.org/doi/10.1103/PhysRevLett.106.164501.

R. Bergmann, D. van der Meer, M. Stijnman, M. Sandtke, A. Prosperetti, and D. Lohse. Giant bubble pinch-off. *Phys. Rev. Lett.*, 96:154505, Apr 2006. doi: 10.1103/PhysRevLett.96.154505. URL https://link.aps.org/doi/10.1103/PhysRevLett.96.154505.

A. L. Bertozzi, A. Münch, X. Fanton, and A. M. Cazabat. Contact line stability and "undercompressive shocks" in driven thin film flow. *Phys. Rev. Lett.*, 81:5169–5172, Dec 1998.

A L Bertozzi, G Grün, and T P Witelski. Dewetting films: bifurcations and concentrations. *Nonlinearity*, 14(6):1569–1592, 2001a. URL http://stacks.iop.org/0951-7715/14/i=6/a=309.

A. L. Bertozzi, A. Munch, M. Shearer, and K. Zumbrun. Stability of compressive and undercompressive thin film travelling waves. *European Journal of Applied Mathematics*, 12(3):253–291, 2001b.

A.L. Bertozzi, A. Münch, and M. Shearer. Undercompressive shocks in thin film flows. *Physica D: Nonlinear Phenomena*, 134(4):431–464, 1999.

Andrea L Bertozzi. The mathematics of moving contact lines in thin liquid films. *Notices of the AMS*, 45(6):689–697, 1998.

Andrea L. Bertozzi. Designer shocks for carving out microscale surface morphologies. *Proceedings of the National Academy of Sciences*, 113(41):11384–11386, 2016.

Andrea L. Bertozzi and Michael P. Brenner. Linear stability and transient growth in driven contact lines. *Physics of Fluids*, 9(3):530–539, 1997.

J Bibette, F Leal Calderon, and P Poulin. Emulsions: basic principles. *Reports on Progress in Physics*, 62(6):969–1033, 1999. URL http://stacks.iop.org/0034-4885/62/i=6/a=203.

J. Bico, C. Tordeux, and D. Quéré. Rough wetting. *EPL (Europhysics Letters)*, 55 (2):214, 2001.

J. Bischof, D. Scherer, S. Herminghaus, and P. Leiderer. Dewetting modes of thin metallic films: Nucleation of holes and spinodal dewetting. *Physical Review Letters*, 77:1536–1539, Aug 1996. doi: 10.1103/PhysRevLett.77.1536. URL http://link.aps.org/doi/10.1103/PhysRevLett.77.1536.

S. Blake. Volcanism and the dynamics of open magma chambers. *Nature*, 289:783–785, 02 1981. URL http://dx.doi.org/10.1038/289783a0.

T. D. Blake and J. De Coninck. Dynamics of wetting and kramers'theory. *The European Physical Journal Special Topics*, 197(1):249, 2011. doi: 10.1140/epjst/e2011-01467-2. URL https://doi.org/10.1140/epjst/e2011-01467-2.

T. D. Blake and K. J. Ruschak. A maximum speed of wetting. *Nature*, 282(5738): 489–491, 11 1979.

T.D Blake and J.M Haynes. Kinetics of liquid liquid displacement. *J. Colloid Interface Sci.*, 30(3):421 – 423, 1969. ISSN 0021-9797. doi: http://dx.doi.org/10.1016/0021-9797(69)90411-1. URL http://www.sciencedirect.com/science/article/pii/0021979769904111.

Terence D. Blake. The physics of moving wetting lines. *J. Colloid Interface Sci.*, 299 (1):1–13, 2006.

Ralf Blossey. *Thin liquid films: dewetting and polymer flow.* Springer Science & Business Media, 2012.

Martin J Blunt. *Multiphase Flow in Permeable Media: A Pore-Scale Perspective.* Cambridge University Press, 2017.

Lyderic Bocquet and Elisabeth Charlaix. Nanofluidics, from bulk to interfaces. *Chem. Soc. Rev.*, 39:1073–1095, 2010. doi: 10.1039/B909366B. URL http://dx.doi.org/10.1039/B909366B.

Lyderic Bocquet and Patrick Tabeling. Physics and technological aspects of nanofluidics. *Lab Chip*, 14:3143–3158, 2014. doi: 10.1039/C4LC00325J. URL http://dx.doi.org/10.1039/C4LC00325J.

R. Bolaños-Jiménez, A. Sevilla, C. Martínez-Bazán, D. van der Meer, and J. M. Gordillo. The effect of liquid viscosity on bubble pinch-off. *Physics of Fluids*, 21(7):072103, 2009. doi: 10.1063/1.3173195. URL https://doi.org/10.1063/1.3173195.

C. Bollinne, S. Cuenot, B. Nysten, and A. M. Jonas. Spinodal-like dewetting of thermodynamically-stable thin polymer films. *The European Physical Journal E*, 12(3):389–396, 2003. ISSN 1292-895X. doi: 10.1140/epje/e2004-00007-6. URL http://dx.doi.org/10.1140/epje/e2004-00007-6.

D. Bonn, J. Eggers, J. Indekeu, J. Meunier, and E. Rolley. Wetting and spreading. *Rev. Mod. Phys.*, 81:739–805, May 2009. doi: 10.1103/RevModPhys.81.739. URL http://link.aps.org/doi/10.1103/RevModPhys.81.739.

Mark Bowen, Jeanman Sur, Andrea L. Bertozzi, and Robert P. Behringer. Nonlinear dynamics of two-dimensional undercompressive shocks. *Physica D: Nonlinear Phenomena*, 209(1):36 – 48, 2005.

Richard J. Braun. Dynamics of the tear film. *Annual Review of Fluid Mechanics*, 44(1):267–297, 2012. doi: 10.1146/annurev-fluid-120710-101042. URL https://doi.org/10.1146/annurev-fluid-120710-101042.

A. J. Bray. Theory of phase ordering kinetics. *Adv. Phys.*, 43:357–459, 1994.

M. P. Brenner, X. D. Shi, and S. R. Nagel. Iterated instabilities during droplet fission. *Phys. Rev. Lett.*, 73:3391–3394, Dec 1994. doi: 10.1103/PhysRevLett.73.3391. URL https://link.aps.org/doi/10.1103/PhysRevLett.73.3391.

M. P. Brenner, J. R. Lister, and H. A. Stone. Pinching threads, singularities and the number 0.0304... *Physics of Fluids*, 8(11):2827–2836, 1996. doi: 10.1063/1.869086. URL https://doi.org/10.1063/1.869086.

Michael Brenner and Andrea Bertozzi. Spreading of droplets on a solid surface. *Phys. Rev. Lett.*, 71:593–596, Jul 1993. doi: 10.1103/PhysRevLett.71.593. URL http://link.aps.org/doi/10.1103/PhysRevLett.71.593.

Michael P. Brenner. Instability mechanism at driven contact lines. *Phys. Rev. E*, 47: 4597–4599, Jun 1993.

F. P. Bretherton. The motion of long bubbles in tubes. *Journal of Fluid Mechanics*, 10(2):166–188, 1961. doi: 10.1017/S0022112061000160.

A. J. Briant and J. M. Yeomans. Lattice boltzmann simulations of contact line motion. ii. binary fluids. *Phys. Rev. E*, 69: 031603, Mar 2004. doi: 10.1103/PhysRevE.69.031603. URL https://link.aps.org/doi/10.1103/PhysRevE.69.031603.

A. J. Briant, A. J. Wagner, and J. M. Yeomans. Lattice boltzmann simulations of contact line motion. i. liquid-gas systems. *Phys. Rev. E*, 69:031602, Mar 2004a. doi: 10.1103/PhysRevE.69.031602. URL https://link.aps.org/doi/10.1103/PhysRevE.69.031602.

A. J. Briant, A. J. Wagner, and J. M. Yeomans. Lattice boltzmann simulations of contact line motion. i. liquid-gas systems. *Phys. Rev. E*, 69:031602, Mar 2004b. doi: 10.1103/PhysRevE.69.031602. URL https://link.aps.org/doi/10.1103/PhysRevE.69.031602.

F. Brochard-Wyart and Pierre-Gilles de Gennes. Dynamics of partial wetting. *Adv. Colloid Interface Sci.*, 39(0):1 – 11, 1992. doi: 10.1016/0001-8686(92)80052-Y. URL http://www.sciencedirect.com/science/article/pii/000186869280052Y.

F. Brochard-Wyart, P. Martin, and C. Redon. Liquid/liquid dewetting. *Langmuir*, 9 (12):3682–3690, 1993. doi: 10.1021/la00036a053.

Françoise Brochard-Wyart, Jean Marc Di Meglio, David. Quéré, and Pierre-Gilles de Gennes. Spreading of nonvolatile liquids in a continuum picture. *Langmuir*, 7 (2):335–338, 1991. doi: 10.1021/la00050a023.

J. S. Buckley, Y. Liu, and S. Monsterleet. Mechanisms of wetting alteration by crude oils. *Soc. Pet.Eng. J.*, 3(54), 1998.

J. C. Burton and P. Taborek. Role of dimensionality and axisymmetry in fluid pinch-off and coalescence. *Phys. Rev. Lett.*, 98: 224502, May 2007. doi: 10.1103/PhysRevLett.98.224502. URL https://link.aps.org/doi/10.1103/PhysRevLett.98.224502.

J. C. Burton and P. Taborek. Bifurcation from bubble to droplet behavior in inviscid pinch-off. *Phys. Rev. Lett.*, 101: 214502, Nov 2008. doi: 10.1103/PhysRevLett.101.214502. URL https://link.aps.org/doi/10.1103/PhysRevLett.101.214502.

J. C. Burton, R. Waldrep, and P. Taborek. Scaling and instabilities in bubble pinch-off. *Phys. Rev. Lett.*, 94:184502, May 2005. doi: 10.1103/PhysRevLett.94.184502. URL https://link.aps.org/doi/10.1103/PhysRevLett.94.184502.

J. W. Cahn. On spinodal decomposition. *Acta Metallurgica*, 9(9):795–801, 1961. ISSN 0001-6160. doi: http://dx.doi.org/10.1016/0001-6160(61)90182-1. URL http://www.sciencedirect.com/science/article/pii/0001616061901821.

John W. Cahn and John E. Hilliard. Free energy of a nonuniform system. i. interfacial free energy. *J. Chem. Phys.*, 28(2):258–267, 1958. doi: 10.1063/1.1744102. URL http://link.aip.org/link/?JCP/28/258/1.

Roberto Camassa and H. Reed Ogrosky. On viscous film flows coating the interior of a tube: thin-film and long-wave models. *J. Fluid Mech.*, 772:569–599, 2015. doi: 10.1017/jfm.2015.221.

Isabelle Cantat. Liquid meniscus friction on a wet plate: Bubbles, lamellae, and foams. *Physics of Fluids*, 25(3):031303, 2013.

J. M. Carlson and J. S. Langer. Properties of earthquakes generated by fault dynamics. *Phys. Rev. Lett.*, 62:2632–2635, May 1989. doi: 10.1103/PhysRevLett.62.2632. URL https://link.aps.org/doi/10.1103/PhysRevLett.62.2632.

Jaume Casademunt. Viscous fingering as a paradigm of interfacial pattern formation: Recent results and new challenges. *Chaos: An Interdisciplinary Journal of Nonlinear Science*, 14(3):809–824, 2004. doi: 10.1063/1.1784931. URL http://link.aip.org/link/?CHA/14/809/1.

Katharine V. Cashman, R. Stephen J. Sparks, and Jonathan D. Blundy. Vertically extensive and unstable magmatic systems: A unified view of igneous processes. *Science*, 355(6331), 2017. ISSN 0036-8075. doi: 10.1126/science.aag3055. URL http://science.sciencemag.org/content/355/6331/eaag3055.

A. B. D. Cassie and S. Baxter. Wettability of porous surfaces. *Trans. Faraday Soc.*, 40:546–551, 1944.

J. R. Castrejón-Pita et al. Plethora of transitions during breakup of liquid filaments. *Proceedings of the National Academy of Sciences*, 112(15): 4582–4587, 2015. ISSN 0027-8424. doi: 10.1073/pnas.1418541112. URL http://www.pnas.org/content/112/15/4582.

A. M. Cazabat, F. Heslot, S. M. Troian, and P. Carles. Fingering instability of thin spreading films driven by temperature gradients. *Nature*, 346:824–826, 08 1990.

T. S. Chan, S. Srivastava, A. Marchand, B. Andreotti, L. Biferale, F. Toschi, and J. H. Snoeijer. Hydrodynamics of air entrainment by moving contact lines. *Phys. Fluids*, 25(7):074105, 2013.

Tak Shing Chan, Jacco H. Snoeijer, and Jens Eggers. Theory of the forced wetting transition. *Physics of Fluids*, 24(7):072104, 2012.

H. Henry Chen, Omar A. Urquidez, Stefan Ichim, L. Humberto Rodriquez, Michael P. Brenner, and Michael J. Aziz. Shocks in ion sputtering sharpen steep surface features. *Science*, 310(5746):294–297, 2005.

Hsuan-Yi Chen, David Jasnow, and Jorge Viñals. Interface and contact line motion in a two phase fluid under shear flow. *Phys. Rev. Lett.*, 85:1686–1689, Aug 2000. doi: 10.1103/PhysRevLett.85.1686. URL https://link.aps.org/doi/10.1103/PhysRevLett.85.1686.

Jing-Den Chen. Experiments on a spreading drop and its contact angle on a solid. *J. Colloid Interface Sci.*, 122(1):60–72, 1988. doi: http://dx.doi.org/10.1016/0021-9797(88)90287-1. URL http://www.sciencedirect.com/science/article/pii/0021979788902871.

Jiun-Tai Chen, Mingfu Zhang, and Thomas P. Russell. Instabilities in nanoporous media. *Nano Letters*, 7(1):183–187, 2007. doi: 10.1021/nl0621241. URL http://dx.doi.org/10.1021/nl0621241.

Lei Chen, Jiapeng Yu, and Hao Wang. Convex nanobending at a moving contact line: The missing mesoscopic link in dynamic wetting. *ACS Nano*, 8(11):11493–11498, 2014. doi: 10.1021/nn5046486.

Peila Chen and Kishore Mohanty. Surfactant-mediated spontaneous imbibition in carbonate rocks at harsh reservoir conditions. *Soc. Pet.Eng. J.*, 18(124), 2013.

Yi-Feng Chen, Shu Fang, Dong-Sheng Wu, and Ran Hu. Visualizing and quantifying the crossover from capillary fingering to viscous fingering in a rough fracture. *Water Resources Research*, 53(9):7756–7772, 2017.

Marek Cieplak and Mark O. Robbins. Dynamical transition in quasistatic fluid invasion in porous media. *Phys. Rev. Lett.*, 60: 2042–2045, May 1988. doi: 10.1103/PhysRevLett.60.2042. URL http://link.aps.org/doi/10.1103/PhysRevLett.60.2042.

Marek Cieplak and Mark O. Robbins. Influence of contact angle on quasistatic fluid invasion of porous media. *Physical Review B*, 41: 11508–11521, Jun 1990. doi: 10.1103/PhysRevB.41.11508. URL http://link.aps.org/doi/10.1103/PhysRevB.41.11508.

Yildiray Cinar and Amir Riaz. Carbon dioxide sequestration in saline formations: Part 2—review of multiphase flow modeling. *Journal of Petroleum Science and Engineering*, 124:381 – 398, 2014. ISSN 0920-4105. doi: https://doi.org/10.1016/j.petrol.2014.07.023. URL http://www.sciencedirect.com/science/article/pii/S0920410514002216.

Xavier Clotet, Jordi Ortín, Jordi'in, and Stéphane Santucci. Disorder-induced capillary bursts control intermittency in slow imbibition. *Phys. Rev. Lett.*, 113:074501, Aug 2014. doi: 10.1103/PhysRevLett.113.074501. URL http://link.aps.org/doi/10.1103/PhysRevLett.113.074501.

I. Cohen, M. P. Brenner, J. Eggers, and S. R. Nagel. Two fluid drop snap-off problem: Experiments and theory. *Phys. Rev. Lett.*, 83:1147–1150, Aug 1999. doi: 10.1103/PhysRevLett.83.1147. URL https://link.aps.org/doi/10.1103/PhysRevLett.83.1147.

A. Colin, T. M. Squires, and L. Bocquet. Soft matter principles of microfluidics. *Soft Matter*, 8:10527–10529, 2012. doi: 10.1039/C2SM90116A. URL http://dx.doi.org/10.1039/C2SM90116A.

Y. Couder, O. Cardoso, D. Dupuy, P. Tavernier, and W. Thom. Dendritic growth in the saffman-taylor experiment. *EPL (Europhysics Letters)*, 2(6):437, 1986a.

Y. Couder, N. Gérard, and M. Rabaud. Narrow fingers in the saffman-taylor instability. *Phys. Rev. A*, 34:5175–5178, Dec 1986b.

R. G. Cox. The dynamics of the spreading of liquids on a solid surface. part 1. viscous flow. *J. Fluid Mech.*, 168:169–194, 6 1986.

R. V. Craster and O. K. Matar. Dynamics and stability of thin liquid films. *Rev. Mod. Phys.*, 81:1131–1198, Aug 2009.

M. C. Cross and P. C. Hohenberg. Pattern formation outside of equilibrium. *Reviews of Modern Physics*, 65:851–1112, Jul 1993. doi: 10.1103/RevModPhys.65.851. URL http://link.aps.org/doi/10.1103/RevModPhys.65.851.

T. Cubaud, M. Tatineni, X. Zhong, and C-M. Ho. Bubble dispenser in microfluidic devices. *Phys. Rev. E*, 72:037302, Sep 2005. doi: 10.1103/PhysRevE.72.037302. URL https://link.aps.org/doi/10.1103/PhysRevE.72.037302.

L. Cueto-Felgueroso and R. Juanes. Nonlocal interface dynamics and pattern formation in gravity-driven unsaturated flow through porous media. *Phys. Rev. Lett.*, 101:244504, 2008a.

L. Cueto-Felgueroso and R. Juanes. Nonlocal interface dynamics and pattern formation in gravity-driven unsaturated flow through porous media. *Phys. Rev. Lett.*, 101:244504, 2008b.

Luis Cueto-Felgueroso and Ruben Juanes. Macroscopic phase-field model of partial wetting: Bubbles in a capillary tube. *Physical Review Letters*, 108:144502, Apr 2012. doi: 10.1103/PhysRevLett.108.144502. URL http://link.aps.org/doi/10.1103/PhysRevLett.108.144502.

Luis Cueto-Felgueroso and Ruben Juanes. A phase-field model of two-phase hele-shaw flow. *Journal of Fluid Mechanics*, 758:522–552, 2014. doi: 10.1017/jfm.2014.512.

Luis Cueto-Felgueroso and Ruben Juanes. A discrete-domain description of multiphase flow in porous media: Rugged energy landscapes and the origin of hysteresis. *Geophysical Research Letters*, 43(4):1615–1622, 2016.

Bing Dai, L. Gary Leal, and Antonio Redondo. Disjoining pressure for nonuniform thin films. *Phys. Rev. E*, 78:061602, Dec 2008. doi: 10.1103/PhysRevE.78.061602. URL http://link.aps.org/doi/10.1103/PhysRevE.78.061602.

Anton A. Darhuber and Sandra M. Troian. Principles of microfluidic actuation by modulation of surface stresses. *Annual Review of Fluid Mechanics*, 37(1):425–455, 2005. doi: 10.1146/annurev.fluid.36.050802.122052. URL https://doi.org/10.1146/annurev.fluid.36.050802.122052.

Benny Davidovitch, Esteban Moro, and Howard A. Stone. Spreading of viscous fluid drops on a solid substrate assisted by thermal fluctuations. *Physical Review Letters*, 95:244505, Dec 2005. doi: 10.1103/PhysRevLett.95.244505. URL http://link.aps.org/doi/10.1103/PhysRevLett.95.244505.

R. F. Day, E. J. Hinch, and J. R. Lister. Self-similar capillary pinchoff of an inviscid fluid. *Phys. Rev. Lett.*, 80:704–707, Jan 1998. doi: 10.1103/PhysRevLett.80.704. URL https://link.aps.org/doi/10.1103/PhysRevLett.80.704.

J. De Coninck and T.D. Blake. Wetting and molecular dynamics simulations of simple liquids. *Annual Review of Materials Research*, 38 (1):1–22, 2008. doi: 10.1146/annurev.matsci.38.060407.130339. URL https://doi.org/10.1146/annurev.matsci.38.060407.130339.

P. G. de Gennes. Deposition of langmuir-blodgett layers. *Colloid and Polymer Science*, 264(5):463–465, 1986.

Pierre-Gilles de Gennes. Dynamics of fluctuations and spinodal decomposition in polymer blends. *The Journal of Chemical Physics*, 72 (9):4756–4763, 1980. doi: http://dx.doi.org/10.1063/1.439809. URL http://scitation.aip.org/content/aip/journal/jcp/72/9/10.1063/1.439809.

Pierre-Gilles de Gennes. Wetting: statics and dynamics. *Reviews of Modern Physics*, 57:827–863, Jul 1985. doi: 10.1103/RevModPhys.57.827. URL http://link.aps.org/doi/10.1103/RevModPhys.57.827.

Pierre-Gilles de Gennes, X. Hua, and P. Levinson. Dynamics of wetting: local contact angles. *J. Fluid Mech.*, 212:55–63, 3 1990. doi: 10.1017/S0022112090001859.

Pierre-Gilles de Gennes, Françoise Brochard-Wyart, and David Quéré. *Capillarity and Wetting Phenomena: Drops, Bubbles, Pearls, Waves*. Springer, 2004.

M. J. de Ruijter, J. De Coninck, and G. Oshanin. Droplet spreading: partial wetting regime revisited. *Langmuir*, 15(6):2209–2216, 1999. doi: 10.1021/la971301y. URL http://pubs.acs.org/doi/abs/10.1021/la971301y.

A. Deblais, R. Harich, A. Colin, and H. Kellay. Taming contact line instability for pattern formation. *Nature Communications*, 7:12458, 08 2016.

G. Delon, M. Fermigier, J. H. Snoeijer, and B. Andreotti. Relaxation of a dewetting contact line. part 2. experiments. *Journal of Fluid Mechanics*, 604:55—75, 2008.

Yajun Deng, Lei Chen, Qiao Liu, Jiapeng Yu, and Hao Wang. Nanoscale view of dewetting and coating on partially wetted solids. *The Journal of Physical Chemistry Letters*, 7(10):1763–1768, 2016. doi: 10.1021/acs.jpclett.6b00620. URL http://dx.doi.org/10.1021/acs.jpclett.6b00620.

B. V. Derjaguin. On the thickness of a layer of liquid remaining on the walls of vessels after their emptying, and the theory of the application of photoemulsion after coating on the cine film. *Acta Physicochim, URSS*, 20(349), 1943.

BV Derjaguin, NV Churaev, and VM Muller. *Surface Forces*. Springer, 1987.

Olivier Devauchelle, Alexander P. Petroff, Hansjörg F. Seybold, and Daniel H. Rothman. Ramification of stream networks. *Proceedings of the National Academy of Sciences*, 109(51):20832–20836, 2012. ISSN 0027-8424. doi: 10.1073/pnas.1215218109. URL http://www.pnas.org/content/109/51/20832.

David A. DiCarlo. Stability of gravity-driven multiphase flow in porous media: 40 years of advancements. *Water Resources Research*, 49(8):4531–4544, 2013. doi: 10.1002/wrcr.20359. URL https://agupubs.onlinelibrary.wiley.com/doi/abs/10.1002/wrcr.20359.

Javier A. Diez and L. Kondic. Contact line instabilities of thin liquid films. *Phys. Rev. Lett.*, 86:632–635, Jan 2001.

Javier A. Diez and Lou Kondic. On the breakup of fluid films of finite and infinite extent. *Physics of Fluids*, 19(7):072107, 2007. doi: 10.1063/1.2749515. URL http://link.aip.org/link/?PHF/19/072107/1.

Javier A. Diez, L. Kondic, and Andrea Bertozzi. Global models for moving contact lines. *Phys. Rev. E*, 63:011208, Dec 2000. doi: 10.1103/PhysRevE.63.011208. URL http://link.aps.org/doi/10.1103/PhysRevE.63.011208.

Javier A. Diez, Alejandro G. González, and Roberto Fernández. Metallic-thin-film instability with spatially correlated thermal noise. *Physical Review E*, 93:013120, Jan 2016. doi: 10.1103/PhysRevE.93.013120. URL http://link.aps.org/doi/10.1103/PhysRevE.93.013120.

Hang Ding and Peter D. M. Spelt. Wetting condition in diffuse interface simulations of contact line motion. *Phys. Rev. E*, 75:046708, Apr 2007. doi: 10.1103/PhysRevE.75.046708. URL https://link.aps.org/doi/10.1103/PhysRevE.75.046708.

B. Dollet, W. van Hoeve, J-P. Raven, P. Marmottant, and M. Versluis. Role of the channel geometry on the bubble pinch-off in flow-focusing devices. *Phys. Rev. Lett.*, 100:034504, Jan 2008a. doi: 10.1103/PhysRevLett.100.034504. URL https://link.aps.org/doi/10.1103/PhysRevLett.100.034504.

B. Dollet, W. van Hoeve, J.-P. Raven, P. Marmottant, and M. Versluis. Role of the channel geometry on the bubble pinch-off in flow-focusing devices. *Phys. Rev. Lett.*, 100:034504, 2008b.

P. Doshi, I. Cohen, W. W. Zhang, M. Siegel, P. Howell, O. A. Basaran, and S. R. Nagel. Persistence of memory in drop breakup: The breakdown of universality. *Science*, 302(5648):1185–1188, 2003. ISSN 0036-8075. doi: 10.1126/science.1089272. URL http://science.sciencemag.org/content/302/5648/1185.

Cyril Duez, Christophe Ybert, Christophe Clanet, and Lyderic Bocquet. Making a splash with water repellency. *Nat. Phys.*, 3(3):180–183, 03 2007.

E. B. Dussan V. The moving contact line: the slip boundary condition. *J. Fluid Mech.*, 77:665–684, 10 1976. doi: 10.1017/S0022112076002838.

Elizabeth B. Dussan V. and Stephen H. Davis. On the motion of a fluid-fluid interface along a solid surface. *J. Fluid Mech.*, 65:71–95, 7 1974. doi: 10.1017/S0022112074001261.

Damien Duvivier, Terence D. Blake, and Joël De Coninck. Toward a predictive theory of wetting dynamics. *Langmuir*, 29(32):10132–10140, 2013. doi: 10.1021/la4017917. URL https://doi.org/10.1021/la4017917. PMID: 23844877.

I.E. Dzyaloshinskii, E.M. Lifshitz, and L.P. Pitaevskii. The general theory of van der Waals forces. *Advances in Physics*, 10(38):165–209, 1961. doi: 10.1080/00018736100101281.

H. E. Edgerton, E. A. Hauser, and W. B. Tucker. Studies in drop formation as revealed by the high-speed motion camera. *The Journal of Physical Chemistry*, 41(7):1017–1028, 1937. doi: 10.1021/j150385a012. URL https://doi.org/10.1021/j150385a012.

A. M. J. Edwards, R. Ledesma-Aguilar, M. I. Newton, C. V. Brown, and G. McHale. Not spreading in reverse: The dewetting of a liquid film into a single drop. *Sci. Adv.*, 2:e1600183, 2016.

J. Eggers. Universal pinching of 3D axisymmetric free-surface flow. *Phys. Rev. Lett.*, 71:3458–3460, Nov 1993. doi: 10.1103/PhysRevLett.71.3458. URL https://link.aps.org/doi/10.1103/PhysRevLett.71.3458.

J. Eggers. Nonlinear dynamics and breakup of free-surface flows. *Rev. Mod. Phys.*, 69:865–930, Jul 1997. doi: 10.1103/RevModPhys.69.865. URL https://link.aps.org/doi/10.1103/RevModPhys.69.865.

J. Eggers. *Singularities at Interfaces*, volume 98 of *Lecture Notes of the Les Houches Summer School*, pages 101–132. Oxford University Press, 2012.

J. Eggers and M. A. Fontelos. *Singularities: Formation, Structure, and Propagation.* Cambridge University Press, 2015.

J. Eggers and E. Villermaux. Physics of liquid jets. *Reports on Progress in Physics*, 71(3):036601, 2008. URL http://stacks.iop.org/0034-4885/71/i=3/a=036601.

J. Eggers, M. A. Fontelos, D. Leppinen, and J. H. Snoeijer. Theory of the collapsing axisymmetric cavity. *Phys. Rev. Lett.*, 98:094502, Mar 2007. doi: 10.1103/PhysRevLett.98.094502. URL https://link.aps.org/doi/10.1103/PhysRevLett.98.094502.

Jens Eggers. Hydrodynamic theory of forced dewetting. *Phys. Rev. Lett.*, 93:094502, Aug 2004. doi: 10.1103/PhysRevLett.93.094502. URL https://link.aps.org/doi/10.1103/PhysRevLett.93.094502.

Jens Eggers. Existence of receding and advancing contact lines. *Physics of Fluids*, 17 (8):082106, 2005.

Jens Eggers and Howard A. Stone. Characteristic lengths at moving contact lines for a perfectly wetting fluid: the influence of speed on the dynamic contact angle. *J. Fluid Mech.*, 505:309–321, 3 2004. doi: 10.1017/S0022112004008663.

Jonathan P. Ennis-King and Lincoln Paterson. Role of convective mixing in the long-term storage of carbon dioxide in deep saline formations. *Soc. Pet.Eng. J.*, 2005. doi: 10.2118/84344-PA.

M. Fermigier and P. Jenffer. An experimental investigation of the dynamic contact angle in liquid–liquid systems. *J. Colloid Interface Sci.*, 146(1):226–241, 1991a.

Marc Fermigier and Patrice Jenffer. An experimental investigation of the dynamic contact angle in liquid-liquid systems. *J. Colloid Interface Sci.*, 146(1):226 – 241, 1991b. ISSN 0021-9797. doi: http://dx.doi.org/10.1016/0021-9797(91)90020-9. URL http://www.sciencedirect.com/science/article/pii/0021979791900209.

R. Fetzer, K. Jacobs, A. Münch, B. Wagner, and T. P. Witelski. New slip regimes and the shape of dewetting thin liquid films. *Physical Review Letters*, 95:127801, Sep 2005. doi: 10.1103/PhysRevLett.95.127801. URL http://link.aps.org/doi/10.1103/PhysRevLett.95.127801.

R. Fetzer, A. Münch, B. Wagner, M. Rauscher, and K. Jacobs. Quantifying hydrodynamic slip: a comprehensive analysis of dewetting profiles. *Langmuir*, 23(21):10559–10566, 2007a. doi: 10.1021/la7010698. URL http://dx.doi.org/10.1021/la7010698.

R. Fetzer, M. Rauscher, R. Seemann, K. Jacobs, and K. Mecke. Thermal noise influences fluid flow in thin films during spinodal dewetting. *Physical Review Letters*, 99:114503, Sep 2007b. doi: 10.1103/PhysRevLett.99.114503. URL http://link.aps.org/doi/10.1103/PhysRevLett.99.114503.

Daniel S. Fisher. Threshold behavior of charge-density waves pinned by impurities. *Phys. Rev. Lett.*, 50:1486–1489, May 1983. doi: 10.1103/PhysRevLett.50.1486. URL https://link.aps.org/doi/10.1103/PhysRevLett.50.1486.

Dieter Forster, David R. Nelson, and Michael J. Stephen. Large-distance and long-time properties of a randomly stirred fluid. *Physical Review A*, 16:732–749, Aug 1977. doi: 10.1103/PhysRevA.16.732. URL http://link.aps.org/doi/10.1103/PhysRevA.16.732.

Jason D. Fowlkes, Lou Kondic, Javier Diez, Yueying Wu, and Philip D. Rack. Self-assembly versus directed assembly of nanoparticles via pulsed laser induced dewetting of patterned metal films. *Nano Letters*, 11(6):2478–2485, 2011. doi: 10.1021/nl200921c. URL http://dx.doi.org/10.1021/nl200921c.

Andrés Franco-Gómez, Alice B. Thompson, Andrew L. Hazel, and Anne Juel. Sensitivity of saffman–taylor fingers to channel-depth perturbations. *Journal of Fluid Mechanics*, 794:343–368, 2016. doi: DOI: 10.1017/jfm.2016.131. URL https://www.cambridge.org/core/article/sensitivity-of-saffmantaylor-fingers-to-chan

Jonathan B. Freund. The atomic detail of a wetting/de-wetting flow. *Phys. Fluids*, 15(5):L33–L36, 2003. doi: http://dx.doi.org/10.1063/1.1565112. URL http://scitation.aip.org/content/aip/journal/pof2/15/5/10.1063/1.1565112.

N. Fries and M. Dreyer. The transition from inertial to viscous flow in capillary rise. *J. Colloid Interface Sci.*, 327:125–128, 2008.

M. J. Fuerstman, P. Garstecki, and G. M. Whitesides. Coding/decoding and reversibility of droplet trains in microfluidic networks. *Science*, 315(5813): 828–832, 2007. ISSN 0036-8075. doi: 10.1126/science.1134514. URL http://science.sciencemag.org/content/315/5813/828.

A. M. Gañán Calvo and J. M. Gordillo. Perfectly monodisperse microbubbling by capillary flow focusing. *Phys. Rev. Lett.*, 87: 274501, Dec 2001. doi: 10.1103/PhysRevLett.87.274501. URL https://link.aps.org/doi/10.1103/PhysRevLett.87.274501.

Y. Gai, C. M. Leong, W. Cai, and S. K. Y. Tang. Spatiotemporal periodicity of dislocation dynamics in a two-dimensional microfluidic crystal flowing in a tapered channel. *Proceedings of the National Academy of Sciences*, 113(43): 12082–12087, 2016. ISSN 0027-8424. doi: 10.1073/pnas.1606601113. URL http://www.pnas.org/content/113/43/12082.

M. Galvagno, D. Tseluiko, H. Lopez, and U. Thiele. Continuous and discontinuous dynamic unbinding transitions in drawn film flow. *Phys. Rev. Lett.*, 112:137803, Apr 2014.

A. M. Gañán-Calvo, R. González-Prieto, P. Riesco-Chueca, M. A. Herrada, and M. Flores-Mosquera. Focusing capillary jets close to the continuum limit. *Nature Physics*, 3:737–742, 09 2007. URL http://dx.doi.org/10.1038/nphys710.

Peng Gao and Xi-Yun Lu. On the wetting dynamics in a couette flow. *Journal of Fluid Mechanics*, 724:R1, 2013.

Peng Gao, Lei Li, James J. Feng, Hang Ding, and Xi-Yun Lu. Film deposition and transition on a partially wetting plate in dip coating. *Journal of Fluid Mechanics*, 791:358—383, 2016.

P. Garstecki, I. Gitlin, W. DiLuzio, G. M. Whitesides, E. Kumacheva, and H. A. Stone. Formation of monodisperse bubbles in a microfluidic flow-focusing device. *Applied Physics Letters*, 85(13):2649–2651, 2004a.

P. Garstecki, I. Gitlin, W. DiLuzio, G. M. Whitesides, E. Kumacheva, and H. A. Stone. Formation of monodisperse bubbles in a microfluidic flow-focusing device. *Appl. Phys. Lett.*, 85(13):2649–2651, 2004b.

P. Garstecki, M. J. Fuerstman, and G. M. Whitesides. Nonlinear dynamics of a flow-focusing bubble generator: An inverted dripping faucet. *Phys. Rev. Lett.*, 94:234502, Jun 2005a. doi: 10.1103/PhysRevLett.94.234502. URL https://link.aps.org/doi/10.1103/PhysRevLett.94.234502.

P. Garstecki, M. J. Fuerstman, and G. M. Whitesides. Oscillations with uniquely long periods in a microfluidic bubble generator. *Nature Physics*, 1:168–171, 12 2005b. URL http://dx.doi.org/10.1038/nphys176.

P. Garstecki, H. A. Stone, and G. M. Whitesides. Mechanism for flow-rate controlled breakup in confined geometries: A route to monodisperse emulsions. *Phys. Rev. Lett.*, 94:164501, Apr 2005c. doi: 10.1103/PhysRevLett.94.164501. URL https://link.aps.org/doi/10.1103/PhysRevLett.94.164501.

P. Garstecki, M. J. Fuerstman, H. A. Stone, and G. M. Whitesides. Formation of droplets and bubbles in a microfluidic T-junction-scaling and mechanism of break-up. *Lab Chip*, 6:437–446, 2006a. doi: 10.1039/B510841A. URL http://dx.doi.org/10.1039/B510841A.

P. Garstecki, M. J. Fuerstman, H. A. Stone, and G. M. Whitesides. Formation of droplets and bubbles in a microfluidic t-junction—scaling and mechanism of break-up. *Lab Chip*, 6:437–446, 2006b.

B. D. Gates, Q. Xu, M. Stewart, D. Ryan, C. G. Willson, and G. M. Whitesides. New approaches to nanofabrication: molding, printing, and other techniques. *Chemical Reviews*, 105(4):1171–1196, 2005. doi: 10.1021/cr030076o.

Hartmut Gau, Stephan Herminghaus, Peter Lenz, and Reinhard Lipowsky. Liquid morphologies on structured surfaces: From microchannels to microchips. *Science*, 283(5398):46, 01 1999.

P.A. Gauglitz and C.J. Radke. An extended evolution equation for liquid film breakup in cylindrical capillaries. *Chem. Eng. Sci.*, 43(7):1457 – 1465, 1988. ISSN 0009-2509. doi: https://doi.org/10.1016/0009-2509(88)85137-6. URL http://www.sciencedirect.com/science/article/pii/0009250988851376.

S. Gekle, A. van der Bos, R. Bergmann, D. van der Meer, and D. Lohse. Noncontinuous Froude number scaling for the closure depth of a cylindrical cavity. *Phys. Rev. Lett.*, 100:084502, Feb 2008. doi: 10.1103/PhysRevLett.100.084502. URL https://link.aps.org/doi/10.1103/PhysRevLett.100.084502.

S. Gekle, J. H. Snoeijer, D. Lohse, and D. van der Meer. Approach to universality in axisymmetric bubble pinch-off. *Phys. Rev. E*, 80:036305, Sep 2009. doi: 10.1103/PhysRevE.80.036305. URL https://link.aps.org/doi/10.1103/PhysRevE.80.036305.

Denis Gentili, Giulia Foschi, Francesco Valle, Massimiliano Cavallini, and Fabio Biscarini. Applications of dewetting in micro and nanotechnology. *Chem. Soc. Rev.*, 41:4430–4443, 2012. doi: 10.1039/C2CS35040H. URL http://dx.doi.org/10.1039/C2CS35040H.

Mark Geoghegan and Georg Krausch. Wetting at polymer surfaces and interfaces. *Progress in Polymer Science*, 28(2):261–302, 2003. ISSN 0079-6700. doi: http://dx.doi.org/10.1016/S0079-6700(02)00080-1. URL http://www.sciencedirect.com/science/article/pii/S0079670002000801.

Dimitrios Geromichalos, Frieder Mugele, and Stephan Herminghaus. Non-local dynamics of spontaneous imbibition fronts. *Phys. Rev. Lett.*, 89:104503, Aug 2002. doi: 10.1103/PhysRevLett.89.104503. URL http://link.aps.org/doi/10.1103/PhysRevLett.89.104503.

T. Getta and S. Dietrich. Line tension between fluid phases and a substrate. *Physical Review E*, 57:655–671, Jan 1998. doi: 10.1103/PhysRevE.57.655. URL http://link.aps.org/doi/10.1103/PhysRevE.57.655.

Alberto Giacomello, Lothar Schimmele, and Siegfried Dietrich. Wetting hysteresis induced by nanodefects. *Proceedings of the National Academy of Sciences*, 113(3):E262–E271, 2016. doi: 10.1073/pnas.1513942113. URL http://www.pnas.org/content/113/3/E262.

Ronaldo Giro, Peter W. Bryant, Michael Engel, Rodrigo F. Neumann, and Mathias B. Steiner. Adsorption energy as a metric for wettability at the nanoscale. *Scientific Reports*, 7(46317), 04 2017.

K. Glasner. Ostwald ripening in thin film equations. *SIAM Journal on Applied Mathematics*, 69(2):473–493, 2008. doi: 10.1137/080713732.

K. B. Glasner and T. P. Witelski. Coarsening dynamics of dewetting films. *Physical Review E*, 67:016302, Jan 2003. doi: 10.1103/PhysRevE.67.016302. URL http://link.aps.org/doi/10.1103/PhysRevE.67.016302.

K.B. Glasner and T.P. Witelski. Collision versus collapse of droplets in coarsening of dewetting thin films. *Physica D: Nonlinear Phenomena*, 209(1–4):80–104, 2005. ISSN 0167-2789. doi: http://dx.doi.org/10.1016/j.physd.2005.06.010.

Yury Gogotsi, Joseph A. Libera, Almila Güvenç-Yazicioglu, and Constantine M. Megaridis. In situ multiphase fluid experiments in hydrothermal carbon nanotubes. *Applied Physics Letters*, 79(7):1021–1023, 2001. doi: 10.1063/1.1391228.

R. Golestanian and E. Raphaël. Relaxation of a moving contact line and the landau-levich effect. *EPL (Europhysics Letters)*, 55(2):228, 2001.

Ramin Golestanian and Elie Raphaël. Dissipation in dynamics of a moving contact line. *Physical Review E*, 64:031601, Aug 2001.

Ramin Golestanian and Elie Raphaël. Roughening transition in a moving contact line. *Physical Review E*, 67:031603, 2003.

J. P. Gollub and J. S. Langer. Pattern formation in nonequilibrium physics. *Reviews of Modern Physics*, 71:S396–S403, Mar 1999. doi: 10.1103/RevModPhys.71.S396. URL http://link.aps.org/doi/10.1103/RevModPhys.71.S396.

J. M. Gordillo, A. Sevilla, J. Rodríguez-Rodríguez, and C. Martínez-Bazán. Axisymmetric bubble pinch-off at high Reynolds numbers. *Phys. Rev. Lett.*, 95:194501, Nov 2005. doi: 10.1103/PhysRevLett.95.194501. URL https://link.aps.org/doi/10.1103/PhysRevLett.95.194501.

Steve Granick, Yingxi Zhu, and Hyunjung Lee. Slippery questions about complex fluids flowing past solids. *Nat. Mater.*, 2(4):221–227, 04 2003. URL http://dx.doi.org/10.1038/nmat854.

M. B. Gratton and T. P. Witelski. Coarsening of unstable thin films subject to gravity. *Phys. Rev. E*, 77:016301, Jan 2008. doi: 10.1103/PhysRevE.77.016301. URL http://link.aps.org/doi/10.1103/PhysRevE.77.016301.

Michael B Gratton. *Coarsening of Thin Fluid Films*. PhD thesis, Department of Mathematics, Duke University, 2008.

Michael B. Gratton and Thomas P. Witelski. Transient and self-similar dynamics in thin film coarsening. *Physica D: Nonlinear Phenomena*, 238(23–24):2380–2394, 2009. ISSN 0167-2789. doi: http://dx.doi.org/10.1016/j.physd.2009.09.015. URL http://www.sciencedirect.com/science/article/pii/S0167278909002899.

W. G. Gray, A. L. Dye, J. E. McClure, L. J. Pyrak-Nolte, and C. T. Miller. On the dynamics and kinematics of two-fluid-phase flow in porous media. *Water Resources Research*, 51(7):5365–5381, 2015. ISSN 1944-7973. doi: 10.1002/2015WR016921. URL http://dx.doi.org/10.1002/2015WR016921.

William G. Gray and Cass T. Miller. Thermodynamically constrained averaging theory approach for modeling flow and transport phenomena in porous medium systems: 1. motivation and overview. *Advances in Water Resources*, 28(2):161 – 180, 2005. ISSN 0309-1708. doi: http://dx.doi.org/10.1016/j.advwatres.2004.09.005. URL http://www.sciencedirect.com/science/article/pii/S0309170804001551.

William G. Gray, Cass T. Miller, and Bernhard A. Schrefler. Averaging theory for description of environmental problems: What have we learned? *Advances in Water Resources*, 51:123 – 138, 2013. ISSN 0309-1708. doi: http://dx.doi.org/10.1016/j.advwatres.2011.12.005. URL http://www.sciencedirect.com/science/article/pii/S030917081100234X. 35th Year Anniversary Issue.

Peter F. Green. Wetting and dynamics of structured liquid films. *Journal of Polymer Science Part B: Polymer Physics*, 41(19):2219–2235, 2003. ISSN 1099-0488. doi: 10.1002/polb.10601. URL http://dx.doi.org/10.1002/polb.10601.

Günther Grün, Klaus Mecke, and Markus Rauscher. Thin-film flow influenced by thermal noise. *Journal of Statistical Physics*, 122(6):1261–1291, 2006. ISSN 0022-4715. doi: 10.1007/s10955-006-9028-8. URL http://dx.doi.org/10.1007/s10955-006-9028-8.

Xiaodan Gu, Leo Shaw, Kevin Gu, Michael F. Toney, and Zhenan Bao. The meniscus-guided deposition of semiconducting polymers. *Nature Communications*, 9(1):534, 2018.

Dongshi Guan, Yong Jian Wang, Elisabeth Charlaix, and Penger Tong. Asymmetric and speed-dependent capillary force hysteresis and relaxation of a suddenly stopped moving contact line. *Phys. Rev. Lett.*, 116:066102, Feb 2016. doi: 10.1103/PhysRevLett.116.066102. URL https://link.aps.org/doi/10.1103/PhysRevLett.116.066102.

Ankur Gupta, H. Burak Eral, T. Alan Hatton, and Patrick S. Doyle. Nanoemulsions: formation, properties and applications. *Soft Matter*, 12:2826–2841, 2016. doi: 10.1039/C5SM02958A. URL http://dx.doi.org/10.1039/C5SM02958A.

Nicolas G. Hadjiconstantinou. Combining atomistic and continuum simulations of contact-line motion. *Phys. Rev. E*, 59:2475–2478, Feb 1999. doi: 10.1103/PhysRevE.59.2475. URL http://link.aps.org/doi/10.1103/PhysRevE.59.2475.

P. S. Hammond. Nonlinear adjustment of a thin annular film of viscous fluid surrounding a thread of another within a circular cylindrical pipe. *J. Fluid Mech.*, 137:363–384, 1983. doi: 10.1017/S0022112083002451.

Naima H. Hammoud, Philippe H. Trinh, Peter D. Howell, and Howard A. Stone. Influence of van der waals forces on a bubble moving in a tube. *Physical Review Fluids*, 2:063601, Jun 2017. doi: 10.1103/PhysRevFluids.2.063601. URL https://link.aps.org/doi/10.1103/PhysRevFluids.2.063601.

Wei Han and Zhiqun Lin. Learning from "coffee rings": Ordered structures enabled by controlled evaporative self-assembly. *Angewandte Chemie International Edition*, 51(7):1534–1546, 2012. ISSN 1521-3773. doi: 10.1002/anie.201104454. URL http://dx.doi.org/10.1002/anie.201104454.

Peter Hänggi, Peter Talkner, and Michal Borkovec. Reaction-rate theory: fifty years after kramers. *Rev. Mod. Phys.*, 62:251–341, Apr 1990. doi: 10.1103/RevModPhys.62.251. URL https://link.aps.org/doi/10.1103/RevModPhys.62.251.

Majid Hassanizadeh and William G Gray. General conservation equations for multi-phase systems: 1. averaging procedure. *Advances in Water Resources*, 2:131 – 144, 1979a. ISSN 0309-

1708. doi: http://dx.doi.org/10.1016/0309-1708(79)90025-3. URL http://www.sciencedirect.com/science/article/pii/0309170879900253.

Majid Hassanizadeh and William G Gray. General conservation equations for multi-phase systems: 2. mass, momenta, energy, and entropy equations. *Advances in Water Resources*, 2:191 – 203, 1979b. ISSN 0309-1708. doi: http://dx.doi.org/10.1016/0309-1708(79)90035-6. URL http://www.sciencedirect.com/science/article/pii/0309170879900356.

Majid Hassanizadeh and William G. Gray. General conservation equations for multi-phase systems: 3. constitutive theory for porous media flow. *Advances in Water Resources*, 3(1):25 – 40, 1980. ISSN 0309-1708. doi: http://dx.doi.org/10.1016/0309-1708(80)90016-0. URL http://www.sciencedirect.com/science/article/pii/0309170880900160.

S. Majid Hassanizadeh. Derivation of basic equations of mass transport in porous media, part 1. macroscopic balance laws. *Advances in Water Resources*, 9(4):196 – 206, 1986a. ISSN 0309-1708. doi: http://dx.doi.org/10.1016/0309-1708(86)90024-2. URL http://www.sciencedirect.com/science/article/pii/0309170886900242.

S. Majid Hassanizadeh. Derivation of basic equations of mass transport in porous media, part 2. generalized darcy's and fick's laws. *Advances in Water Resources*, 9(4):207 – 222, 1986b. ISSN 0309-1708. doi: http://dx.doi.org/10.1016/0309-1708(86)90025-4. URL http://www.sciencedirect.com/science/article/pii/0309170886900254.

S. Majid Hassanizadeh and William G. Gray. Thermodynamic basis of capillary pressure in porous media. *Water Resources Research*, 29(10):3389–3405, 1993a.

S. Majid Hassanizadeh and William G. Gray. Toward an improved description of the physics of two-phase flow. *Advances in Water Resources*, 16(1):53 – 67, 1993b. ISSN 0309-1708. doi: http://dx.doi.org/10.1016/0309-1708(93)90029-F. URL http://www.sciencedirect.com/science/article/pii/030917089390029F. Research Perspectives in Hydrology.

S. Majid Hassanizadeh, Michael A. Celia, and Helge K. Dahle. Dynamic effect in the capillary pressure–saturation relationship and its impacts on unsaturated flow. *Vadose Zone Journal*, 1(1):38–57, 2002. doi: 10.2113/1.1.38. URL http://vzj.geoscienceworld.org/content/1/1/38.abstract.

S.Majid Hassanizadeh and William G. Gray. Mechanics and thermodynamics of multiphase flow in porous media including interphase boundaries. *Advances in Water Resources*, 13(4):169 – 186, 1990. ISSN 0309-1708. doi: http://dx.doi.org/10.1016/0309-1708(90)90040-B. URL http://www.sciencedirect.com/science/article/pii/030917089090040B.

Mengfei He and Sidney R Nagel. Characteristic interfacial structure behind a rapidly moving contact line. *arXiv preprint arXiv:1807.11910*, 2018.

Shanjin He, Galathara L. M. K. S. Kahanda, and Po-zen Wong. Roughness of wetting fluid invasion fronts in porous media. *Physical Review Letters*, 69:3731–3734, Dec 1992. doi: 10.1103/PhysRevLett.69.3731. URL http://link.aps.org/doi/10.1103/PhysRevLett.69.3731.

Dirk Helbing. Traffic and related self-driven many-particle systems. *Rev. Mod. Phys.*, 73:1067–1141, 2001.

S. Herminghaus, K. Jacobs, and R. Seemann. The glass transition of thin polymer films: some questions, and a possible answer. *The European Physical Journal E*, 5(1):531–538, 2001. ISSN 1292-8941. doi: 10.1007/s101890170036. URL http://dx.doi.org/10.1007/s101890170036.

Stephan Herminghaus, Karin Jacobs, Klaus Mecke, Jörg Bischof, Andreas Fery, Mohammed Ibn-Elhaj, and Stefan Schlagowski. Spinodal dewetting in liquid crystal and liquid metal films. *Science*, 282(5390):916–919, 1998. doi: 10.1126/science.282.5390.916. URL http://www.sciencemag.org/content/282/5390/916.abstract.

Stephan Herminghaus, Ralf Seemann, and Karin Jacobs. Generic morphologies of viscoelastic dewetting fronts. *Physical Review Letters*, 89:056101, Jul 2002. doi: 10.1103/PhysRevLett.89.056101. URL https://link.aps.org/doi/10.1103/PhysRevLett.89.056101.

F. Heslot, A. M. Cazabat, P. Levinson, and N. Fraysse. Experiments on wetting on the scale of nanometers: Influence of the surface energy. *Physical Review Letters*, 65:599–602, Jul 1990. doi: 10.1103/PhysRevLett.65.599. URL http://link.aps.org/doi/10.1103/PhysRevLett.65.599.

M. A. Hesse, F. M. Orr, and H. A. Tchelepi. Gravity currents with residual trapping. *Journal of Fluid Mechanics*, 611:35–60, 2008. doi: 10.1017/S002211200800219X.

A. M. Higgins and R. A. L. Jones. Anisotropic spinodal dewetting as a route to self-assembly of patterned surfaces. *Nature*, 404(6777):476–478, 03 2000. URL http://dx.doi.org/10.1038/35006597.

A. Hoang and H. P. Kavehpour. Dynamics of nanoscale precursor film near a moving contact line of spreading drops. *Phys. Rev. Lett.*, 106:254501, Jun 2011. doi: 10.1103/PhysRevLett.106.254501. URL http://link.aps.org/doi/10.1103/PhysRevLett.106.254501.

L. M. Hocking. The spreading of a thin drop by gravity and capillarity. *Q. J. Mech. Appl. Math.*, 36(1):55–69, 1983. doi: 10.1093/qjmam/36.1.55. URL http://qjmam.oxfordjournals.org/content/36/1/55.abstract.

L. M. Hocking. The influence of intermolecular forces on thin fluid layers. *Physics of Fluids A: Fluid Dynamics*, 5(4):793–799, 1993. doi: 10.1063/1.858627. URL `http://link.aip.org/link/?PFA/5/793/1`.

R. L. Hoffman. A study of the advancing interface. I. Interface shape in liquid–gas systems. *J. Colloid Interface Sci.*, 50(2):228–241, 1975a.

R. L. Hoffman. A study of the advancing interface. II. Theoretical prediction of the dynamic contact angle in liquid–gas systems. *J. Colloid Interface Sci.*, 94(2): 470–486, 1983.

Richard L Hoffman. A study of the advancing interface. i. interface shape in liquid—gas systems. *J. Colloid Interface Sci.*, 50(2):228 – 241, 1975b. ISSN 0021-9797. doi: http://dx.doi.org/10.1016/0021-9797(75)90225-8. URL `http://www.sciencedirect.com/science/article/pii/0021979775902258`.

P. C. Hohenberg and B. I. Halperin. Theory of dynamic critical phenomena. *Rev. Mod. Phys.*, 49:435–479, 1977. doi: 10.1103/RevModPhys.49.435. URL `http://link.aps.org/doi/10.1103/RevModPhys.49.435`.

Scott J. Hollister. Porous scaffold design for tissue engineering. *Nature Materials*, 4: 518, 07 2005.

G M Homsy. Viscous fingering in porous media. *Annual Review of Fluid Mechanics*, 19(1):271–311, 1987.

A. E. Hosoi and John W. M. Bush. Evaporative instabilities in climbing films. *Journal of Fluid Mechanics*, 442:217–239, 2001. doi: 10.1017/S0022112001005018.

Ran Hu, Dong-Sheng Wu, Zhibing Yang, and Yi-Feng Chen. Energy conversion reveals regime transition of imbibition in a rough fracture. *Geophysical Research Letters*, 2018.

David M. Huang, Christian Sendner, Dominik Horinek, Roland R. Netz, and Lydéric Bocquet. Water slippage versus contact angle: A quasiuniversal relationship. *Phys. Rev. Lett.*, 101:226101, Nov 2008. doi: 10.1103/PhysRevLett.101.226101. URL `http://link.aps.org/doi/10.1103/PhysRevLett.101.226101`.

J. Huang, F. Kim, A. R. Tao, S. Connor, and P. Yang. Spontaneous formation of nanoparticle stripe patterns through dewetting. *Nature Materials*, 4(12):896–900, 12 2005.

Jian Yu Huang, Yu-Chich Lo, Jun Jie Niu, Akihiro Kushima, Xiaofeng Qian, Li Zhong, Scott X. Mao, and Ju Li. Nanowire liquid pumps. *Nature Nanotechnology*, 8(4):277–281, 04 2013. URL `http://dx.doi.org/10.1038/nnano.2013.41`.

A. Huerre, V. Miralles, and M-C. Jullien. Bubbles and foams in microfluidics. *Soft Matter*, 10:6888–6902, 2014. doi: 10.1039/C4SM00595C. URL `http://dx.doi.org/10.1039/C4SM00595C`.

Axel Huerre, Olivier Theodoly, Alexander M. Leshansky, Marie-Pierre Valignat, Isabelle Cantat, and Marie-Caroline Jullien. Droplets in microchannels: Dynamical properties of the lubrication film. *Physical Review Letters*, 115:064501, Aug 2015. doi: 10.1103/PhysRevLett.115.064501. URL https://link.aps.org/doi/10.1103/PhysRevLett.115.064501.

C. Huh and L. E. Scriven. Hydrodynamic model of steady movement of a solid/liquid/fluid contact line. *J. Colloid Interface Sci.*, 35(1):85–101, 1971a.

C. Huh and L.E Scriven. Hydrodynamic model of steady movement of a solid/liquid/fluid contact line. *Journal of Colloid and Interface Science*, 35(1): 85 – 101, 1971b. ISSN 0021-9797. doi: 10.1016/0021-9797(71)90188-3. URL http://www.sciencedirect.com/science/article/pii/0021979771901883.

H. E. Huppert and A. W. Woods. The role of volatiles in magma chamber dynamics. *Nature*, 420:493–495, 12 2002. URL http://dx.doi.org/10.1038/nature01211.

Herbert E. Huppert. The propagation of two-dimensional and axisymmetric viscous gravity currents over a rigid horizontal surface. *Journal of Fluid Mechanics*, 121: 43–58, 8 1982a. ISSN 1469-7645. doi: 10.1017/S0022112082001797.

Herbert E. Huppert. Flow and instability of a viscous current down a slope. *Nature*, 300:427, 12 1982b.

A. Imhof and D.J. Pine. Stability of nonaqueous emulsions. *Journal of Colloid and Interface Science*, 192(2):368–374, 1997. ISSN 0021-9797. doi: http://dx.doi.org/10.1006/jcis.1997.5020. URL http://www.sciencedirect.com/science/article/pii/S0021979797950207.

C. Ishino, M. Reyssat, E. Reyssat, K. Okumura, and D. Quéré. Wicking within forests of micropillars. *EPL (Europhysics Letters)*, 79(5):56005, 2007.

Jacob N Israelachvili. *Intermolecular and Surface Forces*. Academic Press, 2011.

Amber S. Jackson, Cass T. Miller, and William G. Gray. Thermodynamically constrained averaging theory approach for modeling flow and transport phenomena in porous medium systems: 6. two-fluid-phase flow. *Advances in Water Resources*, 32(6):779 – 795, 2009. ISSN 0309-1708. doi: http://dx.doi.org/10.1016/j.advwatres.2008.11.010. URL http://www.sciencedirect.com/science/article/pii/S0309170808002157.

Karin Jacobs, Stephan Herminghaus, and Klaus R. Mecke. Thin liquid polymer films rupture via defects. *Langmuir*, 14(4):965–969, 1998. doi: 10.1021/la970954b.

D. Jacqmin. Onset of wetting failure in liquid–liquid systems. *Journal of Fluid Mechanics*, 517:209—228, 2004.

David Jacqmin. Calculation of two-phase navier–stokes flows using phase-field modeling. *Journal of Computational Physics*, 155(1): 96 – 127, 1999. doi: https://doi.org/10.1006/jcph.1999.6332. URL http://www.sciencedirect.com/science/article/pii/S0021999199963325.

David Jacqmin. Contact-line dynamics of a diffuse fluid interface. *Journal of Fluid Mechanics*, 402:57–88, 2000. doi: 10.1017/S0022112099006874.

P. P. Jadhunandan and N. R. Morrow. Effect of wettability on waterflood recovery for crude-oil/brine/rock systems. *SPE Reservoir Eng*, 10(40), 1995.

D. Jang, D. Kim, and J. Moon. Influence of fluid physical properties on ink-jet printability. *Langmuir*, 25:2629–2635, 2009.

V. Joekar-Niasar, S.M. Hassanizadeh, and A. Leijnse. Insights into the relationships among capillary pressure, saturation, interfacial area and relative permeability using pore-network modeling. *Transport in Porous Media*, 74 (2):201–219, 2008. ISSN 0169-3913. doi: 10.1007/s11242-007-9191-7. URL http://dx.doi.org/10.1007/s11242-007-9191-7.

Ruben Juanes, Elizabeth J. Spiteri, Franklin M. Orr, and Martin J. Blunt. Impact of relative permeability hysteresis on geological co2 storage. *Water Resources Research*, 42(12), 2006. doi: 10.1029/2005WR004806. URL https://agupubs.onlinelibrary.wiley.com/doi/abs/10.1029/2005WR004806.

Anne Juel, Draga Pihler-Puzović, and Matthias Heil. Instabilities in blistering. *Annual Review of Fluid Mechanics*, 50(1): 691–714, 2018. doi: 10.1146/annurev-fluid-122316-045106. URL https://doi.org/10.1146/annurev-fluid-122316-045106.

Leo P Kadanoff. *Statistical Physics: Statics, Dynamics and Renormalization*. World Scientific Publishing Company, 2000.

M. Kahlweit. Ostwald ripening of precipitates. *Advances in Colloid and Interface Science*, 5(1):1–35, 1975. ISSN 0001-8686. doi: http://dx.doi.org/10.1016/0001-8686(75)85001-9. URL http://www.sciencedirect.com/science/article/pii/0001868675850019.

Serafim Kalliadasis and Hsueh-Chia Chang. Dynamics of liquid spreading on solid surfaces. *Ind. Eng. Chem.*, 35(9):2860–2874, 1996. doi: 10.1021/ie950670r.

Mehran Kardar. Nonequilibrium dynamics of interfaces and lines. *Physics Reports*, 301(1–3):85 – 112, 1998. ISSN 0370-1573. doi: http://dx.doi.org/10.1016/S0370-1573(98)00007-6. URL http://www.sciencedirect.com/science/article/pii/S0370157398000076.

Mehran Kardar. *Statistical Physics of Fields*. Cambridge University Press, 2007.

Mehran Kardar, Giorgio Parisi, and Yi-Cheng Zhang. Dynamic scaling of growing interfaces. *Physical Review Letters*, 56:889–892, Mar 1986.

G. Katsikis, J. S. Cybulski, and M. Prakash. Synchronous universal droplet logic and control. *Nature Physics*, 11:588–596, 06 2015. URL http://dx.doi.org/10.1038/nphys3341.

H. Pirouz Kavehpour, Ben Ovryn, and Gareth H. McKinley. Microscopic and macroscopic structure of the precursor layer in spreading viscous drops. *Phys. Rev. Lett.*, 91:196104, Nov 2003. doi: 10.1103/PhysRevLett.91.196104. URL http://link.aps.org/doi/10.1103/PhysRevLett.91.196104.

N. C. Keim, P. Møller, W. W. Zhang, and S. R. Nagel. Breakup of air bubbles in water: Memory and breakdown of cylindrical symmetry. *Phys. Rev. Lett.*, 97:144503, Oct 2006. doi: 10.1103/PhysRevLett.97.144503. URL https://link.aps.org/doi/10.1103/PhysRevLett.97.144503.

L. Keiser, H. Bense, P. Colinet, J. Bico, and E. Reyssat. Marangoni bursting: Evaporation-induced emulsification of binary mixtures on a liquid layer. *Physical Review Letters*, 118:074504, Feb 2017. doi: 10.1103/PhysRevLett.118.074504. URL https://link.aps.org/doi/10.1103/PhysRevLett.118.074504.

Joseph B. Keller and Gregory J. Merchant. Flexural rigidity of a liquid surface. *Journal of Statistical Physics*, 63(5-6):1039–1051, 1991. ISSN 0022-4715. doi: 10.1007/BF01029998. URL http://dx.doi.org/10.1007/BF01029998.

David A. Kessler, Joel Koplik, and Herbert Levine. Pattern selection in fingered growth phenomena. *Advances in Physics*, 37(3):255–339, 1988.

V. V. Khatavkar, P. D. Anderson, and H. E. H. Meijer. Capillary spreading of a droplet in the partially wetting regime using a diffuse-interface model. *Journal of Fluid Mechanics*, 572:367–387, 2007. doi: 10.1017/S0022112006003533.

Hyoungsoo Kim, Fran çois Boulogne, Eujin Um, Ian Jacobi, Ernie Button, and Howard A. Stone. Controlled uniform coating from the interplay of marangoni flows and surface-adsorbed macromolecules. *Phys. Rev. Lett.*, 116:124501, Mar 2016a. doi: 10.1103/PhysRevLett.116.124501. URL https://link.aps.org/doi/10.1103/PhysRevLett.116.124501.

Jungchul Kim, Myoung-Woon Moon, and Ho-Young Kim. Dynamics of hemiwicking. *Journal of Fluid Mechanics*, 800:57–71, 2016b.

Onyu Kim and Jaewook Nam. Confinement effects in dip coating. *Journal of Fluid Mechanics*, 827:1—30, 2017.

E. Kirkinis and S. H. Davis. Hydrodynamic theory of liquid slippage on a solid substrate near a moving contact line. *Phys. Rev. Lett.*, 110:234503, Jun 2013. doi: 10.1103/PhysRevLett.110.234503. URL https://link.aps.org/doi/10.1103/PhysRevLett.110.234503.

E. Klaseboer, R. Gupta, and R. Manica. An extended bretherton model for long taylor bubbles at moderate capillary numbers. *Physics of Fluids*, 26(3):032107, 2014.

Yong Lin Kong, François Boulogne, Hyoungsoo Kim, Janine Nunes, Jie Feng, and Howard A. Stone. Deposition of quantum dots in a capillary tube. *Langmuir*, 31(45):12560–12566, 2015. doi: 10.1021/acs.langmuir.5b03443. URL http://dx.doi.org/10.1021/acs.langmuir.5b03443.

Yong Lin Kong, Maneesh K. Gupta, Blake N. Johnson, and Michael C. McAlpine. 3D printed bionic nanodevices. *Nano Today*, 11(3):330 – 350, 2016. ISSN 1748-0132. doi: https://doi.org/10.1016/j.nantod.2016.04.007. URL http://www.sciencedirect.com/science/article/pii/S1748013216300342.

Joel Koplik, Jayanth R. Banavar, and Jorge F. Willemsen. Molecular dynamics of poiseuille flow and moving contact lines. *Physical Review Letters*, 60:1282–1285, Mar 1988. doi: 10.1103/PhysRevLett.60.1282. URL http://link.aps.org/doi/10.1103/PhysRevLett.60.1282.

Joel Koplik, Jayanth R. Banavar, and Jorge F. Willemsen. Molecular dynamics of fluid flow at solid surfaces. *Physics of Fluids A: Fluid Dynamics (1989-1993)*, 1(5):781–794, 1989. doi: http://dx.doi.org/10.1063/1.857376. URL http://scitation.aip.org/content/aip/journal/pofa/1/5/10.1063/1.857376.

R. Krechetnikov. On application of lubrication approximations to nonunidirectional coating flows with clean and surfactant interfaces. *Physics of Fluids*, 22(9):092102, 2010.

R. Krechetnikov and G. M. Homsy. Experimental study of substrate roughness and surfactant effects on the landau-levich law. *Physics of Fluids*, 17(10):102108, 2005.

Michael J. Kreder, Jack Alvarenga, Philseok Kim, and Joanna Aizenberg. Design of anti-icing surfaces: smooth, textured or slippery? *Nature Reviews Materials*, 1: 15003, 01 2016.

S. Kumar. Liquid transfer in printing processes: Liquid bridges with moving contact lines. *Annual Review of Fluid Mechanics*, 47(1):67–94, 2015.

Akshay Kundan, Thao T. T. Nguyen, Joel L. Plawsky, Peter C. Wayner, David F. Chao, and Ronald J. Sicker. Condensation on highly superheated surfaces: Unstable thin films in a wickless heat pipe. *Physical Review Letters*, 118:094501, Mar 2017. doi: 10.1103/PhysRevLett.118.094501. URL https://link.aps.org/doi/10.1103/PhysRevLett.118.094501.

H. Kusumaatmaja, E. J. Hemingway, and S. M. Fielding. Moving contact line dynamics: from diffuse to sharp interfaces. *Journal of Fluid Mechanics*, 788:209–227, 2016. doi: 10.1017/jfm.2015.697.

K. S. Lackner. A guide to CO2 sequestration. *Science*, 300(5626):1677–1678, 2003. ISSN 0036-8075. doi: 10.1126/science.1079033. URL `http://science.sciencemag.org/content/300/5626/1677`.

L.D. Landau and B.V. Levich. Dragging of a liquid by a moving plate. *Acta Physicochim. URSS*, 17(42), 1942.

LD Landau and EM Lifshitz. *Fluid mechanics, 2nd Edition, Course of theoretical physics (Volume 6)*. Pergamon Press, 1987.

J. S. Langer. Dendrites, viscous fingers, and the theory of pattern formation. *Science*, 243(4895):1150–1156, 1989. ISSN 0036-8075. doi: 10.1126/science.243.4895.1150. URL `http://science.sciencemag.org/content/243/4895/1150`.

J.S Langer. Theory of spinodal decomposition in alloys. *Annals of Physics*, 65(1):53–86, 1971. ISSN 0003-4916. doi: http://dx.doi.org/10.1016/0003-4916(71)90162-X. URL `http://www.sciencedirect.com/science/article/pii/000349167190162X`.

Eric Lauga, Michael Brenner, and Howard Stone. *Microfluidics: The No-Slip Boundary Condition*, pages 1219–1240. Springer Berlin Heidelberg, 2007.

P. D. Lax. Hyperbolic systems of conservation laws ii. *Communications on Pure and Applied Mathematics*, 10(4):537–566, 1957.

Peter D Lax. *Hyperbolic Systems of Conservation Laws and the Mathematical Theory of Shock Waves*. SIAM, 1973.

N. Le Grand, A. Daerr, and L. Limat. Shape and motion of drops sliding down an inclined plane. *Journal of Fluid Mechanics*, 541:293—315, 2005.

L. G. Leal. Flow induced coalescence of drops in a viscous fluid. *Physics of Fluids*, 16(6):1833–1851, 2004. doi: 10.1063/1.1701892.

R. Ledesma-Aguilar, A. Hernández-Machado, and I. Pagonabarraga. Three-dimensional aspects of fluid flows in channels. i. meniscus and thin film regimes. *Physics of Fluids (1994-present)*, 19(10), 2007a.

R. Ledesma-Aguilar, I. Pagonabarraga, and A. Hernández-Machado. Three-dimensional aspects of fluid flows in channels. ii. effects of meniscus and thin film regimes on viscous fingers. *Physics of Fluids (1994-present)*, 19(10), 2007b.

R. Ledesma-Aguilar, R. Nistal, A. Hernández-Machado, and I. Pagonabarraga. Controlled drop emission by wetting properties in driven liquid filaments. *Nature Materials*, 10:367–371, 04 2011.

R. Ledesma-Aguilar, A. Hernández-Machado, and I. Pagonabarraga. Theory of wetting-induced fluid entrainment by advancing contact lines on dry surfaces. *Phys. Rev. Lett.*, 110:264502, Jun 2013.

Roland Lenormand, Eric Touboul, and Cesar Zarcone. Numerical models and experiments on immiscible displacements in porous media. *Journal of Fluid Mechanics*, 189:165–187, 1988.

Bertrand Levaché and Denis Bartolo. Revisiting the Saffman–Taylor experiment: Imbibition patterns and liquid-entrainment transitions. *Phys. Rev. Lett.*, 113:044501, Jul 2014.

Randall J LeVeque. *Numerical Methods for Conservation Laws*. Springer, 1990.

B Levich and L Landau. Dragging of liquid by a plate. *Acta Physiochim.*, 17:42–54, 1942.

V G Levich and V S Krylov. Surface-tension-driven phenomena. *Annual Review of Fluid Mechanics*, 1(1):293–316, 1969. doi: 10.1146/annurev.fl.01.010169.001453. URL http://www.annualreviews.org/doi/abs/10.1146/annurev.fl.01.010169.001453.

Romain Lhermerout, Hugo Perrin, Etienne Rolley, Bruno Andreotti, and Kristina Davitt. A moving contact line as a rheometer for nanometric interfacial layers. *Nature Communications*, 7:12545, 2016.

Jie Li. Macroscopic model for head-on binary droplet collisions in a gaseous medium. *Physical Review Letters*, 117: 214502, Nov 2016. doi: 10.1103/PhysRevLett.117.214502. URL http://link.aps.org/doi/10.1103/PhysRevLett.117.214502.

Kenneth G. Libbrecht. Physical dynamics of ice crystal growth. *Annual Review of Materials Research*, 47(1):271–295, 2017. doi: 10.1146/annurev-matsci-070616-124135. URL https://doi.org/10.1146/annurev-matsci-070616-124135.

I.M. Lifshitz and V.V. Slyozov. The kinetics of precipitation from supersaturated solid solutions. *Journal of Physics and Chemistry of Solids*, 19(1):35–50, 1961. ISSN 0022-3697. doi: http://dx.doi.org/10.1016/0022-3697(61)90054-3. URL http://www.sciencedirect.com/science/article/pii/0022369761900543.

M. J. Lighthill and G. B. Whitham. On kinematic waves ii. a theory of traffic flow on long crowded roads. *Proceedings of the Royal Society of London A: Mathematical, Physical and Engineering Sciences*, 229(1178):317–345, 1955.

Ratchana Limary and Peter F. Green. Late-stage coarsening of an unstable structured liquid film. *Physical Review E*, 66:021601, Aug 2002. doi: 10.1103/PhysRevE.66.021601.

Ratchana Limary and Peter F. Green. Dynamics of droplets on the surface of a structured fluid film: late-stage coarsening. *Langmuir*, 19(6):2419–2424, 2003. doi: 10.1021/la026560o.

L. Limat and H. A. Stone. Three-dimensional lubrication model of a contact line corner singularity. *EPL (Europhysics Letters)*, 65(3):365, 2004.

J. R. Lindner. Microbubbles in medical imaging: current applications and future directions. *Nature Reviews Drug Discovery*, 3:527–533, 06 2004. URL http://dx.doi.org/10.1038/nrd1417.

D. R. Link, S. L. Anna, D. A. Weitz, and H. A. Stone. Geometrically mediated breakup of drops in microfluidic devices. *Phys. Rev. Lett.*, 92:054503, Feb 2004. doi: 10.1103/PhysRevLett.92.054503. URL https://link.aps.org/doi/10.1103/PhysRevLett.92.054503.

J. R. Lister and H. A. Stone. Capillary breakup of a viscous thread surrounded by another viscous fluid. *Physics of Fluids*, 10(11):2758–2764, 1998. doi: 10.1063/1.869799. URL https://doi.org/10.1063/1.869799.

LiChi Liu and Subhash H. Risbud. Quantum-dot size-distribution analysis and precipitation stages in semiconductor doped glasses. *Journal of Applied Physics*, 68 (1):28–32, 1990. doi: 10.1063/1.347130.

Alan Lo and Rex T. Skodje. Kinetic and monte carlo models of thin film coarsening: Cross over from diffusion-coalescence to ostwald growth modes. *The Journal of Chemical Physics*, 112(4):1966–1974, 2000. doi: 10.1063/1.480756. URL http://dx.doi.org/10.1063/1.480756.

Detlef Lohse and Xuehua Zhang. Surface nanobubbles and nanodroplets. *Reviews of Modern Physics*, 87:981–1035, Aug 2015. doi: 10.1103/RevModPhys.87.981. URL https://link.aps.org/doi/10.1103/RevModPhys.87.981.

M. S. Longuet-Higgins, B. R. Kerman, and K. Lunde. The release of air bubbles from an underwater nozzle. *Journal of Fluid Mechanics*, 230:365–390, 1991. doi: 10.1017/S0022112091000836.

Ward A. Lopes and Heinrich M. Jaeger. Hierarchical self-assembly of metal nanostructures on diblock copolymer scaffolds. *Nature*, 414(6865):735–738, 12 2001. URL http://dx.doi.org/10.1038/414735a.

Jaime Lopez, Clarence A Miller, and Eli Ruckenstein. Spreading kinetics of liquid drops on solids. *Journal of Colloid and Interface Science*, 56(3):460 – 468, 1976. doi: http://dx.doi.org/10.1016/0021-9797(76)90111-9. URL http://www.sciencedirect.com/science/article/pii/0021979776901119.

V. Ludviksson and E. N. Lightfoot. The dynamics of thin liquid films in the presence of surface-tension gradients. *AIChE Journal*, 17(5):1166–1173, 1971.

Knut Jørgen Måløy, Jens Feder, and Torstein Jøssang. Viscous fingering fractals in porous media. *Physical Review Letters*, 55: 2688–2691, Dec 1985. doi: 10.1103/PhysRevLett.55.2688. URL http://link.aps.org/doi/10.1103/PhysRevLett.55.2688.

L. G. MacDowell, J. Benet, N. A. Katcho, and J. M.G. Palanco. Disjoining pressure and the film-height-dependent surface tension of thin liquid films: New insight from capillary wave fluctuations. *Advances in Colloid and Interface Science*, 206: 150–171, 2014. doi: http://dx.doi.org/10.1016/j.cis.2013.11.003.

Luis G. MacDowell, Jorge Benet, and Nebil A. Katcho. Capillary fluctuations and film-height-dependent surface tension of an adsorbed liquid film. *Physical Review Letters*, 111:047802, Jul 2013. doi: 10.1103/PhysRevLett.111.047802. URL http://link.aps.org/doi/10.1103/PhysRevLett.111.047802.

Maniya Maleki, Etienne Reyssat, David Quéré, and Ramin Golestanian. On the landaulevich transition. *Langmuir*, 23(20):10116–10122, 2007.

Vinothan N. Manoharan. Colloidal matter: Packing, geometry, and entropy. *Science*, 349(6251), 2015. doi: 10.1126/science.1253751.

Eduardo Jose Manrique, Viviana Eugenia Muci, and Mariano E. Gurfinkel. Eor field experiences in carbonate reservoirs in the united states. *SPE Reservoir Evaluation Eng*, 10(667), 2007.

Hubert Mantz, Karin Jacobs, and Klaus Mecke. Utilizing Minkowski functionals for image analysis: a marching square algorithm. *Journal of Statistical Mechanics: Theory and Experiment*, (12), 2008. URL http://stacks.iop.org/1742-5468/2008/i=12/a=P12015.

A. Marchand, J. H. Weijs, J. H. Snoeijer, and B. Andreotti. Why is surface tension a force parallel to the interface? *American Journal of Physics*, 79(10):999–1008, 2011. doi: 10.1119/1.3619866. URL http://link.aip.org/link/?AJP/79/999/1.

Antonin Marchand, Tak Shing Chan, Jacco H. Snoeijer, and Bruno Andreotti. Air entrainment by contact lines of a solid plate plunged into a viscous fluid. *Phys. Rev. Lett.*, 108:204501, 2012.

Nicos Martys, Marek Cieplak, and Mark O. Robbins. Critical phenomena in fluid invasion of porous media. *Physical Review Letters*, 66:1058–1061, Feb 1991. doi: 10.1103/PhysRevLett.66.1058. URL http://link.aps.org/doi/10.1103/PhysRevLett.66.1058.

Omar K. Matar and Satish Kumar. Dynamics and stability of flow down a flexible incline. *Journal of Engineering Mathematics*, 57(2):145–158, Feb 2007.

A. Mavromoustaki, O. K. Matar, and R. V. Craster. Shock-wave solutions in two-layer channel flow. i. one-dimensional flows. *Physics of Fluids*, 22(11):112102, 2010.

A. Mavromoustaki, O. K. Matar, and R. V. Craster. Shock-wave solutions in two-layer channel flow. ii. linear and nonlinear stability. *Physics of Fluids*, 23(11): 112101, 2011.

K.V. McCloud and J.V. Maher. Experimental perturbations to saffman-taylor flow. *Physics Reports*, 260(3):139–185, 1995.

J. D. McGraw, O. Bäumchen, M. Klos, S. Haefner, M. Lessel, S. Backes, and K. Jacobs. Nanofluidics of thin polymer films: Linking the slip boundary condition at solid–liquid interfaces to macroscopic pattern formation and microscopic interfacial properties. *Advances in Colloid and Interface Science*, 210:13 – 20, 2014. ISSN 0001-8686. doi: http://dx.doi.org/10.1016/j.cis.2014.03.010. URL http://www.sciencedirect.com/science/article/pii/S0001868614001353.

Joshua D. McGraw, Tak Shing Chan, Simon Maurer, Thomas Salez, Michael Benzaquen, Elie Raphaël, Martin Brinkmann, and Karin Jacobs. Slip-mediated dewetting of polymer microdroplets. *Proceedings of the National Academy of Sciences*, 113(5):1168–1173, 2016. doi: 10.1073/pnas.1513565113. URL http://www.pnas.org/content/113/5/1168.abstract.

J. T. McKeown, Y. Wu, J. D. Fowlkes, P. D. Rack, and G. H. Campbell. Simultaneous in-situ synthesis and characterization of co@cu core-shell nanoparticle arrays. *Advanced Materials*, 27(6):1060–1065, 2015. ISSN 1521-4095. doi: 10.1002/adma.201404374. URL http://dx.doi.org/10.1002/adma.201404374.

G. H. McKinley. Visco-elasto-capillary thinning and break-up of complex fluids. *Rheology Reviews*, 3:1–48, 2005.

Klaus Mecke and Markus Rauscher. On thermal fluctuations in thin film flow. *Journal of Physics: Condensed Matter*, 17(45):S3515, 2005. URL http://stacks.iop.org/0953-8984/17/i=45/a=042.

Klaus R. Mecke. Integral geometry in statistical physics. *International Journal of Modern Physics B*, 12(09):861–899, 1998. doi: 10.1142/S0217979298000491.

L. Meli and P. F. Green. Aggregation and coarsening of ligand-stabilized gold nanoparticles in poly(methyl methacrylate) thin films. *ACS Nano*, 2(6):1305–1312, 2008. doi: 10.1021/nn800045s. URL http://dx.doi.org/10.1021/nn800045s.

Gregory J. Merchant and Joseph B. Keller. Contact angles. *Physics of Fluids A: Fluid Dynamics*, 4(3):477–485, 1992. doi: 10.1063/1.858320. URL http://link.aip.org/link/?PFA/4/477/1.

J. Carson Meredith, Archie P. Smith, Alamgir Karim, and Eric J. Amis. Combinatorial materials science for polymer thin-film dewetting. *Macromolecules*, 33(26):9747–9756, 2000. doi: 10.1021/ma001298g. URL http://dx.doi.org/10.1021/ma001298g.

D. Merkt, A. Pototsky, M. Bestehorn, and U. Thiele. Long-wave theory of bounded two-layer films with a free liquid–liquid interface: Short- and long-time evolution. *Physics of Fluids*, 17(6):064104, 2005. doi: http://dx.doi.org/10.1063/1.1935487.

C.A Miller and E Ruckenstein. The origin of flow during wetting of solids. *Journal of Colloid and Interface Science*, 48(3):368–373, 1974. ISSN 0021-9797. doi: http://dx.doi.org/10.1016/0021-9797(74)90179-9. URL http://www.sciencedirect.com/science/article/pii/0021979774901799.

Cass T. Miller and William G. Gray. Thermodynamically constrained averaging theory approach for modeling flow and transport phenomena in porous medium systems: 2. foundation. *Advances in Water Resources*, 28(2):181 – 202, 2005. ISSN 0309-1708. doi: http://dx.doi.org/10.1016/j.advwatres.2004.09.006. URL http://www.sciencedirect.com/science/article/pii/S030917080400154X.

Vladimir S. Mitlin. Dewetting of solid surface: Analogy with spinodal decomposition. *Journal of Colloid and Interface Science*, 156(2):491–497, 1993. ISSN 0021-9797. doi: http://dx.doi.org/10.1006/jcis.1993.1142. URL http://www.sciencedirect.com/science/article/pii/S0021979783711422.

M. E. Toimil Molares, A. G. Balogh, T. W. Cornelius, R. Neumann, and C. Trautmann. Fragmentation of nanowires driven by rayleigh instability. *Applied Physics Letters*, 85(22):5337–5339, 2004. doi: 10.1063/1.1826237. URL http://dx.doi.org/10.1063/1.1826237.

Norman Morrow and Jill Buckley. Improved oil recovery by low-salinity waterflooding. *J. Pet. Tech.*, 63(106), 2011. doi: 10.2118/129421-JPT.

Rabibrata Mukherjee and Ashutosh Sharma. Instability, self-organization and pattern formation in thin soft films. *Soft Matter*, 11:8717–8740, 2015. doi: 10.1039/C5SM01724F. URL http://dx.doi.org/10.1039/C5SM01724F.

Andreas Münch. Pinch-off transition in marangoni-driven thin films. *Phys. Rev. Lett.*, 91:016105, 2003.

Andreas Münch and P.L. Evans. Marangoni-driven liquid films rising out of a meniscus onto a nearly-horizontal substrate. *Physica D: Nonlinear Phenomena*, 209(1):164–177, 2005.

Mathias Nagel and François Gallaire. A new prediction of wavelength selection in radial viscous fingering involving normal and tangential stresses. *Physics of Fluids*, 25(12):124107, 2013. doi: http://dx.doi.org/10.1063/1.4849495. URL http://scitation.aip.org/content/aip/journal/pof2/25/12/10.1063/1.4849495.

Sidney R. Nagel. Experimental soft-matter science. *Rev. Mod. Phys.*, 89:025002, Apr 2017. doi: 10.1103/RevModPhys.89.025002. URL https://link.aps.org/doi/10.1103/RevModPhys.89.025002.

S. Nesic, R. Cuerno, E. Moro, and L. Kondic. Fully nonlinear dynamics of stochastic thin-film dewetting. *Physical Review E*, 92: 061002, Dec 2015. doi: 10.1103/PhysRevE.92.061002. URL http://link.aps.org/doi/10.1103/PhysRevE.92.061002.

Chiara Neto, Karin Jacobs, Ralf Seemann, Ralf Blossey, Jürgen Becker, and Günther Grün. Satellite hole formation during dewetting: experiment and simulation. *Journal of Physics: Condensed Matter*, 15(19):3355–3366, 2003. URL http://stacks.iop.org/0953-8984/15/i=19/a=334.

Chiara Neto, Drew R Evans, Elmar Bonaccurso, Hans-Jürgen Butt, and Vincent S J Craig. Boundary slip in newtonian liquids: a review of experimental studies. *Reports on Progress in Physics*, 68(12):2859, 2005. URL http://stacks.iop.org/0034-4885/68/i=12/a=R05.

Trung Dac Nguyen, Miguel Fuentes-Cabrera, Jason D. Fowlkes, and Philip D. Rack. Coexistence of spinodal instability and thermal nucleation in thin-film rupture: Insights from molecular levels. *Physical Review E*, 89:032403, Mar 2014. doi: 10.1103/PhysRevE.89.032403. URL https://link.aps.org/doi/10.1103/PhysRevE.89.032403.

Jennifer Niessner, Steffen Berg, and S.Majid Hassanizadeh. Comparison of two-phase darcy's law with a thermodynamically consistent approach. *Transport in Porous Media*, 88(1):133–148, 2011. ISSN 0169-3913. doi: 10.1007/s11242-011-9730-0. URL http://dx.doi.org/10.1007/s11242-011-9730-0.

Amy Novick-Cohen. The nonlinear Cahn-Hilliard equation: Transition from spinodal decomposition to nucleation behavior. *Journal of Statistical Physics*, 38(3):707–723, 1985. ISSN 1572-9613. doi: 10.1007/BF01010486. URL http://dx.doi.org/10.1007/BF01010486.

Céleste Odier, Bertrand Levaché, Enric Santanach-Carreras, and Denis Bartolo. Forced imbibition in porous media: A fourfold scenario. *Phys. Rev. Lett.*, 119: 208005, Nov 2017.

H. N. Oguz and A. Prosperetti. Dynamics of bubble growth and detachment from a needle. *Journal of Fluid Mechanics*, 257:111–145, 1993. doi: 10.1017/S0022112093003015.

Alexander Oron. Three-dimensional nonlinear dynamics of thin liquid films. *Physical Review Letters*, 85:2108–2111, Sep 2000. doi: 10.1103/PhysRevLett.85.2108. URL https://link.aps.org/doi/10.1103/PhysRevLett.85.2108.

Alexander Oron, Stephen H. Davis, and S. George Bankoff. Long-scale evolution of thin liquid films. *Reviews of Modern Physics*, 69:931–980, 1997.

F.M. Orr and J.J. Taber. Use of carbon dioxide in enhanced oil recovery. *Science*, 224:563–569, 1984.

Jordi Ortín and Stéphane Santucci. Avalanches, non-gaussian fluctuations and intermittency in fluid imbibition. In *Avalanches in Functional Materials and Geophysics*, pages 261–292. Springer, 2017.

W. Ostwald. Studien über die Bildung und Umwandlung fester Körper: Übersättigung und Überkaltung. *Zeitschrift für Physikalische Chemie*, 22:289–330, February 1897.

Felix Otto, Tobias Rump, and Dejan Slepcev. Coarsening rates for a droplet model: Rigorous upper bounds. *SIAM Journal on Mathematical Analysis*, 38(2):503–529, 2006. doi: 10.1137/050630192.

Amir A. Pahlavan, Luis Cueto-Felgueroso, Gareth H. McKinley, and Ruben Juanes. Thin films in partial wetting: Internal selection of contact-line dynamics. *Physical Review Letters*, 115:034502, Jul 2015. doi: 10.1103/PhysRevLett.115.034502. URL http://link.aps.org/doi/10.1103/PhysRevLett.115.034502.

D. T. Papageorgiou. On the breakup of viscous liquid threads. *Physics of Fluids*, 7(7):1529–1544, 1995. doi: 10.1063/1.868540. URL https://doi.org/10.1063/1.868540.

C.-W. Park and G. M. Homsy. Two-phase displacement in hele shaw cells: theory. *Journal of Fluid Mechanics*, 139:291–308, 1984.

C. W. Park and G. M. Homsy. The instability of long fingers in Hele–Shaw flows. *Phys. Fluids*, 28(6):1583, 1985.

J. I. Park, A. Saffari, S. Kumar, A. Günther, and E. Kumacheva. Microfluidic synthesis of polymer and inorganic particulate materials. *Annual Review of Materials Research*, 40(1):415–443, 2010.

A. Parmigiani, S. Faroughi, C. Huber, O. Bachmann, and Y. Su. Bubble accumulation and its role in the evolution of magma reservoirs in the upper crust. *Nature*, 532: 492–495, 04 2016. URL http://dx.doi.org/10.1038/nature17401.

L. Paterson. Radial fingering in a Hele-Shaw cell. *J. Fluid Mech.*, 113:513–529, 1981.

Lincoln Paterson. Diffusion-limited aggregation and two-fluid displacements in porous media. *Physical Review Letters*, 52:1621–1624, Apr 1984. doi: 10.1103/PhysRevLett.52.1621. URL http://link.aps.org/doi/10.1103/PhysRevLett.52.1621.

Matthew Pelliccione and Toh-Ming Lu. *Evolution of thin film morphology*, volume 108. Springer, 2008.

D. H. Peregrine, G. Shoker, and A. Symon. The bifurcation of liquid bridges. *Journal of Fluid Mechanics*, 212:25–39, 1990. doi: 10.1017/S0022112090001835.

Joy C. Perkinson, Michael J. Aziz, Michael P. Brenner, and Miranda Holmes-Cerfon. Designing steep, sharp patterns on uniformly ion-bombarded surfaces. *Proceedings of the National Academy of Sciences*, 113(41):11425–11430, 2016.

H. Perrin, D. Belardinelli, M. Sbragaglia, and B. Andreotti. Response function of a moving contact line. *Phys. Rev. Fluids*, 3: 044001, Apr 2018a. doi: 10.1103/PhysRevFluids.3.044001. URL https://link.aps.org/doi/10.1103/PhysRevFluids.3.044001.

Hugo Perrin, Romain Lhermerout, Kristina Davitt, Etienne Rolley, and Bruno Andreotti. Defects at the nanoscale impact contact line motion at all scales. *Phys. Rev. Lett.*, 116:184502, May 2016.

Hugo Perrin, Romain Lhermerout, Kristina Davitt, Etienne Rolley, and Bruno Andreotti. Thermally activated motion of a contact line over defects. *Soft Matter*, 14:1581–1595, 2018b. doi: 10.1039/C7SM02211E. URL http://dx.doi.org/10.1039/C7SM02211E.

J. Taylor Perron, James W. Kirchner, and William E. Dietrich. Formation of evenly spaced ridges and valleys. *Nature*, 460:502–505, 2009.

Bo NJ Persson. *Sliding friction: physical principles and applications*. Springer Science & Business Media, 2013.

Ivo Peters, Jacco H. Snoeijer, Adrian Daerr, and Laurent Limat. Coexistence of two singularities in dewetting flows: Regularizing the corner tip. *Phys. Rev. Lett.*, 103: 114501, Sep 2009.

P. Petrov and I. Petrov. A combined molecular-hydrodynamic approach to wetting kinetics. *Langmuir*, 8(7):1762–1767, 1992. doi: 10.1021/la00043a013. URL http://pubs.acs.org/doi/abs/10.1021/la00043a013.

Olivier Pierre-Louis. Solid-state wetting at the nanoscale. *Progress in Crystal Growth and Characterization of Materials*, 62(2):177–202, 2016. ISSN 0960-8974. doi: http://dx.doi.org/10.1016/j.pcrysgrow.2016.04.009. URL http://www.sciencedirect.com/science/article/pii/S0960897416300122.

Len M. Pismen and Yves Pomeau. Disjoining potential and spreading of thin liquid layers in the diffuse-interface model coupled to hydrodynamics. *Phys. Rev. E*, 62:2480–2492, Aug 2000. doi: 10.1103/PhysRevE.62.2480. URL http://link.aps.org/doi/10.1103/PhysRevE.62.2480.

Len M. Pismen and Boris Y. Rubinstein. Kinetic slip condition, van der waals forces, and dynamic contact angle. *Langmuir*, 17(17):5265–5270, 2001. doi: 10.1021/la001452s. URL http://pubs.acs.org/doi/abs/10.1021/la001452s.

E. Pitts. Penetration of fluid into a hele–shaw cell: the saffman–taylor experiment. *Journal of Fluid Mechanics*, 97(1):53–64, 1980.

Ramon Planet, Stéphane Santucci, and Jordi Ortín. Avalanches and non-gaussian fluctuations of the global velocity of imbibition fronts. *Phys. Rev. Lett.*, 102:094502, Mar 2009. doi: 10.1103/PhysRevLett.102.094502. URL http://link.aps.org/doi/10.1103/PhysRevLett.102.094502.

J.P. Plateau. Recherches expérimentales et théorique sur les figures d'équilibre d'une masse liquide sans pesanteur. *Acad. Sci. Brux. Mem.*, 23:5, 1849.

T. Podgorski, J.-M. Flesselles, and L. Limat. Corners, cusps, and pearls in running drops. *Phys. Rev. Lett.*, 87:036102, Jun 2001.

Boaz Pokroy, Sung H. Kang, L. Mahadevan, and Joanna Aizenberg. Self-organization of a mesoscale bristle into ordered, hierarchical helical assemblies. *Science*, 323 (5911):237–240, 2009. ISSN 0036-8075. doi: 10.1126/science.1165607.

T. Pompe and S. Herminghaus. Three-phase contact line energetics from nanoscale liquid surface topographies. *Physical Review Letters*, 85:1930–1933, Aug 2000. doi: 10.1103/PhysRevLett.85.1930. URL http://link.aps.org/doi/10.1103/PhysRevLett.85.1930.

M N Popescu, G Oshanin, S Dietrich, and A-M Cazabat. Precursor films in wetting phenomena. *J. Phys. Condens. Matter*, 24(24):243102, 2012. URL http://stacks.iop.org/0953-8984/24/i=24/a=243102.

A. Prevost, E. Rolley, and C. Guthmann. Thermally activated motion of the contact line of a liquid ^{4}He meniscus on a cesium substrate. *Phys. Rev. Lett.*, 83:348–351, Jul 1999. doi: 10.1103/PhysRevLett.83.348. URL https://link.aps.org/doi/10.1103/PhysRevLett.83.348.

Bian Qian, Joonsik Park, and Kenneth S. Breuer. Large apparent slip at a moving contact line. *Physics of Fluids*, 27(9):091703, 2015. doi: 10.1063/1.4931915. URL http://aip.scitation.org/doi/abs/10.1063/1.4931915.

Tiezheng Qian, Xiao-Ping Wang, and Ping Sheng. Molecular scale contact line hydrodynamics of immiscible flows. *Physical Review E*, 68:016306, Jul 2003. doi: 10.1103/PhysRevE.68.016306. URL http://link.aps.org/doi/10.1103/PhysRevE.68.016306.

Tiezheng Qian, Xiao-Ping Wang, and Ping Sheng. Power-law slip profile of the moving contact line in two-phase immiscible flows. *Physical Review Letters*, 93:094501, Aug 2004. doi: 10.1103/PhysRevLett.93.094501. URL http://link.aps.org/doi/10.1103/PhysRevLett.93.094501.

Tiezheng Qian, Xiao-Ping Wang, and Ping Sheng. A variational approach to moving contact line hydrodynamics. *J. Fluid Mech.*, 564:333–360, 10 2006. doi: 10.1017/S0022112006001935.

D. Qin, Y. Xia, and G. M Whitesides. Soft lithography for micro- and nanoscale patterning. *Nature Protocols*, 5(3):491–502, 03 2010. URL http://dx.doi.org/10.1038/nprot.2009.234.

D. Quéré, J.-M. di Meglio, and F. Brochard-Wyart. Making van der waals films on fibers. *EPL (Europhysics Letters)*, 10(4):335, 1989.

David Quéré. Fluid coating on a fiber. *Annual Review of Fluid Mechanics*, 31(1): 347–384, 1999.

David Quéré. Wetting and roughness. *Annual Review of Materials Research*, 38(1): 71–99, 2008.

E. Ramé, S. Garoff, and K. R. Willson. Characterizing the microscopic physics near moving contact linesusing dynamic contact angle data. *Phys. Rev. E*, 70:031608, Sep 2004. doi: 10.1103/PhysRevE.70.031608. URL http://link.aps.org/doi/10.1103/PhysRevE.70.031608.

Melanie Ramiasa, John Ralston, Renate Fetzer, Rossen Sedev, Doris M. Fopp-Spori, Christoph Morhard, Claudia Pacholski, and Joachim P. Spatz. Contact line motion on nanorough surfaces: A thermally activated process. *Journal of the American Chemical Society*, 135(19):7159–7171, 2013. doi: 10.1021/ja3104846. URL https://doi.org/10.1021/ja3104846.

M. Rauscher and S. Dietrich. Wetting phenomena in nanofluidics. *Annual Review of Materials Research*, 38(1):143–172, 2008. doi: 10.1146/annurev.matsci.38.060407.132451.

Lord Rayleigh. On the instability of jets. *Proceedings of the London Mathematical Society*, s1-10(1):4–13, 1879. doi: 10.1112/plms/s1-10.1.4. URL https://londmathsoc.onlinelibrary.wiley.com/doi/abs/10.1112/plms/s1-10.1.4.

Lord Rayleigh. Some applications of photography. *Nature*, 44:249–254, 07 1891. URL http://dx.doi.org/10.1038/044249e0.

C. Redon, F. Brochard-Wyart, and F. Rondelez. Dynamics of dewetting. *Phys. Rev. Lett.*, 66(6):715–718, 1991.

C Redon, F Brochard-Wyart, H Hervet, and F Rondelez. Spreading of "heavy" droplets: Ii. experiments. *J. Colloid Interface Sci.*, 149(2):580 – 591, 1992. ISSN 0021-9797. doi: http://dx.doi.org/10.1016/0021-9797(92)90446-S. URL http://www.sciencedirect.com/science/article/pii/002197979290446S.

Paul C. Reeves and Michael A. Celia. A functional relationship between capillary pressure, saturation, and interfacial area as revealed by a pore-scale network model. *Water Resources Research*, 32(8):2345–2358, 1996. ISSN 1944-7973. doi: 10.1029/96WR01105. URL http://dx.doi.org/10.1029/96WR01105.

Günter Reiter. Dewetting of thin polymer films. *Physical Review Letters*, 68:75–78, Jan 1992. doi: 10.1103/PhysRevLett.68.75. URL http://link.aps.org/doi/10.1103/PhysRevLett.68.75.

Günter Reiter. Unstable thin polymer films: rupture and dewetting processes. *Langmuir*, 9(5):1344–1351, 1993. doi: 10.1021/la00029a031.

Günter Reiter and Ashutosh Sharma. Auto-optimization of dewetting rates by rim instabilities in slipping polymer films. *Physical Review Letters*, 87:166103, Oct 2001. doi: 10.1103/PhysRevLett.87.166103. URL https://link.aps.org/doi/10.1103/PhysRevLett.87.166103.

Günter Reiter, Ashutosh Sharma, Alain Casoli, Marie-Odile David, Rajesh Khanna, and Philippe Auroy. Thin film instability induced by long-range forces. *Langmuir*, 15(7):2551–2558, 1999. doi: 10.1021/la981470y. URL http://pubs.acs.org/doi/abs/10.1021/la981470y.

Günter Reiter, Moustafa Hamieh, Pascal Damman, Severine Sclavons, Sylvain Gabriele, Thomas Vilmin, and Elie Raphael. Residual stresses in thin polymer films cause rupture and dominate early stages of dewetting. *Nature Materials*, 4 (10):754–758, 10 2005. URL http://dx.doi.org/10.1038/nmat1484.

Weiqing Ren and Weinan E. Boundary conditions for the moving contact line problem. *Phys. Fluids*, 19(2):022101, 2007.

Weiqing Ren, Dan Hu, and Weinan E. Continuum models for the contact line problem. *Phys. Fluids*, 22(10):102103, 2010.

Osborne Reynolds. On the theory of lubrication and its application to Mr. Beauchamp Tower's experiments, including an experimental determination of the viscosity of olive oil. *Philosophical Transactions of the Royal Society of London*, 177:157–234, 1886.

S. N. Reznik and A. L. Yarin. Spreading of a viscous drop due to gravity and capillarity on a horizontal or an inclined dry wall. *Phys. Fluids*, 14(1):118–132, 2002. doi: http://dx.doi.org/10.1063/1.1426388. URL http://scitation.aip.org/content/aip/journal/pof2/14/1/10.1063/1.1426388.

A. Riaz, M. Hesse, H. A. Tchelepi, and F. M. Orr. Onset of convection in a gravitationally unstable, diffusive boundary layer in porous media. *J. Fluid Mech.*, 548: 87–111, 2006.

Amir Riaz and Hamdi A. Tchelepi. Linear stability analysis of immiscible two-phase flow in porous media with capillary dispersion and density variation. *Physics of Fluids*, 16(12):4727–4737, 2004. doi: 10.1063/1.1812511.

Guillaume Riboux and José Manuel Gordillo. Experiments of drops impacting a smooth solid surface: A model of the critical impact speed for drop splashing. *Phys. Rev. Lett.*, 113:024507, Jul 2014.

Guillaume Riboux and José Manuel Gordillo. The diameters and velocities of the droplets ejected after splashing. *Journal of Fluid Mechanics*, 772:630—648, 2015.

L. A. Richards. Capillary conduction of liquids through porous mediums. *Physics*, 1(5):318–333, 1931. doi: 10.1063/1.1745010. URL https://doi.org/10.1063/1.1745010.

Paul I. Richards. Shock waves on the highway. *Operations Research*, 4(1):42–51, 1956.

E. Rio, A. Daerr, B. Andreotti, and L. Limat. Boundary conditions in the vicinity of a dynamic contact line: Experimental investigation of viscous drops sliding down an inclined plane. *Phys. Rev. Lett.*, 94:024503, Jan 2005.

J. Rodríguez-Rodríguez, A. Sevilla, C. Martínez-Bazán, and J. M. Gordillo. Generation of microbubbles with applications to industry and medicine. *Annual Review of Fluid Mechanics*, 47(1):405–429, 2015.

S. Roman, M. O. Abu-Al-Saud, T. Tokunaga, J. Wan, A. R. Kovscek, and H. A. Tchelepi. Measurements and simulation of liquid films during drainage displacements and snap-off in constricted capillary tubes. *J. Colloid Interface Sci.*, 507: 279–289, 2017.

A. Rothert, R. Richter, and I. Rehberg. Transition from symmetric to asymmetric scaling function before drop pinch-off. *Phys. Rev. Lett.*, 87:084501, Aug 2001. doi: 10.1103/PhysRevLett.87.084501. URL https://link.aps.org/doi/10.1103/PhysRevLett.87.084501.

Jonathan P. Rothstein. Slip on superhydrophobic surfaces. *Annual Review of Fluid Mechanics*, 42(1):89–109, 2010.

John Shipley Rowlinson and Benjamin Widom. *Molecular Theory of Capillarity*. Courier Corporation, 1982.

J.S. Rowlinson. Translation of J. D. van der Waals' "The thermodynamik theory of capillarity under the hypothesis of a continuous variation of density". *Journal of Statistical Physics*, 20(2):197–200, 1979. ISSN 0022-4715. doi: 10.1007/BF01011513. URL http://dx.doi.org/10.1007/BF01011513.

E Ruckenstein and C.S Dunn. Slip velocity during wetting of solids. *J. Colloid Interface Sci.*, 59(1):135 – 138, 1977. doi: http://dx.doi.org/10.1016/0021-9797(77)90347-2. URL http://www.sciencedirect.com/science/article/pii/0021979777903472.

Eli Ruckenstein and Rakesh K. Jain. Spontaneous rupture of thin liquid films. *Journal of Chemical Society, Faraday Transactions. 2*, 70:132–147, 1974. doi: 10.1039/F29747000132. URL http://dx.doi.org/10.1039/F29747000132.

C. Ruppel and J. Kessler. The interaction of climate change and methane hydrates. *Reviews of Geophysics*, 55(1):126–168, 2017. doi: 10.1002/2016RG000534. URL https://agupubs.onlinelibrary.wiley.com/doi/abs/10.1002/2016RG000534.

Kenneth J. Ruschak. Coating flows. *Annual Review of Fluid Mechanics*, 17(1):65–89, 1985. doi: 10.1146/annurev.fl.17.010185.000433. URL https://doi.org/10.1146/annurev.fl.17.010185.000433.

P. G. Saffman and G. I. Taylor. The penetration of a fluid into a porous medium or hele-shaw cell containing a more viscous liquid. *Phil. Trans. R. Soc. Lond. A*, 245 (1242):312–329, 1958.

PG Saffman. Viscous fingering in hele-shaw cells. *Journal of Fluid Mechanics*, 173: 73–94, 1986.

F. Savart. Mémoire sur le choc d'une veine liquide lancée contre un plan circulaire. *Ann. Chim*, 53:337–398, 1833.

M. Sbragaglia, K. Sugiyama, and L. Biferale. Wetting failure and contact line dynamics in a couette flow. *Journal of Fluid Mechanics*, 614:471—493, 2008.

L. Schimmele, M. Napiorkowski, and S. Dietrich. Conceptual aspects of line tensions. *The Journal of Chemical Physics*, 127(16):164715, 2007. doi: 10.1063/1.2799990. URL http://link.aip.org/link/?JCP/127/164715/1.

D. Schmid, B. Scheu, F. B. Wadsworth, B. M. Kennedy, A. Jolly, and D. B. Dingwell. A viscoustobrittle transition in eruptions through clay suspensions. *Geophysical Research Letters*, 44(10):4806–4813, 2017. doi: 10.1002/2017GL073641. URL https://agupubs.onlinelibrary.wiley.com/doi/abs/10.1002/2017GL073641.

L. E. Schmidt, N. C. Keim, W. W. Zhang, and S. R. Nagel. Memory-encoding vibrations in a disconnecting air bubble. *Nature Physics*, 5:343–346, 04 2009. URL http://dx.doi.org/10.1038/nphys1233.

V. Schmidt, J. V. Wittemann, and U. Gösele. Growth, thermodynamics, and electrical properties of silicon nanowires. *Chemical Reviews*, 110(1):361–388, 2010. doi: 10.1021/cr900141g. URL http://dx.doi.org/10.1021/cr900141g.

Reto B. Schoch, Jongyoon Han, and Philippe Renaud. Transport phenomena in nanofluidics. *Reviews of Modern Physics*, 80: 839–883, Jul 2008. doi: 10.1103/RevModPhys.80.839. URL https://link.aps.org/doi/10.1103/RevModPhys.80.839.

L. E. Scriven and C. V. Sterling. The marangoni effects. *Nature*, 187(4733):186–188, 07 1960. URL http://dx.doi.org/10.1038/187186a0.

R.V. Sedev and J.G. Petrov. The critical condition for transition from steady wetting to film entrainment. *Colloids and Surfaces*, 53(1):147–156, 1991.

R. Seemann, S. Herminghaus, and K. Jacobs. Dewetting patterns and molecular forces: A reconciliation. *Physical Review Letters*, 86: 5534–5537, Jun 2001a. doi: 10.1103/PhysRevLett.86.5534. URL http://link.aps.org/doi/10.1103/PhysRevLett.86.5534.

R. Seemann, S. Herminghaus, and K. Jacobs. Shape of a liquid front upon dewetting. *Physical Review Letters*, 87: 196101, Oct 2001b. doi: 10.1103/PhysRevLett.87.196101. URL http://link.aps.org/doi/10.1103/PhysRevLett.87.196101.

Ralf Seemann, Stephan Herminghaus, Chiara Neto, Stefan Schlagowski, Daniel Podzimek, Renate Konrad, Hubert Mantz, and Karin Jacobs. Dynamics and structure formation in thin polymer melt films. *Journal of Physics: Condensed Matter*, 17 (9):S267, 2005. URL `http://stacks.iop.org/0953-8984/17/i=9/a=001`.

Ralf Seemann, Martin Brinkmann, Thomas Pfohl, and Stephan Herminghaus. Droplet based microfluidics. *Rep. Prog. Phys.*, 75(1):016601, 2012. URL `http://stacks.iop.org/0034-4885/75/i=1/a=016601`.

Rachel A. Segalman. Patterning with block copolymer thin films. *Materials Science and Engineering: R: Reports*, 48(6):191–226, 2005. ISSN 0927-796X. doi: http://dx.doi.org/10.1016/j.mser.2004.12.003.

Rachel A. Segalman and Peter F. Green. Dynamics of rims and the onset of spinodal dewetting at liquid/liquid interfaces. *Macromolecules*, 32(3):801–807, 1999. doi: 10.1021/ma981208w.

J. Seiwert, C. Clanet, and D. Quéré. Coating of a textured solid. *Journal of Fluid Mechanics*, 669:55—63, 2011.

Christian Sendner, Dominik Horinek, Lyderic Bocquet, and Roland R. Netz. Interfacial water at hydrophobic and hydrophilic surfaces: Slip, viscosity, and diffusion. *Langmuir*, 25(18):10768–10781, 2009. doi: 10.1021/la901314b. URL `http://dx.doi.org/10.1021/la901314b`. PMID: 19591481.

Pierre Seppecher. Moving contact lines in the cahn-hilliard theory. *International Journal of Engineering Science*, 34(9):977 – 992, 1996. doi: https://doi.org/10.1016/0020-7225(95)00141-7. URL `http://www.sciencedirect.com/science/article/pii/0020722595001417`.

S. A. Setu, R. P. A. Dullens, A. Hernández-Machado, I. Pagonabarraga, D. G. A. L. Aarts, and R. Ledesma-Aguilar. Superconfinement tailors fluid flow at microscales. *Nature Communications*, 6:7297, 06 2015.

Siti Aminah Setu, Ioannis Zacharoudiou, Gareth J. Davies, Denis Bartolo, Sébastien Moulinet, Ard A. Louis, Julia M. Yeomans, and Dirk G. A. L. Aarts. Viscous fingering at ultralow interfacial tension. *Soft Matter*, 9:10599–10605, 2013.

D. Seveno, A. Vaillant, R. Rioboo, H. Adão, J. Conti, and J. De Coninck. Dynamics of wetting revisited. *Langmuir*, 25(22):13034–13044, 2009. doi: 10.1021/la901125a. URL `https://doi.org/10.1021/la901125a`. PMID: 19845346.

Y. Shao-Horn, W. C. Sheng, S. Chen, P. J. Ferreira, E. F. Holby, and D. Morgan. Instability of supported platinum nanoparticles in low-temperature fuel cells. *Topics in Catalysis*, 46(3):285–305, 2007. ISSN 1572-9028. doi: 10.1007/s11244-007-9000-0. URL `http://dx.doi.org/10.1007/s11244-007-9000-0`.

A. Sharma. Many paths to dewetting of thin films: anatomy and physiology of surface instability. *The European Physical Journal E*, 12(3):397–408, 2003. ISSN 1292-895X. doi: 10.1140/epje/e2004-00008-5. URL http://dx.doi.org/10.1140/epje/e2004-00008-5.

Ashutosh Sharma. Relationship of thin film stability and morphology to macroscopic parameters of wetting in the apolar and polar systems. *Langmuir*, 9(3):861–869, 1993a. doi: 10.1021/la00027a042. URL http://pubs.acs.org/doi/abs/10.1021/la00027a042.

Ashutosh Sharma. Relationship of thin film stability and morphology to macroscopic parameters of wetting in the apolar and polar systems. *Langmuir*, 9(3):861–869, 1993b. doi: 10.1021/la00027a042.

Ashutosh Sharma. Equilibrium contact angles and film thicknesses in the apolar and polar systems: role of intermolecular interactions in coexistence of drops with thin films. *Langmuir*, 9(12):3580–3586, 1993c. doi: 10.1021/la00036a038. URL http://pubs.acs.org/doi/abs/10.1021/la00036a038.

Ashutosh Sharma and Rajesh Khanna. Pattern formation in unstable thin liquid films. *Physical Review Letters*, 81:3463–3466, Oct 1998. doi: 10.1103/PhysRevLett.81.3463. URL http://link.aps.org/doi/10.1103/PhysRevLett.81.3463.

Ashutosh Sharma and Günter Reiter. Instability of thin polymer films on coated substrates: Rupture, dewetting, and drop formation. *Journal of Colloid and Interface Science*, 178(2):383 – 399, 1996. ISSN 0021-9797. doi: http://dx.doi.org/10.1006/jcis.1996.0133. URL http://www.sciencedirect.com/science/article/pii/S0021979796901332.

A. Sheludko. Thin liquid films. *Advances in Colloid and Interface Science*, 1(4):391–464, 1967. ISSN 0001-8686. doi: http://dx.doi.org/10.1016/0001-8686(67)85001-2. URL http://www.sciencedirect.com/science/article/pii/0001868667850012.

X. D. Shi, M. P. Brenner, and S. R. Nagel. A cascade of structure in a drop falling from a faucet. *Science*, 265(5169):219–222, 1994. ISSN 0036-8075. doi: 10.1126/science.265.5169.219. URL http://science.sciencemag.org/content/265/5169/219.

Yulii D Shikhmurzaev. Moving contact lines in liquid/liquid/solid systems. *J. Fluid Mech.*, 334:211–249, 2 1997. doi: 10.1017/S0022112096004569.

Yulii D Shikhmurzaev. *Capillary Flows with Forming Interfaces*. CRC Press, 2007.

Tak Shing Chan, Thomas Gueudré, and Jacco H. Snoeijer. Maximum speed of dewetting on a fiber. *Physics of Fluids*, 23(11):112103, 2011.

D. S. Sholl and R. T. Skodje. Late-stage coarsening of adlayers by dynamic cluster coalescence. *Physica A: Statistical Mechanics and its Applications*, 231(4):631 – 647, 1996. ISSN 0378-4371. doi: http://dx.doi.org/10.1016/0378-4371(96)00112-4. URL http://www.sciencedirect.com/science/article/pii/0378437196001124.

David N. Sibley, Nikos Savva, and Serafim Kalliadasis. Slip or not slip? a methodical examination of the interface formation model using two-dimensional droplet spreading on a horizontal planar substrate as a prototype system. *Phys. Fluids*, 24(8):082105, 2012. doi: 10.1063/1.4742895. URL http://link.aip.org/link/?PHF/24/082105/1.

David N. Sibley, Andreas Nold, Nikos Savva, and Serafim Kalliadasis. The contact line behaviour of solid-liquid-gas diffuse-interface models. *Physics of Fluids*, 25(9):092111, 2013. doi: 10.1063/1.4821288. URL https://doi.org/10.1063/1.4821288.

DavidN. Sibley, Andreas Nold, Nikos Savva, and Serafim Kalliadasis. A comparison of slip, disjoining pressure, and interface formation models for contact line motion through asymptotic analysis of thin two-dimensional droplet spreading. *J. Eng. Math.*, pages 1–23, 2014. doi: 10.1007/s10665-014-9702-9. URL http://dx.doi.org/10.1007/s10665-014-9702-9.

A. Siebold, M. Nardin, J. Schultz, A. Walliser, and M. Oppliger. Effect of dynamic contact angle on capillary rise phenomena. *Colloids Surf., A*, 161:81–87, 2000.

A. Sierou and J. R. Lister. Self-similar solutions for viscous capillary pinch-off. *Journal of Fluid Mechanics*, 497:381–403, 2003. doi: 10.1017/S0022112003006736.

E. D. Siggia. Late stages of spinodal decomposition in binary mixtures. *Physical Review A*, 20:595–605, Aug 1979. doi: 10.1103/PhysRevA.20.595. URL https://link.aps.org/doi/10.1103/PhysRevA.20.595.

P. G. Simpkins and V. J. Kuck. Air entrapment in coatings by way of a tip-streaming meniscus. *Nature*, 403:641, 02 2000.

A. Skarke, C. Ruppel, M. Kodis, D. Brothers, and E. Lobecker. Widespread methane leakage from the sea floor on the northern us atlantic margin. *Nature Geoscience*, 7:657–661, 08 2014. URL http://dx.doi.org/10.1038/ngeo2232.

M. Slemrod. Admissibility criteria for propagating phase boundaries in a van der waals fluid. *Archive for Rational Mechanics and Analysis*, 81(4):301–315, 1983.

M v Smoluchowski. Grundriß der koagulationskinetik kolloider lösungen. *Colloid & Polymer Science*, 21(3):98–104, 1917.

J. H. Snoeijer and J. Eggers. Asymptotic analysis of the dewetting rim. *Physical Review E*, 82:056314, 2010.

J. H. Snoeijer, B. Andreotti, G. Delon, and M. Fermigier. Relaxation of a dewetting contact line. part 1. a full-scale hydrodynamic calculation. *Journal of Fluid Mechanics*, 579:63–83, 2007a.

J. H. Snoeijer, N. Le Grand-Piteira, L. Limat, H. A. Stone, and J. Eggers. Cornered drops and rivulets. *Physics of Fluids*, 19(4):042104, 2007b.

J. H. Snoeijer, J. Ziegler, B. Andreotti, M. Fermigier, and J. Eggers. Thick films of viscous fluid coating a plate withdrawn from a liquid reservoir. *Phys. Rev. Lett.*, 100:244502, Jun 2008.

Jacco H. Snoeijer. Free-surface flows with large slopes: Beyond lubrication theory. *Phys. Fluids*, 18(2):021701, 2006.

Jacco H. Snoeijer and Bruno Andreotti. A microscopic view on contact angle selection. *Physics of Fluids*, 20(5):057101, 2008. doi: 10.1063/1.2913675. URL http://link.aip.org/link/?PHF/20/057101/1.

Jacco H. Snoeijer and Bruno Andreotti. Moving contact lines: Scales, regimes, and dynamical transitions. *Annual Review of Fluid Mechanics*, 45(1):269–292, 2013.

Jacco H. Snoeijer, Giles Delon, Marc Fermigier, and Bruno Andreotti. Avoided critical behavior in dynamically forced wetting. *Phys. Rev. Lett.*, 96:174504, 2006.

C. Solans, P. Izquierdo, J. Nolla, N. Azemar, and M. J. Garcia-Celma. Nanoemulsions. *Current Opinion in Colloid and Interface Science*, 10(3–4):102–110, 2005. ISSN 1359-0294. doi: http://dx.doi.org/10.1016/j.cocis.2005.06.004. URL http://www.sciencedirect.com/science/article/pii/S1359029405000348.

M. A. Spaid and G. M. Homsy. Stability of newtonian and viscoelastic dynamic contact lines. *Physics of Fluids (1994-present)*, 8(2):460–478, 1996. doi: http://dx.doi.org/10.1063/1.868800.

Elizabeth J. Spiteri, Ruben Juanes, Martin J. Blunt, and Franklin M. Orr. A new model of trapping and relative permeability hysteresis for all wettability characteristics. *Soc. Pet.Eng. J.*, 13(277), 2008.

James E. Sprittles. Kinetic effects in dynamic wetting. *Phys. Rev. Lett.*, 118:114502, Mar 2017.

T. M. Squires and S. R. Quake. Microfluidics: Fluid physics at the nanoliter scale. *Rev. Mod. Phys.*, 77:977–1026, Oct 2005. doi: 10.1103/RevModPhys.77.977. URL https://link.aps.org/doi/10.1103/RevModPhys.77.977.

D. C. Standnes and T. Austad. Wettability alteration in carbonates: Interaction between cationic surfactant and carboxylates as a key factor in wettability alteration from oil-wet to water-wet conditions. *Colloids and Surfaces A: Physicochemical and Engineering Aspects*, 216(1):243 – 259, 2003. doi: https://doi.org/10.1016/S0927-7757(02)00580-0.

T. G. Stange, D. F. Evans, and W. A. Hendrickson. Nucleation and growth of defects leading to dewetting of thin polymer films. *Langmuir*, 13(16):4459–4465, 1997. doi: 10.1021/la962090k. URL http://dx.doi.org/10.1021/la962090k.

V. M. Starov. Surface forces action in a vicinity of three phase contact line and other current problems in kinetics of wetting and spreading. *Advances in Colloid and Interface Science*, 161(1–2):139–152, 2010. ISSN 0001-8686. doi: http://dx.doi.org/10.1016/j.cis.2010.02.002. URL http://www.sciencedirect.com/science/article/pii/S0001868610000266.

Victor M Starov, Manuel G Velarde, and Clayton J Radke. *Wetting and Spreading Dynamics*. CRC press, 2007.

J. Stenhammar, A. Tiribocchi, R. J. Allen, D. Marenduzzo, and M. E. Cates. Continuum theory of phase separation kinetics for active Brownian particles. *Physical Review Letters*, 111:145702, Oct 2013. doi: 10.1103/PhysRevLett.111.145702. URL http://link.aps.org/doi/10.1103/PhysRevLett.111.145702.

J. P. Stokes, D. A. Weitz, J. P. Gollub, A. Dougherty, M. O. Robbins, P. M. Chaikin, and H. M. Lindsay. Interfacial stability of immiscible displacement in a porous medium. *Phys. Rev. Lett.*, 57: 1718–1721, Oct 1986. doi: 10.1103/PhysRevLett.57.1718. URL https://link.aps.org/doi/10.1103/PhysRevLett.57.1718.

H. A. Stone. Interfaces: in fluid mechanics and across disciplines. *J. Fluid Mech.*, 645:1–25, 2010.

H. A. Stone, A. D. Stroock, and A. Ajdari. Engineering flows in small devices: Microfluidics toward a lab-on-a-chip. *Annual Review of Fluid Mechanics*, 36(1):381–411, 2004. URL https://doi.org/10.1146/annurev.fluid.36.050802.122124.

Yi Sui, Hang Ding, and Peter D.M. Spelt. Numerical simulations of flows with moving contact lines. *Annu. Rev. Fluid Mech.*, 46 (1):97–119, 2014. doi: 10.1146/annurev-fluid-010313-141338. URL http://dx.doi.org/10.1146/annurev-fluid-010313-141338.

Jeanman Sur, Andrea L. Bertozzi, and Robert P. Behringer. Reverse undercompressive shock structures in driven thin film flow. *Phys. Rev. Lett.*, 90:126105, Mar 2003.

J. Swift and P. C. Hohenberg. Hydrodynamic fluctuations at the convective instability. *Physical Review A*, 15:319–328, Jan 1977. doi: 10.1103/PhysRevA.15.319. URL http://link.aps.org/doi/10.1103/PhysRevA.15.319.

Michael L. Szulczewski, Christopher W. MacMinn, Howard J. Herzog, and Ruben Juanes. Lifetime of carbon capture and storage as a climate-change mitigation technology. *Proceedings of the National Academy of Sciences*, 109(14):5185–5189, 2012. doi: 10.1073/pnas.1115347109. URL http://www.pnas.org/content/109/14/5185.abstract.

255

P. Tabeling, G. Zocchi, and A. Libchaber. An experimental study of the saffman-taylor instability. *Journal of Fluid Mechanics*, 177:67–82, 1987.

Kazumasa A. Takeuchi, Masaki Sano, Tomohiro Sasamoto, and Herbert Spohn. Growing interfaces uncover universal fluctuations behind scale invariance. *Scientific Reports*, 1(34):1–5, 2011.

D. V. Talapin, A. L. Rogach, M. Haase, and H. Weller. Evolution of an ensemble of nanoparticles in a colloidal solution: theoretical study. *The Journal of Physical Chemistry B*, 105(49):12278–12285, 2001. doi: 10.1021/jp012229m. URL http://dx.doi.org/10.1021/jp012229m.

L H Tanner. The spreading of silicone oil drops on horizontal surfaces. *Journal of Physics D: Applied Physics*, 12(9):1473, 1979. URL http://stacks.iop.org/0022-3727/12/i=9/a=009.

Y. Tao, A. Yeckel, and J. J. Derby. Steady-state and dynamic models for particle engulfment during solidification. *Journal of Computational Physics*, 315:238–263, 2016. ISSN 0021-9991. doi: http://dx.doi.org/10.1016/j.jcp.2016.03.050. URL http://www.sciencedirect.com/science/article/pii/S0021999116300092.

G. I. Taylor. Deposition of a viscous fluid on the wall of a tube. *Journal of Fluid Mechanics*, 10(2):161–165, 1961a. doi: 10.1017/S0022112061000159.

G. I. Taylor. Deposition of a viscous fluid on the wall of a tube. *J. Fluid Mech.*, 10: 161–165, 1961b.

P. Taylor. Ostwald ripening in emulsions. *Advances in Colloid and Interface Science*, 75(2):107–163, 1998. ISSN 0001-8686. doi: http://dx.doi.org/10.1016/S0001-8686(98)00035-9. URL http://www.sciencedirect.com/science/article/pii/S0001868698000359.

U. Thiele. Patterned deposition at moving contact lines. *Advances in Colloid and Interface Science*, 206:399–413, 2014.

U. Thiele, M. Mertig, and W. Pompe. Dewetting of an evaporating thin liquid film: Heterogeneous nucleation and surface instability. *Physical Review Letters*, 80:2869–2872, Mar 1998. doi: 10.1103/PhysRevLett.80.2869. URL http://link.aps.org/doi/10.1103/PhysRevLett.80.2869.

U. Thiele, M. G. Velarde, K. Neuffer, and Y. Pomeau. Film rupture in the diffuse interface model coupled to hydrodynamics. *Physical Review E*, 64:031602, Aug 2001a. doi: 10.1103/PhysRevE.64.031602. URL http://link.aps.org/doi/10.1103/PhysRevE.64.031602.

Uwe Thiele, Manuel G. Velarde, and Kai Neuffer. Dewetting: Film rupture by nucleation in the spinodal regime. *Phys. Rev. Lett.*, 87: 016104, Jun 2001b. doi: 10.1103/PhysRevLett.87.016104. URL http://link.aps.org/doi/10.1103/PhysRevLett.87.016104.

C V Thompson. Grain growth in thin films. *Annual Review of Materials Science*, 20(1):245–268, 1990. doi: 10.1146/annurev.ms.20.080190.001333. URL https://doi.org/10.1146/annurev.ms.20.080190.001333.

C. V. Thompson. Solid-state dewetting of thin films. *Annual Review of Materials Research*, 42(1):399–434, 2012. doi: 10.1146/annurev-matsci-070511-155048. URL https://doi.org/10.1146/annurev-matsci-070511-155048.

Peter A. Thompson and Mark O. Robbins. Simulations of contact-line motion: Slip and the dynamic contact angle. *Phys. Rev. Lett.*, 63:766–769, Aug 1989. doi: 10.1103/PhysRevLett.63.766. URL http://link.aps.org/doi/10.1103/PhysRevLett.63.766.

S. T. Thoroddsen, T. G. Etoh, and K. Takehara. Experiments on bubble pinch-off. *Physics of Fluids*, 19(4):042101, 2007. doi: 10.1063/1.2710269. URL https://doi.org/10.1063/1.2710269.

S. T. Thoroddsen, T. G. Etoh, and K. Takehara. High-speed imaging of drops and bubbles. *Annual Review of Fluid Mechanics*, 40(1):257–285, 2008.

Todd Thorsen, Richard W. Roberts, Frances H. Arnold, and Stephen R. Quake. Dynamic pattern formation in a vesicle-generating microfluidic device. *Phys. Rev. Lett.*, 86:4163–4166, Apr 2001. doi: 10.1103/PhysRevLett.86.4163. URL https://link.aps.org/doi/10.1103/PhysRevLett.86.4163.

M. Tjahjadi, H. A. Stone, and J. M. Ottino. Satellite and subsatellite formation in capillary breakup. *Journal of Fluid Mechanics*, 243:297–317, 1992. doi: 10.1017/S0022112092002738.

S. M. Troian, E. Herbolzheimer, S. A. Safran, and J. F. Joanny. Fingering instabilities of driven spreading films. *EPL (Europhysics Letters)*, 10(1):25, 1989.

Mathias Trojer, Michael L. Szulczewski, and Ruben Juanes. Stabilizing fluid-fluid displacements in porous media through wettability alteration. *Physical Review Applied*, 3:054008, May 2015. doi: 10.1103/PhysRevApplied.3.054008. URL http://link.aps.org/doi/10.1103/PhysRevApplied.3.054008.

A. S. Utada et al. Monodisperse double emulsions generated from a microcapillary device. *Science*, 308(5721):537–541, 2005. ISSN 0036-8075. doi: 10.1126/science.1109164. URL http://science.sciencemag.org/content/308/5721/537.

C. van Duijn, L. Peletier, and I. Pop. A new class of entropy solutions of the buckley-leverett equation. *SIAM Journal on Mathematical Analysis*, 39(2):507–536, 2007.

Richard van Hameren, Peter Schön, Arend M. van Buul, Johan Hoogboom, Sergiy V. Lazarenko, Jan W. Gerritsen, Hans Engelkamp, Peter C. M. Christianen, Hans A. Heus, Jan C. Maan, Theo Rasing, Sylvia Speller, Alan E. Rowan, Johannes A.

A. W. Elemans, and Roeland J. M. Nolte. Macroscopic hierarchical surface patterning of porphyrin trimers via self-assembly and dewetting. *Science*, 314(5804): 1433, 12 2006.

W. van Hoeve, B. Dollet, M. Versluis, and D. Lohse. Microbubble formation and pinch-off scaling exponent in flow-focusing devices. *Physics of Fluids*, 23(9):092001, 2011. doi: 10.1063/1.3631323. URL https://doi.org/10.1063/1.3631323.

Wim van Saarloos. Front propagation into unstable states. *Physics Reports*, 386(2): 29–222, 2003.

V. van Steijn, C. R. Kleijn, and M. T. Kreutzer. Flows around confined bubbles and their importance in triggering pinch-off. *Phys. Rev. Lett.*, 103:214501, Nov 2009a. doi: 10.1103/PhysRevLett.103.214501. URL https://link.aps.org/doi/10.1103/PhysRevLett.103.214501.

V. van Steijn, C. R. Kleijn, and M. T. Kreutzer. Flows around confined bubbles and their importance in triggering pinch-off. *Phys. Rev. Lett.*, 103:214501, 2009b.

E. Vandre, M. S. Carvalho, and S. Kumar. On the mechanism of wetting failure during fluid displacement along a moving substrate. *Physics of Fluids*, 25(10): 102103, 2013.

E. Vandre, M. S. Carvalho, and S. Kumar. Characteristics of air entrainment during dynamic wetting failure along a planar substrate. *J. Fluid Mech.*, 747:119–140, 2014.

Eric Vandre, Marcio S. Carvalho, and Satish Kumar. Delaying the onset of dynamic wetting failure through meniscus confinement. *J. Fluid Mech.*, 707:496–520, 2012.

O.V. Voinov. Hydrodynamics of wetting. *Fluid Dynamics*, 11(5):714–721, 1976. ISSN 0015-4628. doi: 10.1007/BF01012963. URL http://dx.doi.org/10.1007/BF01012963.

P.W. Voorhees. The theory of Ostwald ripening. *Journal of Statistical Physics*, 38(1-2):231–252, 1985. ISSN 0022-4715. doi: 10.1007/BF01017860. URL http://dx.doi.org/10.1007/BF01017860.

A. Vrij. Possible mechanism for the spontaneous rupture of thin, free liquid films. *Discuss. Faraday Soc.*, 42:23–33, 1966. doi: 10.1039/DF9664200023. URL http://dx.doi.org/10.1039/DF9664200023.

C. Wagner. Theorie der alterung von niederschlägen durch umlösen (Ostwald-Reifung). *Zeitschrift für Elektrochemie, Berichte der Bunsengesellschaft für physikalische Chemie*, 65(7-8):581–591, 1961. ISSN 0005-9021. doi: 10.1002/bbpc.19610650704. URL http://dx.doi.org/10.1002/bbpc.19610650704.

E. W. Washburn. The dynamics of capillary flow. *Phys. Rev.*, 17(273):273–283, 1921.

Yuli Wei, Cesare M. Cejas, Rémi Barrois, Rémi Dreyfus, and Douglas J. Durian. Morphology of rain water channeling in systematically varied model sandy soils. *Phys. Rev. Applied*, 2:044004, Oct 2014. doi: 10.1103/PhysRevApplied.2.044004. URL https://link.aps.org/doi/10.1103/PhysRevApplied.2.044004.

J. H. Weijs, A. Marchand, B. Andreotti, D. Lohse, and J. H. Snoeijer. Origin of line tension for a Lennard-Jones nanodroplet. *Physics of Fluids*, 23(2):022001, 2011. doi: 10.1063/1.3546008. URL http://link.aip.org/link/?PHF/23/022001/1.

Steven J. Weinstein and Kenneth J. Ruschak. Coating flows. *Annual Review of Fluid Mechanics*, 36(1):29–53, 2004. doi: 10.1146/annurev.fluid.36.050802.122049. URL https://doi.org/10.1146/annurev.fluid.36.050802.122049.

Robert N. Wenzel. Resistance of solid surafces to wetting by water. *Industrial & Engineering Chemistry*, 28(8):988–994, 1936.

Jason S. Wexler, Ian Jacobi, and Howard A. Stone. Shear-driven failure of liquid-infused surfaces. *Phys. Rev. Lett.*, 114:168301, Apr 2015.

D.A. White and J.A. Tallmadge. Theory of drag out of liquids on flat plates. *Chemical Engineering Science*, 20(1):33–37, 1965.

G. M. Whitesides. The origins and the future of microfluidics. *Nature*, 442:368–373, 2006.

H. Wijshoff. The dynamics of the piezo inkjet printhead operation. *Physics Reports*, 491(4):77–177, 2010. ISSN 0370-1573. doi: https://doi.org/10.1016/j.physrep.2010.03.003. URL http://www.sciencedirect.com/science/article/pii/S0370157310000827.

D Wilkinson and J F Willemsen. Invasion percolation: a new form of percolation theory. *Journal of Physics A: Mathematical and General*, 16(14):3365, 1983.

M. B Williams and S. H Davis. Nonlinear theory of film rupture. *Journal of Colloid and Interface Science*, 90(1):220–228, 1982. ISSN 0021-9797. doi: http://dx.doi.org/10.1016/0021-9797(82)90415-5. URL http://www.sciencedirect.com/science/article/pii/0021979782904155.

A M Willis and J B Freund. Enhanced droplet spreading due to thermal fluctuations. *Journal of Physics: Condensed Matter*, 21(46):464128, 2009. URL http://stacks.iop.org/0953-8984/21/i=46/a=464128.

S. D. R. Wilson. The drag-out problem in film coating theory. *Journal of Engineering Mathematics*, 16(3):209–221, 1982.

T. A. Witten and L. M. Sander. Diffusion-limited aggregation, a kinetic critical phenomenon. *Physical Review Letters*, 47:1400–1403, Nov 1981.

R. Wittkowski, A. Tiribocchi, J. Stenhammar, R. J. Allen, D. Marenduzzo, and M. E. Cates. Scalar 4 field theory for active-particle phase separation. *Nature Communications*, 5(4351), 07 2014. URL http://dx.doi.org/10.1038/ncomms5351.

T. J. Woehl, C. Park, J. E. Evans, I. Arslan, W. D. Ristenpart, and N. D. Browning. Direct observation of aggregative nanoparticle growth: Kinetic modeling of the size distribution and growth rate. *Nano Letters*, 14(1):373–378, 2014. doi: 10.1021/nl4043328. URL http://dx.doi.org/10.1021/nl4043328.

Tak-Sing Wong, Sung Hoon Kang, Sindy K. Y. Tang, Elizabeth J. Smythe, Benjamin D. Hatton, Alison Grinthal, and Joanna Aizenberg. Bioinspired self-repairing slippery surfaces with pressure-stable omniphobicity. *Nature*, 477:443, 09 2011.

A. M. Worthington. *A Study of Splashes*. Longmans, Green, and Company, 1908.

L. Wu, Z. Dong, M. Kuang, Y. Li, F. Li, L. Jiang, and Y. Song. Printing patterned fine 3D structures by manipulating the three phase contact line. *Advanced Functional Materials*, 25(15):2237–2242, 2015. ISSN 1616-3028. doi: 10.1002/adfm.201404559. URL http://dx.doi.org/10.1002/adfm.201404559.

Qingfang Wu and Harris Wong. A slope-dependent disjoining pressure for non-zero contact angles. *J. Fluid Mech.*, 506:157–185, 5 2004. doi: 10.1017/S0022112004008420.

F. Brochard Wyart and J. Daillant. Drying of solids wetted by thin liquid films. *Canadian Journal of Physics*, 68(9):1084–1088, 1990. doi: 10.1139/p90-151.

Y. Xia and G. M. Whitesides. Soft lithography. *Annual Review of Materials Science*, 28(1):153–184, 1998. doi: 10.1146/annurev.matsci.28.1.153. URL http://www.annualreviews.org/doi/abs/10.1146/annurev.matsci.28.1.153.

R. Xie, A. Karim, J. F. Douglas, C. C. Han, and R. A. Weiss. Spinodal dewetting of thin polymer films. *Physical Review Letters*, 81:1251–1254, Aug 1998. doi: 10.1103/PhysRevLett.81.1251. URL https://link.aps.org/doi/10.1103/PhysRevLett.81.1251.

Lei Xu, Wendy W. Zhang, and Sidney R. Nagel. Drop splashing on a dry smooth surface. *Phys. Rev. Lett.*, 94:184505, 2005.

Xinpeng Xu and Tiezheng Qian. Contact line motion in confined liquid–gas systems: Slip versus phase transition. *The Journal of Chemical Physics*, 133(20):204704, 2010. doi: 10.1063/1.3506886. URL https://doi.org/10.1063/1.3506886.

D. Yamamoto, C. Nakajima, A. Shioi, M. P. Krafft, and K. Yoshikawa. The evolution of spatial ordering of oil drops fast spreading on a water surface. *Nature Communications*, 6:7189 EP –, 05 2015. URL http://dx.doi.org/10.1038/ncomms8189.

E.K. Yeh, John Newman, and C.J. Radke. Equilibrium configurations of liquid droplets on solid surfaces under the influence of thin-film forces: Part I. Thermodynamics. *Colloids and Surfaces A: Physicochemical and Engineering Aspects*, 156(1–3):137–144, 1999. ISSN 0927-7757. doi: http://dx.doi.org/10.1016/S0927-7757(99)00065-5. URL http://www.sciencedirect.com/science/article/pii/S0927775799000655.

S. G. Yiantsios and R. H. Davis. Close approach and deformation of two viscous drops due to gravity and van der Waals forces. *Journal of Colloid and Interface Science*, 144(2):412–433, 1991. ISSN 0021-9797. doi: http://dx.doi.org/10.1016/0021-9797(91)90407-Y. URL http://www.sciencedirect.com/science/article/pii/002197979190407Y.

Thomas Young. An essay on the cohesion of fluids. *Philos. Trans. R. Soc. Lond.*, 95: 65–87, 1805. URL http://www.jstor.org/stable/107159.

Tony S. Yu, Vladimir Bulović, and A. E. Hosoi. Coarsening and solidification via solvent-annealing in thin liquid films. *Journal of Fluid Mechanics*, 723:69–90, 005 2013. doi: 10.1017/jfm.2013.115. URL https://www.cambridge.org/core/article/div-class-title-coarsening-and-solidification

P. Yue, J. J. Feng, C. Liu, and J. Shen. A diffuse-interface method for simulating two-phase flows of complex fluids. *Journal of Fluid Mechanics*, 515:293–317, 2004. doi: 10.1017/S0022112004000370.

P. Yue, C. Zhou, and J. J. Feng. Sharp-interface limit of the cahn–hilliard model for moving contact lines. *Journal of Fluid Mechanics*, 645:279–294, 2010. doi: 10.1017/S0022112009992679.

Pengtao Yue and James J. Feng. Wall energy relaxation in the cahn–hilliard model for moving contact lines. *Physics of Fluids*, 23(1):012106, 2011. doi: 10.1063/1.3541806. URL https://doi.org/10.1063/1.3541806.

H. Zeng, B. Zhao, Y. Tian, M. Tirrell, L. G. Leal, and J. N. Israelachvili. Transient surface patterns during adhesion and coalescence of thin liquid films. *Soft Matter*, 3:88–93, 2007. doi: 10.1039/B613198K. URL http://dx.doi.org/10.1039/B613198K.

Zorana Zeravcic, Vinothan N. Manoharan, and Michael P. Brenner. Colloquium: Toward living matter with colloidal particles. *Rev. Mod. Phys.*, 89:031001, Sep 2017. doi: 10.1103/RevModPhys.89.031001. URL https://link.aps.org/doi/10.1103/RevModPhys.89.031001.

B. Zhao, C. W. MacMinn, and R. Juanes. Wettability control on multiphase flow in patterned microfluidics. *Proc. Natl. Acad. Sci. U.S.A.*, 113(37):10251–6, 2016.

Benzhong Zhao, Amir Alizadeh Pahlavan, Luis Cueto-Felgueroso, and Ruben Juanes. Forced wetting transition and bubble pinch-off in a capillary tube. *Phys. Rev. Lett.*, 120:084501, Feb 2018.

Meng-Hua Zhao, Xiao-Peng Chen, and Qing Wang. Wetting failure of hydrophilic surfaces promoted by surface roughness. *Scientific Reports*, 4:5376, 06 2014.

B. V. Zhmud, F. Tiberg, and K. Hallstensson. Dynamics of capillary rise. *J. Colloid Interface Sci.*, 228:263–269, 2000.

L. Zhornitskaya and A. Bertozzi. Positivity-preserving numerical schemes for lubrication-type equations. *SIAM Journal on Numerical Analysis*, 37(2):523–555, 1999. doi: 10.1137/S0036142998335698. URL https://doi.org/10.1137/S0036142998335698.

Min-Yao Zhou and Ping Sheng. Dynamics of immiscible-fluid displacement in a capillary tube. *Physical Review Letters*, 64: 882–885, Feb 1990. doi: 10.1103/PhysRevLett.64.882. URL http://link.aps.org/doi/10.1103/PhysRevLett.64.882.

Yingxi Zhu and Steve Granick. Rate-dependent slip of newtonian liquid at smooth surfaces. *Phys. Rev. Lett.*, 87: 096105, Aug 2001. doi: 10.1103/PhysRevLett.87.096105. URL http://link.aps.org/doi/10.1103/PhysRevLett.87.096105.